Nature-inspired microfluidic propulsion using magnetic artificial cilia

Khaderi, Syed Nizamuddin

Nature-inspired microfluidic propulsion using magnetic artificial cilia

Syed Nizamuddin Khaderi

Nature-inspired microfluidic propulsion using magnetic artificial cilia

Syed Nizamuddin Khaderi

PhD Thesis
University of Groningen
The Netherlands

University of Groningen
Zernike Institute
for Advanced Materials

Zernike Institute for Advanced Materials
ISBN: 978-90-367-5072-1
This work is part of the 6th Framework European Union project 'Artic', under contract STRP 033274.

RIJKSUNIVERSITEIT GRONINGEN

Nature-inspired microfluidic propulsion using magnetic artificial cilia

Proefschrift

ter verkrijging van het doctoraat in de
Wiskunde en Natuurwetenschappen
aan de Rijksuniversiteit Groningen
op gezag van de
Rector Magnificus, dr. E. Sterken,
in het openbaar te verdedigen op
vrijdag 16 september 2011
om 13.15 uur

door

Syed Nizamuddin Khaderi

geboren op 22 oktober 1982
te Chennai, India

Promotor:	Prof. dr. ir. P. R. Onck
Beoordelingscommissie:	Prof. dr. S. Verpoorte Prof. dr. R. Superfine Prof. dr. H. Gao

ISBN: 978-90-367-5072-1

To my parents

Contents

Chapter 1
Introduction

1.1 Lab-on-a-chip

Lab-on-a-chip (LOC) is a technology that aims at performing analyses of biological samples (such as blood and urine), conventionally performed in a clinical lab, on a small chip. The analyses range from simple tests on biological samples to sophisticated DNA and cell analysis. The primary reason for the development of LOC is that the reduction in the sample size of the analyte enhances control and accuracy of bio-chemical reactions. The added advantage of the small size of the device is that smaller amounts of analyte and reagents are needed to perform the reactions, and the device becomes portable. As the facilities needed to perform the bio-chemical analysis are encapsulated in a small device, it was aptly named a micro-total analysis system (micro-TAS) by Manz *et al.* (1990).

The important tasks performed in a micro-TAS are the treatment of an analyte with suitable reagents, subsequent chemical reactions, separation of the molecules resulting from the reactions and the detection of these molecules. One example of bio-chemical reactions is a polymerase chain reaction (PCR), which is performed to amplify the concentration of specific DNA strands by orders of magnitude. In this process, the analyte (containing a few DNA strands) is subjected to cyclic heating and cooling. When a PCR is miniaturised, because of the small sample size, the thermal response time becomes low leading to a drastic reduction in the PCR cycle time (Kopp *et al.*, 1998). In another example, it was shown that the miniaturisation can lead to very rapid separation of bio-molecules using methods such as electrophoresis and chromatography (Manz *et al.*, 1994; Harrison *et al.*, 1993).

The micro-TAS can be encapsulated into a hand-held device which can be used for point-of-care (POC) testing, where the clinical diagnosis can be performed at the location of the patient even by an untrained person. Instruments to perform simple analyses such as to measure glucose levels (e.g. Bayer Contour, see www.bayercontourusb.us), hemoglobin levels (e.g. Hemocue, see www.hemocue.com) and lithium levels (e.g. Medimate Multireader, see www.medimate.com) have been commercialised. The importance of POC testing is especially applicable to patients with Type I diabetes, for which self monitoring of blood glucose is considered as an integral part of their treatment (Klonoff, 2007). It is also proven that POC devices can reduce the mortality rates in critical care units of hospitals (Rossi & Khan, 2004). Such instruments are also of immense help in disaster-affected areas, where it is difficult to perform regular clinical tests (Kost *et al.*, 2006).

As the surface to volume ratio is high in a LOC, physical phenomena associated with surfaces (e.g. surface tension and electrokinetics) gain importance. In addition, as the length scales involved are small (typically less than a millimetre), the viscous

forces in the fluid dominate over the inertial forces leading to laminar flow profiles in typical micro-TAS (Squires & Quake, 2005). While some of these are beneficial, the presence of others are detrimental. For instance, the fabrication of devices to perform individual operations on a micro-TAS cannot always be done by simply downscaling conventional methodologies. Mixing of an analyte with another fluid is difficult to achieve in a microfluidic device due to the laminar nature of flow at these length scales. Another challenge is the pumping of fluids through the microchannels and testing chambers on a lab-on-a-chip. In some applications, a local control of the flow is also necessary, which calls for a localised pumping system that can be embedded into a microchannel.

The fluid propulsion in microfluidic systems is performed using three different approaches: (i) mechanical methods – such as external syringe pumps, peristaltic pumps (Pilarski *et al.*, 2005; Liao *et al.*, 2005; Grover *et al.*, 2003; Svensson *et al.*, 2010; Lai & Folch, 2011; Gu *et al.*, 2004) and membrane pumps, (ii) using the electrokinetic properties of the fluids – such as in electro-osmotic pumps (Zeng *et al.*, 2002; Litster *et al.*, 2010) and magneto-hydrodynamic pumps (Lemoff & Lee, 2000; Homsy *et al.*, 2000; Jang & Lee, 2000; West *et al.*, 2002) – and (iii) acoustic methods (Langelier *et al.*, 2009; Nguyen & White, 1999; Yeo & Friend, 2009; Y. Bourquin & Cooper, 2010). These fluid propulsion mechanisms have been developed only in recent years. On the other hand, nature has been using remarkable fluid propulsion mechanisms at micron length scales for the locomotion and fluid transport, which are primarily based on mechanical actuators that beat back and forth. In this work, we use principles inspired by natural systems to design a fluid propulsion system that can operate inside microchannels and controlled by external force fields.

1.2 Micron-scale fluid manipulation in nature

Micron-scale fluid manipulation occurs in nature for two main reasons: locomotion and fluid transport. These are often (but not always[1]) performed using hair-like motile appendages knows as cilia and flagella (Murase, 1992; Cooper & Hausman, 1992). The cilia can beat in two different ways. Firstly, the cilia on the external surfaces of organisms such as opalina beat in an asymmetric manner with a distinct effective and recovery stroke (see Fig. 1.1 (a)-(c)). During the effective stroke the cilia are straight and push large amounts of fluid, whereas during the recovery stroke they stay closer to the cell surface and pull back only a small amount of fluid. The net fluid propelled is in the direction of the effective stroke (see Fig. 1.1(c)). The hydrodynamic interaction causes adjacent cilia to beat out-of-phase leading to a wave-like motion which is commonly referred to as metachronal waves (see Fig. 1.1 (b)). Secondly, there is another category of cilia, called nodal cilia that are present on node cells of embryos and revolve with a whirling motion about an axis that is non-orthogonal to the surface on which they are attached (see Fig. 1.1 (d)-(e)). These cilia create a large flow when they are away from the surface and a low flow in the opposite direction when they are close to the surface. As a result, a net flow is created in the direction of the upward stroke. A flagellum that is attached to a cell propagates waves of transverse displacement along its length to exert a force on the fluid in the direction of the wave, which causes the flagellum and cell to move in the opposite direction (see Fig. 1.1 (f)-(g)).

[1] The locomotion of a Cyanobacterium takes place by propagating waves of lateral displacement along its surface (Ehlers *et al.*, 1996).

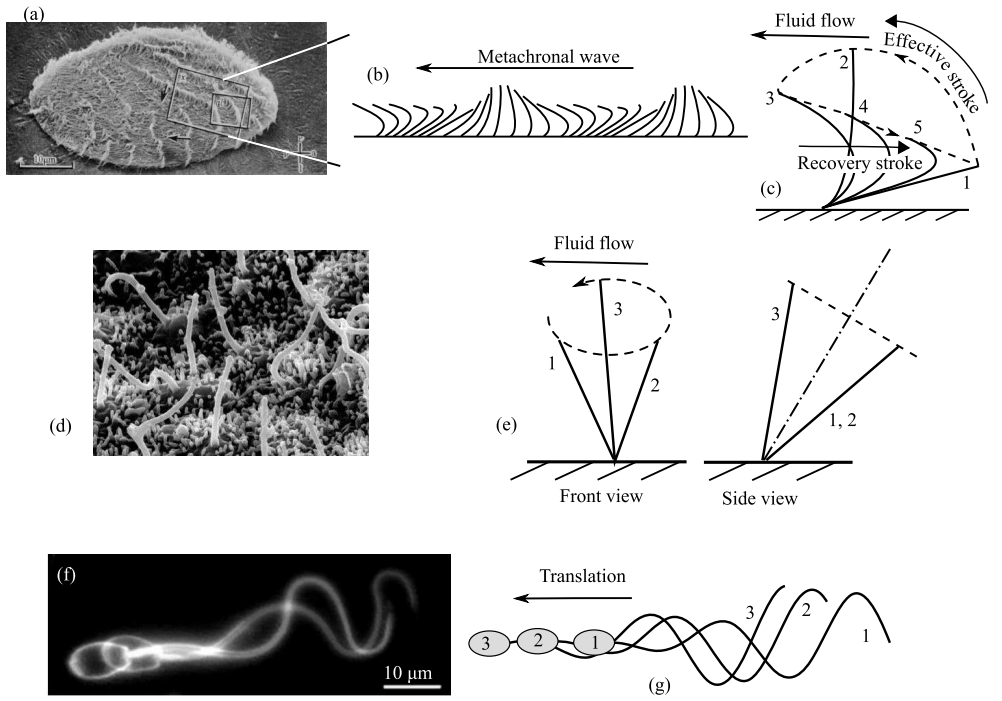

Figure 1.1: *(a) Micrograph of cilia on Opalina (Tamm & Horridge, 1970). (b) Metachronal waves are formed due to out-of-phase beating of the cilia. (c) Schematic diagram showing the movement of cilia. (d) Micrograph of cilia on node cells (http://www.physics.ubc.ca/steve/research/A-TopProt.html). (e) Schematic representation of the motion of nodal cilia. (f) and (g) Snapshots of a flagellum attached to a sperm cell (Woolley, 2010). The numbers refer to the sequences in time. The flagellum creates a wave of transverse displacement for fluid propulsion, whereas the cilia in the case of Opalina beat with a distinct effective and recovery stroke, and in the case of node cells move such that they describes a cone.*

Flagella are primarily known for locomotion (Lighthill, 1976; Brennen & Winet, 1977), whereas the cilia perform different functions like locomotion and fluid transport (Murase, 1992; Brennen & Winet, 1977; Gardiner, 2005). In some cases, the cilia are non-motile and perform sensing function (Gardiner, 2005; Malone *et al.*, 2007). The flagella are usually attached to a cell body, whereas the cilia occur in groups over the surface of microorganisms (for example on the surface of a Paramecium) or tissues of organs. The cilia are associated with micro- as well as macroorganisms. Microorganisms (such as Paramecia, Opalina and Centophores) have cilia on their outer surface for locomotion. In organisms such as Lophophorates, the cilia create a water current that brings suspended food particles near the organism's mouth (Strathmann, 1973). The nodal cilia create a fluid flow that initiates the left-right asymmetry during embryonic development (Halbert *et al.*, 1976; Ibanez-Tallon *et al.*, 2003). The cilia on the surfaces of ventricular system of the brain play an important role in the transport of the cerebro-spinal fluid (Roth *et al.*, 1985; Ibanez-Tallon *et al.*, 2003). Cilia are also present in the inner-lining of the respiratory tract and propel mucus out of the lungs.

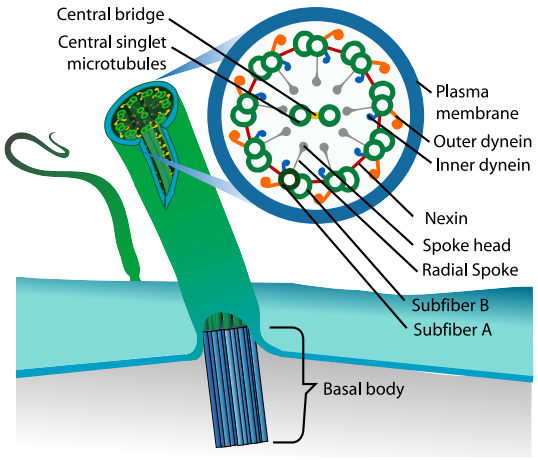

Figure 1.2: *Cartoon showing the microstructure of the axoneme (www.en.wikipedia.org/wiki/cilium).*

1.3 Structure of cilia and flagella

The cilia and flagella are appendages that protrude from the cell surface (see Fig. 1.2). They have a similar microstructure, the axoneme, which consists of a circular array of nine microtubular doublets (composed of microtubules A and B) that are connected together with the linker proteins called nexin. At the centre of the doublet array two microtubules are connected through rigid links to form the central pair. Each doublet is connected to the central pair through radial spokes. The axoneme is driven by the ATP-powered motor protein dynein that are attached to the inner and outer sides of microtubule A. During an operation cycle, the dyneins attach themselves to microtubule B of the adjacent doublet and exert a force such that two adjacent microtubular doublets slide relative to each other (Sale & Satir, 1977). As the axoneme is fixed to the cell at its base, this sliding is translated into bending of the axoneme. Interestingly, local actuation of the dyneins creates a global beating of a flagellum or a cilium. However, a clear picture of how the dynein actuation is translated into a global motion of the cilia and flagella is not yet available. The typical length scales associated with cilia and flagella are as follows. The length of cilia is usually between 10 and 20 microns, whereas flagella can have a length up to 200 microns. The diameter of the axoneme is 250 nm. The distance between two inner and outer dyneins along the length of a microtubule is 96 nm and 24 nm (Ibanez-Tallon *et al.*, 2003), respectively. In the non-motile and nodal cilia the central pair is absent, while in the former also the motor proteins are absent.

1.4 Hydrodynamics at small length scales

At the small length scales of cilia and flagella (up to hundreds of microns), viscous forces dominate over the inertial forces leading to low values in Reynolds number[2] (Re $<<$ 1)- the ratio of fluid inertial forces to the viscous forces. To get a feel for the viscous forces, consider a microorganism swimming at a steady velocity. The distance (normalised to

[2]For cilia of length 10 μm that beat at a frequency of 20 Hz the Reynolds number is 2×10^{-3}.

its body length) this organism continues to move after its propulsion mechanism has stopped scales with Re[3] (Lauga & Powers, 2009). Since Re << 1, the organism cannot coast after it has stopped its propulsion mechanism. This is because the viscous forces are so huge that they dissipate the kinetic energy of the organism instantaneously.

There are two consequences of high viscous forces. Firstly, a certain class of cyclic actuator motion – called reciprocal motion, in which the forward motion is exactly the same as the backward motion – cannot lead to a net fluid propulsion. An example of reciprocal motion is the back and forth oscillation of a rigid rod about one of its ends. During a reciprocal motion of the actuator the flow created during the forward motion of the actuator will be cancelled by the flow of the backward motion, creating zero net fluid transport. Secondly, the fluid behaviour is rate independent, i.e., even if the forward reciprocal motion of the actuator takes place faster than its backward motion, there will be no net fluid flow. The flow created by the fast forward motion will be exactly cancelled by the slow reverse motion of the actuator. Rigorous mathematical proofs of these two properties can be found elsewhere (Childress, 1981; Lauga & Powers, 2009).

As the cilia and flagella are able to create a fluid flow, their motion should be 'non-reciprocal'. The cilia motion is non-reciprocal because of its distinct effective and recovery stroke. In the case of flagella, the wave of transverse displacements causes the slope of any segment before and after it has reached a maximum displacement to differ by a sign. This makes the flagella motion to be non-reciprocal. The non-reciprocal motion can also occur at larger length scales. For instance, a Cyanobacterium swims through a fluid by propagating waves of lateral displacement on its surface. Individual points on the surface oscillate about a mean position in a reciprocal fashion, but the directional wave of lateral displacements makes the surface motion non-reciprocal (Stone & Samuel, 1996).

1.5 Objective of the thesis

The goal of this thesis is to mimic the non-reciprocal motion of natural cilia in order to propel fluids through microchannels. As the local dynein actuation mechanism is not yet fully understood, we take an alternative approach. The idea is to design artificial cilia that are attached to the inner surface of microchannels and to actuate them with externally-applied force fields (not through dynein-like internal forcing), so that they can beat in an asymmetric motion and create a fluid transport. These artificial cilia can be realised using thin polymer films with embedded magnetic nano-particles that can respond to an external magnetic field, see Fig. 1.3. Depending on the nature of the magnetic particles the film can be either paramagnetic or permanently magnetic.

The objective of this thesis is two-fold: Firstly, to identify for what geometries, material properties and applied magnetic fields a magnetic film will mimic the asymmetric motion of natural cilia. Secondly, to identify how the created flow can be enhanced by controlling different factors such as the cilia geometry, magnetic field, cilia spacing, channel height, fluid inertia and out-of-phase motion. We answer these questions using numerical models that capture the physical behaviour of magnetically-driven artificial cilia. These numerical models predict the cilia deformation and the resulting fluid flow by solving the Maxwell's equations, solid dynamics equations and Navier-Stokes equations in a fully-coupled manner.

[3]Assuming the mass density of the organism is the same as the fluid.

1.6 Thesis outline

The outline of the thesis is as follows. In chapter 2, we derive the equations of a two-dimensional coupled solid-fluid magneto-mechanical model used to simulate the cilia motion. We model the cilia as elastic Euler-Bernoulli beams taking into consideration geometric non-linearity and inertia of the cilia in a Lagrangian framework. The magnetic field is calculated by solving the Maxwell's equations using a boundary element approach. The Navier-Stokes equations, which capture the behaviour of the fluid flow, are solved within an Eulerian setting for the velocity and pressure using finite elements. The solid-fluid coupling is performed by imposing the no-slip condition at the nodal points of the Euler-Bernoulli beam elements using Lagrange multipliers within a fictitious domain framework. The physical dimensionless parameters that govern the behaviour of the artificial cilia are derived from the principle of virtual work.

A number of artificial cilia configurations that show an asymmetric beat motion are designed by choosing different material properties, initial geometries and magnetic fields in chapter 3. The fluid flow created by these cilia is analysed in the limit of low Reynolds number (Stokes regime). The performance of the cilia is also analysed in terms of dimensionless parameters, introduced in chapter 2, which leads to the parameter space in which the cilia can perform optimally.

The flow and pressure generated are typical parameters that specify the characteristics of any pumping device. These are analysed as a function of the cilia spacing and channel geometry in chapter 4. It will be shown that the flow and pressure generated increase when the cilia spacing is decreased. However, when the channel height is decreased, the flow generated decreases, while the pressure increases. This chapter provides guidelines for selecting the optimal channel size, cilia spacing and cilia length for a specific channel morphology.

Literature suggests that the performance of cilia can be improved for mixing applications by exploiting inertial forces. In chapter 5, we analyse the effect of inertial forces on the fluid transported by the artificial cilia. It will be shown that the presence of inertia brings in many interesting phenomena. The flow created by the cilia can be significantly larger than in the Stokes regime, and it becomes unidirectional in some cases. The flow created is due to the combination of the asymmetric area and temporal asymmetry (char-

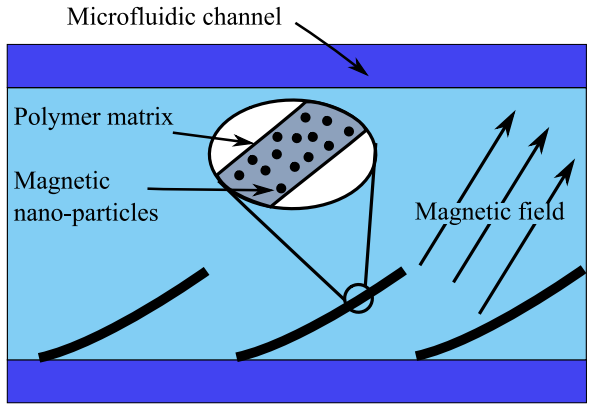

Figure 1.3: *Schematic picture of the approach taken. The artificial cilia consist of a polymer matrix with embedded magnetic nano-particles. The cilia exhibit an asymmetric motion when a tuned external magnetic field is applied.*

acterised by a slow effective and fast recovery stroke). In order to delineate the effect of asymmetric area, temporal and orientational (characterised by the asymmetry of the cilia motion with respect to the microchannel) asymmetries we study the flow created using a model problem in which the individual contributions of these three asymmetries can be identified (chapter 6).

In nature, adjacent cilia beat with a phase difference (see Fig. 1.1 (b)), which will induce an additional non-reciprocating motion, on top of the asymmetric motion of individual cilia. This leads to the formation of metachronal waves. In chapter 7, we analyse the effect of magnetically-induced metachronal waves on the fluid transport created by the cilia.

In chapter 8, we explore the principle used by Cyanobacteria for fluid transport: collective non-reciprocal motion. The cilia are made to oscillate about a mean position in a reciprocal manner, but such that they have a phase difference with their neighbours. This causes the cilia motion to be collectively non-reciprocal. We investigate the physical mechanisms that cause the fluid transport and find under what conditions the flow created reaches a maximum value.

So far we used a two-dimensional numerical model to simulate the fluid transport caused by the cilia. This framework assumes that the width of the cilia is much larger than the cilia length and channel height. To explore the effect of cilia width and out-of-plane motion on the resulting flow, a three-dimensional numerical model is developed in chapter 9. The flow created by an array of cilia with the metachronal waves travelling in and perpendicular to the beating plane is also investigated.

The main results of the thesis are finally summarised and guidelines for the optimal design of the artificial cilia are given.

Chapter 2
Magneto-mechanical model

2.1 Introduction

In this chapter we derive the numerical model and dimensionless parameters used in this thesis for two-dimensional simulations of fluid flow due to magnetically-driven artificial cilia. The physical quantities to be solved for are the magnetic field, cilia motion and fluid flow. The magnetic field and magnetization of the cilia are calculated by solving the Maxwell's equations using a boundary element approach at every instant in the deformed configuration. From the magnetization and the applied magnetic field, the magnetic forces acting on the cilia are calculated, which are given as input to the solid dynamics model. The solid dynamics model considers the cilia to be an assemblage of Euler-Bernoulli beam elements, taking into consideration inertia and geometric nonlinearity within an updated Lagrangian framework. The Navier-Stokes equation, which describes the fluid behaviour, is solved using an Eulerian finite element approach. The solid and fluid domains are coupled using the no-slip boundary condition on the cilia within a fictitious domain framework (van Loon *et al.*, 2006).

In the magneto-mechanical model a range of forces can be identified: the elastic and inertia forces of the cilia, the viscous and inertia forces of the fluid and the magnetic forces acting on the cilia. By introducing relevant length and time scales into the principle of virtual work, we derive how these forces scale with the different parameters involved. From the dimensionless form of the virtual work equation, we identify five dimensionless parameters: the magnetic number - the ratio of magnetic forces to elastic forces, the fluid number - the ratio of fluid viscous forces to elastic forces, the inertia number - the ratio of inertial to elastic forces of the cilia, the flapping Reynolds number - the ratio of inertia forces to viscous forces in the fluid and the diffusion Reynolds number - the ratio of momentum diffusion time to ciliary cycle time. These five dimensionless parameters completely capture the physical behaviour of the cilia and fluid flow, in addition to the geometric parameters such as cilia spacing and channel height.

Based on Khaderi, *et al. Nature-inspired microfluidic propulsion using magnetic actuation*, Physical Review E, 2009, **79**, 046304 and Khaderi, *et al. Magnetically-actuated artificial cilia: the effect of fluid inertia and metachrony*, submitted.

2.2 Equations of motion

2.2.1 Solid dynamics model

As a starting point for the Euler-Bernoulli beam element formulation we use the principle of virtual work (Malvern, 1977); i.e., the virtual work of the external forces ($\delta W_{\text{ext}}^{t+\Delta t}$) is equal to the internal virtual work ($\delta W_{\text{int}}^{t+\Delta t}$),

$$\delta W_{\text{int}}^{t+\Delta t} = \delta W_{\text{ext}}^{t+\Delta t}, \tag{2.1}$$

with

$$\delta W_{\text{int}}^{t+\Delta t} = \int_V \left(\sigma \delta\epsilon + \rho(\ddot{u}\delta u + \ddot{v}\delta v)\right) dV, \tag{2.2}$$

where u and v are the axial and transverse displacements of a point along the beam and ρ is the mass density. Furthermore, σ is the axial stress and ϵ is the corresponding strain, given by

$$\epsilon = \frac{\partial u}{\partial x} + \frac{1}{2}\left(\frac{\partial v}{\partial x}\right)^2 - y\frac{\partial^2 v}{\partial x^2}.$$

The external virtual work is

$$\begin{aligned} \delta W_{\text{ext}}^{t+\Delta t} = &\int \left(f_x \delta u + f_y \delta v + N_z \frac{\partial \delta v}{\partial x}\right) A dx \\ &+ \int \left(t_x \delta u + t_y \delta v\right) b dx, \end{aligned} \tag{2.3}$$

where f_x and f_y are the magnetic body forces in axial and transverse directions, N_z is the magnetic body couple in the out-of-plane direction, t_x and t_y are the surface tractions and b is the out-of-plane thickness of the film.

It is assumed that the solid material is isotropic and linear elastic, specified by the elastic modulus E and Poisson's ration ν. We follow the approach used by Annabattula *et al.* (2010) to linearise and discretise the principal of virtual work to arrive at the discretised form of the virtual work equation at time $t + \Delta t$ (see appendix A),

$$\delta \boldsymbol{p}^T \left(\boldsymbol{K}\Delta \boldsymbol{p} + \boldsymbol{M}\ddot{\boldsymbol{p}}^{\mathrm{t}+\Delta \mathrm{t}} - \boldsymbol{F}_{\text{ext}}^{\mathrm{t}+\Delta \mathrm{t}} + \boldsymbol{F}_{\text{int}}^{\mathrm{t}}\right) = 0, \tag{2.4}$$

where $\boldsymbol{K}$ is the stiffness matrix that combines both material and geometric contributions, $\boldsymbol{M}$ is the mass matrix which can be found in (Cook *et al.*, 2001), $\boldsymbol{F}_{\text{ext}}^{\mathrm{t}+\Delta \mathrm{t}}$ is the external force vector, $\boldsymbol{F}_{\text{int}}^{\mathrm{t}}$ is the internal force vector, $\Delta \boldsymbol{p}$ is the nodal displacement increment vector and $\ddot{\boldsymbol{p}}$ is the nodal acceleration vector.

2.2.2 Fluid dynamics model

The principle of virtual work in the rate form for the fluid problem is (Bathe, 1996)

$$\int_V \sigma_{ij}\delta D_{ij} dV + \rho^f \int_V \frac{du_i}{dt}\delta u_i dV + \int_V \delta p \frac{\partial u_i}{\partial x_i} dV = 0, \tag{2.5}$$

where the first and the second terms represent the work due to the internal stresses and inertia forces in the fluid, respectively, while the third term imposes the incompressibility

condition. In Eqn. 2.5, σ_{ij} represent the components of stress tensor in the fluid, D_{ij} represent the components of the deformation rate tensor in the fluid, ρ^f is the fluid density, u_i[1] represents the components of fluid velocity in the i^{th} direction, $\frac{d}{dt} = \frac{\partial}{\partial t} + u_i \frac{\partial}{\partial x_i}$ represents the total derivative, p is the pressure and $dV = bdxdy$. The constitutive relation for the fluid is $\sigma_{ij} = -p\delta_{ij} + 2\mu D_{ij}$, where μ is the fluid viscosity. It is to be noted that x represents a spatial point in the fluid domain (Eulerian point of view), while it represents the position occupied by a material point on the beam in the solid domain (Lagrangian point of view). The following shape functions are used to interpolate velocity and pressure:

$$\begin{aligned} \left\{ \begin{array}{c} u_1 \\ u_2 \end{array} \right\} &= \left[\begin{array}{cccccccc} \phi_1 & 0 & \phi_2 & 0 & \phi_3 & 0 & \dots \\ 0 & \phi_1 & 0 & \phi_2 & 0 & \phi_3 & \dots \end{array} \right] \left\{ \begin{array}{cccc} u_1^1, & u_2^1, & \dots \end{array} \right\}^T \\ &= \phi_{Ii} U_I = \boldsymbol{\phi}^T \boldsymbol{U}, \\ p &= \left[\begin{array}{cccc} \psi_1 & \psi_2 & \psi_3 & \dots \end{array} \right] \left\{ \begin{array}{cccc} p^1, & p^2, & p^3 & \dots \end{array} \right\}^T = \psi_I P_I = \boldsymbol{\psi}^T \boldsymbol{P}, \end{aligned} \tag{2.6}$$

where, u_i^J represents the components of fluid velocity in the i^{th} direction at the J^{th} node, p^J represents the magnitude of pressure at the J^{th} node and ϕ_J and ψ_J are the shape functions used to interpolate the nodal velocities and pressure, respectively. The shape functions are chosen so that the resulting element satisfies the Inf-Sup condition. In this work we use the Taylor-Hood Q_2Q_1 element which interpolates the velocities quadratically and the pressures linearly (Bathe, 1996). Using Eqn. 2.6 the various terms in the virtual work equation are evaluated (see appendix B):

$$\int_V \sigma_{ij} \delta D_{ij} dV = \int_V \left(-p\delta_{ij} + 2\mu D_{ij}\right) \delta D_{ij} = \delta \boldsymbol{U}^T \left(\boldsymbol{K^{UU}} \boldsymbol{U} + \boldsymbol{K^{UP}} \boldsymbol{P} \right), \tag{2.7}$$

$$\int_V \delta p \frac{\partial u_i}{\partial x_i} dV = \int_V \delta p_I \psi_I \frac{\partial \phi_{Ji}}{\partial x_i} U_J dV = \delta p_I \int_V \psi_I \frac{\partial \phi_{Ji}}{\partial x_i} dV U_J = \delta \boldsymbol{P}^T \left(\boldsymbol{K^{UP}} \right)^{\boldsymbol{T}} \boldsymbol{U}. \tag{2.8}$$

Assuming that the solution at time t is known, the convective term is linearized with respect to the known solution at time t and the time derivative of velocity is discretised using an implicit Euler scheme. Neglecting the higher order terms we get (see appendix B):

$$\begin{aligned} \int_V \frac{du_i^{t+\Delta t}}{dt} \delta u_i dV &= \rho^f \int_V \left(\delta u_i \frac{\partial u_i^{t+\Delta t}}{\partial t} + \delta u_i \frac{\partial u_i^{t+\Delta t}}{\partial x_j} u_j^{t+\Delta t} \right) dV \\ &= \delta \boldsymbol{U}^T \hat{\boldsymbol{M}} \boldsymbol{U} + \delta \boldsymbol{U}^T \boldsymbol{K}^1 \boldsymbol{U} + \delta \boldsymbol{U}^T \boldsymbol{K}^2 \boldsymbol{U} - \delta \boldsymbol{U}^T \boldsymbol{F^f}. \end{aligned}$$

Substituting the above expressions in Eqn. 2.5 yields its discretised form

$$\delta \boldsymbol{U}^T \boldsymbol{K^{UP}} \boldsymbol{P} + \delta \boldsymbol{U}^T \hat{\boldsymbol{K}}_{\boldsymbol{f}} \boldsymbol{U} - \delta \boldsymbol{U}^T \boldsymbol{F^f} + \delta \boldsymbol{P}^T (\boldsymbol{K^{UP}})^{\boldsymbol{T}} \boldsymbol{U} = 0, \tag{2.9}$$

where $\hat{\boldsymbol{K}}_{\boldsymbol{f}} = \boldsymbol{K^{UU}} + \hat{\boldsymbol{M}} + \boldsymbol{K}^1 + \boldsymbol{K}^2$.

[1] u (without a subscript) represents the axial displacement of a point on the beam, while u_i (with a subscript) represents the fluid velocity.

2.2.3 Fluid-structure interaction

We now couple the Lagrangian beam element formulation of section 2.2.1 to the Eulerian finite element fluid model of section 2.2.2. The solid beam is considered as an internal boundary to the fluid domain. The solid and fluid models are coupled using the constraint that the velocity (or displacement) of the solid is equal to the velocity (or displacement) of the fluid. This coupling is established using the method of Lagrange multipliers (Lanczos, 1952). In what follows, we apply the constraint to the fluid dynamics model, then add the virtual work done by the constraint force to the solid dynamics model and finally couple the equations so that the solid and the fluid equations of motion can be solved implicitly.

We first add the variation of the Lagrange multiplier times the constraint to the fluid dynamics model,

$$\begin{aligned}\delta \boldsymbol{U}^T \boldsymbol{K^{UP}} \boldsymbol{P} + \delta \boldsymbol{U}^T \hat{\boldsymbol{K}}_{\boldsymbol{f}} \boldsymbol{U} - \delta \boldsymbol{U}^T \boldsymbol{F^f} + \delta \boldsymbol{P}^T (\boldsymbol{K^{UP}})^{\boldsymbol{T}} \boldsymbol{U} \\ + \delta(\lambda_i^J (u_i^{Jf} - \dot{p}_i^J)) = 0,\end{aligned} \tag{2.10}$$

where, u_i^{Jf} and $\dot{p}_i^J$ represent the components of the fluid and solid beam velocity, respectively, in the i^{th} direction at the location where the J^{th} node of the solid beam is present. Discretising the constraint equation (see appendix B) yields,

$$\begin{aligned}\delta \boldsymbol{U}^T \boldsymbol{K^{UP}} \boldsymbol{P} + \delta \boldsymbol{U}^T \hat{\boldsymbol{K}}_{\boldsymbol{f}} \boldsymbol{U} - \delta \boldsymbol{U}^T \boldsymbol{F^f} + \delta \boldsymbol{P}^T (\boldsymbol{K^{UP}})^{\boldsymbol{T}} \boldsymbol{U} + \delta \boldsymbol{U}^T \boldsymbol{\phi}^J \boldsymbol{\lambda}^J \\ + \delta \boldsymbol{\lambda}^{JT} (\boldsymbol{\phi^{JT}} \boldsymbol{U} - \boldsymbol{A} \dot{\boldsymbol{p}}^J) = 0,\end{aligned}$$

where $\boldsymbol{A}$ is a matrix that eliminates the rotational degrees of freedom from $\dot{\boldsymbol{p}}$. It can be noted that the term $\delta \boldsymbol{U}^T \boldsymbol{\phi}^J \boldsymbol{\lambda}^J$ in the above equation represents the virtual work done by the Lagrange multiplier, i.e., the Lagrange multiplier acts as a force due to the constraint. Hence, the components of the Lagrange multiplier are to be interpreted as fluid drag forces. Invoking the arbitrary nature of the virtual fields and performing the standard finite element assembly yields the following set of equations

$$\hat{\boldsymbol{K}}_{\boldsymbol{f}} \boldsymbol{U} + \boldsymbol{K^{UP}} \boldsymbol{P} + \boldsymbol{\Phi} \boldsymbol{\lambda} = \boldsymbol{F^f}, \quad \left(\boldsymbol{K^{UP}}\right)^{\boldsymbol{T}} \boldsymbol{U} = 0, \quad \boldsymbol{\Phi^T} \boldsymbol{U} - \boldsymbol{A} \dot{\boldsymbol{p}} = 0. \tag{2.11}$$

The fluid drag forces are now considered as nodal forces, whose virtual work is an additional contribution to Eqn. 2.4. This leads to

$$\delta \boldsymbol{p}^T \left(\boldsymbol{K} \Delta \boldsymbol{p} + \boldsymbol{M} \ddot{\boldsymbol{p}}^{\mathrm{t}+\Delta \mathrm{t}} - \boldsymbol{F}_{\mathrm{ext}}^{\mathrm{t}+\Delta \mathrm{t}} + \boldsymbol{F}_{\mathrm{int}}^{\mathrm{t}} \right) - \boldsymbol{\lambda}^T \boldsymbol{A} \delta \boldsymbol{p} = 0, \tag{2.12}$$

where

$$\boldsymbol{\lambda} = \left\{ \begin{array}{cc} \boldsymbol{\lambda}^1, & \boldsymbol{\lambda}^2 \end{array} \right\}^T = \left\{ \begin{array}{cccc} \lambda_1^1, & \lambda_2^1, & \lambda_1^2, & \lambda_2^2 \end{array} \right\}^T$$

is the Lagrange multiplier vector, λ_i^J is the Lagrange multiplier at the J^{th} node in the i^{th} direction. In general, the node of the solid beam is present inside a fluid element and does not coincide with a fluid node, so that the constraint is satisfied in an approximate sense. As the virtual quantity $\delta \boldsymbol{p}$ is arbitrary, we can write

$$\boldsymbol{K} \Delta \boldsymbol{p} + \boldsymbol{M} \ddot{\boldsymbol{p}}^{\mathrm{t}+\Delta \mathrm{t}} - \boldsymbol{F}_{\mathrm{ext}}^{\mathrm{t}+\Delta \mathrm{t}} + \boldsymbol{F}_{\mathrm{int}}^{\mathrm{t}} - \boldsymbol{A}^T \boldsymbol{\lambda} = 0. \tag{2.13}$$

The motion of the film with time is obtained by solving Eqn. 2.13 with appropriate initial and boundary conditions. Newmark's integration scheme is used to integrate Eqn. 2.13 in time, based on which Eqn. 2.13 can be re-written to solve for the nodal velocities as

$$\hat{\boldsymbol{K}} \dot{\boldsymbol{p}}^{\mathrm{t}+\Delta \mathrm{t}} - \boldsymbol{A}^T \boldsymbol{\lambda} = \boldsymbol{F}_s^{\mathrm{t}+\Delta \mathrm{t}}, \tag{2.14}$$

where

$$\begin{aligned}\hat{\boldsymbol{K}} &= \frac{1}{\gamma\Delta t}(\Delta t^2\beta\boldsymbol{K}+\boldsymbol{M}),\\ \boldsymbol{F}_s^{\mathrm{t}+\Delta\mathrm{t}} &= \boldsymbol{F}_{\mathrm{ext}}^{\mathrm{t}+\Delta\mathrm{t}} - \boldsymbol{F}_{\mathrm{int}}^{\mathrm{t}} - \Delta t\boldsymbol{K}\left[\dot{\boldsymbol{p}}^{\mathrm{t}} + \frac{1}{2}\Delta t(1-2\beta)\ddot{\boldsymbol{p}}^{\mathrm{t}}\right]\\ &\quad + (\Delta t^2\beta\boldsymbol{K}+\boldsymbol{M})\frac{\dot{\boldsymbol{p}}^t + \ddot{\boldsymbol{p}}^t\Delta t(1-\gamma)}{\gamma\Delta t},\end{aligned} \tag{2.15}$$

and γ and β are integration parameters. Equation 2.14 contains the discretised equations of motion for one beam element. After performing the standard finite element assembly procedure (Cook *et al.*, 2001) we get the discretised equations of motion for the whole film (dropping the superscript $(t+\Delta t)$):

$$\hat{\boldsymbol{K}}_{\boldsymbol{s}}\dot{\boldsymbol{p}} - \boldsymbol{A}^T\boldsymbol{\lambda} = \boldsymbol{F}_{\boldsymbol{s}}. \tag{2.16}$$

Combining the equations of motion for the solid (Eqn. 2.16) and fluid (Eqn. 2.11) results in

$$\begin{bmatrix} \hat{\boldsymbol{K}}_{\boldsymbol{f}} & \boldsymbol{K}^{\boldsymbol{UP}} & \boldsymbol{0} & \boldsymbol{\Phi} \\ (\boldsymbol{K}^{\boldsymbol{UP}})^{\boldsymbol{T}} & \boldsymbol{0} & \boldsymbol{0} & \boldsymbol{0} \\ \boldsymbol{0} & \boldsymbol{0} & \hat{\boldsymbol{K}}_s & -\boldsymbol{A}^T \\ \boldsymbol{\Phi}^{\boldsymbol{T}} & \boldsymbol{0} & -\boldsymbol{A} & \boldsymbol{0} \end{bmatrix} \begin{Bmatrix} \boldsymbol{U} \\ \boldsymbol{P} \\ \dot{\boldsymbol{p}} \\ \boldsymbol{\lambda} \end{Bmatrix} = \begin{Bmatrix} \boldsymbol{F}^{\boldsymbol{f}} \\ \boldsymbol{0} \\ \boldsymbol{F}_s \\ \boldsymbol{0} \end{Bmatrix}. \tag{2.17}$$

This set of equations is solved to obtain the velocities at the solid and fluid nodal points, the pressure in the fluid and the Lagrange multipliers at the solid nodal points. It is to be noted that in Eqn. 2.17 the velocity of the film and the fluid are simultaneously solved for every time increment. This approach is commonly referred to as the monolithic approach.

2.2.4 Magnetostatics

Maxwell's equations for the magnetostatic problem with no free currents are (Jackson, 1974)

$$\boldsymbol{\nabla}\cdot\boldsymbol{B} = 0 \tag{2.18}$$

$$\boldsymbol{\nabla}\times\boldsymbol{H} = 0, \tag{2.19}$$

with the constitutive relation

$$\boldsymbol{B} = \mu_0(\boldsymbol{M}+\boldsymbol{H}), \tag{2.20}$$

where $\boldsymbol{B}$ is the magnetic flux density (or magnetic induction), $\boldsymbol{H}$ is the magnetic field, $\boldsymbol{M}$ is the magnetization which includes the remnant magnetization, and μ_0 is the permeability of free space. Substituting Eqn. 2.20 into Eqn. 2.18 yields

$$\boldsymbol{\nabla}\cdot\boldsymbol{H} = -\boldsymbol{\nabla}\cdot\boldsymbol{M}. \tag{2.21}$$

As $\boldsymbol{\nabla}\times\boldsymbol{H}=0$, a scalar potential ϕ exists, such that $\boldsymbol{H}=-\boldsymbol{\nabla}\phi$. Substituting this in Eqn. 2.21 yields a Poisson equation for ϕ, $\nabla^2\phi = -\boldsymbol{\nabla}\cdot\boldsymbol{M}$. By taking into consideration

the effect of discontinuity in the medium, the general solution of the Poisson equation can be found (Jackson, 1974), resulting in

$$\phi(\boldsymbol{x}) = -\frac{1}{4\pi}\oint \frac{\boldsymbol{n'}\cdot\boldsymbol{M}(\boldsymbol{x'})}{|\boldsymbol{x}-\boldsymbol{x'}|}dS' + \frac{1}{4\pi}\int \frac{\boldsymbol{\nabla'}\cdot\boldsymbol{M}(\boldsymbol{x'})}{|\boldsymbol{x}-\boldsymbol{x'}|}dV'. \tag{2.22}$$

where $\boldsymbol{n'}$ is the outward normal to the surface of V. The magnetic field $\boldsymbol{H}(x)$ can be found from the gradient of $\phi(x)$.

We now discretise the film into a chain of rectangular segments, within which the magnetization is assumed to be uniform. So that $\boldsymbol{\nabla'}\cdot\boldsymbol{M} = 0$ and the volume integral vanishes. The field now is only due to the jump of magnetization across the surface of each segment and is given by the surface integral in Eqn. 2.22. The magnetic field in coordinates local to the segment i (denoted by $\hat{}$) due its four surfaces can now be calculated at any position $(\hat{x}, \hat{y})$ by evaluating the surface integral in Eqn. 2.22, resulting in

$$\hat{\boldsymbol{H}}_i \;\; = \boldsymbol{G}_i\; \hat{\boldsymbol{M}}_i. \tag{2.23}$$

where $\hat{\boldsymbol{M}} = [\;\hat{M}_x \quad \hat{M}_y\;]^T$, $\hat{\boldsymbol{H}} = [\;\hat{H}_x \quad \hat{H}_y\;]^T$ and $\boldsymbol{G}_i$ can be obtained from Eqn. 2.22 (see appendix C). Note that in this section Einstein's summation convention is not applied. The field due to segment i with respect to the global coordinates is

$$\boldsymbol{H}_i = \boldsymbol{R}_i\; \hat{\boldsymbol{H}}_i, \tag{2.24}$$

where $\boldsymbol{R}_i$ is

$$\boldsymbol{R}_i = \begin{bmatrix} \cos\theta_i & -\sin\theta_i \\ \sin\theta_i & \cos\theta_i \end{bmatrix}, \tag{2.25}$$

with θ_i the orientation of the segment i with respect to the global coordinates. The field at any element j because of the magnetization of all the segments throughout the film is

$$\boldsymbol{H}_j \;\; = \;\; \boldsymbol{H}_0 + \sum_{i=1}^{N} \boldsymbol{R}_i\boldsymbol{G}_{ij}\hat{\boldsymbol{M}}_i = \boldsymbol{H}_0 + \boldsymbol{H}_{\text{self}}, \tag{2.26}$$

where $\boldsymbol{G}_{ij}$ properly accounts for the relative positioning of segments i and j and the geometry of segment i, $\boldsymbol{H}_0$ is the externally applied magnetic field, far away from the film, and N is the total number of segments. Equation 2.26 clearly shows that the magnetic field $\boldsymbol{H}$ in the film is the sum of the external field $\boldsymbol{H}_0$ and the demagnetizing field $\boldsymbol{H}_{\text{self}}$. By rotating $\boldsymbol{H}_j$ back to the local coordinates we get

$$\hat{\boldsymbol{H}}_j \;\; = \;\; \boldsymbol{R}_j^T\boldsymbol{H}_0 + \sum_{i=1}^{N} \boldsymbol{R}_j^T\boldsymbol{R}_i\boldsymbol{G}_{ij}\hat{\boldsymbol{M}}_i. \tag{2.27}$$

For the situation of a permanently magnetized film with magnetization $\hat{\boldsymbol{M}}_i, i = 1, \ldots, N$, Eqn. 2.27 gives the magnetic field in all the segments.

However, in case of a super-paramagnetic film, the magnetization $\hat{\boldsymbol{M}}_j$ is not known a-priori, but depends on the local magnetic field through

$$\begin{aligned} \hat{\boldsymbol{M}}_j \;\; &= \;\; \hat{\boldsymbol{\chi}}\;\hat{\boldsymbol{H}}_j \\ &= \;\; \hat{\boldsymbol{\chi}}\boldsymbol{R}_j^T\boldsymbol{H}_0 + \sum_{i=1}^{N} \hat{\boldsymbol{\chi}}\boldsymbol{R}_j^T\boldsymbol{R}_i\boldsymbol{G}_{ij}\hat{\boldsymbol{M}}_i, \end{aligned} \tag{2.28}$$

with

$$\boldsymbol{\chi} = \begin{bmatrix} \hat{\chi}_x & \hat{\chi}_{xy} \\ \hat{\chi}_{xy} & \hat{\chi}_y \end{bmatrix}.$$

There are N similar pairs of equations. In total these are $2 \times N$ equations for the $2 \times N$ unknown magnetizations. This set of equations is solved to get the magnetization with respect to the local coordinate frame. From the magnetization, the field can be found from Eqn. 2.27 and the magnetic flux density can be found by using Eqn. 2.20. The advantage of the proposed method is that we need not model the medium around the magnetic film to determine the magnetic field in the film. The verification of the model is performed using a super-paramagnetic film and is given in appendix D. Once the magnetization is calculated by solving Eqn. 2.28, the magnetic body couple and body force per unit volume can be found from $\boldsymbol{N} = \boldsymbol{M} \times \boldsymbol{B}_0$ and $\boldsymbol{f} = \boldsymbol{M} \cdot \boldsymbol{\nabla} \boldsymbol{B}_0$ (with $\boldsymbol{B}_0 = \mu_0 \boldsymbol{H}_0$), and given as input to Eqn. 2.3.

The magneto-mechanical fluid-structure interaction model developed in this section is benchmarked against a reference case in appendix E, and the spatial and temporal convergence of the method in the context of cilia caused flow is shown in appendix F.

2.3 Dimensional analysis

In this section we use the principle of virtual work to identify the dimensionless parameters that govern the deformation behaviour of the artificial cilia. Considering only the transverse deformations and magnetic body torques we have,

$$\int EI \frac{\partial^2 v}{\partial x^2} \frac{\partial^2 \delta v}{\partial x^2} dx + \int \rho A \frac{\partial^2 v}{\partial t^2} \delta v dx - \int N_z \frac{\partial \delta v}{\partial x} A dx - \int \lambda \delta v b dx = 0,$$

where, the first term represents the virtual elastic work done by the internal moments, the second term represents the virtual work done by the inertial forces of the beam, the third term represents the virtual work done by the magnetic couple and the last term represents the work done by the fluid drag forces. In the above equation, λ is the traction due to fluid drag on the film in the transverse direction and has units of force per unit area. This is in contrast to the λ used in section 2.2.3, which has units of force per unit out-of-plane width. We introduce the dimensionless variables V, T and X, such that $v = VL$, $x = XL$ and $t = Tt_{\text{ref}}$, where L is a characteristic length (taken to be the length of the cilia) and t_{ref} is a characteristic time. Substitution yields

$$\int \left(\frac{Ebh^3}{12L^2} \frac{\partial^2 V}{\partial X^2} \frac{\partial^2 \delta V}{\partial X^2} + \frac{\rho bhL^2}{t_{\text{ref}}^2} \delta V \frac{\partial^2 V}{\partial T^2} \right) dX - \int \left(N_z hb \frac{\partial \delta V}{\partial X} - \lambda L \delta V b \right) dX = 0, \quad (2.29)$$

from which the elastic ($Ebh^3/12L^2$), the inertial ($\rho bhL^2/t_{\text{ref}}^2$), the magnetic ($N_z hb$) and the viscous ($\lambda L \delta V b$) terms can be easily identified. By normalising with the elastic term, we get

$$\int \left(\left(\frac{\partial^2 V}{\partial X^2} \frac{\partial^2 \delta V}{\partial X^2} \right) + I_n \left(\frac{\partial^2 V}{\partial T^2} \delta V \right) \right) dX - \int \left(M_n \left(\frac{\partial \delta V}{\partial X} \right) + F_n \delta V \right) dX = 0. \quad (2.30)$$

Here, the three governing dimensionless numbers are defined as the inertia number $I_n = 12(\rho/E)(L/t_{\text{ref}})^2(L/h)^2$ (the ratio of inertial to elastic force), the magnetic number $M_n = 12(N_z/E)(L/h)^2$ (the ratio of magnetic to elastic force) and the fluid number

$F_n = 12(\lambda/E)(L/h)^3$ (the ratio of fluid to elastic force). From dimensional considerations λ should scale with μ/t_{ref}, leading to $F_n = 12(\mu/Et_{\text{ref}})(L/h)^3$. To identify the dimensionless parameters that govern the fluid flow, we start from the Navier-Stokes equations for the fluid

$$-\boldsymbol{\nabla}\cdot\boldsymbol{\sigma} + \rho\frac{d\boldsymbol{u}}{dt} = 0 \quad \text{in } A, \tag{2.31}$$

$$-\|\boldsymbol{\sigma}\|\cdot\boldsymbol{n} + \boldsymbol{\lambda} = 0 \quad \text{on } \Gamma_s. \tag{2.32}$$

The ciliary motion creates a flow that has a dominant velocity in the channel direction, i.e. x-direction. Therefore, we consider only the x-component of Eqn. 2.31. Using the constitutive relation for the fluid gives:

$$\rho^f\left(\frac{\partial u_x}{\partial t} + u_x\frac{\partial u_x}{\partial x}\right) = -\frac{\partial p}{\partial x} + \mu\left(\frac{\partial^2 u_x}{\partial x^2} + \frac{\partial^2 u_x}{\partial y^2}\right). \tag{2.33}$$

The relevant length scales can be identified by looking at the mechanism of fluid flow inside the channel (Fig. 1.3). The cilia of length L are placed periodically at a distance a in a channel of height H. The fluid inbetween the cilia is directly driven by them, and the momentum diffuses from this region upwards into the channel. The relevant length scales are the cilia spacing a in the x-direction, L and $H-L$ in the y-direction, and the relevant time scale is t_{ref}. Because the velocity of the fluid after a units will be the same (in the case of uniformly beating cilia), the net velocity and pressure gradients in the x-direction vanish over a distance a. Now, introducing these length and time scales in the above equation leads to:

$$\text{Re}_{\text{f}}\left(\frac{\partial \bar{u}_x}{\partial \bar{t}}\right) \approx \left(\frac{\partial^2 \bar{u}_x}{\partial \bar{y}^2}\right) \quad \text{for } 0 < y < L, \tag{2.34}$$

$$\text{Re}_{\text{H}}\left(\frac{\partial \bar{u}_x}{\partial \bar{t}}\right) \approx \left(\frac{\partial^2 \bar{u}_x}{\partial \bar{y}^2}\right) \quad \text{for } L < y < H, \tag{2.35}$$

where the terms in brackets are nondimensional, $\text{Re}_{\text{H}} = \rho^f(H-L)^2/\mu t_{\text{ref}} = t_{\text{diff}}/t_{\text{ref}}$ is the diffusion Reynolds number and $\text{Re}_{\text{f}} = \rho^f L^2/\mu t_{\text{ref}}$ is the flapping Reynolds number. The diffusion Reynolds number signifies how long it takes for the momentum to diffuse into the fluid (t_{diff}) compared to t_{ref}, whereas the flapping Reynolds number Re_{f} quantifies how large the inertia forces are compared to the viscous forces[2]. The question one might ask is, which of these Reynolds numbers is important? We show with the help of a simple analytical model (see appendix G) that Re_{H} has two effects; first, it determines the duration of the transient period and secondly, it reduces the fluctuating component of the fluid transported. However, the mean propulsion velocity created by the cilia in the steady state is independent of Re_{H}, leaving the flapping Reynolds number Re_{f} to be the main parameter that governs the fluid transported. In the following, we take Re $\equiv \text{Re}_{\text{f}} = \rho^f L^2/t_{\text{ref}}$. Another interesting observation is that the convection terms in the Navier-Stokes equation do not contribute to the fluid momentum (as also verified by our simulations).

[2]The fluid velocity near the cilia, the velocity gradient and the viscous energy dissipated per unit time scale with $\frac{L}{t_{\text{ref}}}$, $\frac{1}{t_{\text{ref}}}$ and $\mu\frac{1}{t_{\text{ref}}^2}$, respectively. The inertia forces scale with $\rho\frac{L}{t_{\text{ref}}^2}$, hence the kinetic energy input per unit time to the system scales with $\rho\frac{L}{t_{\text{ref}}^2}\frac{L}{t_{\text{ref}}}$. Their ratio gives the flapping Reynolds number Re_{f}.

Before proceeding, we identify the origin of the magnetic couple N_z for the two magnetic material systems considered in this work: (i) permanently magnetic (PM) and (ii) super-paramagnetic (SPM) materials. For permanently magnetic materials, having a local remanent magnetization ($\hat{M}_x$) pointing along the axial direction of the film: $(\hat{M}_x, \hat{M}_y) = (\hat{M}_x, 0)$, we can write

$$N_z = \hat{M}_x \hat{B}_y - \hat{M}_y \hat{B}_x = \hat{M}_x \hat{B}_y = \hat{M}_x B_0 \hat{f}(\theta), \tag{2.36}$$

where θ is the film orientation and B_0 is the amplitude of the applied magnetic field. To identify the form of the magnetic couple for a SPM film, we have to analyse how the magnetic field inside a SPM film depends on the applied magnetic field, the geometry of the film and the magnetic properties of the film. To this end let us subject the SPM film to an external magnetic field (H_{x0}, H_{y0}). By assuming that the magnetization induced by an applied field is uniform, we can calculate the magnetic field induced by the magnetization $\boldsymbol{H}_{\text{self}}$ (see appendix C):

$$(H_{\text{xself}}, H_{\text{yself}}) = (-\alpha M_x, -\beta M_y)\,,$$

where $\alpha = 2\tan^{-1}(h/L)/\pi$ and $\beta = 2\tan^{-1}(L/h)/\pi$ are positive factors which depend on the geometry of the film. The field $\boldsymbol{H}_{\text{self}}$ is nearly in the direction opposite to the magnetization, hence $\boldsymbol{H}_{\text{self}}$ is called a demagnetizing field. For slender films $h << L$, the factor α approaches zero and the factor β approaches unity. This makes the demagnetizing field to be negligible along the length (or tangential direction) and equal to the magnetization in magnitude along the thickness (or transverse direction). The magnetic field $\boldsymbol{H}$ in the film is the sum of the external field $\boldsymbol{H}_0$ and the demagnetizing field $\boldsymbol{H}_{\text{self}}$, see Eqn. 2.26. As the magnetization $\boldsymbol{M}$ and $\boldsymbol{H}$ are related through $\boldsymbol{\chi}$, we have two equations that can be solved to find the magnetization:

$$(M_x, M_y) = \left(\hat{\chi}_x \frac{H_{x0}}{1+\hat{\chi}_x\alpha}, \hat{\chi}_y \frac{H_{y0}}{1+\hat{\chi}_y\beta}\right).$$

The magnetization along the length is enhanced due to the shape of the film (through α and β) and also due to the magnetic anisotropy (for $\hat{\chi}_y < \hat{\chi}_x$). The magnetic flux density reads $\boldsymbol{B} = \mu_0\,(\boldsymbol{M} + \boldsymbol{H}_0 + \boldsymbol{H}_{\text{self}})$. It can be seen that the demagnetizing field $\boldsymbol{H}_{\text{self}}$ has the effect of decreasing the magnetic flux density. For a slender film, the magnetic flux density in the thickness direction is nearly equal to the applied magnetic field (because $H_{\text{yself}} \approx -M_y$), and along the length it is the sum of the magnetization and the external magnetic field (because $H_{\text{xself}} \approx 0$). As we know the magnetization in terms of the applied magnetic field, we can calculate the magnetic couple (N_z) acting on the film:

$$N_z = \frac{\mu_0 H_0^2 \sin 2\theta\,(\hat{\chi}_x - \hat{\chi}_y + \hat{\chi}_x\hat{\chi}_y(\beta-\alpha))}{1+\alpha\beta\hat{\chi}_x\hat{\chi}_y + \alpha\hat{\chi}_x + \beta\hat{\chi}_y}. \tag{2.37}$$

The magnetic couple is directly proportional to the square of the applied field, depends on twice the angle made by the magnetic field vector with the film, the difference in the susceptibility (magnetic anisotropy) and difference between α and β (geometric anisotropy). The main message from Eqn. 2.37 is that for a magnetic couple to act on the film, we need an anisotropy - either magnetic or geometric. As the magnetic cilia are thin magnetic films, a shape anisotropy is always present.

Chapter 3
Asymmetric configurations

Abstract

In this chapter we mimic the efficient propulsion mechanism of natural cilia by magnetically actuating thin films in a cyclic but non-reciprocating manner. By simultaneously solving the elasto-dynamic, magnetostatic and fluid mechanics equations, we show that the amount of fluid propelled is proportional to the area swept by the cilia. By using the intricate interplay between film magnetization and applied field we are able to generate a pronounced asymmetry and associated flow. We delineate the functional response of the system in terms of three dimensionless parameters that capture the relative contribution of elastic, inertial, viscous and magnetic forces.

3.1 Introduction

A rapidly growing field in biotechnology is the use of lab-on-a-chip devices to analyse bio-fluids (Laser & Santiago, 2004; Whitesides, 2006; Chang *et al.*, 2007). Such fluids have to be preprocessed (for example, mixed with other fluids (den Toonder *et al.*, 2008)) and transported to and from one or many micro-chambers where the biochemical analyses are performed. The microfluid transport through these stages is usually performed by downscaling conventional methods such as syringe pumps (Schilling *et al.*, 2002; Jeon *et al.*, 2000), micropumps (Laser & Santiago, 2004), or by exploiting electro-magnetic actuation, as in electro-osmotic (Zeng *et al.*, 2002; Chen *et al.*, 2003) and magnetohydrodynamic devices (Lemoff & Lee, 2000; Homsy *et al.*, 2000). However, when transporting biological fluids (which usually have high conductivity), the use of electric fields may induce heating, bubble formation and pH gradients from electrochemical reactions (Studer *et al.*, 2004; Wu *et al.*, 2007; Bruss *et al.*, 2004). In this chapter, we explore a new way to manipulate fluids in microfluidic systems, inspired by nature, through the magnetic actuation of artifical cilia.

Fluid dynamics at the micrometre scale is dominated by viscosity rather than inertia. This has important consequences for fluid propulsion mechanisms (Purcell, 1977). In particular, mechanical actuation will only be effective in propelling fluids if their motion is cyclic, but asymmetric in shape change. Nature has solved this problem by means of hair-like structures, called cilia, whose beating pattern is asymmetric and consists of an effective and a recovery stroke (Murase, 1992). While natural cilia use an internal forcing system based on motor proteins (dyneins), the key challenge for its artificial equivalent

Based on Khaderi, *et al. Nature-inspired microfluidic propulsion using magnetic actuation*, Physical Review E, 2009, **79**, 046304.

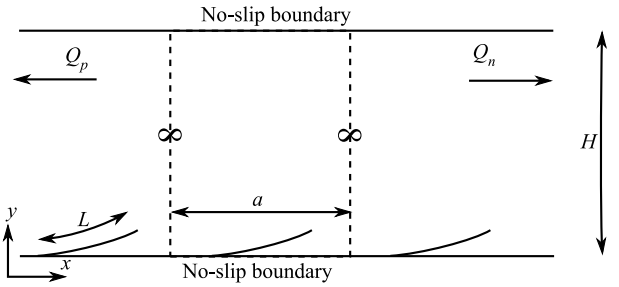

Figure 3.1: *Schematic side view of the microfluidic channel used in the simulations. The unit-cell used is shown using dashed lines.*

is the design of an externally-applied loading system that will generate a similar non-reciprocating motion. Recently, electrostatic artificial cilia have been experimentally shown to induce effective micro-mixing (den Toonder *et al.*, 2008). In addition, magnetic fields are also used to induce flow, but the asymmetry generated was found to be relatively small (Gauger *et al.*, 2009). In this chapter we report on the identification of four magnetically-driven configurations that can exhibit an asymmetric motion. We will show that the fluid propelled is linearly proportional to the swept area by the film (the configurational space). The first configuration is based on a partially magnetic film that can have different stiffnesses during the effective and recovery stroke. The next two are based on a magnetic instability that develops when the applied magnetic field is opposite to the direction of the magnetization in a permanently magnetic film. In the fourth configuration we will demonstrate that asymmetry can be achieved in a super-paramagnetic film, based on the intricate inter-play between the geometry of the film, the externally-applied field and the induced magnetization.

3.2 Results

We use the numerical model developed in chapter 2 to study a periodic arrangement of cilia in a microfluidic channel of height $5L$, with the cilia spaced $5L$ apart in the limit of low Reynolds numbers, where L is the length of the cilia. A square unit-cell is identified consisting of one cilium. No-slip boundary conditions are applied at the top and bottom boundaries of the channel and periodic boundary conditions at the left and right ends of the unit-cell (see Fig. 3.1). The fluid has a viscosity $\mu = 1$ mPas. The film has a thickness $h = 2$ μm, an elastic modulus of 1 MPa and a density $\rho = 1600$ kg/m^3, unless mentioned otherwise. In the following, the Eulerian fluid mesh is not shown for clarity.

3.2.1 Partly magnetic film with cracks.

Early studies on the mechanical properties of a cilium, when no information on the microstructure was available, showed that the natural cilium has a larger stiffness during the effective stroke compared to the recovery stroke (Gray, 1922). Because of the large stiffness, the cilium does not deform during the effective stroke, while due to the low stiffness the drag forces cause the cilium to deform considerably so that it stays closer to the cell boundary during the recovery stroke. To use this concept the magnetic film needs to possess a large bending stiffness in the effective stroke while pushing the fluid and to

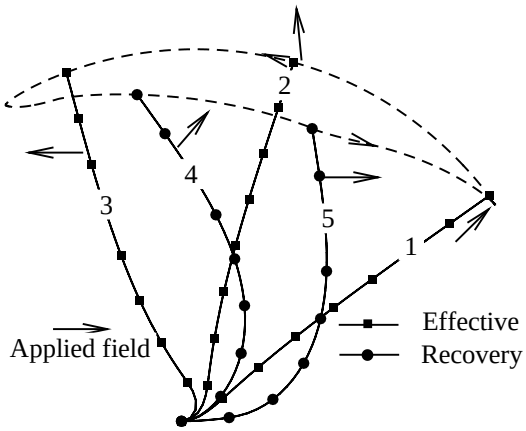

Figure 3.2: *Film with cracks with only a part (20% of the length) near the fixed end magnetized. Instances 1, 2, 3, 4 and 5 refer to a time of 5, 11, 20, 27 and 30 ms, respectively. The arrows show the direction of the applied field.*

possess a low stiffness during the recovery stroke. This can be achieved by introducing cracks on one side of the film and by making only a portion of the film magnetic. The film, which is straight initially, is attached at the left end and has cracks of size 1 μm at the bottom. As only a part of the film is magnetic, it behaves like a flexible oar (as also mentioned by Purcell (1977)). Only 20% of the film near the fixed end is magnetic. The assumed remnant magnetization is 15 kA/m, with the magnetization vector pointing from the fixed end to the free end. The applied magnetic field ($B_0 = 75$ mT) initially points in the positive x-direction, after which it is rotated by 180° in the counterclockwise direction in 20 ms and then rotated back to the initial position in the next 10 ms, thereafter this cycle is repeated. The movement of the film under the action of the applied magnetic field is shown in Fig. 3.2. When the external magnetic field is applied, for the first 20 ms, the magnetic couples act on the magnetized portion of the film in a counterclockwise manner. The drag forces are acting on the top part of the film, which close the cracks and make the film stiff. The cilium thus remains nearly straight and rotates about the fixed end to perform the effective stroke (see instances 1, 2 and 3 in Fig. 3.2). When the applied field rotates back to the initial position during the next 10 ms, the drag forces act on the bottom part of the film which open the cracks making the film floppy and bend it (see instances 4 and 5 in Fig. 3.2). Such an interaction of magnetic couples, elastic forces and drag forces leads to an asymmetric motion, as can be seen from Fig. 3.2.

3.2.2 Buckling of a straight magnetic film

In this configuration, a straight horizontal magnetic film with a perturbation is used to achieve an asymmetric motion. The film considered here has a uniform remanent magnetization of 15 kA/m with the direction of magnetization pointing from the fixed end of the film to the free end. When an external magnetic field is applied in the direction opposite to the film's magnetization, there will be no resulting magnetic couple when the

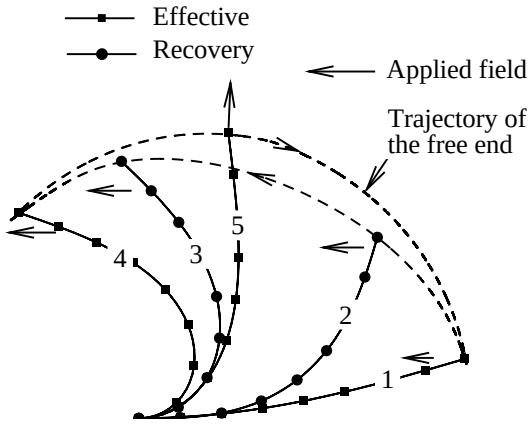

Figure 3.3: *Asymmetric motion of a perturbed permanently magnetic film. The magntization points from the fixed to free end. During instances 1 and 2, the cilium buckles and exhibits a recovery stroke and during instances 3, 4 and 5 it performs effective stroke. Instances 1, 2, 3, 4 and 5 correspond 2, 10, 12, 15 and 20 ms, respectively.*

film is straight, hence the film will not move. However, if the film is not initially straight but given an initial perturbation, due to, for instance, manufacturing imperfections, then it will buckle under the influence of the external magnetic field. By assuming a uniform magnetization in the film and neglecting drag forces, the critical magnetic field that will cause buckling can be calculated (see Appendix I). Figure 3.3 shows the asymmetric motion due to the buckling of a magnetic film. The length of the film is 100 microns. The external magnetic field is linearly increased from zero to a maximum of B_0 (25 mT) in the direction opposite to the magnetization in the film in 15 ms. Then it is rotated by 180° degrees in the clockwise direction in the next 15 ms, after which it is reduced to zero in the next 1 ms and the cycle is repeated. At instant 1 in Fig. 3.3 when the film is nearly horizontal the magnitude of the counterclockwise magnetic couple acting on the film is low. Under the influence of this magnetic couple, the film buckles to instances 2 and 3 and performs the recovery stroke. When the applied field is rotated by 180° in the clockwise direction, the film follows the applied field to perform the effective stroke and comes back to the initial position (instances 4 and 5). The effective fluid propulsion takes place when the film returns to the initial position.

3.2.3 Curled permanently magnetic film

The effect of the buckling-induced recovery stroke can be enhanced by choosing the initial geometry of the film to be a quarter of a circle with radius 100 μm, see instant 1 in Fig. 3.4(a). The direction of the magnetization is along the film with the magnetization vector pointing from the fixed end to the free end. The remanent magnetization of the film is taken to be $M_r = 15$ kA/m. A uniform external field of magnitude $B_0 = 13.3$ mT is applied at 225° to the x axis from $t = 0$ ms to $t = 1$ ms and then linearly reduced to zero in the next 0.2 ms. The results of the non-reciprocating motion of the film in the fluid during magnetic actuation are shown in Fig. 3.4(a). When the external field is

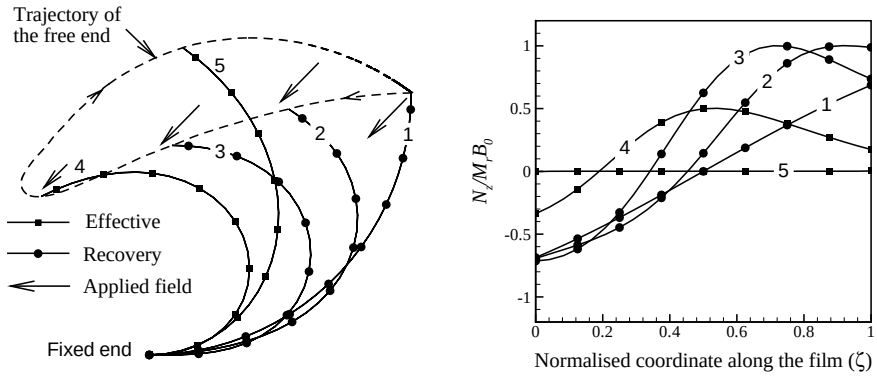

(a) (b)

Figure 3.4: *Buckling of a curled permanently magnetic (PM) film as a result of magnetic actuation, during the propulsion of fluid. (a) Snapshots of the film at 0 ms, 0.3 ms, 0.6 ms, 1.1 ms and 3 ms. (b) Normalised torque distribution along the film corresponding to the snapshots shown in (a).*

applied, clockwise torques (N_z is the magnetic body torque) are acting on the portion near the fixed end of the film while near the free end counter-clockwise torques develop (see instance 1 in Fig. 3.4(b)). Under the influence of such a system of moments, the film undergoes a buckling-kind of instability. This can be nicely seen from instances 1 and 2 in Figs. 3.4(a) and 3.4(b). During this stage the position of zero torque is almost fixed, while the torques at the free end increase. This causes the film to snap through to configurations 3 and 4 during which the zero-torque position travels to the fixed end. Clearly, the initially opposing directions of the internal magnetization and the applied magnetic field are essential in generating an instability that causes a large bending deformation during application of the field. Then, the applied field is reduced to zero and the film returns to the initial position through instance 5 in Fig. 3.4(a). Note that the propulsive action in the effective stroke (red) takes place during the elastic recovery of the film, while the film stays low in the recovery stroke due to the buckling-enforced snap-through.

3.2.4 Super-paramagnetic film

For a PM film the torques are maximum when the local magnetic film is perpendicular to the (remanent) magnetization. For a super-paramagnetic (SPM) film, however, the magnetization is induced by the field itself, posing different requirements on the applied magnetic fields in order to deform the film. A straight, magnetically anisotropic SPM film (having susceptibilities 4.6 and 0.8 in the tangential and normal directions, respectively (van Rijsewijk, 2006)), is subjected to a magnetic field with magnitude $B_0 = 31.5$ mT that is rotated from 0° to 180° in $t = 10$ ms and then kept constant during the rest of the cycle. The film has a length $L = 100$ μm. Its cross-section is tapered, with the thickness varying linearly along its length, having $h = 2$ μm at the left (attached) end and $h = 1$ μm at the right end. Figure 3.5(a) shows that in the effective stroke the portion of the beam near the free end is nearly straight. This is due to the fact that in this region

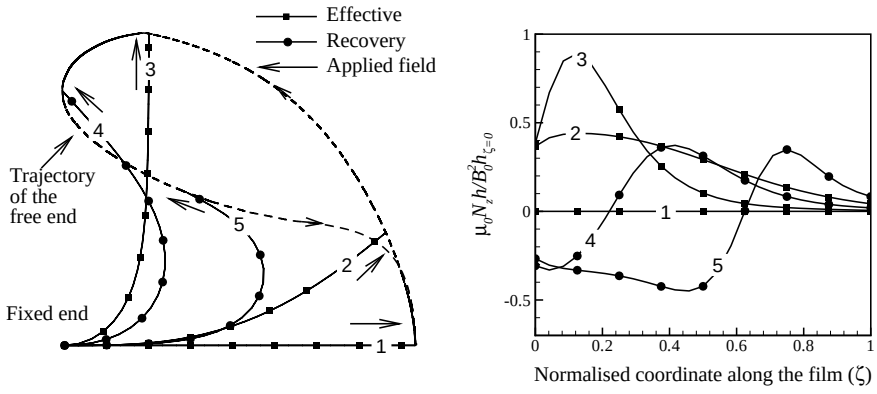

(a) (b)

Figure 3.5: *Motion of a super-paramagnetic (SPM) film in a rotating magnetic field, during the propulsion of fluid. (a) Snapshots of the film at 0 ms, 2.5 ms, 5.0 ms, 7.5 ms and 8.5 ms. (b) Normalised torque distribution along the film corresponding to the snapshots shown in (a). Here μ_0 is the permeability of vacuum, h is the thickness at position ζ and $h_{\zeta=0}$ is the thickness at the fixed end.*

the film can easily follow the applied field so that the field and magnetization are almost parallel, causing the magnetic torque to be low in this region of the film (instances 2, 3 and 4 in Fig. 3.5(b)). When the film has reached position 4, the magnetization in the film is such that the torques are oriented clockwise near the fixed end and anticlockwise near the free end, resulting in strong bending of the film. From Fig. 3.5(b) it can be seen that during the recovery stroke (shown using circles) the position of zero torque propagates from the fixed end to the free end (from instance 4 to 5). Here the tapering is essential, causing the torque per unit length to be higher at the fixed end, allowing the film to recover to the initial position (1). The generated asymmetric motion is very similar to that of natural cilia (Murase, 1992). It is to be noted that the film recovers in the presence of an applied magnetic field. This sensitive interplay between stored elastic energy and controlled applied field can be exploited to provide a large asymmetry in motion.

3.2.5 Fluid propelled

Next we analyse how much fluid is propelled by the cilia. The asymmetry is large only in the cases of the curled permanently magnetic film and tapered super-paramagnetic film; hence, we analyse only these cases. We record the fluid volume transported through the channel per cycle and per unit out-of-plane thickness, giving an area flow per cycle (or volume flow per unit width). As a measure for the asymmetry, we compute the area swept by the free end of the film during one cycle (i.e. the area enclosed by the dashed lines in Figs. 3.4(a) and 3.5(a)) and vary this area by tuning the magnitude of the applied magnetic field (all other parameters remain unchanged). Figure 3.6 shows the area flow per cycle as a function of the swept area for several different cases. We have normalised both quantities by the maximum area that the tip can sweep, $\pi L^2/2$. For three values of the magnetic field we plot the film tip trajectories for the PM and

SPM configurations. The cycle times are 35 and 10 ms, respectively. The flux across the channel shows a linear dependence on the swept area. A similar result has been reported by Golestanian & Ajdari (2008) where it is shown that the velocity of a three sphere swimmer is proportional to the area swept in the configurational space. Due to

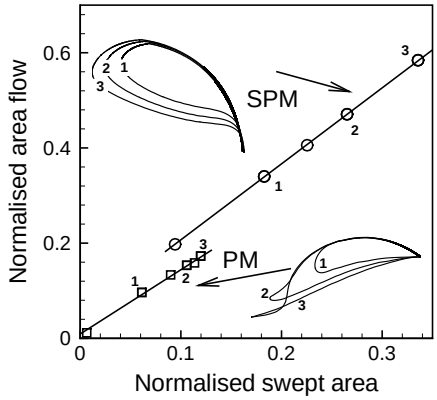

Figure 3.6: *Variation of normalised area flow with swept area.*

the linear correlation between the swept area and the fluid flow, the swept area can be used as a measure of effectiveness of the actuator, representing the fluid volume displaced. This allows uncoupling the magneto-mechanical motion of the cilia from the computationally-intensive fluid dynamics calculations. Instead, we account for the fluid by means of velocity-proportional drag forces (using resistive force theory (Johnson & Brokaw, 1979)) on the cilia, with the drag coefficients calibrated to the coupled solid-fluid model (see appendix H).

3.2.6 Parametric study

To identify the dimensionless parameters that govern the behaviour of the system, we start from the virtual work equation for the film , neglecting the axial deformations:

$$\int EI\frac{\partial^2 v}{\partial x^2}\frac{\partial^2 \delta v}{\partial x^2}dx + \int \rho A\frac{\partial^2 v}{\partial t^2}\delta v dx - \int N_z\frac{\partial \delta v}{\partial x}Adx + \int C_y\frac{\partial v}{\partial t}\delta v b dx = 0, \qquad (3.1)$$

where $I = bh^3/12$ is the second moment of area with b the out-of-plane thickness, $A = bh$ is the cross-sectional area of the film and v is the transverse displacement. In the virtual work equation the first, second, third and last terms respectively represent the virtual work done by the elastic internal bending moments, the inertial forces, the magnetic couple and the fluid drag forces. We introduce the dimensionless variables V, T and X, such that $v = VL$, $x = XL$ and $t = Tt_{\text{ref}}$, where L is a characteristic length (taken to be the length of the film) and t_{ref} a characteristic time. Substitution of these variables in the virtual work equation and normalisation with the elastic term reveals the three governing dimensionless numbers: the inertia number, $I_n = 12\rho L^4/Eh^2t_{\text{ref}}^2$, i.e. the ratio of inertial to elastic force, the magnetic number $M_n = 12N_zL^2/Eh^2$, i.e. the ratio of magnetic to elastic force and the fluid number $F_n = 12C_yL^4/Eh^3t_{\text{ref}}$, the ratio of fluid to elastic force. By substituting the torque expression for the two different magnetic materials,

the magnetic number M_n for the PM film is linear in the applied field, $12M_rB_0L^2/Eh^2$, while for the SPM film it is quadratic, $12B_0^2L^2/\mu_0Eh^2$.

We proceed by exploring the functional response of the system in terms of the swept area and cycle time, in dependence of the three dimensionless parameters. We analysed many different combinations of I_n, M_n and F_n, the results of which are summarized in Figs. 3.7(a)-3.7(c) for the PM system and in Figs. 3.7(d)-3.7(f) for the SPM system. Figs. 3.7(a) and 3.7(d) show the swept area as a function of M_n for several combinations of I_n and F_n. The combinations are indicated by the different symbols, corresponding to specific locations in Figs. 3.7(b) and 3.7(e). The effect of all three parameters can also be nicely summarised by analysing what magnetic number and cycle time is needed to sweep a normalised area of 0.2, for a given range of I_n and F_n values (see Figs. 3.7(b), 3.7(c), 3.7(e), 3.7(f)). The swept area increases with M_n reaching a maximum of 0.4 for the PM system (see Fig. 3.7(a)), while values of 0.7 can be reached by the SPM system (see Fig. 3.7(d)). For both systems the M_n needed strongly increases with F_n. In other words, for a given elastic parameter set, larger magnetic forces are needed to overcome the drag forces imposed by the fluid (see Figs. 3.7(a), 3.7(b), 3.7(d) and 3.7(e)). It can be seen from Figs. 3.7(a) and 3.7(d) that the effect of F_n is gradual for the PM system, while for the SPM case it is absent for small F_n, but suddenly kicks in for F_n larger than 10. In addition, the inertial forces assist in generating asymmetry for both cases, although for the SPM system inertial effects are only triggered for very large fluid numbers (see Fig. 3.7(d)).

For the analysis of the normalised cycle time the reference time was taken to be the time during which the field was applied (PM) or rotated (SPM). It was observed that the cycle time dependence on M_n and I_n was very weak and mostly completely absent. The only clear dependence found was on F_n which we show in the inset of Figs. 3.7(a) and 3.7(d) in terms of the normalised cycle times averaged over all different M_n values analysed and in Figs. 3.7(c) and 3.7(f) as the time required to sweep a normalised area of 0.2. For the PM case the effective stroke is generated through the elastic recovery of the deformed film, without noticeable effect of inertial forces. For such overdamped systems the time taken by the system to return to the initial position scales linearly with F_n, the ratio of fluid to elastic forces. The variation of normalised cycle time with F_n for the SPM case is much smaller. This is due to the fact that the total cycle is performed in the presence of magnetic forces. For small F_n and I_n the mean normalised cycle time (see Fig. 3.7(f)) is approximately equal to one; only for large F_n and I_n the cycle time is increased. At large F_n the system relies on the recovery (going from instance 5 to instance 1 in Fig. 3.5) of the curved tip against high viscous forces (see Figs. 3.7(d), 3.7(f)). The systems demonstrate an underdamped behaviour at large I_n values causing inertial forces to generate large oscillations leading to a larger normalised time (see Fig. 3.7(f)). For a normalised area of 0.2 the response of both systems in the range $I_n < 0.1$ and $F_n < 10$ is quasi-static, i.e. independent of inertial and viscous effects.

3.3 Summary

To summarize, we have proposed and analysed magnetic artificial cilia which can transport fluid in microfluidic channels. The main result is that we have found four actuation mechanisms, of which two can display a pronounced asymmetric motion. One configu-

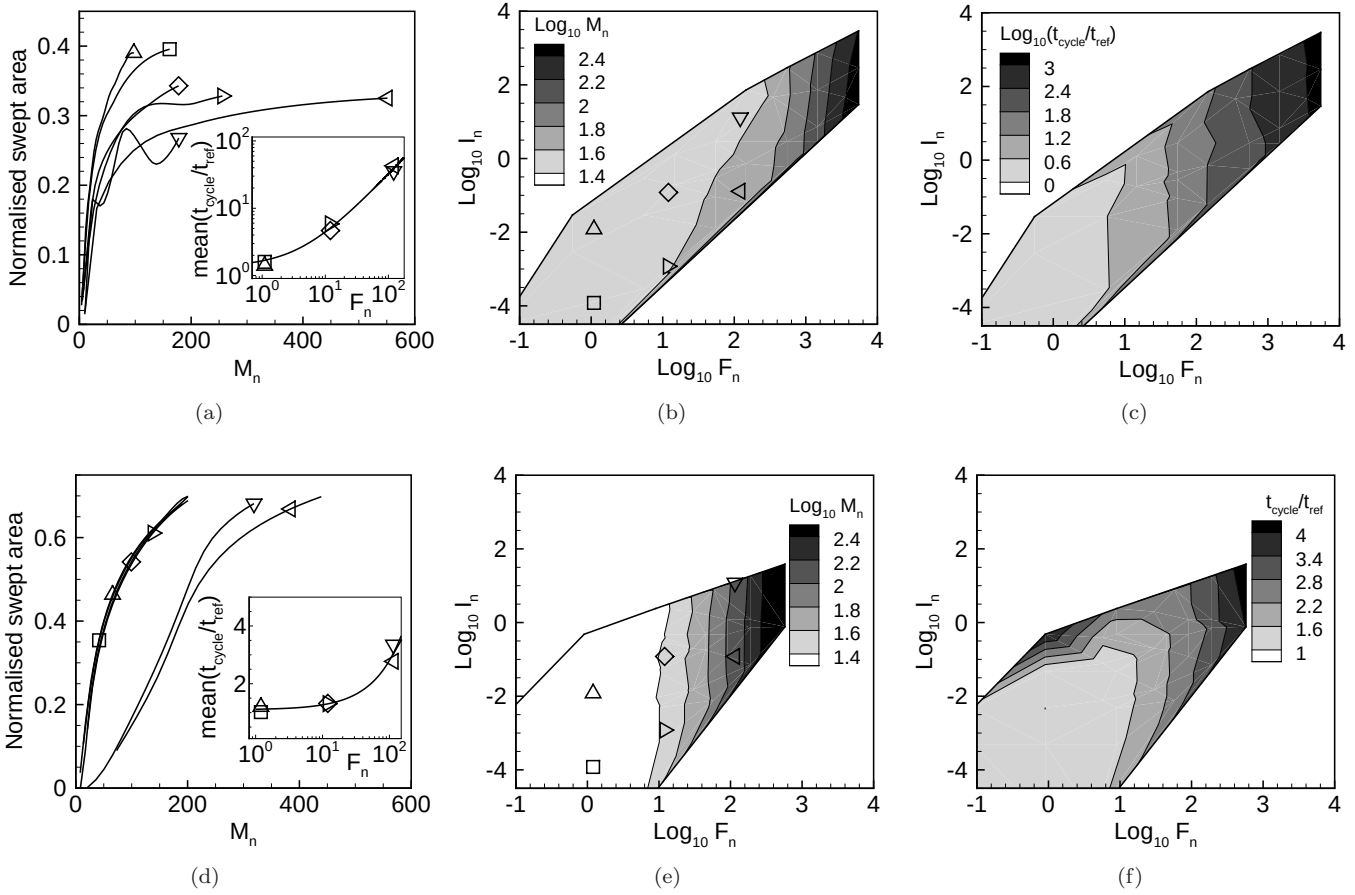

Figure 3.7: *Functional response of the PM system (top row, (a)-(c)) and the SPM system (bottom row, (d)-(f)). (a) (d) Normalised swept area as a function of M_n for several combinations of I_n and F_n, corresponding to the symbols of Figs. (b) and (e). The inset shows the mean normalised cycle time as a function of F_n. The mean is obtained by averaging all times corresponding to the data points that make up the specific M_n-swept area curve. (b) (e) Contours of M_n needed to sweep a normalised area of 0.2 for a wide range of I_n and F_n values. (c) (f) Contours of normalised cycle time corresponding to (b) and (e).*

ration is based on the buckling of a permanently magnetic film and the other is based on the intricate interaction between the applied field and the magnetization in a superparamagnetic film. We have shown that the fluid propelled is linearly proportional to the area swept by the film, which has so far only been shown for a non-actuated kinetic system (Najafi & Golestanian, 2004). Finally, we have identified the range of dimensionless parameters for which the artificial cilia exhibit an optimal behaviour. The analysis presented can be used as a guideline to make artificial cilia for microfluidic transport in lab-on-a-chip systems.

Chapter 4
Effect of cilia spacing and channel height

Abstract

In chapter we quantitatively analyse the performance of magnetically-driven artificial cilia for lab-on-a-chip applications. To perform the analysis we use a coupled magneto-mechanical solid-fluid model that accurately captures the interaction between the magnetic field, cilia and fluid. The performance of the artificial cilia is characterised for two channel configurations that are of practical importance: An open-loop and a closed-loop channel. We show that the flow and pressure head generated by the artificial cilia can be as high as 70 microlitres per minute and 11 mm of water, respectively. The obtained results can provide guidelines for the optimal design of magnetically-driven artificial cilia for microfluidic propulsion.

4.1 Introduction

A typical lab-on-a-chip system for the biochemical analysis of small volumes of fluids consists of a network of microfluidic channels that connect microchambers where dedicated tests are carried out. One of the challenges in the design of these microfluidic/lab-on-a-chip systems is to propel the fluids through the channels at these small (micro- and submicrometer) length scales. Fluid transport can be generated through physical forces such as electro-osmosis (Chen *et al.*, 2003; Zeng *et al.*, 2002), magneto-hydrodynamics (West *et al.*, 2002), acoustic streaming (Marmottant & Hilgenfeldt, 2003), or by downscaling conventional pumping systems (Laser & Santiago, 2004; Jeon *et al.*, 2000; Schilling *et al.*, 2002). Alternatively, nature can be used for inspiration by mimicking biological fluid propulsion mechanisms by means of cilia, operative at typical microfluidic length scales (den Toonder *et al.*, 2008; Oh *et al.*, 2009; van Oosten *et al.*, 2009; Evans *et al.*, 2007; Dreyfus *et al.*, 2005). Cilia are hair-like structures that cover e.g., the outer surface of microorganisms (e.g. Paramecia) and the inner layer of mammalian trachea for the expulsion of mucus from the lungs (Fulford & Blake, 1986), see Fig. 4.1.

At typical cilia and microfluidic length scales, viscous forces in the fluid dominate over inertial forces and thus the Reynolds number is low. To effectively actuate fluids at low Reynolds numbers an asymmetric motion is required, which, in nature, is provided by ciliary beating through distinct effective and recovery strokes. Moreover, when many cilia operate together, hydrodynamic interactions cause them to beat out-of-phase, leading to the formation of metachronal waves, and an enhanced fluid flow (Satir & Sleigh, 1990). Many examples have appeared in the recent literature of synthesised artificial

Based on Khaderi, *et al. Magnetically-actuated artificial cilia for microfluidic propulsion*, Lab Chip, 2011, **11**, 2002-2010.

Figure 4.1: *Cilia on the inner surface of mammalian trachea. These cilia work against gravity expelling mucus from the lungs (www.differencebetween.net).*

cilia for microfluidic applications, such as fluid mixing and transport. These artificial cilia are actuated by various external forces, including electrostatic (den Toonder *et al.*, 2008), piezo actuation (Oh *et al.*, 2009), light (van Oosten *et al.*, 2009) and magnetic (Evans *et al.*, 2007; Fahrni *et al.*, 2009; Shields *et al.*, 2010; Timonen *et al.*, 2010). Different models have been developed to understand the behaviour of artificial cilia and the related fluid motion (Kim & Netz, 2006; Gauger *et al.*, 2009; Khaderi *et al.*, 2009; Baltussen *et al.*, 2009; Alexeev *et al.*, 2008*a*). The principal advantage of the modelling not only lies in understanding the underlying physical behaviour of the artificial cilia, but also in exploring their parameter space in search for an optimal design.

In the last chapter we designed nature-inspired super-paramagnetic artificial cilia that exhibit an asymmetric motion when actuated by an external magnetic field, able to generate microfluidic propulsion (see Fig. 4.2(c)). These artificial cilia can be realised using thin polymer films, embedded by super-paramagnetic (SPM) nanoparticles, using photolithography techniques and can be actuated by applying a rotating external magnetic field (see Fig. 4.3). It was shown, by means of coupled solid-fluid simulations, that asymmetric motion can be achieved through the interaction between the applied field, the magnetization of the cilia and the competing magnetic, elastic and viscous forces. The flow generated was found to be proportional to the area swept by the cilia, see the shaded region in Fig. 4.2(c).

In the present chapter we study how these magnetic artificial cilia should be designed for typical lab-on-a-chip channel geometries, and how the generated flux and pressure can be optimized. We answer these questions using a computational model that couples all essential physical mechanisms (magneto-statics, solid dynamics and fluid dynamics) to simulate fluid flow through a microchannel. Although the results presented are based on magnetic artificial cilia, they are equally applicable to any ciliary system in which the cilia exhibit an asymmetric and out-of-phase motion.

The chapter is organized as follows. In section 4.2 we briefly explain the computational model used. In sections 4.3.1 and 4.3.2, we analyse two different channel geometries which are of practical interest: the closed-loop and the open-loop channel geometry, see Fig. 4.2. We study how the generated pressure and fluid flow depends on the size and spacing of the artificial cilia in relation to the height of the channel. Finally, conclusions are drawn in section 4.4.

4.2 Computational model

We model the cilia as elastic Euler-Bernoulli beams taking into consideration geometric non-linearity and inertia of the cilia in a Lagrangian framework. The magnetic field is calculated by solving the Maxwell's equations using a boundary element approach for each ciliary configuration. The Stokes equations, which capture the behaviour of the fluid flow at low Reynolds numbers, are solved within an Eulerian setting for the velocity and pressure using finite elements. The velocity is interpolated quadratically, while the pressure is interpolated linearly within each element. The solid-fluid coupling is performed by imposing the velocity of the cilia to be equal to the velocity of the fluid. This condition is enforced at the nodal points of the Euler-Bernoulli beam elements using Lagrange multipliers (point collocation method) within a fictitious domain framework (van Loon *et al.*, 2006). Details concerning the governing equations and numerical implementation can be found in chapter 2. The solution procedure can be summarized as follows. The Maxwell's equations are solved at every time instant to solve for the magnetic field, from which the magnetic body couple acting on the cilia is calculated. This body couple is provided as an external load to the implicitly-coupled solid-fluid model, which simultaneously solves for the cilia velocity, and the velocity and pressure of the fluid. The velocity of the cilia is integrated using Newmark's algorithm to calculate its new position, and this procedure is repeated. The particle tracking and streamlines calculations are performed from the velocity field in the fluid using the visualization software Tecplot (Tecplot, 2008).

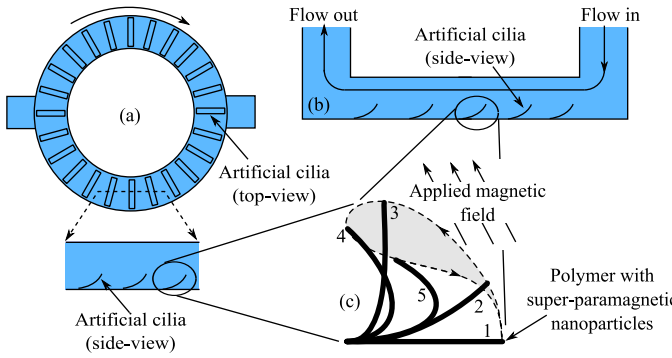

Figure 4.2: *Two possible applications of artificial cilia in microfluidics: (a) Closed-loop channel and (b) open-loop channel. In the closed-loop channel, the cilia can be used to propel the fluid inside a circular channel for a well-defined period of time. The closed-loop channel can, for example, be used to perform a polymerase chain reaction (PCR). In the open-loop channel, the cilia intake the fluid from one end of the channel and pump it to the other end. (c) Schematic representation of the typical motion of a magnetically-actuated artificial cilium during its beat cycle. The shaded region bounded by a dashed curve represents the area swept by the cilium. The direction of motion of the cilium is shown using the arrow on the dashed curve. The effective stroke is represented by the instances 1, 2 and 3, and the recovery stroke by the instances 4 and 5.*

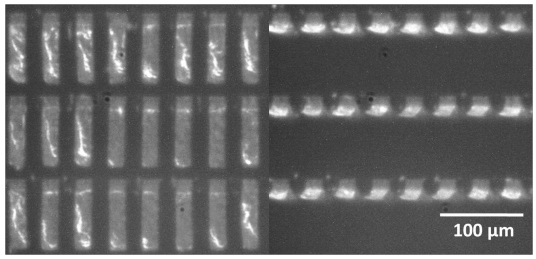

Figure 4.3: *Top-view of a surface covered with magnetic artificial cilia fabricated by the group of Prof. Rühe at the University of Freiburg (Belardi* et al.*, 2011). These magnetic artificial cilia are polymer thin films manufactured using photolithography techniques and are embedded with super-paramagnetic nanoparticles. Left: Artificial cilia in the unactivated state. Right: Artificial cilia under the influence of a magnetic field.*

4.3 Results and discussion

We study two channel configurations that are typically encountered in lab-on-a-chip applications: (i) A closed-loop channel (see Fig. 4.2(a)), and (ii) an open-loop channel (see Fig. 4.2(b)). In the closed-loop channel, fluid is initially pumped in by an external device and then it is propelled around the channel. Closed-loop channels are used, for instance, to perform polymerase chain reaction (PCR) (West *et al.*, 2002). In an open-loop channel we have well-defined inlet and outlet points for the fluid to enter and leave the channel. The fluid is propelled by an array of artificial cilia inside the channel. For example, the open-loop channel can be used to supply the fluid to a closed-loop channel. For the closed-loop channel, we assume the radius of the loop to be much larger than the width of the channel and the spacing between the cilia. In that case, the analysis can be performed by using a periodic unit-cell which contains one cilium. However, in the case of the open-loop channel there is a no periodicity due to the presence of the inlet and outlet, and the analysis has to be performed with the channel containing multiple cilia. The cilia span the entire width of the channels for an optimal performance (see Fig. 4.2), and the width of the channels is taken to be larger than the height. As a result, two-dimensional simulations are sufficient for both channel geometries.

The performance of the artificial cilia is quantified by the flux and pressure they can generate. We describe the performance of the artificial cilia for a given set of parameters as a function of the channel height H and cilia spacing a, normalised by their length L. The following set of parameters are used: The length of the super-paramagnetic cilia (L) is 100 microns, they have linearly varying tapered cross-section with a thickness being $h = 2$ μm at the fixed end and 1 μm at the free end, an elastic modulus $E = 1$ MPa, and density $\rho = 1600$ kg/m^3. The fluid viscosity $\mu = 1$ mPas. The super-paramagnetic cilia are subjected to a magnetic field with magnitude $B_0 = 31.5$ mT that is rotated from 0° to 180° in $t = 10$ ms and then kept constant during the rest of the cycle. At 0°, the magnetic field is directed along the original length of the cilia (instance 1 in Fig. 4.2(c)). The anisotropic magnetic susceptibilities of the cilia are 4.6 along the length and 0.8 along the thickness (van Rijsewijk, 2006).

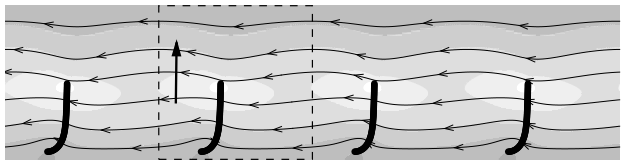

(a) Effective stroke

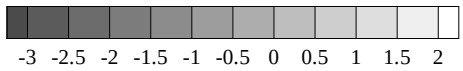

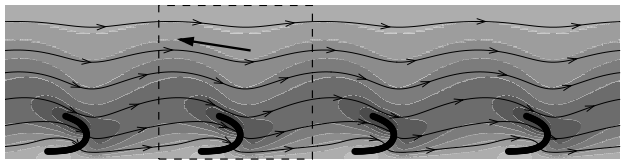

(b) Recovery stroke

Figure 4.4: *Velocity field and streamlines during the effective stroke (a) and recovery stroke (b) for $H = 2L$, $a = 2L$. The contours represent the absolute velocity along the channel (positive to the left) normalised with L/t_{ref}. The dashed box represents the unit-cell used for the simulations. The top and bottom boundaries of the unit-cell are no-slip boundaries, while the left and right are periodic in velocity. The magnetic field is shown by black arrows.*

4.3.1 Closed-loop channel

The unit-cell for the closed-loop channel has a width a and height H, containing one cilium of length L (see the dashed box in Fig. 4.4). The top and bottom surfaces of the unit-cell are no-slip boundaries, while the left and right boundaries are periodic in velocity. This results in a pressure distribution which is also periodic, so that no pressure gradient can be generated by the closed-loop channel.

The velocity field in the closed-loop channel during the effective and recovery stroke is shown in Fig. 4.4 for $H/L = 2$ and $a/L = 2$. The effective stroke is to the left, during which the cilia remain straight and rotate about their fixed end (see Fig. 4.4(a)), thus propelling a large amount of fluid to the left. During the recovery stroke, the cilia become curved and stay closer to the bottom boundary (see Fig. 4.4(b)), propelling less fluid compared to the effective stroke. The fluid transported shows a pulsating behaviour, but since the flux transported during the effective stroke is larger than during the recovery stroke, the net fluid transport occurs in the direction of the effective stroke (i.e., to the left).

To obtain the fluid flow created, we first integrate the velocity field over the height of the channel (at e.g., the inlet), which is then integrated over the ciliary cycle time to give the net "area flow" per cycle. Figure 4.5 shows the area flow per cycle normalised by $(\pi L^2/2)$, as a function of the cilia spacing a/L for various channel heights H/L. Also shown is the corresponding volume flow assuming an out-of-plane channel width of 1 mm. It can be seen that the flow decreases as the cilia spacing is increased. There can be two reasons for the decrease in the flow. Firstly, a decrease in the area swept by the cilia tip decreases the area flux (Khaderi *et al.*, 2009). Secondly, when the cilia spacing is increased, the fluid drag forces imposed by top and bottom channel surfaces

increase and thus the flux gets reduced. It can be seen from Fig. 4.5 that the swept area shows a minor increase for large a/L, indicating that only a limited amount of hydrodynamic interaction is operative when the cilia move apart. Hence, the reduction in flow (as we increase the spacing) is only due to increased fluid viscous forces when the cilia spacing becomes larger. It can also be observed from Fig. 4.5 that the fluid flow

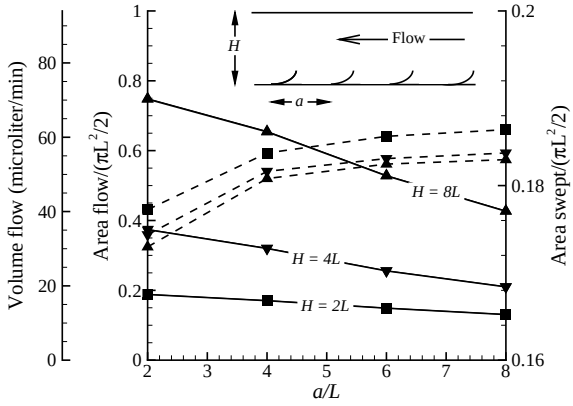

Figure 4.5: *Volume flow (left axis), area flow (left axis) and area swept (right axis) as a function of the cilia spacing (a/L) for different channel heights (H/L) for the closed-loop channel, L is the cilia length. The solid lines correspond to the left axes, and the dashed lines correspond to the right axis. The volume flow is calculated by taking the out-of-plane width of the channel to be 1 mm. The fluid flow increases when the cilia spacing is decreased, and when the channel height is increased. The area swept by the cilia is not substantially influenced by either the cilia spacing or the channel height.*

scales almost linearly with the height of the channel. When the height of the channel is substantially larger than the cilia length ($H > L$), the cilia can be considered to create a fluctuating Couette flow (shear flow) in the channel, with the top boundary being a no-slip boundary and the bottom boundary being displaced with a tangential velocity as imposed by the cilia. In such cases, the flow scales linearly with the height of the channel (Kundu & Cohen, 2008). The typical volume flow rates that can be created with the current configuration is tens of microlitres per minute (for a frequency of 50 Hz), which is comparable to the flow generated by typical dynamic pumps (Laser & Santiago, 2004).

4.3.2 Open-loop channel

Flux calculation

The open-loop microfluidic channel has well-defined inlets and outlets, between which the fluid is propelled by an array of artificial cilia, see Fig. 4.6(a). As mentioned earlier, the performance of any pumping device is characterised by the flux and pressure it can generate. Different experimental set-ups are usually adopted to probe the flux and pressure. The flux measurement for an open system is typically performed by maintaining constant fluid levels at the inlet and outlet when the pumping mechanism is switched on (Jang & Lee, 2000) (see Fig. 4.6(a), top). As a result, the actuating mechanism does not have to work against a pressure gradient, but only has to overcome the frictional resistance of the channel, as in the closed-loop channel of the previous section. The

fluid that spills out at the outlet and that is replenished at the inlet equals the fluid transported by the artificial cilia.

To perform numerical simulations, we neglect the frictional loss in the regions L_1 and L_2 and model only the portion of the channel where the cilia are placed (see Fig. 4.6(a), bottom). By assuming the left and right boundaries of the channel to be traction free, we properly account for the constant fluid levels at the inlet and outlet. For a given cilia spacing, we increase the number of cilia and compute the area flow per cycle. By plotting the area flow as a function of cilia spacing a/L, we found that the open-loop results converge to the closed-loop results depicted in Fig. 4.5 when large number of cilia are used. From this it can be concluded that the dependence of the flux generated by an open-loop channel on the channel height and cilia spacing is the same as that of a closed-loop channel, in situations where sufficiently many cilia are present in the open-loop channel[1].

Pressure calculation

The pressure in the open-loop channels is experimentally measured by comparing the fluid heights between two capillary tubes at the inlet and outlet of the channel (Jang & Lee, 2000; Chen *et al.*, 2003) (see Fig. 4.6(b), top). When the pumping mechanism is switched on, the initially equal fluid heights ($h_1 = h_2$) will become different. After this transient phase, the system reaches a steady state in which h_1 and h_2 remain constant. This level difference $h_1 - h_2$ gives the pressure difference generated by the pumping system. In the numerical analysis, we neglect the transient phase during which the fluid levels are changing, but focus on the steady state. At steady state, the fluid will be in motion only near the artificial cilia. At a distance L_D away from the cilia the velocity will be zero (see Fig. 4.6(b), top). Within this region a circulating flow is established that generates a mean pressure of $\rho g h_1$ and $\rho g h_2$ at the left and right of this region, respectively[2]. This gives a pressure difference $\Delta p = \rho g(h_1 - h_2)$, with ρ the density of the fluid and g the acceleration due to gravity.

Motivated by this, we choose our computational domain to comprise of a closed channel containing multiple cilia, with the distance between the cilia and the left and right channel boundaries being L_D (see Fig. 4.6(b), bottom). We now choose L_D to be large enough, so that the fluid at distances larger than L_D away from the cilia remains static. By performing simulations for different heights and L_D values, we found that the minimum L_D required is equal to the height of the channel (H). Figure 4.7 shows the pressure field for $L_D = H$, $H = 2L$, $a = 2L$ and for 4 cilia ($n = 4$) at a particular instant during the effective stroke. Since the effective stroke is to the left, the pressure builds up to the left, and the fluid circulates clockwise in the channel.

We now calculate the pressure gradient by integrating the pressure difference Δp (between the left and right boundaries) over a cycle and divide by the channel length na^3. Figure 4.8 shows the normalised pressure gradient $L \int_{\text{cycle}} \Delta p dt / n\mu a$ as a function of normalised cilia spacing (a/L) for different channel heights. It can be seen that as the cilia spacing and channel height decrease, the pressure gradient increases. The slope of

[1] For the heights and spacings studied, two cilia ($n = 2$, see Fig. 4.6(a)) placed in the open-loop channel were found to be sufficient to retrieve the results of Fig. 4.5 within 8% error.

[2] Assuming h_1 and h_2 to be much larger than the height of the channel.

[3] We found that by changing the number of cilia in the channel for a fixed a (i.e., by varying n), the pressure gradient remains unaffected for $L_D = H$, so that it is sufficient to perform the calculations for $n = 1$.

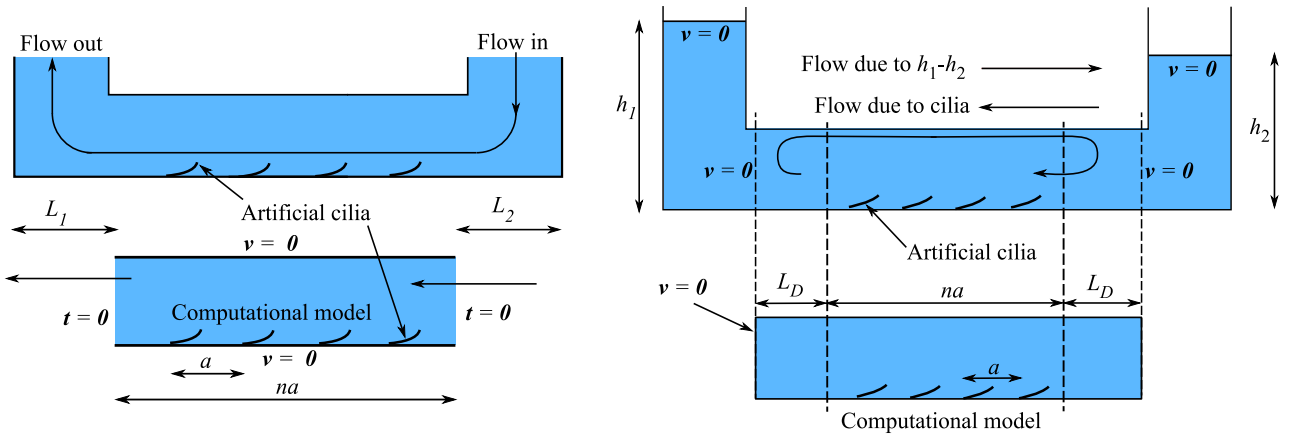

Figure 4.6: *Schematic pictures representing the approaches taken to calculate the flow (a) and pressure (b) for an open-loop channel. (a) Flow calculation: (Top) Experimental method: The cilia inside an open-loop channel intake the fluid from one end and pump it to the other end. The levels of the inlet and outlet are maintained at the same elevation. (Bottom) Computational model: Simplified model to calculate the flow through an open-loop channel. The pipings L_1 and L_2 are ignored for simplicity. (b) Pressure calculation: (Top) Experimental method: The channel on both the ends is attached with capillary tubes. When the cilia operate, there will be a difference in the levels of the liquid between the left and the right capillary tubes, which gives the pressure generated by the cilia. The fluid will be in motion only near the cilia, while far away from the cilia (beyond a distance L_D) the fluid will be stationary. (Bottom) Computational model: In the simulations, the cilia are made to operate in a closed channel with the distance between the left/right boundaries and the cilia is L_D. The difference between the pressure calculated on these two boundaries gives the pressure generated by the cilia.*

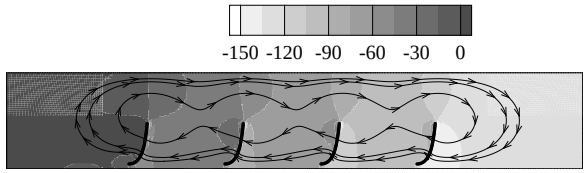

Figure 4.7: *Pressure contours with multiple cilia for $H/L = 2$, $a = 2L$, $n = 4$ and $L_D = H$. Because the channel is closed, the fluid simply circulates in the channel. As the cilia are moving to the left, we see a uniform positive pressure on the left boundary and a uniform negative pressure on the right boundary. The gradual build-up of the pressure due to multiple cilia can be seen.*

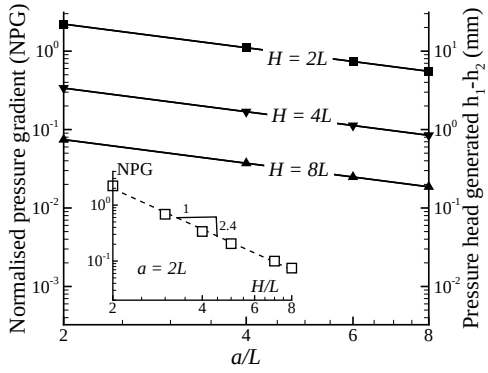

Figure 4.8: *Variation of the pressure gradient generated with cilia spacing a/L for different channel heights (left axis). Also shown (right axis) is the corresponding pressure head generated assuming a total channel length of 10 cm and fluid density of 1000 kg/m^3. The pressure generated decreases when either the cilia spacing or the channel height increase. The inset shows the pressure gradient as a function of the height of the channel for $a = 2L$. The pressure generated decreasing drastically when the height of the channel is increased.*

the lines in Fig. 4.8 is -1, indicating that the pressure jump Δp generated by a cilium is independent of the cilia spacing a. As a result, the total pressure difference generated by an array of n cilia is simply $n\Delta p$. On the right axis of Fig. 4.8 the pressure head generated assuming a total channel length of 10 cm and fluid density of 1000 kg/m^3 is shown. This pressure jump per cilium decreases with the height of the channel.

To investigate the height dependence we plot the pressure gradient as a function of height for $a = 2L$ in the inset of Fig. 4.8. The dashed line is a fit to the data in Log-Log scale. The slope of the fitted line is -2.4. This relatively strong dependence on the height of the channel may be related to two contributions - Firstly, the fluid can more freely flow backwards as the height H is increased, so the cilia have to exert less force. Secondly, the pressure on the boundaries is due to the force exerted by the cilia divided by the boundary area. Since the boundary area scales with H, the pressure is further decreased. It is to be noted that the maximum pressure generated by the cilia is 11 mm, which is lower than the pressure generated by typical dynamic pumps (Laser & Santiago, 2004). Therefore, the artificial cilia can find applications in microfluidic channels where the back pressure to be overcome is moderate.

4.4 Conclusions

Attractive fluid manipulation systems can be created for lab-on-a-chip biochemical analysis by mimicking natural cilia. Using coupled solid-fluid simulations we have quantitatively studied the performance of magnetically-actuated artificial cilia, with a typical length of 100 μm, in propelling fluids in a microfluidic channel, with the height of the channel varying between 200 and 800 μm. Two practically-relevant cases were considered: An open-loop channel and a closed-loop channel. For efficient use, the artificial ciliary systems should generate considerable flow and be able to operate against large pressure gradients. From the analysis performed in this work, it follows that volumetric flow rates on the order of 20-70 microlitres per minute and pressure heads of 0.2-11 mm of water can be achieved by decreasing the spacing between cilia. However, simultaneously achieving a high pressure gradient and large flow by tuning the height for a given inter-ciliary spacing is not possible, because the flow was found to increase linearly with channel height, whereas the pressure gradient generated decreases with an increase in height, following a power law with a slope of -2.4. The flow rates generated by the artificial cilia are of the same order as typical dynamic pumps (Laser & Santiago, 2004) (for a frequency of 50 Hz), but the generated pressures are relatively low. This suggests that the magnetic cilia can find application in channel configurations in which the back pressure to be overcome is moderate. Our results can provide guidelines for artificial cilia dimensions and spacings to achieve practically relevant microfluidic channel geometries with optimal flow characteristics.

Chapter 5

Inertial effects in ciliary flows - artificial cilia

Abstract

Experimental and computational studies show that fluid inertia can improve the mixing of fluids using artificial cilia. In this chapter, we explore whether such an improvement is possible for the case of fluid propulsion as well. We systematically study the fluid propulsion as a function of the Reynolds number and fluid number and show that the fluid propelled can be enhanced only for certain combinations of these parameters. For specific cases of the parameters the fluid propulsion occurs in the direction of the recovery stroke. By exploring the complete parameter space we show that the direction of the fluid transport can be changed by simply changing the frequency of operation.

5.1 Introduction

In chapter 4, the fluid transported by artificial cilia was shown to be comparable to typical electro-hydrodynamic pumps. We now investigate how the fluid transported can be further improved with the help of fluid inertial forces. In recent work (den Toonder *et al.*, 2008; Baltussen *et al.*, 2009) it was shown that the mixing of two fluids can be significantly improved by increasing the fluid inertia. The presence of fluid inertia brings in two effects. Firstly, there is a competition between the inertial forces and viscous forces in the fluid. Secondly, a competition between the time taken for the momentum to diffuse from the cilia into the channel and the frequency of cilia actuation is also introduced. As mentioned in chapter 2, the former is governed by the flapping Reynolds number ($\mathrm{Re_f}$) and the latter by the diffusion Reynolds number ($\mathrm{Re_H}$). At high $\mathrm{Re_f}$, the kinetic energy imparted to the fluid is not dissipated instantly and we see a flow in the direction of the effective stroke during the recovery and vice-versa. However, as we shall see, the inertia-caused flow due to the recovery stroke is obstructed by the subsequent effective stroke, which leads to a higher flow in the direction of the effective stroke compared to the recovery. This results in an increase of fluid transport at high $\mathrm{Re_f}$ compared to the Stokes regime. Although at finite $\mathrm{Re_H}$, the momentum of the cilia does not instantaneously diffuse into the channel (which leads to low values of instantaneous flux), it does not have any influence on the net fluid transported in a steady state. This is proven using a simplified analytical model in appendix G.

In chapter 3, we showed that the asymmetric motion of the cilia does not depend on the (solid) inertia number and that the magnetic number has the effect of increasing

Based on Khaderi, *et al. Magnetically-actuated artificial cilia: the effect of fluid inertia and metachrony*, submitted.

the area swept by the cilia. Therefore, we study the fluid transported as a function of the fluid number F_n and Reynolds number Re[1] for a constant magnetic number. By exploring this parameter space we identified four aspects of fluid propulsion that are associated with finite Reynolds numbers: (i) a unidirectional flow, (ii) a net fluid flow in the direction of the recovery stroke, (iii) a larger quantity of fluid transported compared to the Stokes regime and (iv) a change of the direction of the fluid transport by controlling the frequency of operation.

5.2 Results

5.2.1 Uniform magnetic field: effect of fluid inertia

Cilia deformation and fluid flow at low Reynolds numbers

In this section we study the fluid propulsion created by a two-dimensional array of tapered super-paramagnetic artificial cilia, which are actuated by a rotating magnetic field,

$$B_x = B_0 \cos(\omega t), \qquad B_y = B_0 \sin(\omega t), \tag{5.1}$$

which is uniform in space, B_0 is the magnitude of the applied magnetic field, $\omega = 2\pi/t_{\text{ref}}$ is the angular frequency and t_{ref} is the time period of rotation of the magnetic field. Because the magnetic couple scales with $\sin 2\omega t$ (see Eqn. 2.37), the time taken by the cilia for one beat cycle $t_{\text{beat}} = t_{\text{ref}}/2$.

To perform the simulations, we take a unit-cell containing one cilium. The top and bottom boundaries are no-slip boundaries and the left and right ends are periodic, see Fig. 5.1. The fluid, Reynolds, magnetic and inertia numbers are set to 0.015, 0.001, 10.89 and 4.8×10^{-3}, respectively, indicating that the fluid forces are low compared to the elastic forces, but are large compared to the fluid inertia forces. The values of the dimensionless parameters correspond to $L = 100$ μm, $E = 1$ MPa, the thickness of the cilia decrease linearly from $h = 2$ μm at the fixed end to 1 μm at the free end, $\rho^f = 0.1$ kg/m^3, $\mu = 0.1$ mPas, $\rho = 1000$ kg/m^3, $B_0 = 18.8$ mT and the cycle time $t_{\text{ref}} = 2t_{\text{beat}} = 20$ms. Note that the fluid density and viscosity are so chosen that the Reynolds number and fluid number are low. These values can also be obtained for a different set of fluid properties by properly tuning the frequency. The spacing between the cilia a is equal to $2L$. The magnetic susceptibilities of the cilia are 4.6 along the length and 0.8 along the thickness (van Rijsewijk, 2006). For the simulations, each cilium is divided into 40 beam elements and the fluid domain is divided in to 28×30 elements. The fluid propelled is characterised by two parameters: the net volume of the fluid transported during a ciliary beat cycle and the effectiveness. The velocity field in the fluid, at any x position, integrated along the channel height gives the instantaneous flux through the channel. This flux when integrated in the direction of the effective and recovery strokes gives the positive (Q_p) and negative (Q_n) flows, respectively (see Fig. 5.1). Due to the asymmetric motion, the positive flow is larger than the negative flow, generating a net area flow per cycle ($Q_p - Q_n$) in the direction of the effective stroke. The effectiveness, defined as $(Q_p - Q_n)/(Q_p + Q_n)$, indicates which part of the totally displaced fluid is effectively converted into a net flow. An effectiveness of unity represents unidirectional flow.

[1]The subscript 'f' from Re_f has been omitted.

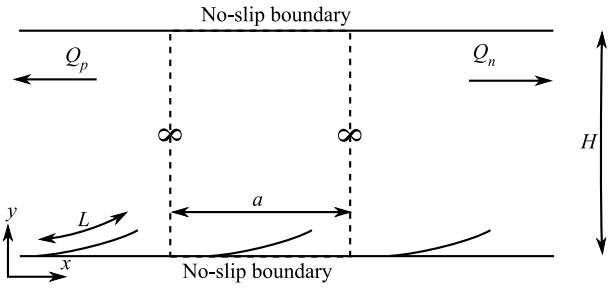

Figure 5.1: *A periodic unit cell used for the analysis is shown using the dashed lines.*

The components of the magnetic field $\boldsymbol{H}$ in the coordinate system local to the cilia is plotted in Figs. 5.2(a) and 5.2(b). The curves with square markers refer to the demagnetizing or self-field ($\boldsymbol{H}_{\text{self}}$, see Eqn. 2.26), the triangles refer to the applied magnetic field ($\boldsymbol{H}_0$) and the lines without marker refer to the total field. The magnetization and magnetic couple are plotted in Figs. 5.2(c) and 5.2(d), respectively. Figure 5.2(e) shows the deformed geometry of a typical cilium at different time instants. The blue arrow heads and the red arrows represent the direction of the magnetization and the applied magnetic field, respectively. The dashed curve represents the trajectory of the tip of the cilium. The contours of absolute fluid velocity normalised with L/t_{beat} are shown in Fig. 5.3(a)-5.3(f). The white arrows represent the applied magnetic field and the white circles represent the fluid particles. The instantaneous flux and the evolution of total flow during the beat cycle are shown in Fig. 5.3(g).

When a rotating magnetic field is applied, the free end of the beam nicely follows the applied magnetic field (Figs. 5.3(a) and 5.3(b)), and is rotated through 135° to form a 'U' bend near the fixed end (see instant (3) in Fig. 5.2(e)). From the magnetic field distribution along the cilia at these instants (see Figs. 5.2(a) and 5.2(b)), it can be seen that the demagnetization is stronger (due to the shape anisotropy) in the transverse or thickness direction (Fig. 5.2(b)) compared to the tangential direction (Fig. 5.2(a)), which reaches a maximum at a position on the cilia where the magnetic field is orthogonal to the cilia. This occurs near the fixed end at time instant (2) and near the half-span of the cilia at instant (3), see the corresponding instants in Fig. 5.2(e). The magnetic field in the transverse direction is significantly lower than the applied magnetic field, whereas this difference in the case of the tangential field is only marginal (see the lines without markers and the lines marked with triangles in Figs. 5.2(a) and 5.2(b)). Because of the formation of the 'U' bend, the magnetic field in the tangential direction changes sign at time instant (3) of Fig. 5.2(e) (see the corresponding instant in Fig. 5.2(a)). The magnetic field $\boldsymbol{H}$ in Figs. 5.2(a) and 5.2(b) leads to a magnetization as shown in Fig. 5.2(c). It can be seen that the magnetization in the tangential direction is much larger than that of the transverse direction (due to shape and magnetic anisotropy). Therefore, the magnetization is always tangential to the cilia. The sign reversal of the magnetic field at instant (3) leads to a direction reversal of the magnetization. In the region between the 'U' bend and the free (or fixed) end the magnetization points towards the free (or fixed) end. The magnetization vector (blue arrow heads) plotted on the cilia in Fig. 5.2(e) clearly shows this behaviour. This magnetization interacts with the applied magnetic field causing anticlockwise (positive) moments to act on the portion of the film between the free end and the 'U' bend, making the film more curved,

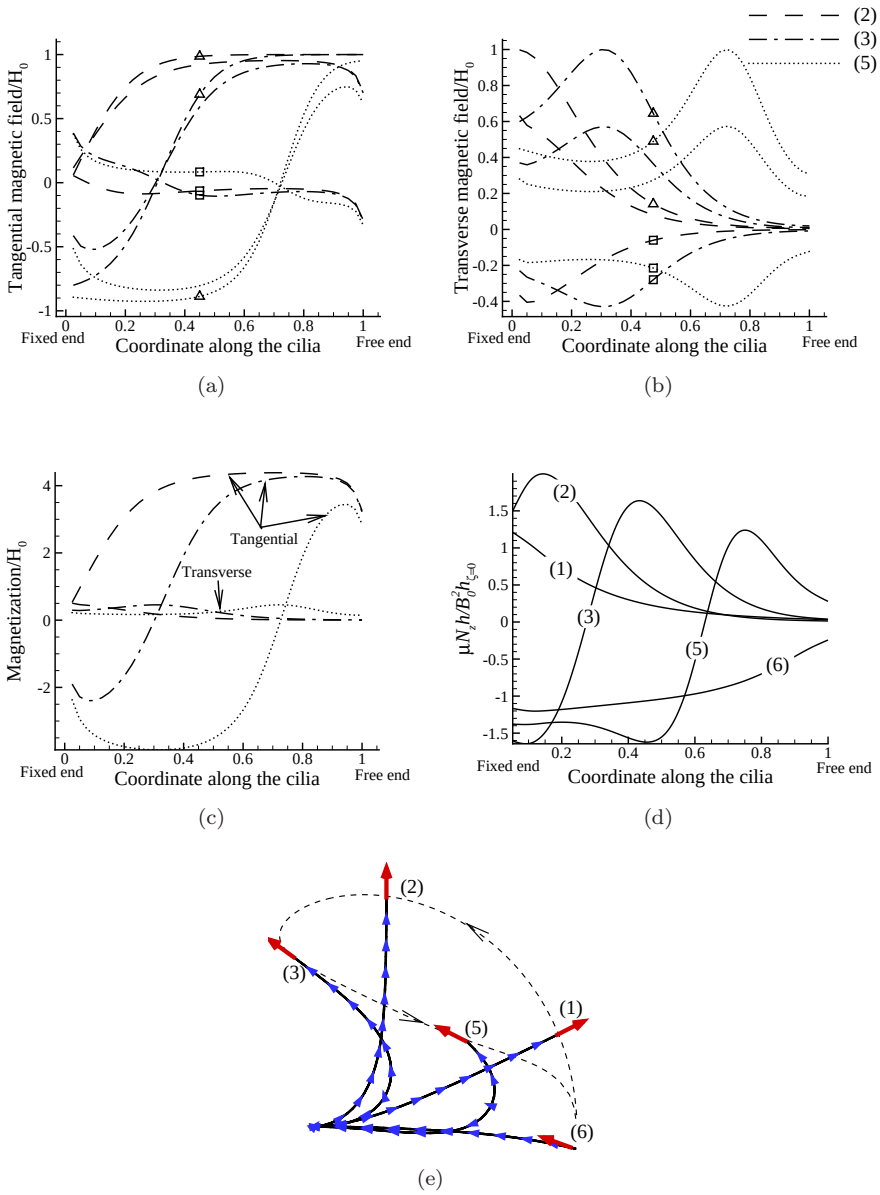

Figure 5.2: *(a) Magnetic field tangential to the local coordinates of the cilia. (b) Magnetic field transverse to the local coordinates of the cilia. Curves without markers and with triangle and square markers represent the total, applied and demagnetizing field, respectively. (c) Magnetization of the cilia in local coordinates of the cilia (d) Magnetic body couple along the length. (e) Deformed configurations of a typical cilium at different time instances. The blue arrow heads represent the direction of the magnetization of the cilium and the thick red arrows at the free end represent the applied magnetic field. Instances (1), (2), (3), (5) and (6) correspond to time instances* $0.15t_{beat}$, $0.5t_{beat}$, $0.8t_{beat}$, $0.85t_{beat}$ *and* $0.89t_{beat}$, *respectively (see also Fig. 5.3). The dashed line indicates the trajectory of the cilia tip, which encloses an area, termed the 'area swept'.*

and clockwise (negative) to moments act on the portion between the fixed end and the 'U' bend, making the film come back to the initial position (see instances (3) and (5) in Fig. 5.2(d)). Due to the tapered nature of the film, the clockwise moments are larger than the anticlockwise moments. Under the influence of such a system of moments, the 'U' bend propagates to the free end and the cilia come back to the initial position. From Fig. 5.2(e), it can be seen that the artificial cilia show an asymmetric motion similar to that of natural cilia (Childress, 1981). The dashed line represents the trajectory of the cilia tip, which encloses an area, termed 'area swept'. The amount of fluid propelled in the Stokes regime scales linearly with the swept area (Khaderi *et al.*, 2009). It is to be noted that the effective stroke takes place for a longer duration of time than the recovery stroke, while in natural cilia the opposite is the case (Childress, 1981).

Let us now analyse the fluid flow due to the ciliary motion. When the cilia move, they set the fluid nearby into motion. The momentum diffuses to the rest of the fluid due to the viscous forces. Since the viscous forces are large compared to the inertia forces, this momentum diffuses instantaneously and the fluid velocity nicely follows the cilia velocity at all time instants. The cilia create a positive flux (to the left) during the effective stroke (see the instantaneous flux at the instances corresponding to Figs. 5.3(a) and 5.3(b) in Fig. 5.3(g)), and drag back a part of the fluid creating a negative flux (to the right) during the recovery stroke (see the instantaneous flux at the instances corresponding to Figs. 5.3(c) - 5.3(e) in Fig. 5.3(g)). The evolution of the flow during the beat cycle can be seen from the total flow created, shown using the solid line in Fig. 5.3(g). The flow created by the cilia increases during the effective stroke and decreases during the recovery. Due to the asymmetric motion of the cilia, the positive flow is larger than the negative flow; the cilia create a net flow of magnitude 0.2 (in units of $\pi L^2/2$) to the left by the end of the cycle ($t = t_{\text{beat}}$). In the process of creating this flow, the cilia push the fluid back and forth, which leads to a low value of the effectiveness (0.2). The position of the fluid particles (which formed a straight line at the beginning of the beat cycle) at the end of the beat cycle provides a Lagrangian perspective of the fluid transported. The recovery stroke takes place with a whip-like motion of the cilia in a short duration of time, which leads to a larger instantaneous fluid velocity and flux during the recovery stroke than the effective stroke (compare instances (4) and (5) with (1) and (2) in Fig. 5.3). As the Reynolds number is low, the kinetic energy input by the cilia is instantaneously dissipated due to the large viscous forces. Therefore, even if the cilia impart a large velocity to the fluid during the whip-like recovery stroke (see Figs. 5.3(d) and 5.3(e)), the velocity and flux drop to zero as soon as the cilia have returned to the initial position (see Fig. 5.3(f) and instant (6) in Fig. 5.3(g)). It is to be noted that due to the low viscous forces (compared to elastic forces) the cilia complete the beat cycle in $0.89t_{\text{beat}}$. The cilia remain idle in this 'dead' position until the start of the next cycle.

Parametric study: effect of Reynolds number

In this section we characterise the response of the microfluidic actuator as a function of the dimensionless numbers that govern the behaviour of the system. The flow through the microfluidic channel depends on the inertia number I_n, fluid number F_n, magnetic number M_n and Reynolds number Re (see section 2.3). The effect of the fluid number, inertia number and magnetic number in the limit of low Reynolds number was studied in (Khaderi *et al.*, 2009). It was shown that the inertia number does not play a major role

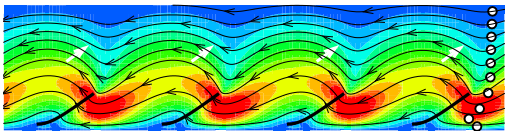

(a) $t = 0.15t_{\text{beat}}$ (instant 1)

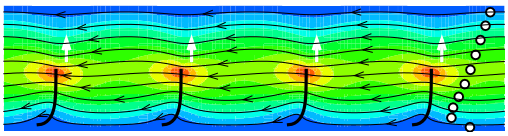

(b) $t = 0.5t_{\text{beat}}$ (instant 2)

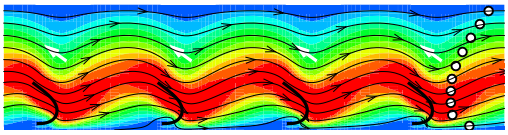

(c) $t = 0.8t_{\text{beat}}$ (instant 3)

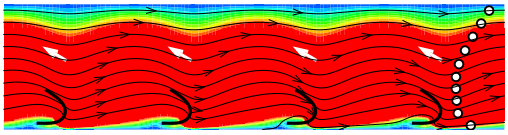

(d) $t = 0.83t_{\text{beat}}$ (instant 4)

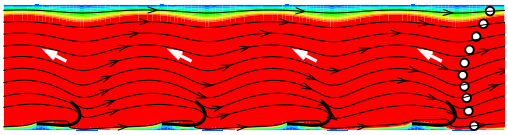

(e) $t = 0.85t_{\text{beat}}$ (instant 5)

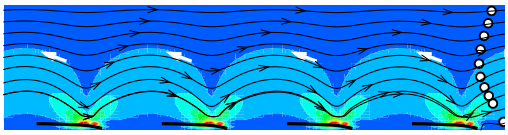

(f) $t = 0.89t_{\text{beat}}$ (instant 6)

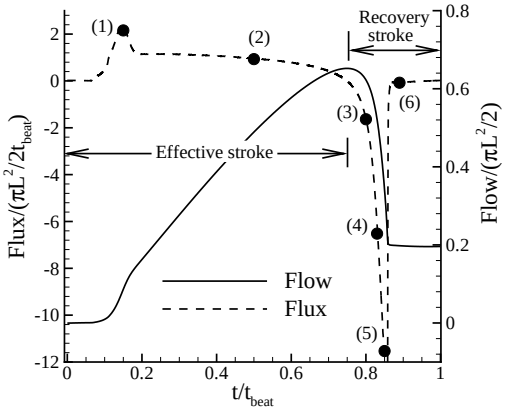

(g)

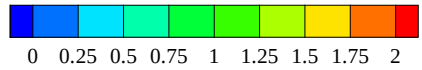

Figure 5.3: *(a)-(f) Contours of absolute velocity (normalised with L/t_{beat}) at different time instants. The direction of the velocity is given by the streamlines and the white arrows represent the magnetic field at the respective time instances. The circles represent fluid particles. The parameters used are $F_n = 0.015$, $Re = 0.001$ and $M_n = 10.89$. Four unit-cells are shown for clarity. (g) Instantaneous flux and accumulated flow as a function of time. The time instances corresponding to (a)-(f) are duly marked.*

and when the fluid number is increased (for a given magnetic number) the asymmetry (and therefore the flow) decreases. Hence, in this section we study the flow through the microfluidic channel as a function of the fluid number and the Reynolds number for a

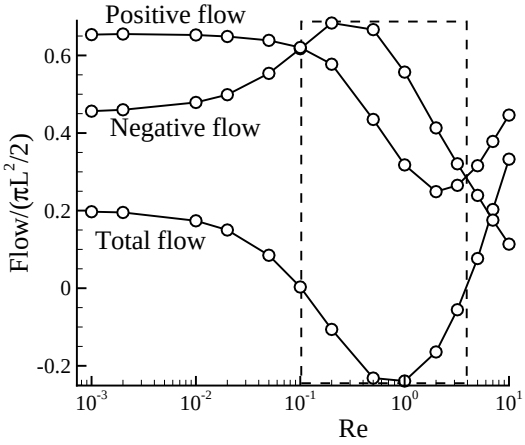

Figure 5.4: *Flow at the end of one cycle as a function of Reynolds number (Re) for $F_n = 0.015$ and $M_n = 10.89$. Fluid propelled by the cilia in the direction of the effective and recovery stroke are termed as positive (Q_p) and negative (Q_n) flows (see also figure 5.1).*

given magnetic number.

The area flow is plotted as a function of the Reynolds number (Re) for a fluid number (F_n) of 0.015 and a magnetic number of 10.89 in Fig. 5.4. As the Reynolds number is increased, the net flow changes direction so that the fluid propelled is in the direction of the recovery stroke (dashed box). On increasing the Reynolds number further, the fluid flow reverses direction again and flow occurs in the direction of the effective stroke. It is to be noted that the flow created at high Reynolds number is larger than that of the Stokes regime. To segregate the contributions to the net fluid flow, we also plot the positive and negative flow created in Fig. 5.4. When the Re is increased, the positive flow remains nearly constant, but the negative flow increases and causes the area flow to decrease. On a further increase of Re, the negative flow reaches a maximum, after which the positive and negative flow start decreasing. At high Re, the positive flow starts increasing again. We now investigate what mechanisms are involved that drive the flow direction reversal at moderate Reynolds number ($\mathrm{Re} \approx 1$) and what causes a higher flow at high Re compared to the Stokes regime.

Before proceeding any further we would like to restate the importance of fluid inertia. At high Reynolds numbers, the viscous forces are relatively low. The energy input to the fluid during the effective and recovery stroke is not instantly dissipated, but is carried over to the next recovery and effective stroke, respectively (effect of $\mathrm{Re_f}$). Also, at high Reynolds numbers, the diffusion from the cilia to the fluid takes place over a finite interval of time (effect of $\mathrm{Re_H}$). As a result, the fluid velocity field does not instantaneously follow the velocity of the cilia.

At Reynolds number $\mathrm{Re} = 1$, the velocity diffusion time t_{diff} is finite (effect of $\mathrm{Re_H}$, see section 2.3). The velocity of the fluid does not follow the cilia velocity instantaneously. This causes a negative velocity only near the bottom half of the channel during the recovery stroke (see Figs. 5.5(b)-5.5(d)), and a consequent reduction of the maximum flux transported at ($\mathrm{Re} \approx 1$) (compare instant (3) in Fig. 5.5(e) against instant (5) in 5.3(g)). As the fluid number is low ($F_n = 0.015$), the cilia return to the initial position

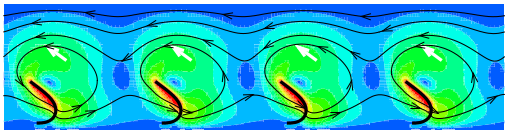

(a) $t = 0.8t_{\text{beat}}$ (instant 1)

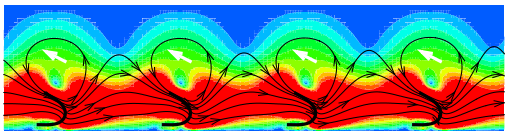

(b) $t = 0.85t_{\text{beat}}$ (instant 2)

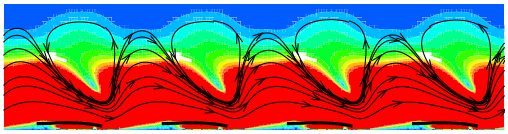

(c) $t = 0.9t_{\text{beat}}$ (instant 3)

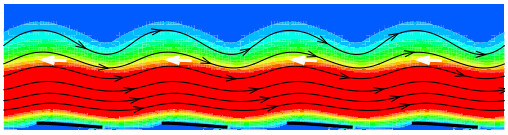

(d) $t = 0.99t_{\text{beat}}$ (instant 4)

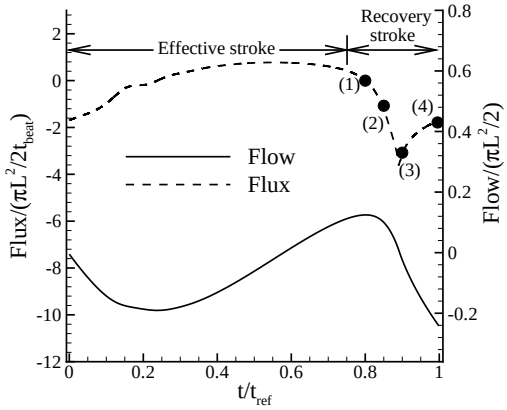

(e)

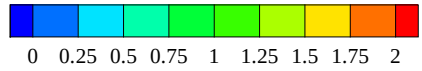

Figure 5.5: *(a)-(e) Contours of absolute velocity (normalised with L/t_{beat}) at different time instants. The direction of the velocity is given by the streamlines and the white arrows represent the magnetic field at the respective time instances. The circles represent fluid particles. The parameters used are $F_n = 0.015$, $M_n = 10.89$ and $Re = 1$. Four unit-cells are shown for clarity. The legend for the contours is the same as that of Fig. 5.3. (e) Instantaneous flux and accumulated flow as a function of time. The time instances corresponding to (a)-(d) are duly marked.*

before $t = t_{\text{beat}}$ and remain idle in the dead position (Figs. 5.5(c)-5.5(d)) until the start of the next cycle. As the viscous forces are comparable to the inertia forces, the kinetic energy input to the fluid during the whip-like recovery stroke, is not dissipated instantly, but creates a large negative flow during the dead position and during the initial part of the effective stroke (Fig. 5.5(d) and 5.5(e)). This causes an increase of the negative flow during recovery stroke compared to the Stokes regime, despite the lower instantaneous flux. Consequently, during the first half of the subsequent effective stroke, the cilia have to spend energy in cancelling the negative flow, instead of creating a positive flow. Hence, the positive flow is lower than that of the Stokes regime. This leads to flow direction reversal at moderate Reynolds numbers.

Next, we analyse the flow behaviour at a Reynolds number Re = 10 (see Fig. 5.6). At Re = 10, the viscous forces are so low compared to inertial forces that they do not dissipate the energy input to the fluid during the effective stroke. This can be seen from the continuous fluid velocity in the direction of the effective stroke near the top of the

channel (see the contour plots of the absolute velocity in Fig. 5.6). This leads to an increase of the positive flow. It is to be noted that because of resistance offered by the fluid inertia forces to the cilia motion, they return to the initial position at $t \approx t_{\text{beat}}$, reducing the idle time in the dead position to zero (see Fig. 5.6(f)). The effect of the increased t_{diff} is to restrict the fluid velocity in the negative direction to a narrow region close to the cilia (see Figs. 5.6(e) and 5.6(f)). This reduces the maximum negative flux even further (compare instant (3) in Fig. 5.5(e) against instant (e) in 5.6(g)). In this situation (low maximum negative flux and the absence of the dead position) the high energy input during the recovery stroke cannot create a substantial flow, because the next effective stroke already starts and effectively blocks the negative flow. This leads to a low negative flow compared to $\text{Re} = 1$. The total flow created by the cilia at the end of the cycle is 0.32 in units of $\pi L^2/2$ (see Fig. 5.6(g)), which is higher than that of the Stokes regime (0.2). This can also be observed from the position of the fluid particles at the end of the beat cycle. The fluid particles have undergone a larger displacement (Fig. 5.6(f)) compared to the Stokes regime (Fig. 5.3(f)).

The observations of this section can be summarised as follows (see Fig. 5.7). The quantity of the negative flow depends on the competition between the inertia-induced negative flow and its obstruction by the subsequent effective stroke. At small Re, the negative flux is large but only occurs over a short duration of time (Fig. 5.3(g)). When Re increases, inertia in the fluid causes the flow to be more local to the cilia but it sustains over a longer period of time so that the total negative flow increases (see Fig. 5.5 and Fig. 5.7). The net effect is that the total flow decreases and becomes negative (i.e., in the recovery direction, see region I of Fig. 5.7). When Re further increases (i.e., region II of Fig. 5.7), the positive flow decreases because a part of the effective stroke is spent in overcoming the negative flow caused by the previous recovery stroke. The negative flow also decreases because of the localization of the negative velocity near the cilia during a recovery stroke. Finally, in the region III, inertia is so dominant that the flow becomes almost unidirectional with the total flux being positive during most of the cycle, only showing a small dip during recovery (see Fig. 5.6). In region III, the flow continues to increase with inertia.

To also include the effect of fluid number (F_n), the flow and effectiveness are calculated for a range of fluid number (F_n) and Reynolds number (Re) in Fig. 5.8. The contour plots suggest three regions of significance, namely A, B and C. Region A represents the Stokes regime where the fluid viscous forces dominate over the inertia forces. In region A, the effectiveness of the fluid propulsion remains constant at ≈ 0.2 (see Fig. 5.8(b)). The fluid propelled decreases when the fluid number is increased; the increase of the fluid number increases the viscous forces, which decrease the area swept by the cilia tip and therefore the flow (see Fig. 5.2(e)). The reader is referred to Khaderi *et al.* (2009) for a more detailed discussion. In region B, the flow is negative and thus takes place in the direction of the recovery stroke. Now, if either the Reynolds number or the fluid number is increased, the fluid flows in the direction of the effective stroke. In region C, the fluid inertia forces are large and the effectiveness of fluid propulsion is high. In this regime, for low fluid numbers the fluid transported is large compared to the Stokes regime. However, when the fluid number is large, the area swept is lower (due to large viscous forces) and the flow created is comparable to that of the Stokes regime. Interestingly, the effectiveness of the fluid propulsion is large even in this region, thus creating an unidirectional flow. This suggests that we can use the inertia forces in the fluid to generate a unidirectional flow with periodically beating artificial cilia. In

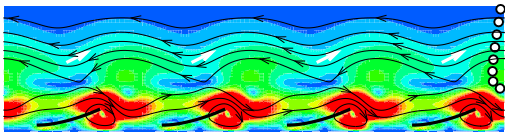

(a) $t = 0.15t_{\text{beat}}$

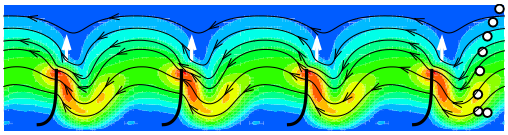

(b) $t = 0.5t_{\text{beat}}$

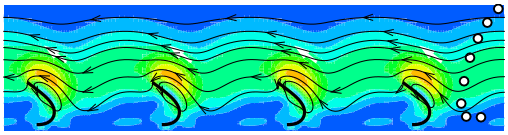

(c) $t = 0.8t_{\text{beat}}$

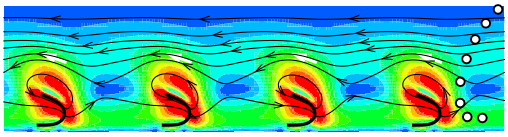

(d) $t = 0.89t_{\text{beat}}$

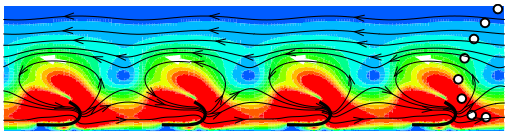

(e) $t = 0.94t_{\text{beat}}$

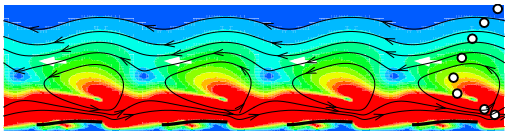

(f) $t = 0.99t_{\text{beat}}$

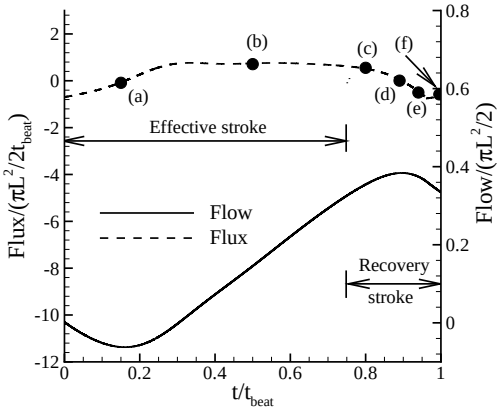

(g)

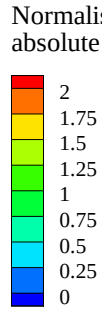

Figure 5.6: *(a)-(f) Contours of absolute velocity (normalised with L/t_{beat}) at different time instants. The direction of the velocity is given by the streamlines and the white arrows represent the magnetic field at the respective time instances. The circles represent fluid particles. The parameters used are $F_n = 0.015$, $Re = 10$ and $M_n = 10.89$. Four unit-cells are shown for clarity. (g) Instantaneous flux and accumulated flow as a function of time. The time instances corresponding to (a)-(f) are duly marked.*

natural ciliary systems such a unidirectional fluid flow is achieved by the hydrodynamic interaction between individual cilia, which leads to a metachronal wave (Satir & Sleigh,

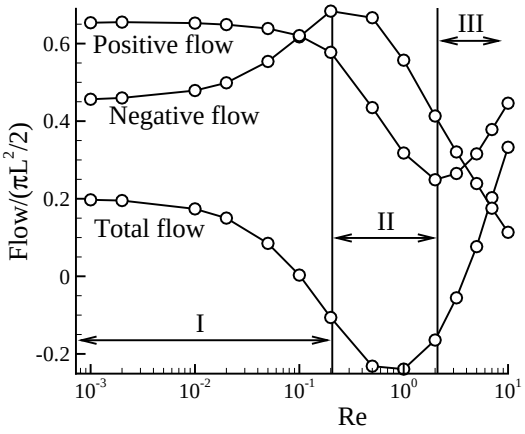

Figure 5.7: *Flow as a function of Reynolds number Re for $F_n = 0.015$, with different regions of significance marked. Region I: The large kinetic energy input during the recovery stroke leads to a negative flow during the dead position. Region II: The negative flow decreases due to the delayed momentum diffusion, and the positive flow decreases because the effective stroke has to first cancel the negative flow. Region III: The positive flow increases because of the continuous velocity in the direction of the effective stroke.*

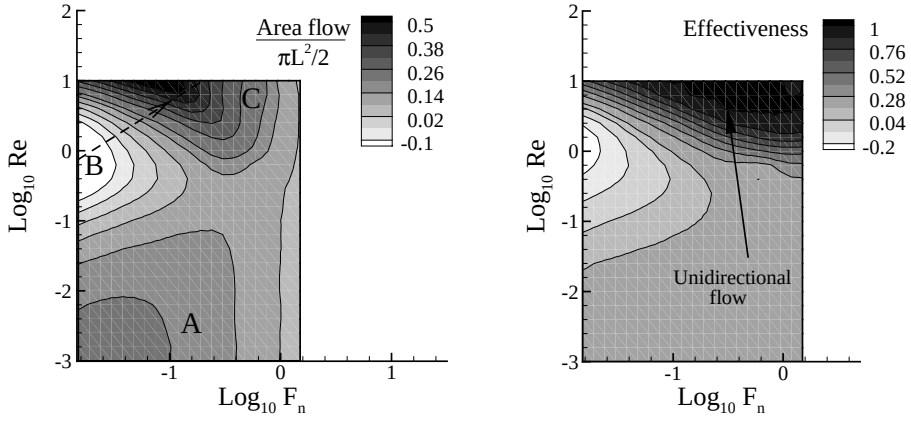

(a) Area flow

(b) Effectiveness

Figure 5.8: *Parametric area flow and effectiveness as a function of fluid number F_n and Reynolds number Re at a magnetic number of 10.89.*

1990). In artificial ciliary systems, however, the metachronal wave can be established by magnetically forcing the cilia to beat out-of-phase (shown in section 7.2.2). The study performed in the current section also suggests that a given ciliary system can be made to switch the flow direction depending on the operating frequency (see the dashed arrow in Fig. 5.8(a), which shows the direction of increasing frequency or decreasing t_{beat}). A ciliary system in region B creates a flow in the direction of the recovery stroke. Now, if the frequency of magnetic actuation is increased, both the fluid number as well as

the Reynolds number will increase, resulting in a strong increase of the effectiveness and large unidirectional flow which is maximal for the range of F_n and Re studied (see Fig. 5.8).

5.3 Conclusion

In this chapter we have analysed the effect of fluid inertia forces on the flow created by magnetically driven artificial cilia in microfluidic channels. The competition between the fluid viscous forces, inertia forces and elastic forces in the cilia was captured using the fluid number (F_n) - the ratio between the fluid drag forces and the Reynolds number (Re) - the ratio of fluid inertia to viscous forces. The fluid inertia has two effects. Firstly, the momentum diffusion from the cilia to the rest of the channel is delayed. Secondly, a part of the energy input to the fluid in the effective stroke is retained even after the effective stroke is finished. When the Reynolds number is high, this leads to an average unidirectional flow over a beat cycle. At low fluid numbers ($F_n < 1$), the flow created at high Reynolds numbers (Re > 1) is much larger than that of the Stokes regime. However, at moderate Reynolds numbers, the fluid flow changes direction and occurs in the direction of the recovery stroke. In these cases, as the fluid numbers are low, the cilia complete the recovery stroke quickly and are idle for a short period of time before the start of the next effective stroke. During this idle position, the high energy input to the fluid by the fast recovery stroke creates a large flow in the direction of the recovery stroke. This recovery flow overcomes the effective flow and creates a net flow in the direction of the recovery stroke. By exploring the parameter space of F_n and Re, we found that the flow created by a given ciliary system can switch direction simply by tuning the frequency of actuation.

Chapter 6

Inertial effects in ciliary flows - model problem

Abstract

In this chapter we investigate biomimetic fluid propulsion due to an array of periodically beating artificial cilia. A generic model system is defined in which the effect of inertial fluid forces and the spatial, temporal and orientational asymmetry of the ciliary motion can be individually controlled. We demonstrate that the so-far unexplored orientational asymmetry plays an important role in generating flow, that the flow increases sharply with Reynolds number and eventually becomes unidirectional. We introduce the concept of configurational symmetry that unifies the spatial, temporal and orientational symmetries. The breaking of configurational symmetry leads to fluid propulsion in microfluidic channels.

6.1 Introduction

One of the principal challenges in lab-on-a-chip applications is to propel the fluids in microchannels (Laser & Santiago, 2004). To propel fluids at these small length scales, nature utilizes cilia and flagella, attached to the surface of organisms to actuate the fluid locally so as to have a net fluid propulsion. A consequence of the small length scales is that viscous forces dominate over inertia forces, which dictates that the actuators have to move periodically in time but in a spatially asymmetric manner. This condition is satisfied in the case of cilia by the distinct effective and recovery stroke during each cycle of their motion (Brennen & Winet, 1977).

Many examples have appeared in recent literature of artificial cilia that mimic the natural ciliary motion through different physical actuation forces, imposed by electric fields, magnetic fields or through base excitation (Evans *et al.*, 2007; den Toonder *et al.*, 2008; Oh *et al.*, 2009; van Oosten *et al.*, 2009; Fahrni *et al.*, 2009; Kim & Netz, 2006; Gauger *et al.*, 2009; Khaderi *et al.*, 2009). In some cases the physical actuation forces get sufficiently large so that also the effect of inertia comes into play (den Toonder *et al.*, 2008; Baltussen *et al.*, 2009). As a result, the breaking of temporal asymmetry can also contribute to propulsion, in addition to the breaking of spatial asymmetry as required at low Reynolds numbers. In general, there are three fundamental mechanisms that are active in artificial cilia-driven fluid flow: (i) spatially asymmetric motion, (ii) temporally asymmetric motion and (iii) orientationally asymmetric motion. The first is the only mechanism that is effective at low Reynolds numbers. Nature effectively makes use of this at small length scales (e. g. cilia). In addition to spatial asymmetry, temporal asymmetry

Based on Khaderi, *et al. Breaking of symmetry in microfluidic propulsion driven by artificial cilia*, Physical Review E, 2010, **82**, 027302.

can enhance flow when inertia forces are no longer negligible (e. g. the locomotion of scallops is entirely based on spatially symmetric motion with temporal asymmetry). In human swimming both spatial and temporal asymmetry are employed. The third mechanism has not been carefully explored until now and is related to the asymmetry of the actuator motion relative to the channel direction. However, due to the intricate interplay of actuation forces (e. g. electric and magnetic), elastic forces, fluid inertia and drag forces, the individual contribution of the three fundamental mechanisms to the generated flow remains unknown. For instance, in the previous chapter the fluid flow was caused primarily due to the asymmetric motion. However, when the inertia forces became prominent, the temporal asymmetry caused a flow reversal and the resulting flow was due to a combination of inertia forces, temporal and spatial asymmetries.

To understand how the fluid flow depends individually on these mechanisms, we analyse a model system in which the relative contribution of the spatial, temporal and orientational asymmetry can be studied as a function of fluid inertia. We show that the inertia forces in the fluid can be usefully exploited to enhance the flow, when compared to the flow in the Stokes regime. Moreover, by utilizing the inertia forces the flow can be made unidirectional, even though the ciliary motion is cyclic. Interestingly, also natural cilia are able to generate a unidirectional flow, but utilize metachrony to achieve this (Satir & Sleigh, 1990). In the absence of any spatial and temporal asymmetry, the orientational symmetry can be broken which leads to flow rates that are comparable to typical spatially asymmetric rates in the Stokes regime. Finally, we unify the asymmetries studied in this analysis and introduce the general concept of configurational symmetry, the breaking of which causes flow.

6.2 Problem definition

The model system consists of an infinitely long array of synchronously beating cilia with an inter-ciliary spacing W, placed in a channel of height H. To perform the simulations, we choose a unit-cell of width $W = 2L$ and height $H = 2L$, whose top and bottom are no-slip boundaries and the left and right boundaries are periodic, see Fig. 6.1. We kinematically prescribe the motion of the cilium such that its tip moves in an elliptical orbit around $(x, y) = (0, 0)$, at an angular velocity of $\omega_e = 2\pi/T_e$ for the effective stroke and $\omega_r = 2\pi/T_r$ for the recovery stroke, resulting in a total cycle time $t_{\text{cycle}} = (T_e+T_r)/2$. Here, with $T_e/2$ and $T_r/2$ are the times taken to complete the effective and recovery stroke, respectively. The lengths of the principal elliptical axes are $2a$ and $2b$, oriented at an angle θ to the channel direction. The remaining portion of the cilium is kinematically prescribed to remain straight, with the lower end of the film fixed at $(-L\tan\theta, -L)$. The angle θ is zero when the principal elliptical axis $2a$ is parallel to the channel axis and is positive in the clockwise direction; the orientation shown in Fig. 6.1 corresponds to $\theta > 0$. The inertia in the fluid is independently controlled by changing the Reynolds number ($\text{Re} = \rho L^2/\mu t_{\text{cycle}}$) through the fluid density ρ, while the fluid viscosity μ is maintained constant. The temporal asymmetry is controlled by changing T_e/T_r, while the total cycle time $(T_e+T_r)/2$ is maintained constant. It is to be noted that when $a = 0$ or $b = 0$ no spatial asymmetry exists, when $T_e = T_r$ no temporal asymmetry exists and when $\theta = 0$ no orientational asymmetry exists.

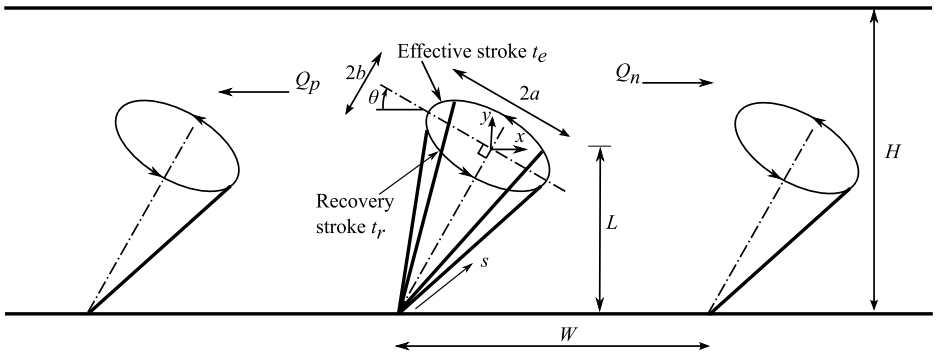

Figure 6.1: *Schematic picture of the model problem showing the parameters involved.*

6.3 Results

The defined problem is solved using the finite element method in which the fluid is assumed to be an incompressible Newtonian liquid. The fluid-structure interaction is performed using the fictitious domain method in which the fluid and the solid (cilia) velocities are coupled through Lagrange multipliers (Khaderi *et al.*, 2009; van Loon *et al.*, 2007). The instantaneous flux is obtained by integrating the horizontal velocity over the channel height, while the net amount of fluid propelled per cycle (termed 'area flow') is calculated by integrating the instantaneous flux over the cycle time. The fluid is initially at rest and it takes some time for the system to reach a steady state, especially at large Reynolds numbers. The outcome of the analysis is quantified in terms of three parameters after a steady state has been reached: area flow, the efficiency and the effectiveness of fluid transport. The latter are detailed in the following. The cilium pushes the fluid forward during the effective stroke, creating a 'positive area flow' Q_p in the direction of the effective stroke (i. e. to the left in Fig. 6.1) and pushes the fluid back during the recovery stroke creating a 'negative area flow' Q_n. Under suitable conditions, the positive flow is larger than the negative flow, generating a positive area flow per cycle $(Q_p - Q_n)$. The effectiveness, defined as $(Q_p - Q_n)/(Q_p + Q_n)$, indicates which part of the totally displaced fluid is effectively converted into a net flow. An effectiveness of unity represents a unidirectional flow. To investigate how efficiently the swept area (area of the ellipse) is converted to fluid flow, we define the efficiency as the area flow per unit area swept.

6.3.1 Effect of spatial and temporal asymmetry

We first study the dependence of the area flow on the area swept, Reynolds number and temporal asymmetry T_r/T_e for a fixed orientation $\theta = 0$ in Fig. 6.2. The swept area is changed by fixing b and changing a. Both the area flow and the swept area are normalised with the maximum area that can be swept by a cilium of length L $(\pi L^2/2)$. It can be seen that for all values of Reynolds number the area flow scales linearly with the swept area, Fig. 6.2(a) (as also observed in (Khaderi *et al.*, 2009) for the Stokes regime). It can be seen from the inset of Fig. 6.2(a) that for $\mathrm{Re} < 0.1$ (Stokes limit) the efficiency (i. e. the area flow/area swept) remains constant, while for $\mathrm{Re} > 0.1$ the efficiency increases sharply with an increase in Reynolds number. Moreover, at high

Reynolds numbers the flow generated increases when the effective stroke is faster than the recovery stroke ($T_e < T_r$), while it decreases when the opposite is true ($T_e > T_r$). Figure 6.2(b) shows the effectiveness as a function of area swept. The effectiveness is low when a large volume of fluid is shifted back and forth with only a modest net effect. This is the case in the Stokes regime. However, with increasing Reynolds number the effectiveness increases, reaching a purely unidirectional flow at Re ≈ 10 and for relatively fast effective strokes. As b is kept constant and a is increased, the velocity of the cilium is enhanced because the cycle time is fixed. Hence, as the swept area is increased, the instantaneous flux also increases due to the larger velocity during the effective as well as the recovery stroke. This results in the effectiveness of fluid actuation to be unchanged (Fig. 6.2(b)), but causes an increase in the net area flow due to the enhanced fluid velocity (Fig. 6.2(a)).

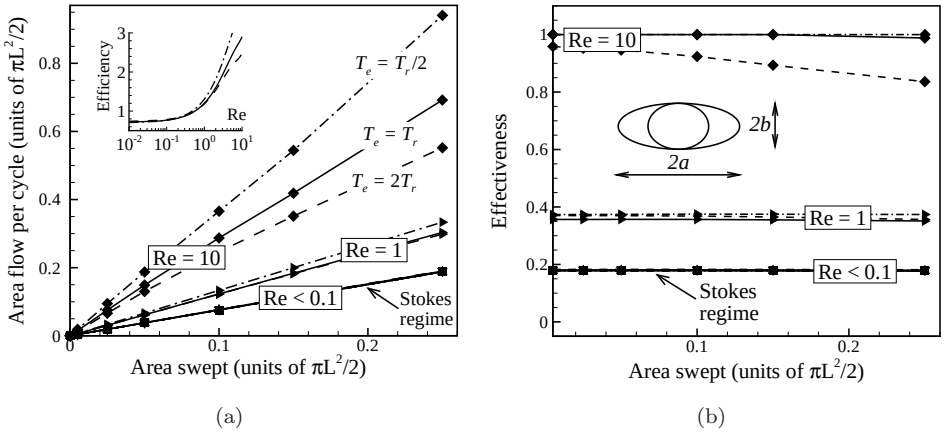

Figure 6.2: *(a) Area flow out of the channel as a function of the area swept ($\theta = 0°$) for different Reynolds numbers. Also plotted are the cases in which the velocity during the effective stroke is different from that of the recovery stroke. The inset shows the efficiency of fluid flow as a function of the Reynolds number. (b) Effectiveness of fluid flow ($(Q_p - Q_n)/(Q_p + Q_n)$) as a function of the area swept for different Reynolds numbers and T_e/T_r values.*

To analyse how the fluid is pumped through each cycle we plot the trajectory of fluid particles for two cycles in Fig. 6.3. We compare the results in the Stokes limit (low Re, Fig. 6.3(a)) with those at large Re (Re = 10, Fig. 6.3(b)). The fluid particles are represented by dots forming initially a straight line in instance 1. The instances 3 and 5 refer to the end of the first and the second cycle, respectively, and instances 2 and 4 refer to the end of the effective stroke of the first and second cycle. In the Stokes limit (i. e. low Re, see Fig. 6.3(a)), the dissipative viscous forces are larger than the inertia forces. As a consequence, the energy gained by the fluid due to the actuation of the cilium will be instantaneously dissipated, so that the momentum imparted by the cilium will be efficiently (instantaneously) transmitted to the surrounding fluid without delay. The fluid particles which initially form a straight line (instance 1) move due to the velocity imposed by the film during the effective stroke. The fluid particles stop and reverse their direction of motion once the film begins the recovery stroke (at instances 2 and 4) leading to back-flow during recovery (ending at instances 3 and 5). Due to the spatial asymmetry in the deformation of the film, we observe a net displacement of fluid

particles over each cycle. As the fluid particles move back and forth during the cycle, the flow exhibits a fluctuating behaviour, leading to a low effectiveness of fluid propulsion, see Fig. 6.2(b). The response of the system does not change when the effective and recovery stroke are performed at different rates.

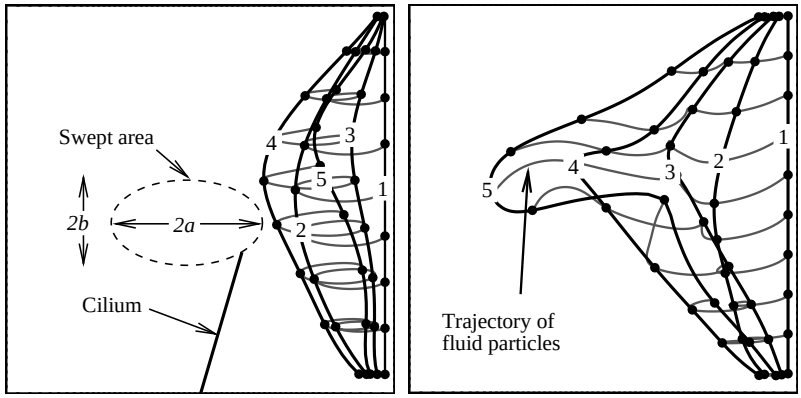

Figure 6.3: *Trajectory of particles over two cycles for $T_e = T_r$, $a = 0.3L$ and $b = 0.25L$. (a) Stokes regime (Re < 0.1); (b) Re = 10.*

When the Reynolds number is high (Fig. 6.3(b)), the dissipative forces are low compared to the inertia forces. Hence, the inertial momentum/energy gained by the fluid during the effective stroke is not dissipated instantaneously, but persists during recovery, which causes a flux in the direction of the effective stroke even during the recovery stroke, see instances 2-3 and 4-5. This effect becomes more prominent as the Reynolds number is increased, leading to a large net fluid flow (Fig. 6.2(a)), high efficiency (inset of Fig. 6.2(a)) and a higher effectiveness (Fig. 6.2(b)). The flow becomes fully unidirectional for $T_e = T_r$ when Re ≥ 10. Note that the particles close to the bottom boundary still fluctuate even at high Re. This is due to the fact that in this region the momentum is not transmitted through viscous forces, but due to the pressure gradient between adjacent cilia. This mode of momentum transfer is equally efficient at low as well as high Reynolds numbers, see Fig. 6.3.

6.3.2 Effect of orientational asymmetry

From the results presented so far, the effect of spatial and temporal asymmetry are independently studied, in the absence of orientational asymmetry ($\theta = 0$). To analyse the effect of orientational asymmetry we analyse the flow as a function of the orientation θ in the absence of spatial asymmetry ($a = 0.25L$ and $b = 0$) in Fig. 6.4. The temporal asymmetry is varied from $T_r = T_e$ (no asymmetry) to $T_r = 3T_e$ and the direction of ciliary motion θ from $-60°$ to $60°$ (see Fig. 6.1) for different Reynolds numbers. The area flow is normalised with $\pi L^2/2\cos^2\theta$. When the motion of the cilium exhibits no temporal asymmetry, we do not observe flow in the Stokes regime (Re < 0.1), for all orientations θ. Now, as we increase the Reynolds number (still $T_r = T_e$), a fluid flow is observed whose direction depends on the orientation θ, reaching a maximum at $\theta = \pm 45°$, see the broken lines in Fig. 6.4. The results are point-symmetric in $(0, 0)$ due to the absence

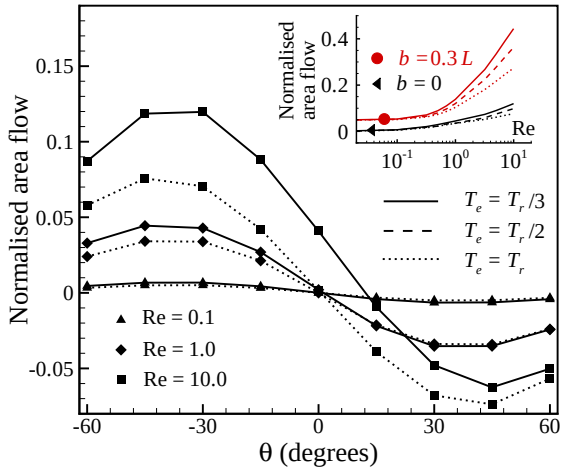

Figure 6.4: *Area flow normalised with $\pi L^2/2\cos^2\theta$ as a function of orientation θ for different Reynolds numbers and temporal asymmetries. The inset shows the normalised area flow as a function of Reynolds number (Re) for $\theta = -45°$ for different temporal and spatial asymmetries. In all the simulations a is taken to be equal to $0.25L$. Legend: The solid lines, dashed lines and broken lines refer to $T_e = T_r/3$, $T_e = T_r/2$ and $T_e = T_r$, respectively.*

of any spatial and temporal asymmetry. The flow generated is therefore entirely due to the breaking of orientational symmetry. When $\theta = -45°$ we obtain a maximal positive flow (i. e. flow in the direction of the effective stroke, see Fig. 6.1) and when the film moves in the direction $\theta = 45°$ we observe a negative flow. When we allow for temporal asymmetry (i. e. $T_e < T_r$), the flow is enhanced in the direction of the effective stroke (positive flow), the extent of which is larger for $\theta < 0$ compared to $\theta > 0$.

Consider the case when no temporal asymmetry exists ($T_r = T_e$), i. e. the dashed lines in Fig. 6.4, for $\theta = -45°$. During the effective stoke, the cilium imparts momentum to the fluid as it moves towards the bottom boundary and away from the moving fluid, allowing the fluid to pass without much obstruction in the direction of the effective stroke. When the cilium performs a recovery stroke, it again imparts momentum to the fluid, but now the cilium moves away from the bottom boundary thereby obstructing the flow during recovery. During the cycle, we thus have a larger flow during the effective stroke than during the recovery stroke, resulting in a net positive fluid flow in the effective direction. It is interesting to note that the observed net flow originates solely from the orientational asymmetry, causing an easy passage of fluid during the effective stroke while obstructing the flow during the recovery. Since there is no spatial or temporal asymmetry, the problem is perfectly symmetric with respect to $\theta = 0$, resulting in an equal-sized but opposite flow for $\theta = 45°$. When the fluid is pushed at a higher rate during the effective stroke, i. e. $T_e < T_r$ (the solid lines in Fig. 6.4), for $\theta < 0$ the motion of the film allows an easy passage of the high-momentum fluid during the effective stroke, while obstructing the low-momentum fluid during recovery. For $\theta > 0$, the film motion obstructs the high-energy fluid during the effective stroke and allows easy passage of low-energy fluid during recovery, resulting in a much smaller enhancement of positive flow than for $\theta < 0$. In the inset of Fig. 6.4 we analyse flow as a function of Reynolds number for $\theta = -45°$, in the presence ($b = 0.3L$) and absence ($b = 0$) of spatial asymmetry. It

can be observed that fluid propulsion can be generated when no temporal and spatial asymmetry exist, provided the fluid inertia is non-negligible (lowest curve). The flow can be increased by including temporal asymmetry (i. e. faster effective than recovery stroke). By adding spatial asymmetry, the effect of orientational and temporal asymmetry can be drastically enhanced, leading to a synergistic combination of all three asymmetries.

6.4 Configurational symmetry

The three independent symmetries studied in this chapter, i. e. spatial, temporal and orientational symmetry, can be generalized into the concept of configurational symmetry. We define a ciliary configuration at any time t by the position of material points $s(x, y)$ of the cilium and their instantaneous velocities $(\dot{x}, \dot{y})$. We define the system to be configurationally symmetric when every configuration (at time t) can find its mirror image after half a cycle (at time $t + t_{\text{cycle}}/2$), with the symmetry plane being perpendicular to the channel, see Fig. 6.5. A net flow will occur in the absence of configurational symmetry. This symmetry can be broken either by spatial, temporal or orientational asymmetry.

It is interesting to note that even a non-reciprocal motion can be configurationally symmetric. For instance, an actuator beating like a flagellum and aligned normal to the channel axis, will find its mirror image after half a cycle and therefore will not generate a net flow. Such an actuator needs to be non-perpendicular to the channel direction in order to break the orientational symmetry and to generate a flow, as has been shown in (Darnton *et al.*, 2004). Examples in the literature where the configurational symmetry is broken through spatial asymmetry leading to fluid flow can be found in (van Oosten *et al.*, 2009; Khaderi *et al.*, 2009; Gauger *et al.*, 2009; Kim & Netz, 2006), employing actuation forces that are generated by magnetic fields (Khaderi *et al.*, 2009; Gauger *et al.*, 2009), internal molecular motors (Kim & Netz, 2006) and light (van Oosten *et al.*, 2009). In the case of electrostatic artificial cilia (den Toonder *et al.*, 2008), the fluid flow was achieved by breaking both temporal and orientational symmetry. On the other hand, a nice example of configurationally symmetric cilia is given in (Oh *et al.*, 2009), where it is shown that a configurationally symmetric motion of cilia cannot generate a fluid flow in the direction of the channel. Thus, the definition of configurational symmetry can be a valuable fundamental concept in understanding existing (and designing new) physical actuation mechanisms for microfluidic propulsion. Moreover, it opens the opportunity of deriving analytical expressions that relate flow to quantitative measures of configurational asymmetry.

6.5 Summary

In this chapter we investigated the fundamental physical mechanisms that govern the microfluidic propulsion caused by artificial cilia. Many examples appeared in the recent literature of artificial cilia, but the understanding of the underlying mechanisms has been hampered by the strong competition between the actuation forces, elastic forces and fluid inertia and drag forces. By analysing a generic model system, we show that, besides the well known cilia-kind of spatially asymmetric motion, temporal and orientational asymmetries play a significant role in microfluidic propulsion.

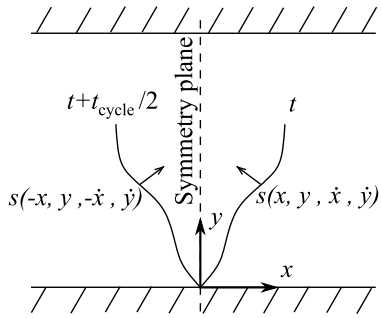

Figure 6.5: *Definition of configurational symmetry: every ciliary configuration (i. e. the current position of all material points $s(x, y)$ and their velocities $(\dot{x}, \dot{y})$) at time t can find its mirror image after half a cycle with the symmetry plane being perpendicular to the channel.*

The two key results of this chapter are: (i) Cilia can generate flow through orientational asymmetry alone, even in the absence of spatial and temporal asymmetry. This has not been fully explored before. (ii) All three fundamental symmetries can be generalized into the concept of configurational symmetry, the breaking of which causes fluid propulsion.

Chapter 7
Effect of metachronal waves

Abstract

In this chapter we study the effect of metachronal waves on the flow created by magnetically-driven artificial cilia in microchannels. We use a coupled magneto-mechanical solid-fluid model that captures the physical interactions between the fluid flow, ciliary deformation and applied magnetic field. When a rotating magnetic field is applied to super-paramagnetic artificial cilia, they mimic the asymmetric motion of natural cilia, consisting of an effective and recovery stroke. Two ways of generating a metachronal motion of cilia are considered; by prescribing an external phase difference and by applying a non-uniform magnetic field. We show that the fluid flow created by the artificial cilia is significantly enhanced in the presence of metachronal waves and that the fluid flow becomes unidirectional. Antiplectic metachrony is observed to lead to a considerable enhancement in flow compared to symplectic metachrony, when the cilia spacing is small. Obstruction of flow in the direction of the effective stroke for the case of symplectic metachrony was found to be the key mechanism that governs this effect.

7.1 Introduction

The control of fluid flow in channels of micron-scale dimensions is essential for proper functioning of any lab-on-a-chip device. The fluid transport in microchannels is often performed by downscaling conventional methods such as syringe pumps, micropumps (Laser & Santiago, 2004; Jeon *et al.*, 2000; Schilling *et al.*, 2002), or by exploiting electromagnetic fluid manipulation principles, as in electro-osmotic (Chen *et al.*, 2003; Zeng *et al.*, 2002) and magneto-hydrodynamic (West *et al.*, 2002) devices. In search for novel ways to propel fluids at micron scales, we let nature be our guide. Nature uses hair-like structures, called cilia, attached to the surfaces of microorganisms, to propel fluids at small length scales. The typical length of a cilium is 10 microns. Cilia beat in a whip-like asymmetric manner consisting of an effective stroke and a recovery stroke. Moreover, when many cilia operate together, hydrodynamic interactions cause them to beat out-of-phase (Gueron *et al.*, 1997), leading to the formation of metachronal waves, and an enhanced fluid flow (Satir & Sleigh, 1990). The specific metachrony is termed symplectic (or antiplectic) when the metachronal wave is in the same (or opposite) direction as the effective stroke. The cilia on a Paramecium exhibit antiplectic metachrony, whereas the cilia on Opalina exhibit symplectic metachrony (Blake, 1972).

Based on Khaderi, *et al. Fluid flow in microchannels due to asymmetric and out-of-phase motion of magnetically-actuated artificial cilia*, Journal of Fluid Mechanics, 2011, accepted for publication and Khaderi, *et al. Magnetically-actuated artificial cilia: the effect of fluid inertia and metachrony*, submitted.

The asymmetric motion of natural cilia is due to the intricate interaction between the cilia microstructure (axoneme) and the internal driving force generated by ATP-enabled conformational changes of the motor protein dynein. It is a challenging task to design the artificial counterpart of natural cilia, by using external force fields for actuation in order to mimic the asymmetric motion of natural cilia. An early attempt to create artificial cilia was based on electrostatic actuation of cilia-like microactuator arrays (den Toonder *et al.*, 2008). Although effective flow and mixing were achieved, movement of these artificial cilia was not asymmetric as in the case of natural cilia. It was predicted using numerical simulations that an array of identical super-paramagnetic or permanently magnetic two-dimensional plate-like cilia can mimic the planar asymmetric motion of natural cilia when exposed to a uniform magnetic field (Khaderi *et al.*, 2009). These magnetic artificial cilia can be realised, for instance, by using polymer films with embedded super-paramagnetic (or permanently magnetic) nano-particles (see e.g. Fahrni *et al.*, 2009; Belardi *et al.*, 2010; Schorr *et al.*, 2010). In contrast with the plate-like cilia, rod-like structures that mimic the three-dimensional motion of nodal cilia to create fluid propulsion have also been fabricated (Vilfan *et al.*, 2010; Shields *et al.*, 2010; Evans *et al.*, 2007). In (Sing *et al.*, 2010), a novel method of fluid propulsion based on magnetic walkers was presented. Artificial cilia based on photo-actuation have also been realised in the recent past (van Oosten *et al.*, 2009).

In previous studies we focused on the flow created by an array of synchronously-beating cilia whose motion is planar and asymmetric, in the absence (Khaderi *et al.*, 2009) and presence of fluid inertia (Khaderi *et al.*, 2010). Using numerical simulations it was reported that a substantial but fluctuating flow is created in the former, while in the latter the flow increases significantly as the Reynolds number is increased. In addition, the fluid flow can become unidirectional in the presence of fluid inertia. In this work we explore another aspect of natural ciliary propulsion - the metachronal motion of cilia, by allowing the asymmetrically-beating artificial cilia to move out-of-phase. The out-of-phase motion of the cilia is achieved by applying a magnetic field that has a phase lag between adjacent cilia. The existing literature on the metachronal motion of natural cilia could provide insights on the flow generated in the presence of metachronal waves.

In the case of natural cilia the metachronal motion is analysed principally for two reasons. First, to find the effect of the metachronal waves on the flow created and second, to find the physical origin of the metachronal waves. Theoretical and numerical studies have been undertaken by biologists and fluid mechanicians to understand the flow created by an array of cilia (see for e.g. the reviews by Brennen & Winet, 1977; Blake & Sleigh, 1974; Smith *et al.*, 2008). Most of these analyses have been performed to model the flow of specific biological systems (e.g. microorganisms or airway cilia), however, a systematic study is lacking. In the following, we outline a number of studies in which the effect of the metachronal waves on fluid transport has been studied. Modelling approaches to understand the cilia-driven flow include the envelope model (Brennen & Winet, 1977; Blake, 1971*a*,*c*), the sublayer model (Blake, 1972; Gueron *et al.*, 1997; Smith *et al.*, 2007; Liron, 1978; Gauger *et al.*, 2009; Gueron & Levit-Gurevich, 1999), fluid-structure interaction models using a lattice-Boltzmann approach (Kim & Netz, 2006), and the immersed boundary method (Dauptain *et al.*, 2008). In the envelope model, the cilia are assumed to be very densely spaced so that the fluid experiences an oscillating surface consisting of the tips of the cilia. The envelope model is accurate only when the cilia are spaced very close together, which has only been observed in the case of symplectic metachrony (Blake, 1971*a*,*c*). In the sublayer model (Blake, 1972),

the cilia are represented by a distribution of Stokeslets with appropriate mirror images to satisfy the no-slip condition on the surface to which the cilia are attached. The sublayer model predicts that for an organism that exhibits antiplectic metachrony, the flow created is lower than for cilia beating in-phase. In the case of an organism exhibiting symplectic metachrony, the opposite trend is observed. In the numerical study of (Gauger *et al.*, 2009), the flow due to the out-of-phase motion of a finite number of magnetic cilia subjected to an oscillating external magnetic field was studied. The magnetic cilia generate an asymmetric motion due to the difference in the speed of oscillation of the magnetic field during the effective and recovery strokes. In contrast to (Blake, 1972), it was predicted that the flow in the case of antiplectic metachrony is larger than the flow created by a symplectic metachrony for a particular inter-cilia spacing.

Early experiments indicated that the hydrodynamic coupling between cilia could be the cause for the formation of the metachronal waves (see for e.g. the review by Kinosita & Murakami, 1967). By mimicking the ciliary motion of Paramecia using an internal actuation mechanism, it was demonstrated that cilia, which were initially beating in-phase, will form an antiplectic metachronal wave after a few beat cycles (Gueron *et al.*, 1997). This behaviour was explained to be an outcome of the hydrodynamic interactions between neighbouring cilia. Similar hydrodynamically-caused metachronal motion of the cilia was also observed by (Mitran, 2007). In (Gueron & Levit-Gurevich, 1999), it was reported that in the presence of the metachronal wave the cilia become more efficient in creating flow. The synchronization and phase locking of the cilia have also been analysed using simple experimental (Qian *et al.*, 2009) and analytical (Niedermayer *et al.*, 2008; Vilfan & Jülicher, 2006) models. It was found that some degree of flexibility is required for the phase locking of the cilia to take place (Niedermayer *et al.*, 2008; Qian *et al.*, 2009). The requirement of the flexibility for synchronization is also confirmed from the more detailed model of (Kim & Netz, 2006). In the aforementioned studies, however, the metachronal wave is an outcome of that specific system, and the flow or the efficiency has not been studied for different types of metachronal waves.

The goal of this chapter is, therefore, to obtain a full understanding of the dependence of flow on the magnetically-induced out-of-phase motion of an array of asymmetrically beating artificial cilia. We will answer the following questions using a coupled solid-fluid magneto-mechanical model. How does the generated flow in the presence of metachrony differ from the flow generated by cilia that beat in-phase? How does the flow depend on the metachronal wave speed and its direction, and how does it depend on the cilia spacing? We answer these questions in the light of magnetic artificial cilia which exhibit an asymmetric motion and beat out-of-phase. However, the results are equally applicable to any ciliary system in which the cilia exhibit an asymmetric and out-of-phase motion.

The out-of-phase motion of artificial cilia can be achieved by applying a non-uniform magnetic field that travels in space and time. However, a non-uniform magnetic field will also cause magnetic body forces to act on the cilia, which will lead to a beat motion that is different compared to that of synchronously beating cilia. Therefore, we study the out-of-phase motion of the cilia in two steps. First, we apply a rotating magnetic field that is uniform over each cilia but has a phase difference between neighbouring cilia. This keeps the asymmetric motion of the cilia nearly unaltered, and enables us to identify the physical mechanisms that are operative when the cilia beat out-of-phase. In the second step, we apply a non-uniform magnetic field to the cilia and study how the body forces influence the beat motion of the cilia and the resulting flow.

The chapter is organised as follows. The boundary value problem and the solution

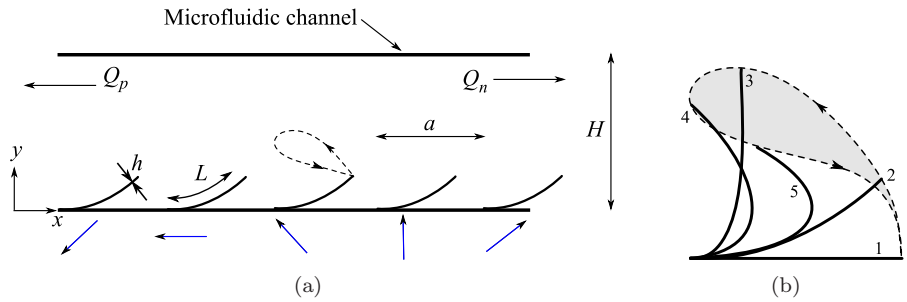

Figure 7.1: *(a) Schematic representation of the problem analysed. We study an infinitely long microfluidic channel consisting of equal-sized cilia spaced a distance a apart. The variation of magnetic field in space is shown using blue arrows. Q_p and Q_n denote the flow in the direction of the effective and recovery stroke, respectively. (b) Typical asymmetric motion of a cilium. The dashed lines represents the trajectory of the tip of an individual cilium.*

methodology are explained in section 7.2.1. In section 7.2.1, the physical mechanisms responsible for the enhanced flow in the presence of metachronal waves are discussed. The quantitative variation of the flow as a function of the phase difference and cilia spacing is given. The deformation of the cilia due to the non-uniform magnetic field and the resulting flow are studied in section 7.2.2. Finally, the outcome of the analysis is summarised in section 7.3.

7.2 Results

7.2.1 Externally imposed out-of-phase motion

We study the flow in an infinitely long channel of height H created by a two-dimensional array of magnetic artificial cilia, which are actuated using a rotating magnetic field which is uniform over each cilium, but with a phase difference between adjacent cilia. The external magnetic field experienced by the i^{th} cilium is

$$B_{xi} = B_0 \cos(\omega t - \phi_i), \qquad B_{yi} = B_0 \sin(\omega t - \phi_i), \tag{7.1}$$

where B_0 is the magnitude of the applied magnetic field, the phase of the magnetic field $\phi_i = 2\pi(i-1)/n$, $\omega = 2\pi/t_{\text{ref}}$ is the angular frequency and t_{ref} is the time period of rotation of the magnetic field. The magnetic field experienced by the individual cilia during a particular instance in time is shown using the blue arrows in Fig. 7.1(a). The phase difference in the applied magnetic field between adjacent cilia is $\Delta\phi = 2\pi/n$. The chosen form of the phase ϕ_i makes the phase of the magnetic field at every n^{th} cilium identical. That is, the magnetic field is periodic after n repeats of cilia. Consequently, the applied magnetic field travels n cilia units in time t_{ref}, so that the phase velocity of the magnetic field is $n/t_{\text{ref}} = \omega/\Delta\phi$ (in cilia per second). The phase velocity is to the right (positive) and the magnetic field at each cilium position rotates counterclockwise with time. The typical asymmetric motion of a cilium is shown in Fig. 7.1(b). The cilia are tethered at one end to the surface, while the other end is free. The trajectory of the free end of a typical cilium is represented by the dashed lines in Fig. 7.1(b), with the arrows representing the direction of motion.

Due to the super-paramagnetic (SPM) nature of the cilia, for which the magnetization is proportional to the magnetic field, the magnetic body couple ($\boldsymbol{N} = \boldsymbol{M} \times \boldsymbol{B}_0$, where $\boldsymbol{M}$ is the magnetization of the cilia and $\boldsymbol{B}_0 = (B_x, B_y)$ is the magnetic field experienced by the cilia) depends only on the orientation and magnitude of the magnetic field, but not on its sign. As a result, the body couple at the i^{th} cilium N_{zi}, which determines its motion, scales with $\sin(2\omega t - 2\phi_i)$ (see Eqn. 2.37). This has consequences for the motion of the cilia, both temporally and spatially. Temporally, the frequency of the magnetic couple is twice that of the applied magnetic field. This results in two cilia beats for one 360° rotation of the magnetic field. Spatially, the phase of the magnetic couple is twice that of the applied magnetic field, so that the phase difference between neighbouring cilia is twice as large. This means that the magnetic couple is periodic after $n/2$ cilia. Since both the frequency and phase difference increase by a factor 2, the phase velocity of the magnetic torque remains equal to that of the magnetic field, i.e. $\omega/\Delta\phi$. Note, however, that the phase velocity of the magnetic torque is equal to the velocity of the metachronal wave (i.e., the actually observed deformational wave travelling over the cilia) only when the phase difference $\Delta\phi$ is small (i.e. n is large).

When the phase difference is too large, the metachronal wave can change sign, so that the metachronal wave is observed to travel in a direction opposite to the direction of the magnetic field (see appendix J). The metachronal wave velocity is equal to $\omega/\Delta\phi$ (i.e. to the right) when $0 < \Delta\phi < \pi/2$, and it is equal to $-\omega/(\pi - \Delta\phi)$ (i.e. to the left) when $\pi/2 < \Delta\phi < \pi$, see Fig. 7.2. When $\Delta\phi = 0$, the magnetic couple is uniform and all cilia beat in-phase. When $\Delta\phi = \pi$, the magnetic couple acting on two neighbouring cilia is the same (because the phase difference of the magnetic couple is $2\Delta\phi = 2\pi$), and again, all the cilia beat in-phase. When $\Delta\phi = \pi/2$, the positive metachronal wave velocity is equal in magnitude to its negative counterpart. In such a condition, a standing wave is observed which causes the adjacent cilia to move in anti-phase. When $0 < \Delta\phi < \pi/2$ the metachronal wave velocity is positive, i.e. to the right in Fig. 7.1. Consequently, the metachronal wave velocity is opposite to the direction of the effective stroke, which is commonly addressed as antiplectic metachrony (AM). When $\pi/2 < \Delta\phi < \pi$, the metachronal wave velocity is in the same direction as the effective stroke and is referred to as symplectic metachrony (SM), see Fig. 7.2.

We model the cilia as elastic Euler-Bernoulli beams taking into consideration geometric non-linearity and inertia of the cilia in a Lagrangian framework. The magnetic field is calculated by solving the Maxwell's equations using a boundary element approach for each ciliary configuration (see chapter 2). The Stokes equations, which capture the behaviour of the fluid flow at low Reynolds numbers, are solved within an Eulerian setting for the velocity and pressure using finite elements. The velocity is interpolated quadratically, while the pressure is interpolated linearly within each element. The solid-fluid coupling is performed by imposing the no-slip condition at the nodal points of the Euler-Bernoulli beam elements using Lagrange multipliers (point collocation method) within a fictitious domain framework (van Loon *et al.*, 2006). The solution procedure is as follows. The Maxwell's equations are solved at every time instant to solve for the magnetic field. From the magnetic field, the magnetic body couple acting on the cilia is calculated and is provided as an external load to the implicitly-coupled solid-fluid model, which simultaneously solves for the cilia velocity, and the velocity and pressure of the fluid. The velocity of the cilia is integrated using Newmark's algorithm to obtain its new position, and the procedure is repeated. For more details on the numerical model the reader is referred to chapter 2. Each cilium is discretised into 40 elements and every fluid

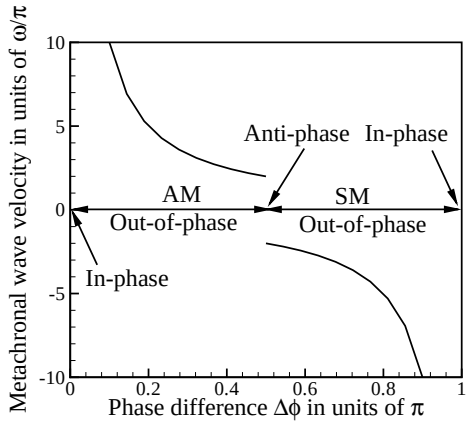

Figure 7.2: *Metachronal wave velocity as a function of the phase difference $\Delta\phi$ in the magnetic field between adjacent cilia. AM and SM refer to antiplectic and symplectic metachrony respectively.*

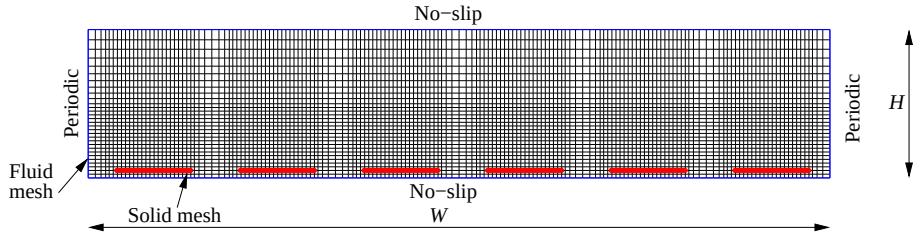

Figure 7.3: *Fluid and solid mesh used for the simulations. The mesh corresponds to $\Delta\phi = \pi/6$ and $a = 1.67L$.*

domain of size $a \times H$ is discretised into 28×30 elements, with the mesh being refined near each cilium. A typical mesh used for the simulations is shown in Fig. 7.3. A fixed time-step of 1 μs is used. The particles and streamlines are obtained from the velocity field in the fluid using the visualization software Tecplot (Tecplot, 2008).

The physical dimensionless numbers that govern the behaviour of the system are the magneto-elastic number $M_n = 12B_0^2L^2/\mu_0 Eh^2$ - the ratio of the magnetic to the elastic forces, the fluid number $F_n = 12\mu L^3/Eh^3 t_{\text{beat}}$ - the ratio of viscous forces acting on the cilia to the elastic forces, and the inertia number $I_n = 12\rho L^4/Eh^2 t_{\text{beat}}^2$ - the ratio of the inertia forces of the cilium to its elastic forces, (see Khaderi *et al.*, 2009). Here, E is the elastic modulus of the cilia, h is the thickness, ρ is the density of the cilia, μ is the fluid viscosity, $t_{\text{beat}}(= t_{\text{ref}}/2)$ is the time period of one beat cycle and μ_0 is the magnetic permeability. The geometric parameters that govern the behaviour of the system are the phase difference $\Delta\phi$, the cilia spacing a, their length L and the height of the channel H. We study the flow created as a function of the cilia spacing a (normalised with the length L) and the phase difference $\Delta\phi$ for the following set of parameters: $F_n = 0.15$, $M_n = 12.2$, $I_n = 4.8 \times 10^{-3}$ and $H/L = 2$. The values of the physical parameters correspond to $L = 100$ microns, $E = 1$ MPa, the thickness of cilia being $h = 2$ μm at the fixed end and 1 μm at the free end, $\rho = 1600$ kg/m^3, $\mu = 1$ mPas, $B_0 = 22.6$ mT and the cycle time $t_{\text{ref}} = 20$ms. The magnetic susceptibilities of the cilia are 4.6 along

the length and 0.8 along the thickness (van Rijsewijk, 2006).

The fluid propelled is characterised by two parameters: the net volume of the fluid transported during a ciliary beat cycle and the effectiveness. The horizontal velocity field in the fluid at any x position, integrated along the channel height gives the instantaneous flux through the channel. This flux integrated in time over the effective and recovery stroke gives the positive (Q_p) and negative (Q_n) flow, respectively (see Fig. 7.1). Due to the asymmetric motion, the positive flow is larger than the negative flow, generating a net area flow per cycle ($Q_p - Q_n$) in the direction of the effective stroke. The effectiveness, defined as $(Q_p - Q_n)/(Q_p + Q_n)$, indicates which part of the totally displaced fluid is effectively converted into a net flow. An effectiveness of unity represents a unidirectional flow. For each value of a/L, we choose n to be a fraction p/q larger than 2, with p and q integers, yielding a range of phase differences $\Delta\phi = 2\pi/n$ between 0 and π. For each value of p/q, a unit-cell of width $W = pa$ needs to be chosen to account for periodicity in the magnetic couple, unless p is an even integer, for which $W = pa/2$ suffices. For example, let $p = 10$ and $q = 3$. Now, $n = 10/3$ and the phase difference $\Delta\phi$ is equal to $3\pi/5$. To maintain periodicity in the magnetic couple, the width of the unit-cell should be $5a$ (containing 5 cilia). The top and bottom of the unit-cell are the channel walls, on which no-slip boundary conditions are applied, while the left and right ends are periodic in velocity.

Results and discussion

To obtain an understanding of fluid flow due to the out-of-phase motion of cilia, we analyse the case of antiplectic metachrony with a phase difference $\Delta\phi = 2\pi/n = 2\pi/12$. Since n is even, a unit-cell of width $6a$ consisting of 6 cilia is chosen, see Fig. 7.4. The contours represent the absolute velocity normalised with L/t_{beat}. The direction of the velocity field can be determined from the arrows on the streamlines. The white arrows represent the applied magnetic field for each cilium.

The snapshots shown in Figs. 7.4(a)-7.4(f) correspond to the time instances when the flux generated by the cilia is maximum. In Fig. 7.4(g) the instantaneous flux as a function of time t (right axis) in addition to the flow (accumulated flux at time t, left axis) are plotted. The time instances corresponding to Figs. 7.4(a)-7.4(f) are marked in Fig. 7.4(g). The motion of the fluid particles near the third cilium under the influence of the velocity field caused by the ciliary motion is also shown. It can be observed from Fig. 7.4(g) that one beat cycle consists of six sub-beats, which correspond to the traveling of the magnetic couple from one cilium to the next. The traveling of the metachronal wave to the right can, for instance, be seen by looking at the cilia which exhibit the recovery stroke (i.e. cilium 1 in Fig. 7.4(a), cilium 2 in Fig. 7.4(b), etc). The negative flow created by the cilia during their recovery stroke is overcome by the flow due to the effective stroke of the rest of the cilia; this leads to a vortex formation near the cilia exhibiting their recovery stroke. As a result, the negative flow is completely obstructed for most of the time during the recovery stroke. It can be observed from Fig. 7.4(g) that no flux (right axis) is transported in the negative direction, and that the flow (left axis) continuously increases during each sub-beat. Moreover, the increase in the flow during each sub-beat is similar (see Fig. 7.4(g)). Thus, the total flow per beat cycle (left axis of Fig. 7.4(g)) is the sum of the flows generated during each sub-beat (i.e. flow per beat = 6×flow generated during one sub-beat). Therefore, it is sufficient to analyse the fluid flow during one sub-beat.

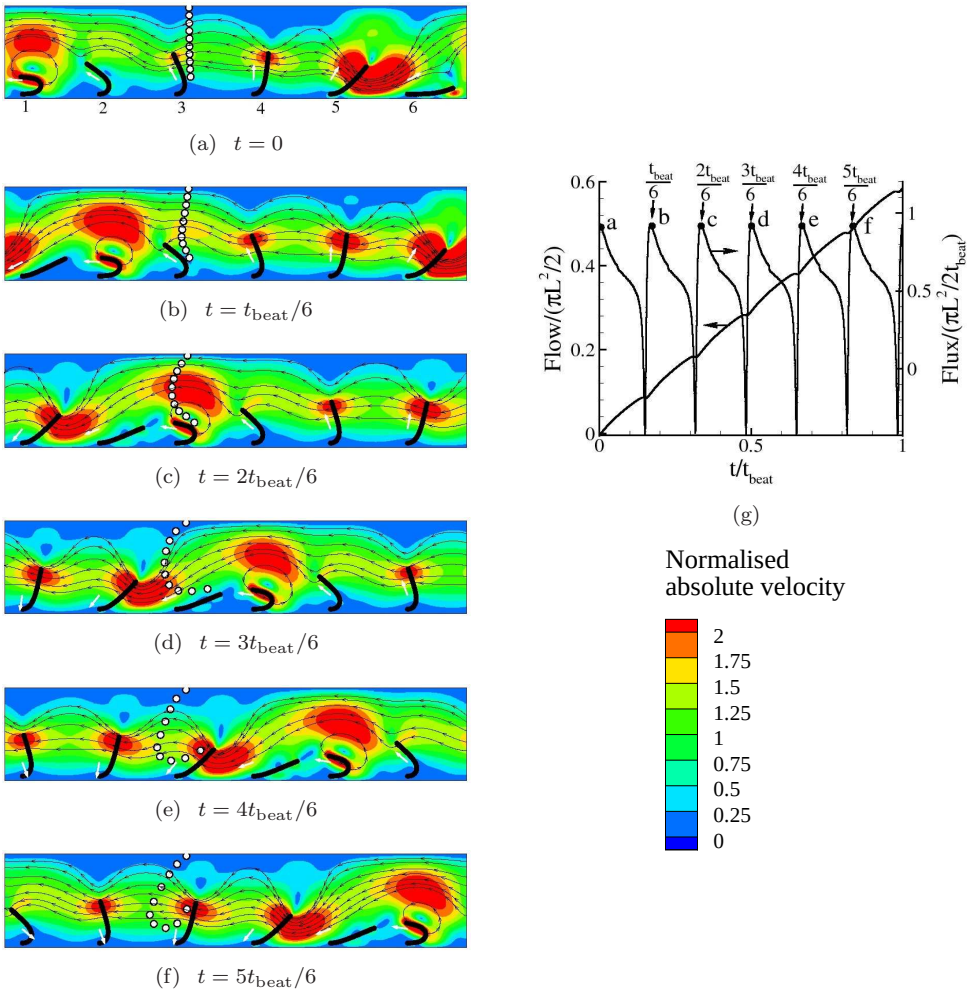

Figure 7.4: *(a)-(f) Out-of-phase motion of cilia during a representative cycle for $\Delta\phi = \pi/6$ ($n = 12$) with the wave moving to the right (antiplectic metachrony) for $a/L = 1.67$. The contours represent the absolute velocity normalised with L/t_{beat}. The direction of the velocity is represented by streamlines. The white circles represent fluid particles. The applied magnetic field at each cilium is represented by the white arrows. (g) Instantaneous flux (right axis) and flow (or accumulated flux, left axis) as a function of time with the instants (a)-(g) duly marked.*

In the following, we analyse the fluid motion and the resulting flow during the second sub-beat. The velocity profiles at different instants of this sub-beat are shown in Figs. 7.5(a)-7.5(d). The corresponding flow and the flux generated are shown in Fig. 7.5(e). At $t_{beat}/6$, the third cilium starts its recovery stroke and the particles near the top boundary are driven by the positive flow created by cilia 4, 5 and 6 (see Fig. 7.5(a)). At this instant, as only one cilium is exhibiting a recovery stroke, the flux created by the cilia is maximum (see instant 'a' in Fig. 7.5(e)). In Fig. 7.5(b), the third cilium also has begun its recovery stroke and now the negative flow caused by both the

second and third cilia is opposed by the effective stroke of the other cilia. The high velocity of the second cilium during its recovery stroke decreases the flux caused by the other cilia (see instant 'b' in Fig. 7.5(e)). When the third cilium is half-way through its recovery stroke (see Fig. 7.5(c)), the second cilium is about to finish its recovery, which generates a large velocity, due to the whip-like action (Khaderi *et al.*, 2009), to the right. Now, the position of the third cilium is such, that it opposes the negative flow caused by the second cilium. This leads to a strong vortex formation near the second and third cilia, with only a small flux in the direction of the recovery stroke (to the right). The small negative flux caused by the whip-like motion of the second cilium can be seen by the instant marked 'c' in Fig. 7.5(e), causing a momentary decrease in the flow. The vortex imparts a high velocity in the direction of the effective stroke to the particles away from the cilia. As the third cilium progresses further in its recovery stroke, the particles come under the influence of the flow due to the rest of cilia, which are now in different phases of their effective stroke (see Fig. 7.5(d)). Now, only the third cilium is in the recovery stroke; this again leads to a maximum value of the flux (similar to Fig. 7.5(a)). The key observation of Figs. 7.4 and 7.5 is that the negative flow created during the recovery stroke of the cilia creates a local vortex due to the positive flow created by other cilia. This shielding effect during the recovery stroke leads to a drastic increase in the net propulsion rate for cilia beating out-of-phase, compared to synchronously beating cilia.

Next, we analyse the instantaneous flux (Fig. 7.6(a)) and flow generated (Fig. 7.6(b)) as a function of time for different phase differences. When the cilia move synchronously ($\Delta\phi = 0$), the flux (see the solid line in Fig. 7.6(a)) is positive for approximately three-quarters of the time and strongly negative during the rest of the cycle. Consequently, the flow generated (see the solid line in Fig. 7.6(b)) increases during the effective stroke, but profoundly decreases when the recovery stroke takes place. This creates a large fluctuation in the flow, with only a small net amount of fluid transported. Once the ciliary motion is metachronal, the negative flux is very small compared to the positive flow (see the cases of a standing wave and antiplectic metachrony in Fig. 7.6(a)). This decreases the fluctuation in the flow generated, causing it to increase nearly monotonously during the beat cycle (see the dashed and dotted lines in Fig. 7.6(b)). We can clearly see that the flow at the end of the beat cycle ($t = t_{\text{beat}}$) for out-of-phase motion is significantly larger than the flow created by the synchronously beating cilia.

The fluid propelled and the corresponding effectiveness are plotted for different values of $\Delta\phi$ and a/L in Fig. 7.7. The metachronal wave velocity (Fig. 7.2) is plotted as a function of $\Delta\phi$ and is shown using dashed lines in Fig. 7.7(a). As mentioned earlier, when the metachronal wave velocity is positive an antiplectic metachrony (AM) results, and when the metachronal wave velocity is negative we get a symplectic metachrony (SM). When all the cilia are moving synchronously ($\Delta\phi = 0$ or π), the flow (normalised by $\pi L^2/2$) will be approximately 0.22 for $a/L = 5$. As the cilia density is increased by decreasing a from $a/L = 5$ to $a/L = 1.67$, the viscous resistance per cilium decreases, which causes the normalised flow to increase to 0.25. When the cilia beat in-phase, the effectiveness of fluid propulsion is very low, see Fig. 7.7(b). The fluid propelled shows a substantial increase once the cilia start beating out-of-phase (Fig. 7.7(a)). When the cilia spacing is large ($a/L = 5$ and 2.5), the flow generated remains approximately constant for all metachronal wave speeds. The increase in flow by decreasing the cilia spacing from $a/L = 5$ to $a/L = 2.5$ is much larger when the cilia beat out-of-phase compared to the increase when the cilia beat in-phase. However, when the cilia spacing is low

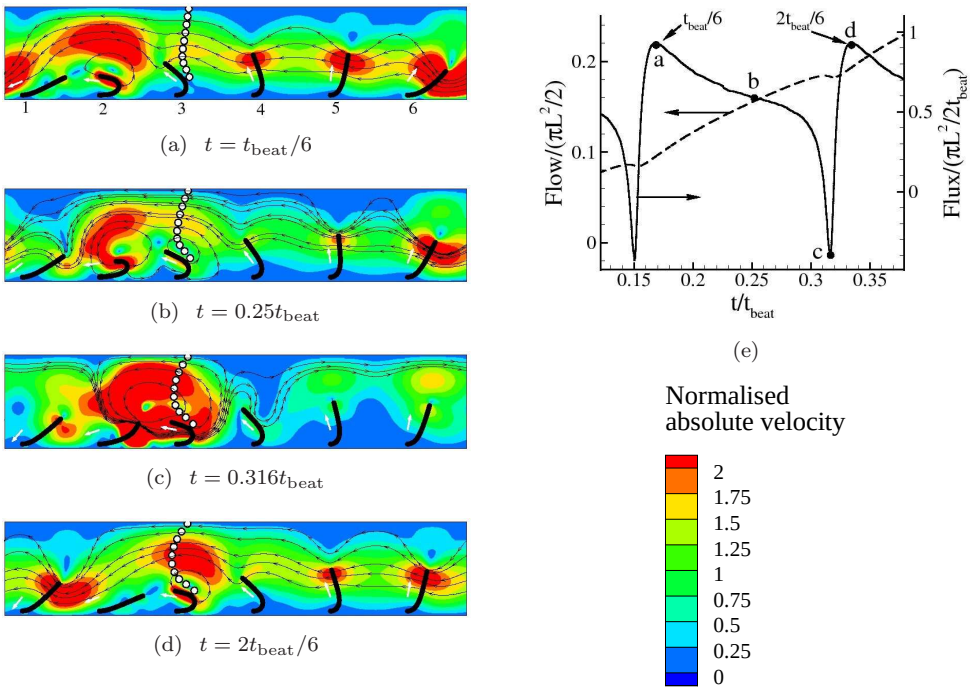

Figure 7.5: *(a)-(d) Snapshots for the out-of-phase motion of cilia between time instances of Figs. 7.4(b) and 7.4(c) for $\Delta\phi = \pi/6$ ($n = 12$) with the wave moving to the right (antiplectic metachrony) for $a/L = 1.67$. The contours represent the absolute velocity normalised with L/t_{beat}. The direction of the velocity is represented by streamlines. The white circles represent fluid particles. The applied magnetic field at each cilium is represented by the white arrows. (e) Instantaneous flux (right axis) and flow (left axis) as a function of time with the instances (a)-(d) duly marked.*

($a/L = 1.67$), we see a larger increase in the fluid flow when there is an antiplectic metachrony(AM) compared to a symplectic metachrony (SM). Also, the effectiveness sharply increases from around 0.3 (i.e., 30% of the totally displaced fluid is converted into net flow) to 1 (fully unidirectional flow), see Fig. 7.7(b). To analyse these trends a bit further, we plot the positive and negative flow (Q_p and Q_n in Fig. 7.1) created during a beat cycle for different phase differences in Fig. 7.8(a). It can be seen that the cilia do not create a negative flow when they beat out-of-phase for all cilia spacings, resulting in a unidirectional flow (effectiveness = 1). This reduction in negative flow is due to the shielding of flow during the recovery stroke caused by the effective flow of other cilia. It can also be noted that the positive flow is also reduced compared to in-phase beating, but the reduction is considerably less than the reduction in negative flow. Thus, the net flow increases as soon as the cilia start to beat out-of-phase (see Fig. 7.7(a)). It can be seen from Fig. 7.8(a) that in the presence of metachronal waves when the cilia spacing is large ($a/L = 5$), the fluid transported during the effective stroke remains nearly the same for all values of the wave velocities. For small cilia spacing ($a/L = 1.67$), however, the positive flow is maximal for antiplectic metachrony, which leads to a larger net flow

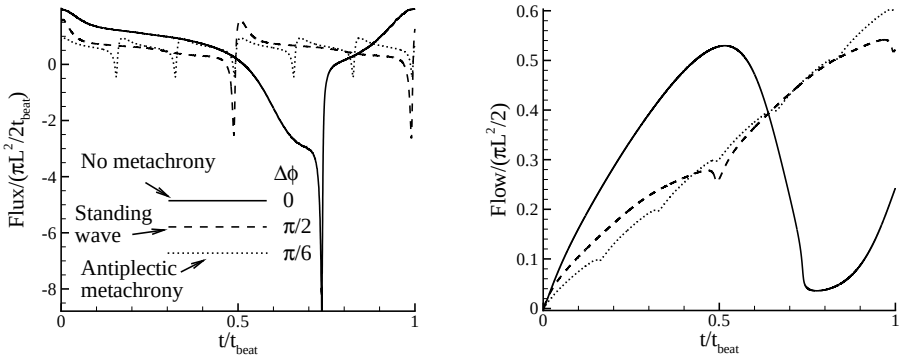

(a) (b)

Figure 7.6: *(a) Normalised fluid flux as a function of time for $a/L = 1.67$ and different values of phase difference $\Delta\phi$. (b) Normalised accumulated flow at any time t during the beat cycle.*

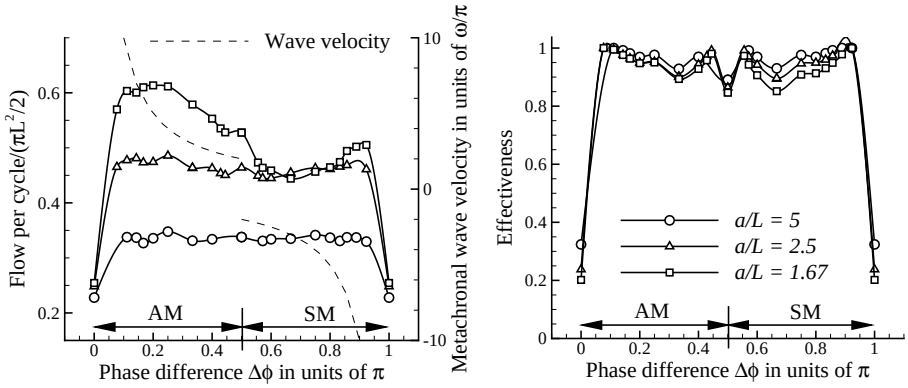

(a) Area flow (b) Effectiveness

Figure 7.7: *Flow and effectiveness as a function of the phase difference $\Delta\phi$ for different inter-cilium spacings a/L. AM and SM refer to antiplectic metachrony (the wave direction is opposite to the direction of the effective stroke) and symplectic metachrony (the wave direction and the effective stroke direction are the same), respectively.*

for antiplectic metachrony compared to symplectic metachrony.

To understand the difference in positive flow for opposite wave directions for small inter-cilium spacing ($a/L = 1.67$), we plot the flux as a function of time scaled with the time taken by the magnetic couple to travel from one cilium to the next t_1, for two different metachronal wave velocities ($3/t_{\text{beat}}$ and $6/t_{\text{beat}}$ cilia per second), see Fig. 7.8(b). The corresponding phase differences are also shown in the legend. It can be seen that the flux in the case of antiplectic metachrony is larger than the flux created by the symplectic metachrony for the same wave speed. This difference in flux for opposite wave directions can be understood by analysing the velocity field corresponding to symplectic and antiplectic metachrony at time instances when the flux is maximum (see Fig. 7.9). Figure 7.9(a) and 7.9(b) correspond to different phase differences ($\Delta\phi = \pi/6$ and $\Delta\phi =$

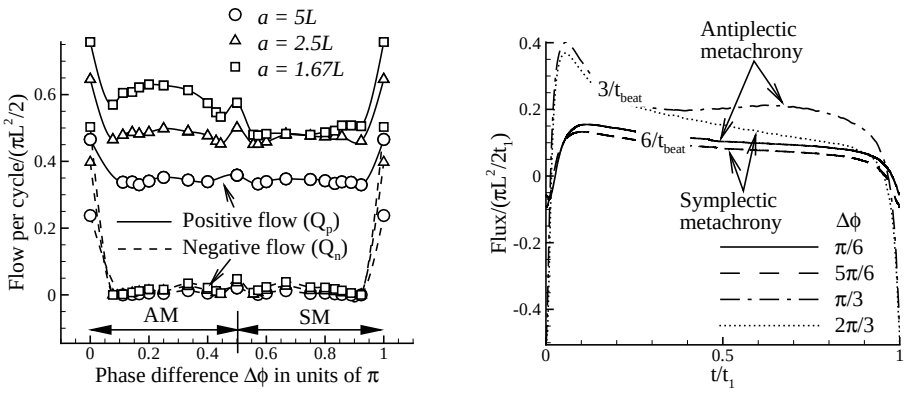

Figure 7.8: *(a) Positive (Q_p) and negative flow (Q_n) (see Fig. 7.1) created by the cilia corresponding to the results presented in Fig. 7.7. (b) Flux vs time (scaled with the time t_1 taken by the magnetic couple to travel from one cilium to the next) for $a/L = 1.67$ and different wave speeds.*

$5\pi/6$, respectively) leading to a similar wave speed of $6/t_{\text{beat}}$ cilia per second (see also Fig. 7.2). The fifth cilium is in the peak of its effective stroke for both AM and SM. In the case of symplectic metachrony, the positive flow created by the fifth cilium is obstructed by the close proximity of the fourth cilium, which has just started its effective stroke. As a result, we observe the formation of a vortex. In the case of antiplectic metachrony, however, the position of the fourth cilium is such that the positive flow created by the fifth cilium is not obstructed. This leads to larger fluid flow in the positive direction, so that the net flow created by an antiplectic metachrony is larger than that created by its symplectic counterpart.

Reports on metachrony and phase locking of beating cilia have appeared in the past (Gauger *et al.*, 2009; Kim & Netz, 2006; Gueron *et al.*, 1997; Gueron & Levit-Gurevich, 1999). The main results are that metachrony enhances flow compared to synchronously beating cilia (Kim & Netz, 2006; Gauger *et al.*, 2009) and that antiplectic metachrony generates a higher flow rate than symplectic metachrony (Gauger *et al.*, 2009). (Kim & Netz, 2006) analysed two cilia, which are driven by internal motors and are moving out-of-phase due to the hydrodynamic interaction. They have shown that the fluid propulsion increases, once the cilia start to beat with a phase difference, which is in agreement with our results. Our results also agree with (Gauger *et al.*, 2009), where it is shown that the fluid flow is larger in the case of antiplectic metachrony than symplectic metachrony when the cilia are close together. However, our results differ from (Gauger *et al.*, 2009) in the sense that we always see an enhancement in flow in the presence of metachrony (compared to cilia beating in-phase) irrespective of the direction and magnitude of the metachronal wave velocity. This is most likely due to the fact that the asymmetry in ciliary motion in our case is much higher. (Gueron *et al.*, 1997) and (Gueron & Levit-Gurevich, 1999) have proposed that the evolution of the out-of-phase motion of cilia in Paramecia is due to hydrodynamic interactions between adjacent cilia leading to antiplectic metachrony. It is interesting to observe that the interplay between the internally-driven actuation and hydrodynamic interaction in nature results in antiplectic

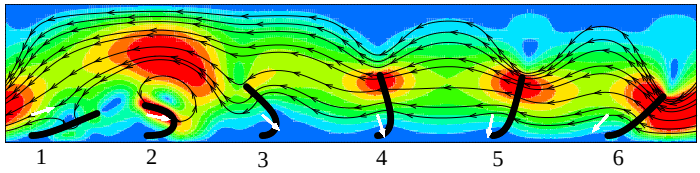

(a) Antiplectic metachrony: wave travels to the right

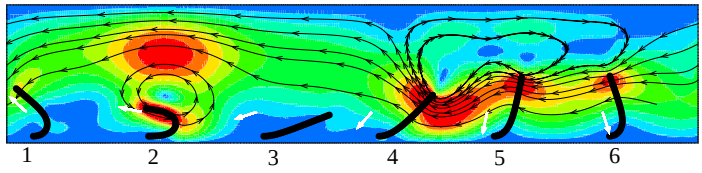

(b) Symplectic metachrony: wave travels to the left

Figure 7.9: *(Colour online) Snapshots for antiplectic ($\Delta\phi = \pi/6$) and symplectic metachrony ($\Delta\phi = 5\pi/6$) for a wave speed of $6/t_{beat}$ cilia per second and cilia spacing $a/L = 1.67$ at $t = 0.1t_1$ of Fig. 7.8(b). The contours represent the absolute velocity normalised with L/t_{beat} (blue and red colours represent a normalised velocity of 0 and 2, respectively). The direction of the velocity is represented by streamlines. The applied magnetic field is shown by the white arrows.*

metachrony. Our results, and those of others (Gauger *et al.*, 2009), show that indeed antiplectic metachrony leads to larger flow than symplectic metachrony for small cilia spacings as typically seen in nature.

7.2.2 Out-of-phase motion caused by a non-uniform magnetic field

Problem statement

We now study the flow generated by magnetic artificial cilia, which are actuated using a rotating and non-uniform magnetic field ($\boldsymbol{B}_0 = (B_{x0}, B_{y0})$) that varies in space and time:

$$B_{x0} = B_0 \cos(\omega t \pm 2\pi x/\lambda), \qquad B_{y0} = B_0 \sin(\omega t \pm 2\pi x/\lambda), \tag{7.2}$$

where B_0 is the magnitude of the applied magnetic field, λ the wavelength of the non-uniform magnetic field, $\omega = 2\pi/t_{\text{ref}}$ is the angular frequency and t_{ref} is the time period of the magnetic field, see Fig. 7.10. The applied magnetic field travels in space and time with a velocity λ/t_{ref}, which is positive (i.e., to the right) when a negative sign is used in Eqn. 7.2, and negative when a positive sign is used.

In addition to the body couple $\boldsymbol{M} \times \boldsymbol{B}_0$ (analysed in sections 2.3 and 5.2.1), the non-uniform magnetic field causes a magnetic body force of magnitude $\boldsymbol{M} \cdot \boldsymbol{\nabla} \boldsymbol{B}_0$ to act on the cilia, where $\boldsymbol{M} = (M_x, M_y)$ is the magnetization of the cilia. Its components in the x and y directions are $M_x B_{x0,x}$ and $M_x B_{y0,x}$, respectively. Since the magnetization M_x scales with B_{x0}, the magnetic body forces in the x and y-direction scale as $\mp \sin 2\theta/\lambda$ and $\pm \cos^2\theta/\lambda = \pm(1 + \cos 2\theta)/2\lambda$, respectively, where $\theta = \omega t \pm 2\pi x/\lambda$; the top and bottom signs are used for a negative and positive wave velocity, respectively. It is to be noted that the magnetic body forces scale with 2θ. From Eqn. 2.37, it can be seen that

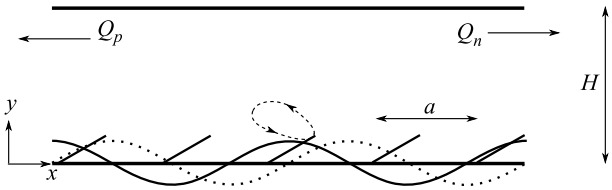

Figure 7.10: *Schematic representation of the problem analysed. We study an infinitely long microfluidic channel consisting of equal-sized cilia spaced a distance a apart. The variation of magnetic field in space at a particular time is shown, which has a wavelength λ and a velocity λ/t_{ref} to the right. Q_p and Q_n denote the flow in the direction of the effective and recovery stroke, respectively. The dashed line represents the trajectory of the tip of a typical cilium. The dotted and continuous sinusoidal curves represent the magnetic field variation in space.*

the magnetic body couple also scales with 2θ. Thus, the frequency of the magnetic body forces and body couple is $\omega_M = 2\pi/t_{\text{beat}} = 2\omega$ and their wavelength is $\lambda_M = \lambda/2$. As mentioned earlier, this causes two ciliary beats in one period of rotation of the magnetic field, and two cilia spaced λ_M apart beat identically. It is important to note that the magnetic body force in the y-direction is positive (or negative) for the magnetic waves travelling to the left (or right). In addition, the magnetic body forces decrease when the wavelength is increased and converges to zero when a uniform field ($\lambda \to \infty$) is applied as in previous section.

As the wavelength of the magnetic forces (both body couple and body forces) is λ_M, the cilia beat in-phase when $a = \lambda_M$ and $a << \lambda_M$ and in anti-phase when $a = \lambda_M/2$. When $0 < a < \lambda_M/2$, the magnetic field causes a metachronal wave whose direction coincides with the direction of the magnetic wave; when $\lambda_M/2 < a < \lambda_M$ the metachronal wave is opposite to the direction of the magnetic wave (Khaderi *et al.*, 2011*b*). The metachronal wave is named symplectic, SM (or antiplectic, AM) when the metachronal wave travels in the same (or opposite) direction as the effective stroke.

We perform the simulations in the Stokes limit with the fluid, magnetic and inertia numbers set to 0.15, 10.89 and 4.8×10^{-3}, respectively. The values of the dimensionless parameters correspond to $L = 100$ microns, $E = 1$ MPa, the thickness of cilia linearly decreased from $h = 2$ μm at the fixed end to 1 μm at the free end, $\rho^f = 0.1$ kg/m^3, $\mu = 1$ mPas, $\rho = 1000$ kg/m^3, $B_0 = 18.8$ mT and the cycle time $t_{\text{ref}} = 2t_{\text{beat}} = 20$ms. The magnetic susceptibilities of the cilia are 4.6 along the length and 0.8 along the thickness (van Rijsewijk, 2006).

Analysis of cilia deformation

The travelling magnetic field leads to a distribution of magnetic couples which is significantly different from the couples in case of a uniform magnetic field. In Fig. 7.11, we neglect the body forces and plot the area swept by the tip of the cilia as a function of L/λ_M for various cilia spacings. For reason shown later, we limit ourself to the cases where the cilia spacing $a < \lambda_M/2$. While performing simulations, we apply the magnetic field in Eqn. 7.2 with positive and negative signs for symplectic and antiplectic metachrony, respectively. The top axis of Fig. 7.11 corresponds to symplectic metachrony, and the bottom axis to antiplectic metachrony. It can be seen that the swept area for the sym-

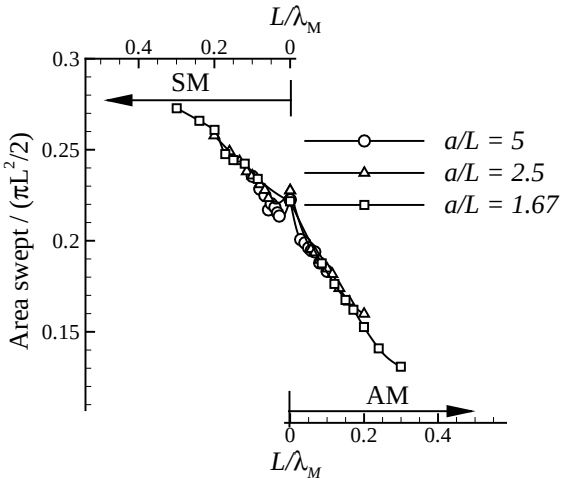

Figure 7.11: *Area swept by the cilia as a function of L/λ_M for different a/L under the sole influence of magnetic body couples caused by a travelling non-uniform magnetic field.*

plectic metachrony is significantly larger compared to synchronously beating cilia (see Fig. 7.11), while the opposite is the case for antiplectic metachrony. This is due to the fact that the cilia are exposed to the system of magnetic couples for longer (shorter) duration of time for SM (AM) compared to synchronously beating cilia, causing an increased (decreased) swept area.

We now analyse the influence of the magnetic body forces on the asymmetry of the ciliary motion for symplectic and antiplectic metachrony. For illustrative purposes, we choose the case of $a = 5L$ and $L/\lambda_M = 0.1$ to plot the motion of a cilium at different time instances after a steady state has been reached (see table 7.1). The thick arrows, hollow arrow heads and thin arrows represent the applied magnetic field, magnetization and magnetic body forces, respectively. Also shown are the signs of the magnetization in the x-direction, field gradients and body forces. As the magnetic field vector at any point rotates counterclockwise irrespective of the travel direction of the wave, the resulting field distribution in space depends on the travel direction. It can be seen that the direction of the magnetization strongly correlates with the direction of the applied magnetic field. The magnetization in the x-direction is maximum during the recovery stroke and initial part of the effective stroke, see the instances (a), (b), (g) and (h) in table 7.1, when the field vector makes an angle 0 or π with the x axis. During these instances $B_{x0,x} \to 0$ and $B_{y0,x}$ is maximum, leading to magnitudes of the body forces that are larger compared to other instances during the beat cycle. It can be seen that the body forces (red arrows in table 7.1) act such that they make the film stay closer to (or further away from) the substrate in the case of antiplectic (or symplectic) metachrony. Therefore, the cilia stay closer to the bottom boundary for antiplectic metachrony, which results in a larger area swept and fluid flow than symplectic metachrony (shown later). The magnetic body forces and body couples complement each other during the beginning of the effective stroke in the case of symplectic metachrony. However, for antiplectic metachrony they oppose each other. As a result, for small wavelengths the magnetic body forces will be very large and do not allow the cilia to beat. The non-uniform magnetic field thus influences the motion of the cilia in two ways: the magnetic body forces (which decrease

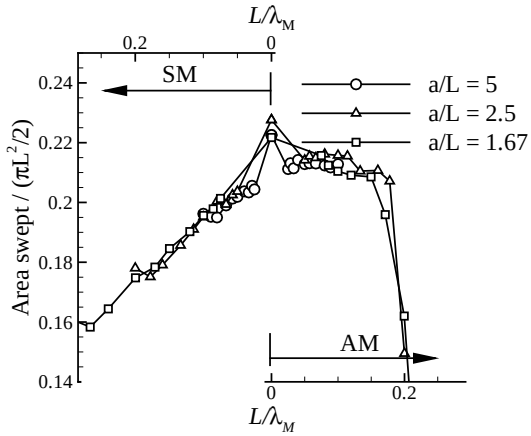

Figure 7.12: *Area swept as a function of L/λ for different inter-cilium spacings a/L under the influence of magnetic couples as well as forces.*

the area swept for symplectic metachrony and enhance it for antiplectic metachrony) and body couple (which increase the area swept for symplectic metachrony and reduce it for antiplectic metachrony). Clearly, the deviation of the swept area from the synchronously beating cilia is governed by the competition between these two effects.

The area swept by the cilia under the influence of both body forces and couples as a function of L/λ_M for different cilia spacings is shown in Fig. 7.12. By comparing Fig. 7.11 with Fig. 7.12, it can be clearly deduced that the effect of body forces dominated over the effect of body couples, leading to a larger swept area for AM compared to SM. As mentioned earlier (see table 7.1), for small wavelengths ($\lambda_M < 0.15L$) the body forces acting towards the bottom boundary in the case of AM are so high that the area swept by the cilia diminishes and in some cases the cilia do not beat at all.

Analysis of fluid flow

Next, we analyse the flow created by the metachrony. We first focus on antiplectic metachrony (the wave moving to the right) for a wavelength $\lambda_M = 6a$ and cilia spacing $a = 1.67L$. The deformed position of the cilia at different time instances in addition to the fluid pressure profiles is shown in Fig. 7.13. The contours represent the pressure in the fluid, the direction of the fluid velocity is shown using the streamlines, the magnetic field distribution is given by the black arrows and the white circles represent the fluid particles. In Fig. 7.13(a) cilium 1 is performing the recovery, in Fig. 7.13(b) cilium 2 is performing the recovery, and so on, clearly showing that the magnetic wave is travelling to the right. It can be seen that the flow and pressure profiles are similar after every $t_{\text{beat}}/6$ seconds, but have translated in the direction of the metachronal wave by one cilium. Let us focus our attention on instance $t = 2t_{\text{beat}}/6$ (Fig. 7.13(b)). The first cilium has just finished its beat cycle and the second cilium is performing the recovery stroke, while the remaining four cilia are in different phases of their effective stroke. Due to the out-of-phase motion of the cilia, the pressure to the right of cilium 2 is much larger than to its left. In this situation the recovery stroke of the cilium 2, instead of creating a negative flow, creates a local vortex. As a result, the negative flux and flow are drastically knocked down, leading to a substantial increase of the net fluid propelled.

Consequently, the created fluid flow is unidirectional. This can also be seen from the variation of the flux and flow as a function of time (see Fig. 7.13(h)). The six periodic dips in the flux profile are caused by the recovery stroke of the cilia. The negative flux, however, is very small compared to the positive flux, which leads to a nearly monotonous increase of the fluid flow with time and a much larger fluid flow at the end of a cycle (0.6 in units of $\pi L^2/2$) compared to the synchronously moving cilia (0.2 in units of $\pi L^2/2$, see Fig. 5.4).

The flow (normalised by $\pi L^2/2$) and effectiveness are plotted as a function of L/λ_M for different cilia spacings in Fig. 7.14. For a given cilia spacing, the flow nicely correlates with the area swept by the free end of the cilia (compare Figs. 7.12 and 7.14(a)). This was also observed in our earlier studies (Khaderi *et al.*, 2009, 2010) for the case of uniformly beating cilia. In the case of symplectic metachrony, as the wavelength gets smaller the magnetic body forces increase, pushing the cilia away from the bottom boundary, which causes a larger negative flow (see the dashed lines in Fig. 7.14(c) for symplectic metachrony), and a resulting decrease in the net fluid transported and effectiveness. At small wavelengths ($\lambda_M < 4L$) of antiplectic metachrony, the magnetic body forces acting during the beginning of the effective stroke are large and do not allow the cilia to exhibit a complete effective stroke. Now, the positive flow is low (see the solid lines in Fig. 7.14(c) for antiplectic metachrony), causing the net fluid transported and effectiveness to attain low values.

In most of the cases, the flow caused by the metachronal motion of the cilia is larger than that of the synchronously beating cilia, even though the area swept in the latter case is larger. This, as seen earlier, is because of the reduction in the negative flow caused by the recovery-induced vortex formation (see also (Khaderi *et al.*, 2011*b*)). In fact, as shown in Fig. 7.14(c), the positive flow is also reduced. However, the reduction in the negative flow is more than the reduction in the positive flow. Consequently, the effectiveness of fluid propulsion is also higher compared to synchronously beating cilia (see Fig. 7.14(b)). When the cilia spacing is decreased the viscous resistance per cilium decreases, which causes the normalised flow to increase. However, decreasing the cilia spacing below $2.5L$ does not increase the fluid propelled for symplectic metachrony. In these cases, the cilia are close together during their effective stroke, which leads to an obstruction of the positive flow of a cilium by its neighbours (Khaderi *et al.*, 2011*b*). It can thus be seen that in the presence of non-uniform magnetic fields we obtain a significant enhancement in the fluid flow for the case of antiplectic metachrony. However in the case of symplectic metachrony, the increase in the flow is only limited.

7.3 Conclusions

We have studied the flow created by a two-dimensional array of artificial cilia as a function of the phase lag and spacing between neighbouring cilia. Two methods of generating a metachronal wave are considered; by prescribing a phase difference between adjacent cilia and by using a non-uniform magnetic field. In the latter case, the magnetic body forces acting on the cilia lead to a reduction of the asymmetric area for the case of symplectic metachrony compared to antiplectic metachrony. The flow per cycle and the effectiveness (which is a measure of the unidirectionality of flow) are considerably enhanced when the cilia start beating out-of-phase, as compared to synchronously beating cilia. While the amount of flow enhancement depends on the inter-cilia spacing, the effectiveness is not

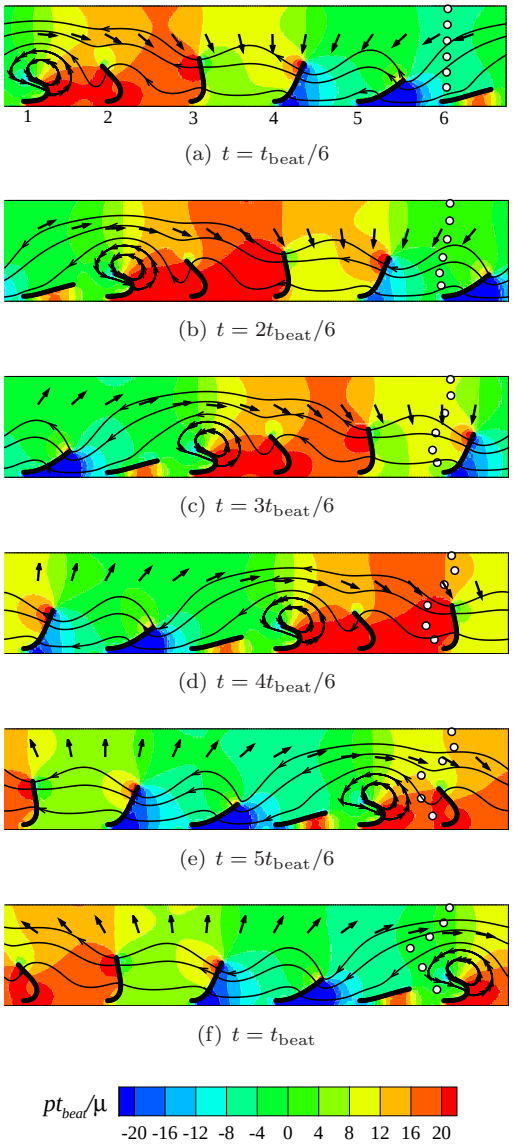

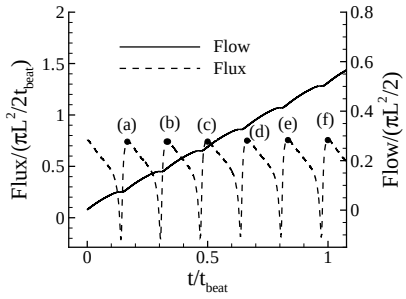

(h)

Figure 7.13: *(a) - (f) Contours of pressure normalised with μ/t_{beat} at different time instances. The direction of the fluid flow is represented by the streamlines, the magnetic field distribution is shown using the black arrows and the white circles represent fluid particles. (h) Flow and flux as a function of time, with the instances corresponding to (a) - (f) duly marked.*

significantly influenced. Metachrony is observed to completely knock-down the negative flow to zero due to the vortex formation caused by the shielding of the recovery stroke. Interestingly, we find that the enhancement is achieved even for small phase differences and large wavelengths. In the case of metachronal waves obtained by prescribing a phase difference, the direction of travel of the metachronal wave is not important for large cilia spacings. In all other cases, the fluid flow is larger for antiplectic metachrony

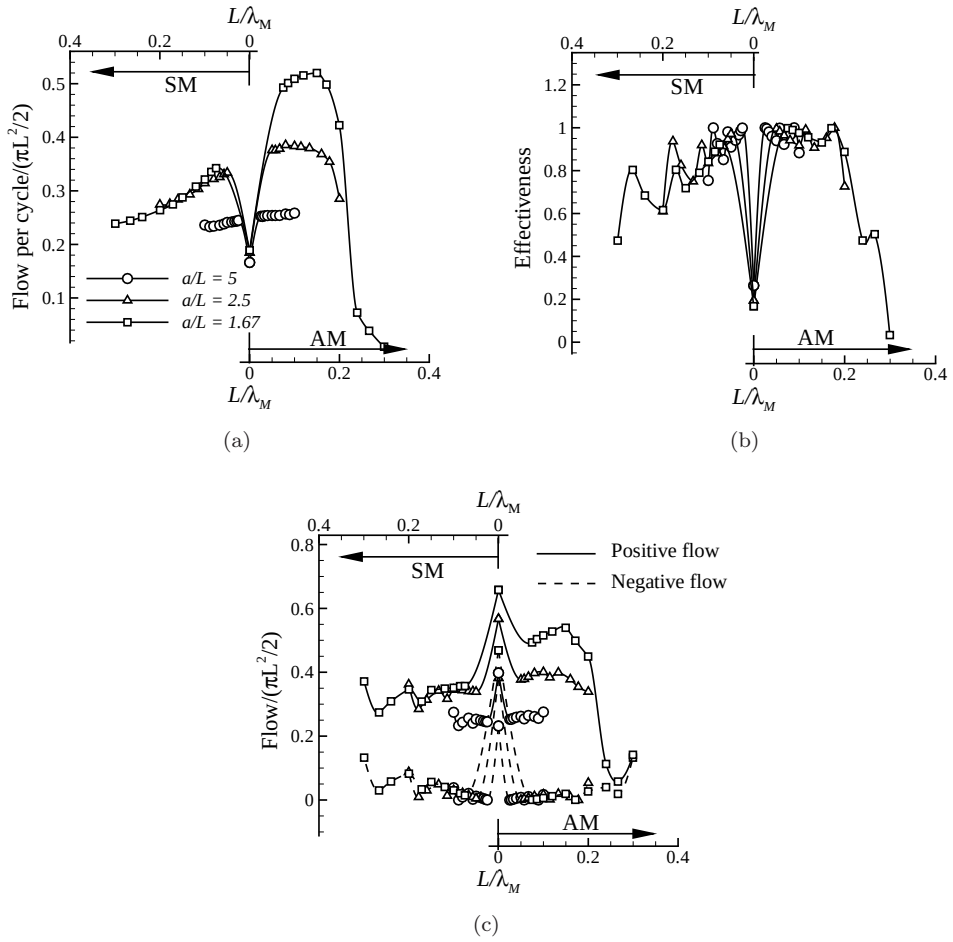

Figure 7.14: *Flow and effectiveness as a function of a/λ for different inter-cilium spacings a/L. AM and SM refer to antiplectic metachrony (the wave direction is opposite to the direction of the effective stroke) and symplectic metachrony (the wave direction and the effective stroke direction are the same), respectively. The area flow is significantly enhanced for an antiplectic metachrony compared to symplectic metachrony.*

compared to symplectic metachrony, which is related to the obstruction of the positive flow for symplectic metachrony. It is therefore beneficial if the magnetic actuation of the artificial cilia is designed such that it results in an antiplectic metachrony. Our results suggest that an antiplectic metachrony is adopted by the cilia on paramecia and in the respiratory system to maximize the fluid propelled. However, ciliary systems (such as on Opalina) that exhibit symplectic metachrony are also present in nature. It will be of interest to investigate what property is optimised by symplectic metachrony in these systems.

M_x $B_{x,x}$ $B_{y,x}$	f_x f_y	Symplectic metachrony	Antiplectic metachrony	M_x $B_{x,x}$ $B_{y,x}$	f_x f_y
+ − +	− +	(a) Time $t = 0$ 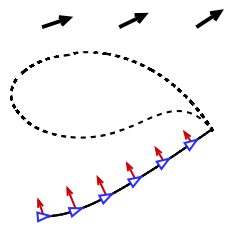	(b) Time $t = 0$ 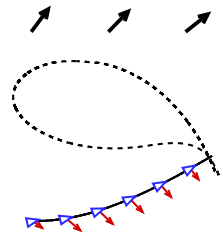	+ − −	− −
+ − +	− +	(c) $t = 2$ ms 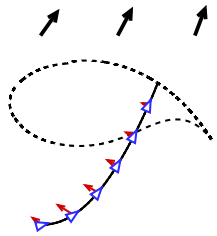	(d) $t = 2$ ms 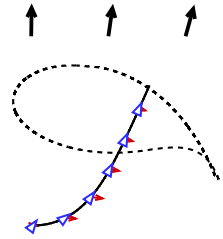	+ + −	+ −
− − −	+ +	(e) $t = 7$ ms 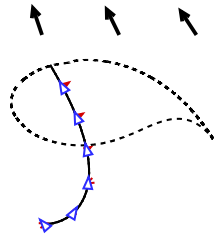	(f) $t = 4$ ms 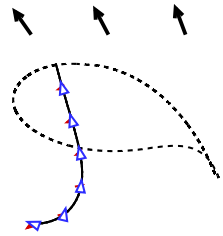	− + +	− −
− 0 −	0 +	(g) $t = 9$ ms 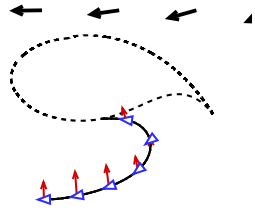	(h) $t = 7.5$ ms 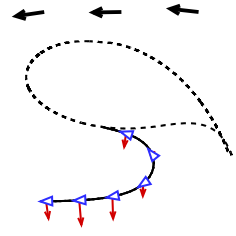	− 0 +	0 −

Table 7.1: *Motion of a super-paramagnetic cilium under the influence of a non-uniform rotating magnetic field that travels in space to the left (symplectic metachrony) and right (antiplectic metachrony). The thick arrows, hollow arrow heads and thin arrows represent the applied magnetic field, magnetization and magnetic body forces, respectively. The direction of the magnetization (M_x), field gradients ($B_{x,x}$ and $B_{y,x}$) and body forces (f_x and f_y) at different instants are also shown using the + and - symbols.*

Chapter 8

Fluid flow caused by collective non-reciprocal motion

Abstract

Using a magneto-mechanical solid-fluid numerical model for permanently magnetic artificial cilia, we show that the metachronal motion of symmetrically-beating cilia establishes a net pressure gradient in the direction of the metachronal wave, which creates a unidirectional flow. The flow generated is characterised as a function of the cilia spacing, the length of the metachronal wave and a dimensionless parameter that characterises the relative importance of the viscous forces over the elastic forces in the cilia.

8.1 Introduction

In lab-on-a-chip devices, working fluids have to be pumped between micro-reaction chambers through micron-sized channels. At these small length scales the viscous forces dominate over the inertial forces. Under this condition, a mechanical actuator has to move in a non-reciprocal manner to cause a net fluid transport (Purcell, 1977). In nature, micron-scale fluid manipulation is often performed using periodically beating hair-like structures called cilia. An example of natural fluid manipulation systems is the expulsion of mucus from the lungs caused by the beating of the cilia attached to the inner layer of mammalian trachea. The ciliary beat consists of distinct effective and recovery strokes, which leads to a non-reciprocal motion. In addition to the non-reciprocal motion of individual cilia, adjacent cilia beat with a constant phase difference leading to a coordinated wave-like motion, which is referred to as metachronal motion. Another example of fluid manipulation is the swimming of Cyanobacteria. Points on the surface of Cyanobacteria oscillate symmetrically and generate waves of lateral displacement along their surface. This wave-like motion causes fluid transport in one direction and the bacteria swim in the opposite direction (Ehlers *et al.*, 1996).

Many examples have appeared in the recent literature of artificial cilia that mimic the natural ciliary motion using different physical actuation forces, imposed by electric fields, magnetic fields or through base excitation (Shields *et al.*, 2010; Evans *et al.*, 2007; den Toonder *et al.*, 2008; Oh *et al.*, 2009; van Oosten *et al.*, 2009; Fahrni *et al.*, 2009; Kim & Netz, 2006; Gauger *et al.*, 2009; Khaderi *et al.*, 2009). In most of the cases the actuation field is uniform (Kim & Netz, 2006; Khaderi *et al.*, 2009; Fahrni *et al.*, 2009; Vilfan *et al.*, 2010), so that all artificial cilia beat in-phase, thus only focusing on the

Based on Khaderi, *et al. Fluid flow due to collective non-reciprocal motion of symmetrically-beating artificial cilia*, submitted.

non-reciprocal motion of individual cilia. The flow generated by synchronously-beating cilia has been analysed in terms of the dimensionless parameters that govern the cilia behaviour (Alexeev *et al.*, 2008*b*; Ghosh *et al.*, 2010; Alexeev *et al.*, 2008*a*; Khaderi *et al.*, 2009; Gauger *et al.*, 2009). The formation of the metachronal waves has been investigated using computational models, which suggest that the coordinated motion is due to the hydrodynamic interaction between adjacent cilia, and that the energy spent per cilium decreases in the presence of metachronal waves (Gueron & Levit-Gurevich, 1999; Gueron *et al.*, 1997; Kim & Netz, 2006; Vilfan & Jülicher, 2006). Recently, it has been shown that the flow generated by magnetically-driven non-reciprocally-beating artificial cilia is substantially enhanced and becomes unidirectional when the cilia beat out-of-phase compared to synchronously beating cilia (Khaderi *et al.*, 2011*b*; Gauger *et al.*, 2009). By modelling cilia that beat out-of-phase and possess only orientational asymmetry (Khaderi *et al.*, 2010) as a porous sublayer, it has been shown that flow can be created in the direction of the metachronal wave (Hussong *et al.*, 2011*a*). However, from a manufacturing and implementation point-of-view, it is not straighforward to generate non-reciprocal motion of the individual cilia. Therefore, it is of interest to investigate whether cilia can create a flow in the absence of any asymmetry but in the sole presence of waves of lateral displacement, similar to that of Cyanobacteria. This is the subject of the present article.

We study an array of permanently magnetic artificial cilia subjected to a non-uniform magnetic field that travels in space and time, such that the cilia beat symmetrically but out-of-phase. The ciliary motion generates a unidirectional fluid flow in a direction opposite to the metachronal wave. The fundamental mechanism which is responsible for the flow is investigated, and the flow is quantified as a function of the parameters of the metachronal wave, cilia spacing, and a physical dimensionless parameter that quantifies the relative importance of the viscous forces compared to the elastic forces. We find that flow reaches a maximum when the wavelength of the metachronal wave is four times the cilia length.

The chapter is organised as follows. The boundary value problem, solution approach and parameters involved in the system are explained in section 8.2. The collective non-reciprocal motion is analysed in section 8.3.1. The mechanisms that cause the flow are analysed from Eulerian and Lagrangian points-of-view in section 8.3.2. The dependence of the flow on the system parameters is analysed in section 8.3.3. We finally summarise the results of the analysis in section 8.4.

8.2 Problem definition

We analyse an infinitely long channel of height H containing an array of cilia of length L, thickness h and inter-cilia spacing a. The cilia have an elastic modulus E and possess a remanent magnetization of magnitude M_r oriented along their length from the fixed end to the free end. A magnetic field with a constant magnitude in the y-direction (B_{0y}) and varying over space and time in the x-direction is applied according to the following form,

$$B_x = B_{0x} \sin\left(\omega t - 2\pi x/\lambda\right), \tag{8.1}$$

where $\omega = 2\pi/t_{\text{ref}}$ is the angular velocity, t_{ref} is the time period of oscillation and λ is the wavelength of the applied magnetic field, see Fig. 8.1. The applied magnetic field has a wave velocity λ/t_{ref} to the right. The magnetic body couple N_z acting on the cilia

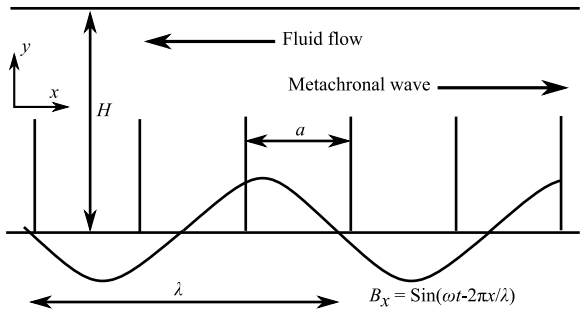

Figure 8.1: *Schematic picture of the problem analysed. We study an infinitely long channel of height H containing equally-spaced cilia that are arranged perpendicular to the channel. A magnetic field which varies in space and time is used for actuation. The resulting flow is opposite to the direction of the metachronal wave.*

at the cilia base can be written as $N_z = M_r B_{0x}$. The velocity of the magnetic couple wave, which causes the out-of-phase motion of the cilia, is also equal to λ/t_{ref}. However, as there are a finite number of cilia per wave length, the metachronal wave velocity also depends on the cilia spacing a. The metachronal velocity in cilia per seconds can be written as $\lambda/at_{\mathrm{ref}}$ for $0 < a < \lambda/2$ and $-(\lambda/at_{\mathrm{ref}})/(\lambda/a - 1)$ for $\lambda/2 < a < \lambda$ (see chapter 7 and appendix J). The fluid to be propelled is assumed to be incompressible and Newtonian with a viscosity μ. The cilia are vertically straight when no magnetic field is applied.

The dimensionless geometric parameter a/λ scales with the phase difference between adjacent cilia and characterises the response of the system together with H/L and a/L. The physical response of the system can be captured through three dimensionless numbers: the fluid number $F_n = 12\mu L^3/Eh^3 t_{\mathrm{ref}}$ - the ratio of the viscous forces to the elastic forces, the inertia number $I_n = 12\rho L^4/Eh^2 t_{\mathrm{beat}}^2$ - the ratio of cilia inertia forces to the elastic forces and the magnetic number $M_n = 12B_{0x}M_r L^2/\mu_0 Eh^2$ - the ratio of magnetic forces to the elastic forces, where E and ρ are the elastic modulus and density of the cilia (Khaderi *et al.*, 2009). In this chapter we explore the effect of a/λ, a/L and F_n for a given value of I_n, M_n and H/L in the limit of low Reynolds numbers. We model the cilia as Euler-Bernoulli beams and the magnetic field using a boundary element approach (Khaderi *et al.*, 2009). The Stokes equations, which capture the behaviour of the fluid at low Reynolds numbers, are solved using the finite element method. The solid and fluid dynamic equations are coupled implicitly using the fictitious domain method (van Loon *et al.*, 2006). The solution procedure can be summarised as follows. The Maxwell's equations are solved at every time instant to obtain the magnetic field. From the magnetic field, we calculate the magnetic body couple acting on the cilia[1]. This body couple is provided as an external load to the implicitly-coupled solid-fluid model, which solves for the velocity of the cilia, and the velocity and pressure of the fluid. Using the velocity of the cilia, its new position is calculated and the procedure is repeated. The reader is referred to Khaderi *et al.* (2009) for a detailed description of the numerical model.

To perform the numerical simulations we choose a unit-cell whose width is equal to

[1]As we have a permanently magnetic film that is magnetized along its length, and because only the magnetic field in the x-direction is non-uniform, no magnetic body forces act on the cilia.

one wavelength containing λ/a cilia. The left and right end of the unit-cell are periodic in velocity, while the top and bottom boundaries are no-slip boundaries. We perform simulations for various values of the phase difference a/λ, while the inter-cilia spacing a/L is maintained constant. Therefore, as λ is increased the number of cilia in a unit-cell also increases.

8.3 Results

8.3.1 Collective non-reciprocal motion

We first show that the out-of-phase motion of the cilia leads to a collective non-reciprocal motion. To elucidate this we plot the schematic positions of the cilia at time instances $t_{\text{ref}}/4$ after and before the first cilium has reached its extreme position (at time t_e) in Fig. 8.2[2]. The thin and thick lines represent the extreme and current positions of the cilia, respectively. The arrows represent the direction of motion of the cilia. We would like to remind that for non-reciprocal motion of an actuator, its position after and before an extreme position is reached should not be identical. In the cases of cilia beating in synchrony and anti-phase, the positions of all the cilia before $(t_e - t_{\text{ref}}/4)$ and after the extreme position $(t_e + t_{\text{ref}}/4)$ is the same; hence the motion is reciprocal. However, in the case for cilia moving out-of-phase, even though the positions of the cilia 1 and 3 are identical before and after t_e, the positions of cilia 2 and 4 are not. Therefore, even though every cilium performs a reciprocal motion, the cilia collectively perform a non-reciprocal motion and, therefore, will cause a net fluid flow in microchannels. This fluid flow is quantitatively analysed in the subsequent sections.

8.3.2 The fundamental mechanism

Eulerian point-of-view

To illustrate the fundamental mechanism that creates the flow, we take $a/L = 2/7$, $a/\lambda = 1/7$, $H/L = 4$, $F_n = 0.15$, $I_n = 3 \times 10^{-3}$ and $M_n = 2.25$ (based on B_{x0}). As $a/\lambda = 1/7$, the metachronal wave travels to the right with a speed λ/t_{ref}. Figure 8.3(a) shows the pressure contours with the streamlines superimposed and Fig. 8.3(b) shows the contours of the absolute value of the horizontal component of the velocity. For clarity, the results are shown for two unit-cells. Because of the travelling magnetic wave and periodicity of the system, the pressure and velocity profiles in the channel remain unchanged in time, but travel with a constant velocity in the direction of the applied magnetic wave (to the right).

At the instant depicted, cilia 2, 3, 4 and 9, 10, 11 move to the right, while cilia 6, 7 and 13, 14 move to the left. The other cilia are nearly stationary (zero velocity). Due to the instantaneous velocity of the cilia, high pressure (hp) and low pressure (lp) regions develop (red and blue regions in Fig. 8.3(a)). Fluid is squeezed out from the hp region and sucked in by the lp regions, as a result of which a series of counter-rotating vortices are formed in the channel. Since the distance between the hp and lp regions opposite to the wave direction is smaller, the pressure gradient is larger, so that the counter-clockwise vortices are stronger (see Fig. 8.3(b)). As a result, the velocity distribution

[2]Note that the cilia will deform by bending – when a magnetic body couple N_z is applied – and will not remain straight as is assumed in this section for simplicity.

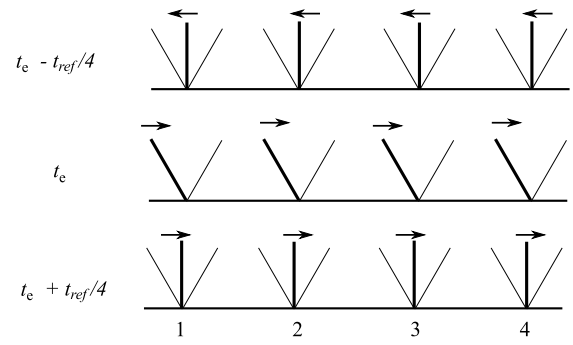

(a) Synchronously beating cilia.

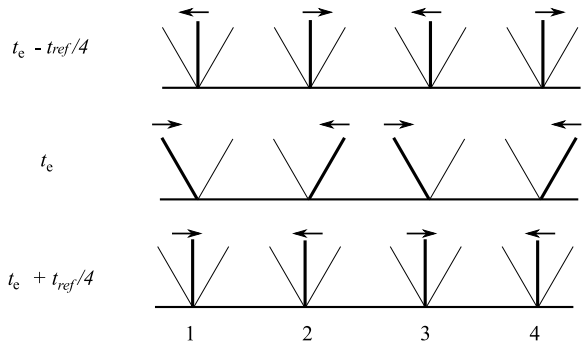

(b) Cilia beating in anti-phase.

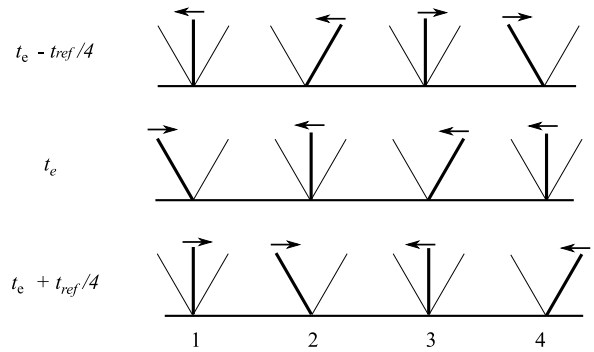

(c) Cilia beating out-of-phase $a/\lambda = 1/4$.

Figure 8.2: *Schematic positions of the cilia at instances* $t_{\text{ref}}/4$ *after* $(t_e + t_{\text{ref}}/4)$ *and before* $(t_e - t_{\text{ref}}/4)$ *the extreme position has been reached by the first cilium at* t_e*. The time* t_e *corresponds to the extreme position of the first cilium from the left. The arrows represent the direction of motion of the cilia. In the cases of cilia beating synchronously and anti-phase, the positions of all the cilia before and after the extreme position is the same; hence the motion is reciprocal. However, it is not the case for cilia moving out-of-phase; hence the motion is non-reciprocal.*

has a dominant horizontal component to the left. Integrating the velocity profile over the channel height results in a net flux to the left. Conservation of mass dictates that the flux at every vertical section through the channel is the same. Since the entire periodic profile, as depicted in Fig. 8.3, travels continuously to the right at a constant pace, the flux remains constant in time. Clearly, the flux magnitude and direction can be directly deduced from the instantaneous pressure distribution profile of Fig. 8.3 as analysed in the following.

Fluid flow occurs in the direction opposite to the net pressure gradient. This pressure gradient is governed by the magnitude of the pressure in the lp and hp regions and the distance between them. The former is governed by the velocity of the individual cilia, whereas the latter is determined by the deflection δ of the cilia tip. Since the velocity and displacements of the cilia are controlled by the magnetic field and its rate of change, it can be deduced that for a considerably smaller than λ the net pressure gradient scales with $\mu\omega\delta^2/\lambda^3$ (see appendix K). As this pressure gradient is positive, the flow occurs in the negative x-direction. Thus, the flow direction is opposite to the metachronal wave, and scales with the square of the amplitude of deflection. When the direction of the applied magnetic wave is reversed, the pressure profile, which is dictated by the cilia velocity, remains alternating. However, the deformed configuration of the cilia changes in such a way that the net pressure gradient is now negative; this creates a flow to the right (again opposite to the metachronal wave). Fluid flow created by oscillating cilia whose motion is kinematically prescribed has been analysed recently using a continuum approach (Hussong *et al.*, 2011*a*). The formation of the vortices was also observed in this work. A rigorous mathematical analysis of the fluid flow induced by a longitudinally oscillating sheet whose material particles comprise of the tip of the cilia also predicts that the flow will occur in the direction opposite to the metachronal wave (Brennen, 1974).

Lagrangian point-of-view

The previous analysis focussed on the channel flow from an Eulerian point-of-view. Instead, we can also adopt a Lagrangian view point and track the motion of fluid particles in time. In the following, all the parameters of the previous section are kept constant, except for H, which we now choose to be $2L$. Figure 8.4 shows a portion of the region between the tips of the cilia and the top boundary. We follow the motion of the fluid particles (that initially form a straight vertical line) when they come under the influence of the travelling vortices (see Fig. 8.4). The contours represent the absolute velocity in the x-direction, and the direction of velocity is represented by the streamlines. From the velocity field, we can see that the out-of-phase motion of cilia creates a series of counter-acting vortices, and that the velocity field travels to the right, which is also the direction of propagation of the applied magnetic field wave.

We focus our attention on the second particle from the bottom. At $t = 0$ the particle is between two vortices. The velocity of the particle is such that it moves downwards. As time progresses, at $t = 0.2t_{\mathrm{ref}}$ the position of the particle is such that it has a low velocity to the right due to the presence of the clockwise vortex. At $t = 0.4t_{\mathrm{ref}}$, the particle moves away from the influence of the clockwise vortex, towards the counter-clockwise vortex. Now the particle has a velocity such that it moves upwards. At $t = 0.6t_{\mathrm{ref}}$, when the particle is under the influence of the stronger counter-clockwise vortex, it has a higher velocity compared to the instance when the particle was under the influence of less strong

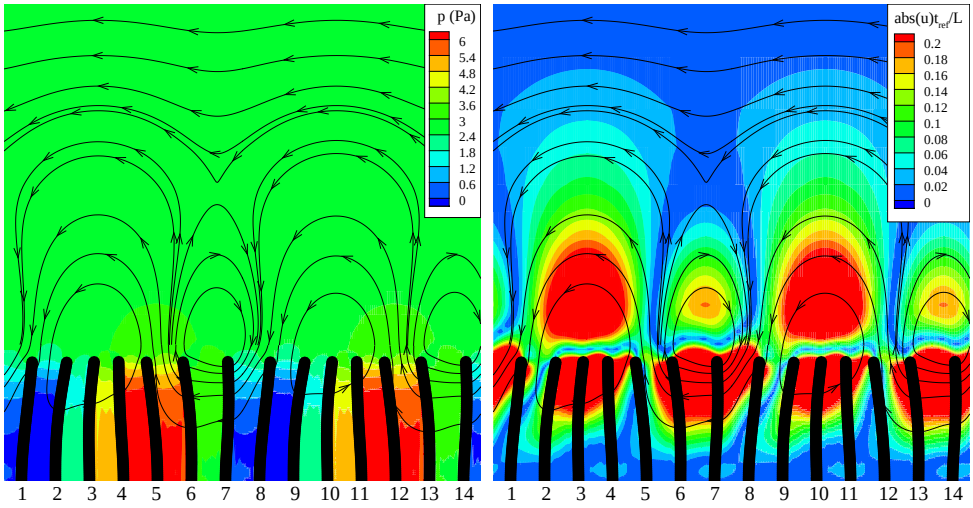

(a) Pressure contours: red is high pressure and blue is low pressure.

(b) Contours represent the magnitude of velocity in x-direction and the streamlines represent the direction of velocity.

Figure 8.3: *Fundamental mechanism causing fluid flow: (a) Contours of pressure and (b) Contours of absolute velocity in x-direction for $a/L = 2/7$ and $a/\lambda = 1/7$ (wave moving to the right) at $t = 0.35t_{ref}$. Due to the velocity of cilia, regions of positive and negative pressure are established in the channel. The deformed position of the cilia causes a lower pressure gradient in direction of the wave compared to that of in the opposite direction. This leads to a high velocity and a net flow to the left.*

clockwise vortex (compare Figs. 8.4(b) and 8.4(d)). Therefore, the particle effectively moves to the left. The displacement perpendicular to the channel is less for the particles near the top boundary. This leads to equal velocities in the channel direction when they come under the influence of the clockwise and counterclockwise vortices, which results in no net displacement of the particles near the top boundary.

It can be seen that the fluid particle near the free end of the cilia moves unidirectionally and that its displacement is much larger compared to the displacement of the rest of the particles. Therefore, the contribution to the flow from the fluid particles near the cilia is much larger compared to other particles. This results in a flow that is nearly unidirectional, even though the cilia motion is oscillatory. An unidirectional flow is also observed when the cilia motion is non-reciprocal in the presence of metachronal waves (chapter 7) and inertia (chapter 5). A similar approach (Lagrangian point-of-view) was used in (Ehlers *et al.*, 1996) to analyse the swimming of microorganisms (based on tangential travelling waves).

8.3.3 Parametric study

We now characterise the flow generated by the cilia as a function of the system parameters such as the cilia spacing a, wavelength λ, amplitude of cilia deflection and fluid number F_n. The output of the cilia is quantified by the area flow created per cycle, which is found by integrating the instantaneous velocity flux through the channel over a representative

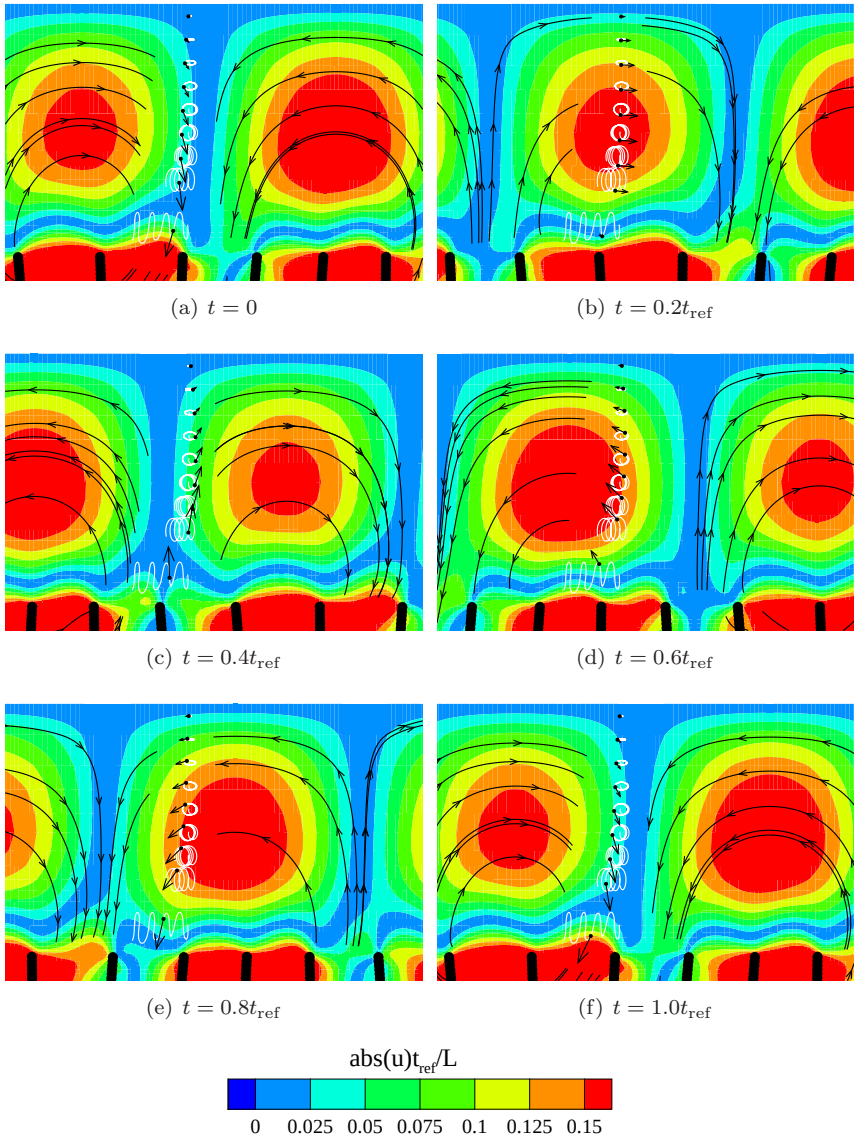

Figure 8.4: *Motion of particles with time: The field-of-view is the region between the oscillating end of cilia and top boundary of the unit-cell with the bottom left corner at* $(x, y) = (0.5L, 0.95L)$ *and the top right corner at* $(x, y) = (1.55L, 2L)$*. The velocity in the channel direction is larger in the direction opposite to the wave than in the direction of the wave. The white curves represent the trajectory of particles and the black dots represent the particles. Particles near the cilia move unidirectionally and show larger displacement, whereas the particles near the top boundary do not show any displacement.*

cycle. The nature of the fluid flow, as seen in section 8.3.2, is unidirectional. We focus our attention on the cases where the direction of the metachronal wave velocity is positive, i.e. $a < \lambda/2$, and perform the analysis for $H = 2L$, $M_n = 1.13$, $F_n = 0.15$

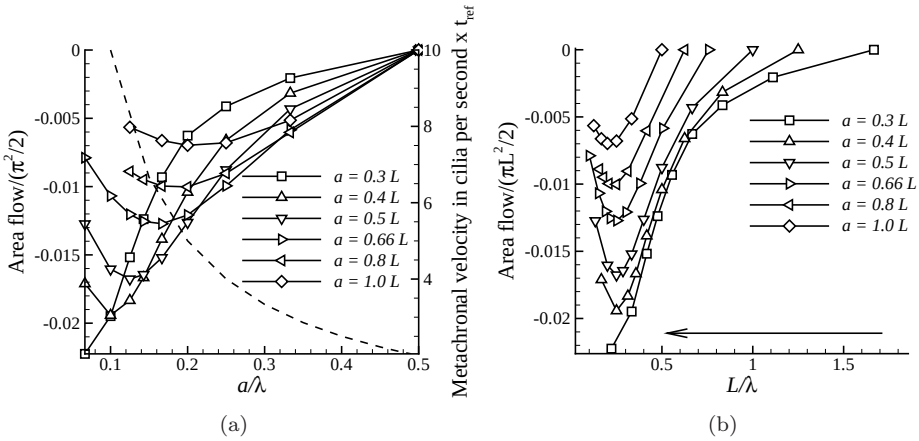

Figure 8.5: *Flow as a function of (a) phase difference a/λ and (b) wavelength L/λ for various cilia densities a/L. The fluid flows in a direction opposite to the metachronal velocity (shown using dashed lines in (a)). The flow is maximum when $\lambda = 4L$. The arrow shows the direction of increase of λ.*

and $I_n = 3 \times 10^{-3}$ unless mentioned otherwise. Figure 8.5(a) shows the flow and the metachronal wave velocity as a function of a/λ. When $a = 0$, the cilia move in-phase. When $a = \lambda/2$, the positive wave velocity and the negative wave velocity are equal and this leads to a standing wave (see chapter 7 and Fig. 8.2(b)). Under these conditions, we do not see metachronal waves and thus no fluid flow is observed. As the magnetic wave travels to the right (see Fig. 8.1), the fluid flows to the left; the opposite occurs for $\lambda/2 > a > \lambda$. To get more insight into the behaviour of the system, we plot the flow as a function of L/λ for the cases shown in Fig. 8.5(a) in Fig. 8.5(b). The arrow shows the direction of increasing λ. The fluid flow increases when the inter-cilia spacing is decreased, and for a given inter-cilia spacing, the flow initially increases with λ, reaches a maximum at $\lambda = 4L$ and then decreases.

As shown in appendix K the pressure gradient responsible for the flow increases when the wavelength decreases, as well as when the deflection of the cilia increases. However, there is an additional dependence. When the wavelength of the magnetic field is increased in Fig. 8.5(b) for a particular cilia spacing, the pressure between the cilia decreases, which reduces the hydrodynamic drag and causes an increased deformation of the cilia (see Fig. 8.6). On the other hand, the pressure gradient will decrease with an increase in the wavelength[3], so that the flow created is due to the relative competition between these two effects. The deflection effect dominates when the wavelength is small, creating an increased flow as we increase the wavelength until $\lambda = 4L$. When we increase the wavelength any further, the effect of the increasing deflection is overcome by the decreasing pressure gradient, which causes the flow to decrease. This is in contrast to the situation where the cilia sweep an asymmetric area (see chapter 7), where it is shown that the flow created does not depend on the phase difference between adjacent cilia. This is due to the different mechanisms that drive the flow: The pressure gradient in the current situation and the asymmetric area in (Khaderi *et al.*, 2011*b*).

[3]Note that the pressure gradient will continue to decrease with an increase in wavelength, whereas its increase because of the increased cilia deflection is limited.

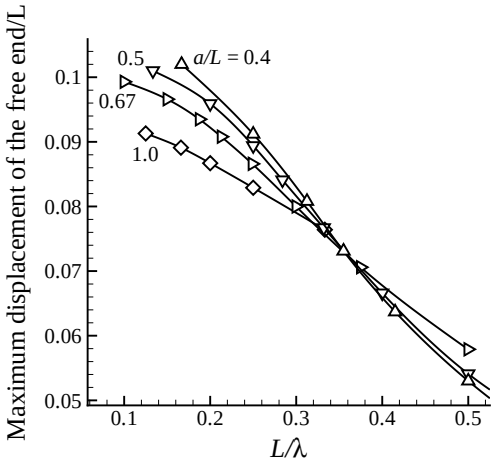

Figure 8.6: *Maximum transverse displacement as a function of L/λ for different cilia spacings (a/L). When L/λ is large the phase difference between adjacent cilia is large, causing them to move against each other, which leads to high drag forces on the cilia causing low deformation.*

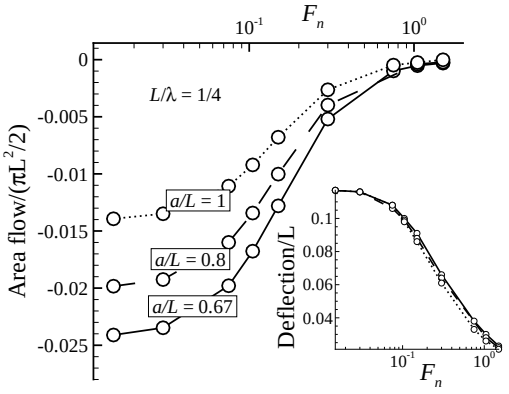

Figure 8.7: *Flow as a function of the fluid number (F_n) for various cilia spacing at $L/\lambda = 1/4$. The maximum transverse displacement of the free end is shown as an inset.*

The flow as a function of the fluid number (F_n) for various cilia spacings at $L/\lambda = 1/4$ is shown in Fig. 8.7; the flow decreases with an increase in the fluid number. As the viscous forces increase with the fluid number, the cilia exhibit lower deflections when F_n is increased (see the inset in Fig. 8.7). As the pressure gradient scales with the cilia deflection, the flow created decreases with the deflection.

When $\lambda >> a$, the fluid experiences an oscillating surface whose material particles are made up of the tip of cilia. The velocity of propulsion in such a case is given by the envelope theory under the assumption that the cilia spacing is much smaller than the wavelength. Brennen (1974) has shown that for a continuous distribution of cilia, the fluid velocity scales with the inverse square of the wavelength, the frequency of oscillation ω and the square of the amplitude of oscillation (Brennen, 1974). Moreover, the flow is in

the direction opposite to the wave velocity. Our model also captures all these aspects. In the following, we show that the flow scales with the square of the amplitude of oscillation even at large amplitudes of deflection and spacing of cilia ($a \approx L$).

To do so, we examine the fluid flow dependence on the magnitude of the transverse deflection of the cilia. We take the case of $a = 2L$ and $a/\lambda = 1/3$. The magnitude of displacement is increased by increasing the magnetic number from 2.25 to 34. The flow as a function of displacement is shown in Fig. 8.8. The flow has a quadratic dependence on the deflection until the deflection is 40% of the cilia length.

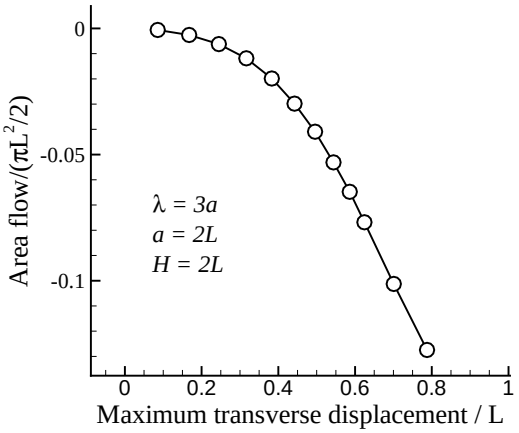

Figure 8.8: *Flow as a function of deflection.*

8.4 Conclusions

In this chapter we analysed the fluid transport created by cilia that beat symmetrically and out-of-phase when actuated by a non-uniform magnetic field, leading to the formation of metachronal waves. Although at the scale of individual cilia the beating is reciprocal, because of the metachronal waves the cilia collectively exhibit a non-reciprocal motion. Using a magneto-mechanical solid-fluid numerical model we analyse the fundamental mechanisms that cause this fluid flow. The out-of-phase motion of cilia creates a net pressure gradient, which results in a unidirectional flow whose direction is opposite to the direction of the wave. The flow increases with the tip deflection of cilia and decreases with the wavelength. Analysis of the motion of fluid particles reveals that the major contribution to the fluid flow comes from the particles located near the free end of the cilia. The flow created reaches a maximum value when $\lambda = 4L$.

Chapter 9
Three-dimensional numerical model

Abstract

A numerical model is developed to analyse the interaction of artificial cilia with the surrounding fluid in a three-dimensional setting in the limit of vanishing fluid inertia forces. The cilia are modelled using finite shell elements based on the superposition of discrete Kirchhoff triangles and constant strain triangles with drilling degrees of freedom. The fluid is modelled using a boundary element approach. The coupling between both the models is performed by imposing no-slip boundary conditions on the surface of the cilia. The performance of the model is verified using various reference problems available in the literature. The application of the developed model is elucidated by simulating the fluid flow due to magnetically actuated artificial cilia.

9.1 Introduction

In the previous chapters we used a two-dimensional model to simulate the cilia, which were constrained to beat in a plane. Such a two-dimensional analysis is valid for cilia widths that are larger than the cilia length and channel height. However, the cilia are, in general, three-dimensional structures and have a finite width (typically one fifth of their length), see Fig. 9.1(a). In these situations, the effect of the cilia width and the spacing between the cilia along the width direction play an important role in determining the fluid transported. Also, in experimental systems the magnetic field can be applied in three spatial directions. In order to model these effects we develop a three-dimensional numerical model which can accurately describe the motion of the cilia, the velocity field in the fluid and the magnetic field in the cilia, for the situation of low Reynolds numbers.

To capture the deformation of the cilia, both the bending and membrane stiffnesses have to be accurately modelled. The bending stiffness of cilia can be modelled using two approaches: Kirchhoff-Love theory and Reissner-Mindlin theory (Zienkiewicz & Taylor, 2002). The Kirchhoff-Love (KL) theory is used for thin plates where only the bending energy is considered, whereas in the Reissner-Mindlin (RM) theory both bending and shear energies are considered. Finite elements based on the RM theory show locking behaviour when modelling slender structures, and in such cases one has to resort to special techniques of numerical integration. On the other-hand, simple finite elements based on KL theory which satisfy all the compatibility requirements are not available (Zienkiewicz & Taylor, 2002). To model the cilia, we adopt the approach proposed by Bathe & Ho (1981) and model the bending of the cilia using discrete Kirchhoff triangles

Based on Khaderi, *et al. Implicitly-coupled finite element/boundary element method for the three-dimensional fluid-structure interaction of magnetic artificial cilia*, submitted.

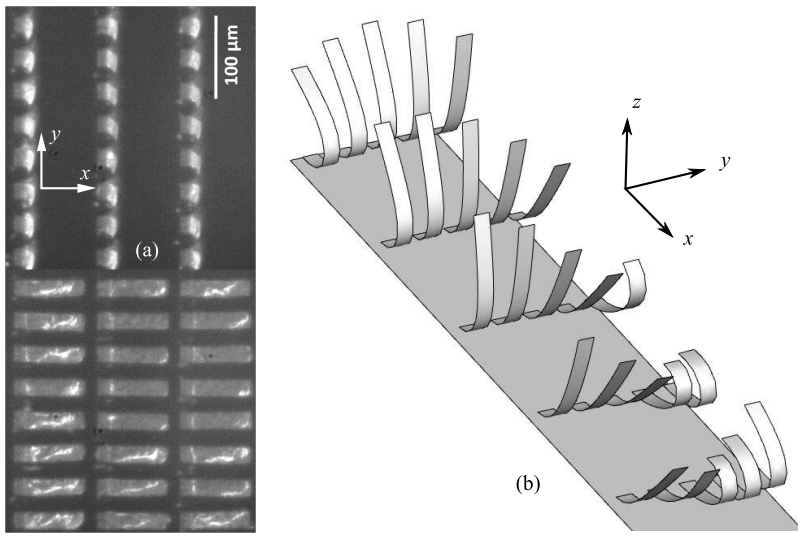

Figure 9.1: *(a) Magnetic artificial cilia consisting of polymer films with embedded nanoparticles (Khaderi* et al.*, 2011*a*; Belardi* et al.*, 2011). Bottom: Cilia in unactivated state; top: Cilia under the influence of a magnetic field. (b) Schematic picture of the problem: A group of cilia in a semi-infinite fluid are attached to a substrate and actuated using an external magnetic field.*

(DKT), while the membrane behaviour is modelled using constant strain triangles (CST). To improve the accuracy during in-plane bending, we add drilling degrees of freedom to the CST (Allman, 1984). The large deformation of the cilia is modelled by adopting an updated Lagrangian procedure.

We assume that the inertia forces in the fluid are negligible. This enables us to model the fluid using the Stokes equation, the solution of which can be written in terms of a Green's function. The Green's function for the case of forces acting in a semi-infinite fluid is provided by Blake (1971*b*). The cilia are considered as internal boundaries to the fluid, which exert a force on the fluid. The drag forces are treated as a distribution of point forces on the cilia. Akin to the solid mechanics model, we use triangular elements to discretise the internal fluid boundary. The drag forces are assumed to vary linearly within each triangular element. Once the drag traction is known, the velocity field in the fluid and the velocity of the internal fluid boundary (the cilia) can be obtained.

Many studies exist in the literature to model the interaction of slender bodies with the surrounding fluid, such as the arbitrary Lagrangian-Eulerian (ALE) method (Donea *et al.*, 1982), fictitious domain method (van Loon *et al.*, 2006), and immersed boundary method (Peskin, 2002). Recently, the extended finite element method has also been used to perform fluid-structure interaction (Gerstenberger & Wall, 2008, 2010). Although implementation of these methods for three-dimensional problems is straightforward, the computational cost is enormous due to the large number of degrees of freedom of the 3D fluid mesh. Therefore, coupling a boundary element model of the fluid with a finite element model of a slender structure provides attractive advantages. Coupling of boundary elements and finite elements has been performed in the past for the interaction of a solid with an ideal fluid (Schneider, 2008; Chen *et al.*, 1998). In this work we couple the previously explained boundary element formulation for the fluid with the shell element

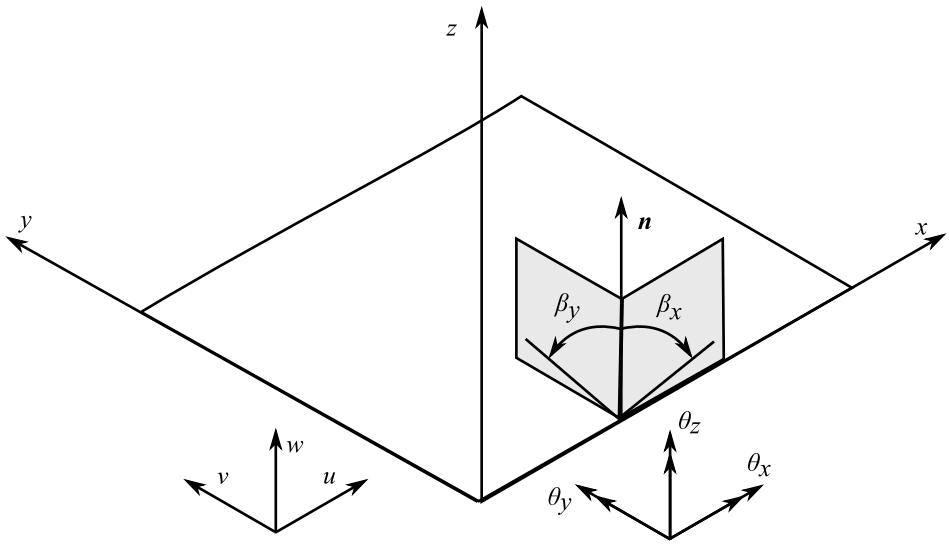

Figure 9.2: *Schematic representation of the parameters involved in the shell element formulation.*

model of the cilia using no-slip boundary conditions on the cilia (the velocity of the fluid boundary is equal to the velocity of the solid shell structure). The coupling is performed in a monolithic fashion. An approach similar to that taken here was used by Salsac *et al.* (2010), where the solid-fluid coupling is implemented in an explicit manner.

The chapter is organised as follows. In section 9.2 we discuss the solid mechanics model followed by the fluid dynamics model and the fluid-structure interaction implementation. The method used to calculate the magnetic fields is then discussed. The applications of the developed model is elucidated by studying the fluid-structure interaction of artificial cilia in section 9.3.

9.2 Formulation

9.2.1 Solid mechanics model

The cilia are modelled using shell elements based on the superposition of the bending and membrane stiffness in the local coordinate axes of the shell element. The membrane stiffness is based on constant strain triangles with drilling degrees of freedom (Allman, 1984), and the bending stiffness is based on the discrete Kirchhoff triangular elements proposed by Batoz *et al.* (1980). We start with the principle of virtual work containing the relevant energies, linearise it, and finally adopt an updated Lagrangian framework to arrive at the final set of equations. The resulting stiffness matrix includes the geometric non-linearity, which accounts for large deformations, but small strains.

Let the displacement of a point on the mid-surface be (u_0, v_0, w_0). As we model the cilia to be shell structures, the displacement of any point on the normal is

$$u = u_0 + z\beta_x,\ v = v_0 - z\beta_y,\ w = w_0, \tag{9.1}$$

where β_x and β_y are the rotations of the normal with respect to the y and x axes,

respectively. Now, the only non-zero components of the Green-Lagrange strain are

$$\epsilon_x = \frac{\partial u}{\partial x} + \frac{1}{2}\left(\frac{\partial w}{\partial x}\right)^2,\ \epsilon_y = \frac{\partial v}{\partial y} + \frac{1}{2}\left(\frac{\partial w}{\partial y}\right)^2,\ 2\epsilon_{xy} = \frac{\partial u}{\partial y} + \frac{\partial v}{\partial x} + \frac{\partial w}{\partial x}\frac{\partial w}{\partial y}. \tag{9.2}$$

Taking the variation of the Green-Lagrange strain and substituting the displacements from Eqn. 9.1, we get

$$\delta\epsilon_x = \frac{\partial \delta u}{\partial x} + \frac{\partial w}{\partial x}\frac{\partial \delta w}{\partial x} = \frac{\partial \delta u_0}{\partial x} + \frac{\partial w_0}{\partial x}\frac{\partial \delta w_0}{\partial x} + z\frac{\partial \delta \beta_x}{\partial x} = \delta\bar{\epsilon}_x + z\delta\kappa_x. \tag{9.3}$$

Similarly,

$$\delta\epsilon_y = \delta\bar{\epsilon}_y + z\delta\kappa_y \text{ and } 2\delta\epsilon_{xy} = \delta\bar{\epsilon}_{xy} + z\delta\kappa_{xy}. \tag{9.4}$$

Here, $\kappa_x = \beta_{x,x}$, $\kappa_y = -\beta_{y,y}$, and $\kappa_{xy} = -\beta_{y,x} + \beta_{x,y}$ are the curvatures[1], and

$$\delta\bar{\epsilon}_x = \frac{\partial \delta u_0}{\partial x} + \frac{\partial w_0}{\partial x}\frac{\partial \delta w_0}{\partial x} = \frac{\partial \delta u_0}{\partial x} + \beta_x\delta\beta_x,$$

$$\delta\bar{\epsilon}_y = \frac{\partial \delta v_0}{\partial y} + \frac{\partial w_0}{\partial y}\frac{\partial \delta w_0}{\partial y} = \frac{\partial \delta u_0}{\partial y} + \beta_y\delta\beta_y,$$

and

$$\delta\bar{\epsilon}_{xy} = \frac{\partial \delta u_0}{\partial y} + \frac{\partial \delta v_0}{\partial x}\frac{\partial w_0}{\partial x}\frac{\partial \delta w_0}{\partial y} + \frac{\partial w_0}{\partial y}\frac{\partial \delta w_0}{\partial x} = \frac{\partial \delta u_0}{\partial y} + \frac{\partial \delta v_0}{\partial x} - \beta_x\delta\beta_y - \beta_y\delta\beta_x$$

are the membrane strains. The subscript $(\cdot)_{,x}$ means a partial derivative with respect to the x-direction. It is to be noted that the membrane strains contain terms which are linear in the in-plane displacements (u_0 and v_0), and non-linear in the rotations.

The internal virtual work is

$$\delta W_{\text{int}} = \int_{V_0} \left(\sigma_x\delta\epsilon_x + \sigma_y\delta\epsilon_y + 2\sigma_{xy}\delta\epsilon_{xy}\right) dV_0, \tag{9.5}$$

where σ_x, σ_y and σ_{xy} are the components of the second Piola-Kichhoff- stress tensor and dV_0 represents an elemental volume in the undeformed configuration. By using the definitions of membrane strains and curvatures, the internal virtual work can be written as:

$$\delta W_{\text{int}} = \int_{A_0} \left(\delta\boldsymbol{\epsilon}\cdot\boldsymbol{P} + \delta\boldsymbol{\kappa}\cdot\boldsymbol{M}\right) dA_0, \tag{9.6}$$

where $\boldsymbol{\kappa} = [\kappa_x \quad \kappa_y \quad \kappa_{xy}]^T$, $\boldsymbol{\epsilon} = [\bar{\epsilon}_x \quad \bar{\epsilon}_y \quad \bar{\epsilon}_{xy}]^T$, dA_0 represents an elemental area in the undeformed configuration,

$$\boldsymbol{P} = \left\{\begin{array}{c} P_x \\ P_y \\ P_{xy} \end{array}\right\} = \frac{hE}{1-\nu^2}\left[\begin{array}{ccc} 1 & -\nu & 0 \\ -\nu & 1 & 0 \\ 0 & 0 & \frac{1-\nu}{2} \end{array}\right]\left\{\begin{array}{c} \bar{\epsilon}_x \\ \bar{\epsilon}_y \\ \bar{\epsilon}_{xy} \end{array}\right\} = \boldsymbol{D^M}\boldsymbol{\epsilon}, \tag{9.7}$$

[1]Consequently, the rotations in $x-z$ plane and $y-z$ plane are β_x and $-\beta_y$, respectively.

and

$$\boldsymbol{M} = \left\{ \begin{array}{c} M_x \\ M_y \\ M_{xy} \end{array} \right\} = \frac{h^3 E}{12(1-\nu^2)} \left[\begin{array}{ccc} 1 & -\nu & 0 \\ -\nu & 1 & 0 \\ 0 & 0 & \frac{1-\nu}{2} \end{array} \right] \left\{ \begin{array}{c} \kappa_x \\ \kappa_y \\ \kappa_{xy} \end{array} \right\} = \boldsymbol{D^B \kappa}, \tag{9.8}$$

with h being the thickness of the shell element, E the elastic modulus and ν the Poisson's ratio. In Eqn. 9.6, the first and second terms represent the virtual work done by the membrane forces and bending moments, respectively. The internal virtual work at time $t + \Delta t$ is

$$\delta W_{\text{int}}^{t+\Delta t} = \int_{A_0} \left(\delta \boldsymbol{\epsilon}^{t+\Delta t} \cdot \boldsymbol{P}^{t+\Delta t} + \delta \boldsymbol{\kappa}^{t+\Delta t} \cdot \boldsymbol{M}^{t+\Delta t} \right) dA_0. \tag{9.9}$$

Expanding this equation linearly in time yields:

$$\begin{aligned} \delta W_{\text{int}}^{t+\Delta t} &= \int_{A_0} \left((\delta \boldsymbol{\epsilon}^t + \Delta \delta \boldsymbol{\epsilon}) \cdot (\boldsymbol{P}^t + \Delta \boldsymbol{P}) + (\delta \boldsymbol{\kappa}^t + \Delta \delta \boldsymbol{\kappa}) \cdot (\boldsymbol{M}^t + \Delta \boldsymbol{M}) \right) dA_0, \\ &= \int_{A_0} \left(\delta \boldsymbol{\epsilon}^t \cdot \boldsymbol{P}^t + \delta \boldsymbol{\kappa}^t \cdot \boldsymbol{M}^t + \Delta \delta \boldsymbol{\epsilon} \cdot \boldsymbol{P}^t + \delta \boldsymbol{\epsilon}^t \cdot \Delta \boldsymbol{P} + \delta \boldsymbol{\kappa}^t \cdot \Delta \boldsymbol{M} \right) dA_0. \end{aligned} \tag{9.10}$$

In the last equation, the higher order terms are neglected and use has been made of the fact that $\Delta \delta \boldsymbol{\kappa} = 0$.

We discretise Eqn. 9.10 using three-noded triangular finite elements. Each element has three displacement u, v, w and three rotational degrees of freedom $\theta_x, \theta_y, \theta_z$ at each node. The nodal displacement vector for each element has 18 degrees of freedom and is written as:

$$\boldsymbol{p} = [u_1 \;\; v_1 \;\; w_1 \;\; \theta_{x1} \;\; \theta_{y1} \;\; \theta_{z1} \;\; u_2 \;\; v_2 \;\; w_2 \;\; \theta_{x2} \;\; \theta_{y2} \;\; \theta_{z2} \;\; u_3 \;\; v_3 \;\; w_3 \;\; \theta_{x3} \;\; \theta_{y3} \;\; \theta_{z3} \;\;]^T.$$

The rotations of the normal (β_x and β_y) are interpolated using the discrete Kirchhoff formulation: $\beta_x = \boldsymbol{H_x p}$ and $\beta_y = \boldsymbol{H_y p}$ and the variation of the curvature is related to the nodal displacement vector as,

$$\delta \boldsymbol{\kappa} = \boldsymbol{C} \delta \boldsymbol{p}. \tag{9.11}$$

The forms of $\boldsymbol{H_x}$, $\boldsymbol{H_y}$ and $\boldsymbol{C}$ are given by Batoz *et al.* (1980). The variation of the membrane strains can be written using the DKT for the non-linear part, and CST with drilling degrees of freedom for the linear part. This gives

$$\begin{aligned} \delta \boldsymbol{\epsilon} &= \left\{ \begin{array}{c} \bar{\epsilon}_x \\ \bar{\epsilon}_y \\ \bar{\epsilon}_{xy} \end{array} \right\} \\ &= \left[\begin{array}{ccccc} 1 & y & 0 & 0 & 0 \\ 0 & 0 & 1 & x & 0 \\ 0 & -x & 0 & -y & 1 \end{array} \right] \boldsymbol{B_1} \delta \boldsymbol{p} + \left[\begin{array}{c} \boldsymbol{p}^T \boldsymbol{H_x}^T \boldsymbol{H_x} \\ \boldsymbol{p}^T \boldsymbol{H_y}^T \boldsymbol{H_y} \\ \boldsymbol{p}^T \left(-\boldsymbol{H_y}^T \boldsymbol{H_x} - \boldsymbol{H_x}^T \boldsymbol{H_y} \right) \end{array} \right] \delta \boldsymbol{p}, \\ &= \left(\boldsymbol{B_L} + \boldsymbol{B_{NL}} \right) \delta \boldsymbol{p}. \end{aligned} \tag{9.12}$$

Here $\boldsymbol{B_1}$ is a matrix which depends on the coordinates of the vertices of the triangle whose form can be found elsewhere (Allman, 1984). Now, the increment of the virtual strain is given by

$$\Delta \delta \boldsymbol{\epsilon} = \left[\;\; \Delta \boldsymbol{p}^T \boldsymbol{H_x}^T \boldsymbol{H_x}, \;\; \Delta \boldsymbol{p}^T \boldsymbol{H_y}^T \boldsymbol{H_y}, \;\; \Delta \boldsymbol{p}^T \left(-\boldsymbol{H_y}^T \boldsymbol{H_x} - \boldsymbol{H_x}^T \boldsymbol{H_y} \right) \;\; \right]^T \delta \boldsymbol{p}. \tag{9.13}$$

The internal virtual work (Eqn. 9.10) can be now written in terms of the interpolation matrices (using Eqns. 9.11, 9.12 and 9.13) as:

$$\begin{aligned}\delta W_{\text{int}}^{t+\Delta t} = \int_{A_0} \Big[& \delta \boldsymbol{p}^T \left(\boldsymbol{B_L}^T + \boldsymbol{B_{NL}}^T \right) \boldsymbol{P}^t + \delta \boldsymbol{p}^T \boldsymbol{C}^T \boldsymbol{M}^t \\ & + \delta \boldsymbol{p}^T \left(\boldsymbol{H_x}^T \boldsymbol{H_x} P_x^t + \boldsymbol{H_y}^T \boldsymbol{H_y} P_y^t - \left(\boldsymbol{H_x}^T \boldsymbol{H_y} + \boldsymbol{H_x}^T \boldsymbol{H_y} \right) P_{xy}^t \right) \Delta \boldsymbol{p} \\ & + \delta \boldsymbol{p}^T \left(\boldsymbol{B_L}^T + \boldsymbol{B_{NL}}^T \right) \boldsymbol{D^M} \left(\boldsymbol{B_L} + \boldsymbol{B_{NL}} \right) \Delta \boldsymbol{p} + \delta \boldsymbol{p}^T \boldsymbol{C}^T \boldsymbol{D^B} \boldsymbol{C} \Delta \boldsymbol{p} \Big] \, dA_0. \end{aligned} \tag{9.14}$$

We now adopt an updated Lagrangian point of view and choose the domain of integration to be the deformed configuration. This makes the total displacements $\boldsymbol{p}$ to be zero so that $\boldsymbol{B_{NL}}$ vanishes. The internal virtual work now becomes:

$$\delta W_{\text{int}}^{t+\Delta t} = \delta \boldsymbol{p}^T \boldsymbol{f}_{\text{int}}^t + \delta \boldsymbol{p}^T \left(\boldsymbol{k_M} + \boldsymbol{k_G} \right) \Delta \boldsymbol{p}, \tag{9.15}$$

where

$$\boldsymbol{f}_{\text{int}}^t = \int_A \left(\boldsymbol{B_L}^T \boldsymbol{P}^t + \boldsymbol{C}^T \boldsymbol{M}^t \right) dA$$

is the internal force vector,

$$\boldsymbol{k_M} = \int_A \left(\boldsymbol{B_L}^T \boldsymbol{D^M} \boldsymbol{B_L} + \boldsymbol{C}^T \boldsymbol{D^B} \boldsymbol{C} \right) dA$$

is the material stiffness matrix and

$$\boldsymbol{k_G} = \int_A \left(\boldsymbol{H_x}^T \boldsymbol{H_x} P_x^t + \boldsymbol{H_y}^T \boldsymbol{H_y} P_y^t - \left(\boldsymbol{H_x}^T \boldsymbol{H_y} + \boldsymbol{H_x}^T \boldsymbol{H_y} \right) P_{xy}^t \right) dA$$

is the geometric stiffness matrix.

The internal virtual work in Eqn. 9.15 is in the local coordinates. This equation after transforming to the global coordinates (Zienkiewicz & Taylor, 2002) and performing the standard finite element assembly can be written as

$$\delta W_{\text{int}}^{t+\Delta t} = \delta \boldsymbol{P}^T \boldsymbol{F}_{\text{int}}^t + \delta \boldsymbol{P}^T \left(\boldsymbol{K_M} + \boldsymbol{K_G} \right) \Delta \boldsymbol{P}, \tag{9.16}$$

where $\boldsymbol{P}$ is the global displacement vector.

The external work at time $t + \Delta t$ due to body forces and body moments can be written as

$$\delta W_{\text{ext}}^{t+\Delta t} = \int_V \left(f_x \delta u + f_y \delta v + f_z \delta w - N_x \delta \beta_y + N_y \delta \beta_x \right) dV, \tag{9.17}$$

where f_x, f_y and f_z are the body forces and N_x and N_y are the body moments. Because the current shell element does not provide an interpolation function for the in-plane rotations, they are incorporated using equivalent point forces acting at the nodes of an element. For the external virtual work, we choose to interpolate the translational displacement using linear shape functions, and for the rotations we use the shape functions from the DKT:

$$\delta W_{\text{ext}}^{t+\Delta t} = \delta \boldsymbol{p}^T \int_V \left(\boldsymbol{N}^T [f_x \quad f_y \quad f_z]^T - \boldsymbol{H_y}^T N_x + \boldsymbol{H_x}^T N_y \right) dV = \delta \boldsymbol{p}^T \boldsymbol{f}_{\text{ext}}^{t+\Delta t}, \tag{9.18}$$

where

$$\boldsymbol{N} = \begin{bmatrix} N_1 & 0 & 0 & 0 & 0 & 0 & N_2 & 0 & 0 & 0 & 0 & 0 & N_3 & 0 & 0 & 0 & 0 & 0 \\ 0 & N_1 & 0 & 0 & 0 & 0 & 0 & N_2 & 0 & 0 & 0 & 0 & 0 & N_3 & 0 & 0 & 0 & 0 \\ 0 & 0 & N_1 & 0 & 0 & 0 & 0 & 0 & N_2 & 0 & 0 & 0 & 0 & 0 & N_3 & 0 & 0 & 0 \end{bmatrix},$$

N_1, N_2 and N_3 are the standard area coordinates of a three noded triangular element (Zienkiewicz & Taylor, 2002). After performing the standard finite element assembly procedure, the external virtual work can be written as

$$\delta W_{\text{ext}}^{t+\Delta t} = \delta \boldsymbol{P}^T \boldsymbol{F}_{\text{ext}}^{t+\Delta t}. \tag{9.19}$$

9.2.2 Fluid dynamics model

To model the fluid we use the boundary element method. The cilia, which are immersed in the fluid and fixed to a substrate, exert forces on the fluid. The velocity $\boldsymbol{u}^{\text{f}}$ at a point in the fluid $\boldsymbol{r}$ due to a point force exerted on the fluid by the cilia at a position $\boldsymbol{r'}$ can be obtained using Green's function as,

$$\boldsymbol{u}^{\text{f}}(\boldsymbol{r}) = \boldsymbol{G}(\boldsymbol{r} - \boldsymbol{r'}, h(\boldsymbol{r'}))\boldsymbol{f}(\boldsymbol{r'}), \tag{9.20}$$

with $h(\boldsymbol{r'})$ being the distance of the point force from the substrate. The Green's function $\boldsymbol{G}(\boldsymbol{r} - \boldsymbol{r'}, h(\boldsymbol{r'}))$ for a point force $\boldsymbol{f}(\boldsymbol{r'})$ acting in a fluid near a no-slip boundary is given by Blake (1971*b*). We assume that this point force is distributed over the boundary of the cilia as a traction $\boldsymbol{t}^{\text{f}}(\boldsymbol{r'})$. Now, the velocity in the fluid can be written as

$$\boldsymbol{u}^{\text{f}}(\boldsymbol{r}) = \int_S \boldsymbol{G}(\boldsymbol{r} - \boldsymbol{r'}, h(\boldsymbol{r'}))\boldsymbol{t}^{\text{f}}(\boldsymbol{r'})dS. \tag{9.21}$$

The cilia surface is discretised using 'nelm' three-noded triangular elements,

$$\boldsymbol{u}^{\text{f}}(\boldsymbol{r}) = \sum_{j=1}^{\text{nelm}} \int_{S_j} \boldsymbol{G}(\boldsymbol{r} - \boldsymbol{r}^j, h(\boldsymbol{r}^j))\boldsymbol{t}^{\text{f}}(\boldsymbol{r}^j)dS_j, \tag{9.22}$$

with the tractions $\boldsymbol{t}^{\text{f}}(\boldsymbol{r}^j)$ assumed to be varying linearly over the element,

$$\boldsymbol{t}^{\text{f}}(\boldsymbol{r}^j) = \boldsymbol{N}\left[\{t_1^x \;\; t_1^y \;\; t_1^z \;\; 0 \;\; 0 \;\; 0 \;\; t_2^x \;\; t_2^y \;\; t_2^z \;\; 0 \;\; 0 \;\; 0 \;\; t_3^x \;\; t_3^y \;\; t_3^z \;\; 0 \;\; 0 \;\; 0\}_j^{\text{f}}\right]^T = \boldsymbol{N}\boldsymbol{T}_j^{\text{f}},$$

where t_k^l is the traction at the k^{th} node in the l^{th} direction. As Eqn. 9.22 is valid for all the nodes on the cilium ($\boldsymbol{r} = \boldsymbol{r}^i$) we get,

$$\begin{aligned} \boldsymbol{u}^{\text{f}}(\boldsymbol{r}^i) &= \sum_{j=1}^{\text{nelm}} \int_{S_j} \boldsymbol{G}(\boldsymbol{r}^i - \boldsymbol{r}^j, h(\boldsymbol{r}^j))\boldsymbol{t}^{\text{f}}(\boldsymbol{r}^j)dS_j, \\ \boldsymbol{u}_i^{\text{f}} &= \sum_{j=1}^{\text{nelm}} \int \boldsymbol{G}_{ij}\boldsymbol{N}dS_j\boldsymbol{T}_j^{\text{f}}, \end{aligned} \tag{9.23}$$

with $\boldsymbol{G}_{ij} = \boldsymbol{G}(\boldsymbol{r}^i - \boldsymbol{r}^j, h(\boldsymbol{r}^j))$. Equation 9.23 relates the velocity of the i^{th} node to all tractions exerted by the surface of the cilia on the fluid. The integration procedure is adopted from reference (Pozrikidis, 2002). Equation 9.23 is evaluated at all nodes on the cilia, and the obtained equations are assembled in a matrix $\boldsymbol{G}$, which relates the traction exerted by the cilia on the fluid to its velocity, $\boldsymbol{U}^{\text{f}} = \boldsymbol{G}\boldsymbol{T}^{\text{f}}$. Once the velocity of the surface is known, this relation can be inverted to obtain the nodal tractions: $\boldsymbol{T}^{\text{f}} = \boldsymbol{G}^{-1}\boldsymbol{U}^{\text{f}}$.

9.2.3 Solid-fluid coupling

The effect of fluid drag is incorporated as an external force to the solid mechanics model, which provides an additional contribution to the external virtual work. The external virtual work at time $t + \Delta t$ on the j^{th} shell element due to the fluid drag is

$$\delta W_{\text{fluid}}^{t+\Delta t} = -\int \boldsymbol{t}_j^{\text{f}} \cdot \delta \boldsymbol{u} dS = -\int (\delta \boldsymbol{u} \cdot \boldsymbol{N})\, dS \boldsymbol{T}_j^{\text{f}} \approx -\delta \boldsymbol{p} \int \boldsymbol{N}^T \boldsymbol{N} dS \boldsymbol{T}_j^{\text{f}} = -\delta \boldsymbol{p} \boldsymbol{M}^j \boldsymbol{T}_j^{\text{f}}, \tag{9.24}$$

where $\boldsymbol{M}^j = \int \boldsymbol{N}^T \boldsymbol{N} dS$, $\boldsymbol{u}$ is the displacement vector and $\boldsymbol{p}$ is the local nodal displacement vector. After performing the standard finite element assembly procedure we get,

$$\delta W_{\text{fluid}}^{t+\Delta t} = -\delta \boldsymbol{P} \boldsymbol{M} \boldsymbol{T}^{\text{f}} = -\delta \boldsymbol{P} \boldsymbol{M} \boldsymbol{G}^{-1} \boldsymbol{U}^{\text{f}}. \tag{9.25}$$

Using the no-slip boundary condition $\boldsymbol{U}^{\text{f}} = \boldsymbol{A} \Delta \boldsymbol{P} / \Delta t$, Eqn. 9.25 can be written as,

$$\delta W_{\text{fluid}}^{t+\Delta t} = -\delta \boldsymbol{P} \boldsymbol{M} \boldsymbol{G}^{-1} \boldsymbol{A} \Delta \boldsymbol{P} / \Delta t, = -\delta \boldsymbol{P}^T \boldsymbol{K}_{\text{f}} \Delta \boldsymbol{P} \tag{9.26}$$

where $\boldsymbol{K}_{\text{f}} = \boldsymbol{M} \boldsymbol{G}^{-1} \boldsymbol{A} / \Delta t$ is the stiffness contribution due to the presence of the fluid and $\boldsymbol{A}$ is a matrix that eliminates the rotational degrees of freedom from the global displacement vector $\Delta \boldsymbol{P}$.

Equating the internal (Eqn. 9.16) and the external virtual work (the sum of Eqns. 9.26 and 9.19), and invoking the arbitrariness of the virtual displacements, we get the final equation of motion for the fluid-structure interaction problem:

$$(\boldsymbol{K}_{\boldsymbol{M}} + \boldsymbol{K}_{\boldsymbol{G}} + \boldsymbol{K}_{\text{f}})\, \Delta \boldsymbol{P} = \boldsymbol{F}_{\text{ext}}^{t+\Delta t} - \boldsymbol{F}_{\text{int}}^{t}. \tag{9.27}$$

After incorporating the appropriate boundary conditions, Eqn. 9.27 is solved for the displacement increment $\Delta \boldsymbol{P}$.

9.2.4 Magneto-static model

The cilia are magnetic films which respond to an external magnetic field. The magnetic response of the cilia is characterised by the magnetic susceptibility tensor $\boldsymbol{\chi}$, through the constitutive relation $\boldsymbol{M} = \boldsymbol{\chi} \boldsymbol{H}$, where $\boldsymbol{M}$ is the magnetization and $\boldsymbol{H}$ is the magnetic field. The magnetic body couple acting on the cilia $\boldsymbol{N_c}$ is obtained from the cross product of the magnetization and the magnetic field intensity $\boldsymbol{N_c} = \boldsymbol{M} \times \boldsymbol{B}_{\text{ext}}$, where $\boldsymbol{M}$ is the magnetization and $\boldsymbol{B}_{\text{ext}}$ is the external magnetic field. The magnetization $\boldsymbol{M}$ has to be found by solving the Maxwell's equations of electromagnetism. However, we adopt a simpler approach and make use of the fact that the cilia are slender enough to not perturb the external magnetic field significantly; the magnetic field just outside the cilia is equal to the applied magnetic field. The magnetic field inside the cilia can be determined from the electromagnetic boundary conditions: $B_z = B_z^{\text{ext}}$, $H_x = H_x^{\text{ext}}$, $H_y = H_y^{\text{ext}}$, where $\boldsymbol{H}_{\text{ext}} = \boldsymbol{B}_{\text{ext}} / \mu_0$, μ_0 is the permeability of free space and x, y and z refer to the local coordinate axes of the shell element. Using the first boundary condition and the constitutive behaviour we can find the field H_z inside the cilia as,

$$H_z = \frac{B_z^{\text{ext}} - \mu_0 \left(H_x^{\text{ext}} \chi_{xz} + H_y^{\text{ext}} \chi_{yz} \right)}{\mu_0 (1 + \chi_{zz})}. \tag{9.28}$$

Once the field in the cilia $\boldsymbol{H}$ is determined, the magnetization of the cilia ($\boldsymbol{M} = \boldsymbol{\chi H}$) and the magnetic body couple ($\boldsymbol{N_c}$) can be found. The only assumption made in this approach is that the magnetic field outside the cilia is the external magnetic field, i. e., we neglect the magnetic field caused by the magnetization of cilia.

9.3 Applications of the coupled magneto-mechanical model

The three-dimensional model is verified through a number of reference problems for the solid mechanics model, the fluid dynamics model, the fluid-structure interaction model and the magneto-static model (see appendix L). In this section we demonstrate the modelling capacity of the developed magneto-mechanical model using a number of physical examples. In the cases shown the length L of the cilia is 100 micron and the thickness h is 2 micron. The elastic modulus of the cilia E is 1 MPa, the Poisson's ratio $\nu = 0.0$ and the fluid viscosity μ is 1 mPas. The magnetic susceptibilities of the cilia are $\chi_{xx} = 4.6$ and $\chi_{yy} = \chi_{zz} = 0.8$ (all other components are taken to be zero). We apply a magnetic field of magnitude 20 mT, rotating about the $-y$ axis with a frequency of 50 Hz (see Fig. 9.1). As the cilia are super-paramagnetic, the cilia complete one beat cycle in t_{beat}=10 ms (Khaderi *et al.*, 2011*b*). In the simulations, the fixed edges of the cilia are placed $0.1L$ above the no-slip boundary, to mimic the presence of the sacrificial layer used during the manufacturing process (den Toonder *et al.*, 2008; Fahrni *et al.*, 2009).

9.3.1 Motion of a cilium with non-uniform width

We first study the motion of one cilium whose width decreases linearly from the fixed end to the free end. To quantify the amount of non-uniformity (tapering) in the width, we define the geometric parameter $T = (b - b_1)/b$, where b and b_1 are the widths of cilium at the fixed and the free edges, respectively. The width of the cilium at the fixed edge is taken to be $L/10$. When T is zero the cilium has uniform width; whereas the cilium is triangular for a tapering T of unity. First, we find what value of T is required to generate an asymmetric motion. The trajectory of the tip of the cilium for different values of T is shown in Fig. 9.3(a). The area swept by the free end of the cilium increases when the tapering T is increased (see the left inset of Fig. 9.3(a)). Snapshots of the ciliary motion is shown in Figs. 9.3(b) and 9.3(c) for a $T = 0$ and 0.5, respectively.

The flow caused by the beating cilium is quantified by calculating the flux through the $y - z$ plane and $x - z$ plane. The far field velocity at a point in the fluid due to the nodal drag forces is given by Blake (1972),

$$8\pi\mu u_i^f = \sum_{j=1}^{\text{nnod}} \frac{12h^j r_i r_k r_3}{|\boldsymbol{r}|^5} f_{\text{f}k}^j + O\left(\frac{1}{|\boldsymbol{r}|^3}\right) \tag{9.29}$$

where $\boldsymbol{r}$ is the position of a point in the fluid relative to the Stokeslet, h^j is the distance between the node j and the no-slip plane, 'nnod' are the total number of nodes, $f_{\text{f}k}^j$ represents the components of the point forces acting on the fluid at the j^{th} node. In Eqn. 9.29 Einstein's summation convention is used for repeated indices. The point forces can be obtained from $\boldsymbol{F}_{\text{f}} = \boldsymbol{K}_f \Delta \boldsymbol{P}/\Delta t$. The velocity flux in the x and y directions (Q_x

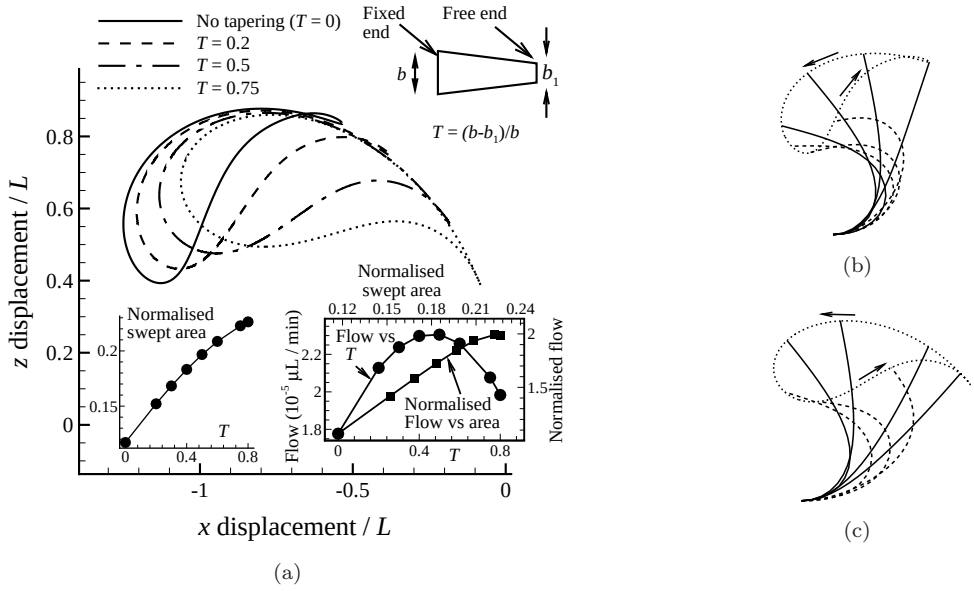

Figure 9.3: *(a) Displacement of the cilia tip for different tapering in the width. The inset at the right shows the fluid flow (in microlitre per minute) for different values of tapering T, and the flow (normalised with $L^2(b_1 + b)/2$) as a function of the area swept (normalised with L^2) and the inset at the left shows the area swept normalised with (L^2) as a function of T. (b) and (c) Snapshots of the motion of the cilia in the $x - z$ plane at different time instances for $T = 0$ and 0.5, respectively. The arrows show the direction of motion of the cilium, the dotted lines shows the trajectory of the free end, the solid lines represent the cilium during the effective stroke, and the dashed lines during the recovery stroke.*

and Q_y) are calculated by integrating the velocity in the x and y directions over the $y-z$ and $x - z$ planes, respectively:

$$Q_x = \int_0^\infty \int_{-\infty}^\infty u_x^f \, dydz = \frac{1}{\pi\mu} \sum_{j=1}^{\text{nnod}} h^j f_{\text{f}x}^j,$$
$$Q_y = \int_0^\infty \int_{-\infty}^\infty u_y^f \, dxdz = \frac{1}{\pi\mu} \sum_{j=1}^{\text{nnod}} h^j f_{\text{f}y}^j. \tag{9.30}$$

This volume flux is integrated over the cycle to obtain the total volume flow during one cycle.

The volume flow per cycle (in microlites per minute) for different values of tapering is shown in the right inset of Fig. 9.3(a). When the tapering is increased the area swept increases, whereas the area of the cilium which drives the flow decreases. Thus the created flow is due to the competition between the swept area and the area of the cilium that pushes the fluid. As a result we see an initial increase of the flow, which reaches a maximum for a tapering T of 0.5, and then decreases. In the same inset, the fluid flow (normalised with $L^2(b_1+b)/2$) is plotted as a function of the area swept (normalised with L^2) in the $x - z$ plane. It is to be noted that normalising the fluid flow with $(b_1 + b)/2$ gives the area flow per unit average width of the cilia, which on further normalisation

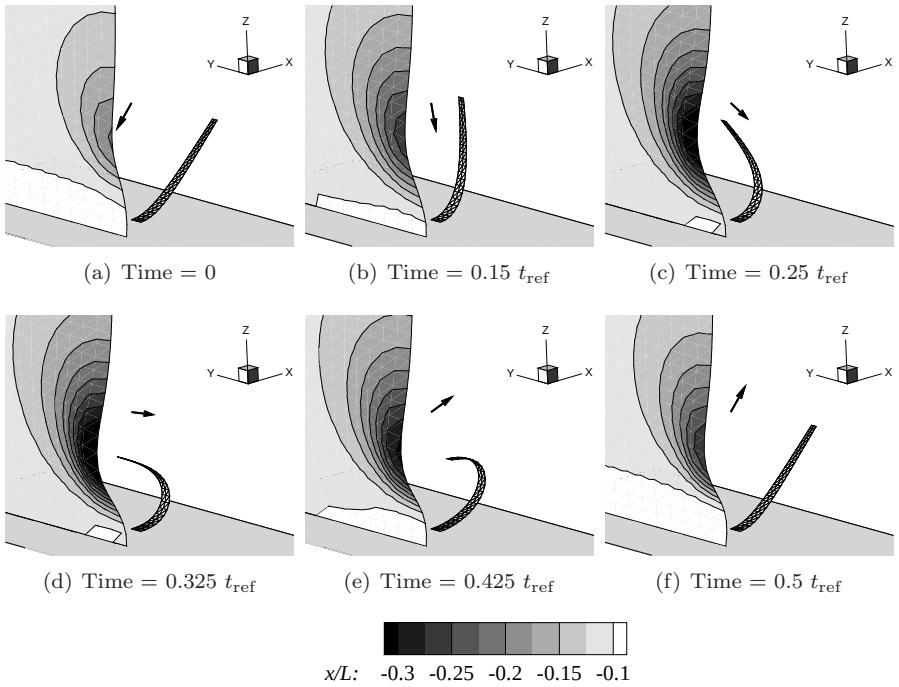

(a) Time = 0 (b) Time = 0.15 t_{ref} (c) Time = 0.25 t_{ref}

(d) Time = 0.325 t_{ref} (e) Time = 0.425 t_{ref} (f) Time = 0.5 t_{ref}

Figure 9.4: *Snapshots of the motion of the cilium, beating in the $x-z$ plane, at different instances of time for a representative cycle. Figures (a)-(c) and (d)-(f) represent the effective and recovery strokes, respectively. The evolving surface represents contours of the x coordinates of fluid particles which at time $t=0$ were parallel to the $y-z$ plane. During the effective stroke, the cilium displaces the fluid particles in the negative x-direction, and during the recovery stroke, the fluid particles are dragged back. The displacement of the fluid particles can be observed by comparing the position of the particles in Figs. (a) and (f).*

with L^2 becomes the normalised area flow. Hence, similar to the two-dimensional cases presented in (Khaderi *et al.*, 2009, 2010), the flow scales linearly with the swept area.

To gain insight on the fluid propulsion, we look at the position of fluid particles[2] which initially formed a plane parallel to the $y-z$ plane for a cilium with a tapering T of 0.5, see Fig. 9.4. During the effective stroke, the cilium displaces the fluid particles in the negative x-direction (see Figs. 9.4(a) and (c)), after which the fluid particles are dragged back during the recovery stroke (see Figs. 9.4(d) and (f)). The displacement of the fluid particles can be observed by comparing the position of the particles in Figs. 9.4(a) and (f). The additional information, which we obtain from the three-dimensional model compared to the two-dimensional model, is the displacement of the fluid particles that are not present in the plane of beat.

[2]At every time instant, the displacement of the fluid particles is calculated using their velocity (Eqn. 9.23). The new position is found by adding the displacement to their current position.

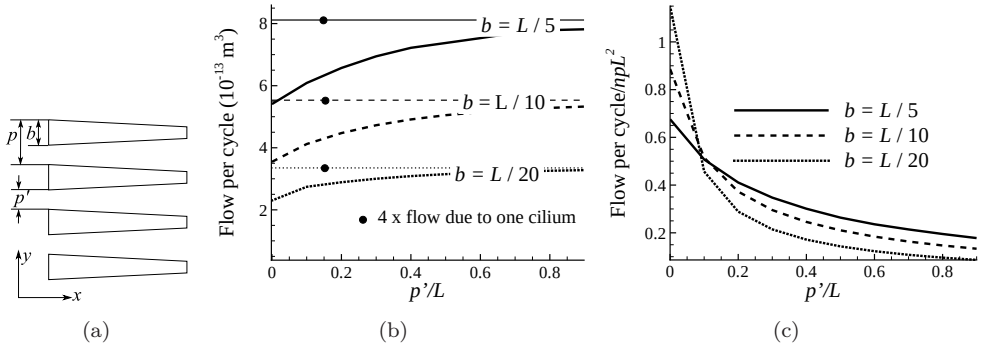

(a) (b) (c)

Figure 9.5: *(a) Parameters used to study the effect of cilia spacing p' and width b for a given tapering. (b)-(c) Flow as a function of width and the pitch of the cilia spacing for cilia having a taper along the width.*

9.3.2 Effect of the cilia width and spacing

We now examine the effect of the width and the cilia spacing on the flow generated by one row of cilia placed along the width. The geometry is shown in Fig. 9.5(a). We take n cilia of width b at the fixed edge whose tapering T is 0.5. The spacing between the cilia is p (the pitch), so that the total width occupied by the cilia row is np. For the simulations we choose $n = 4$ and calculate the flow created as a function of the spacing between the cilia $p' = p - b$. The spacing p' is varied from 0 (no spacing between the cilia at their fixed edge) to 0.9L.

The horizontal lines in Fig. 9.5(b) represent four times the flow created by one cilium for different widths b. In the cases considered the increase of flow does not scale with the increase of the cilium width b. This suggests that the forces acting on the fluid do not scale linearly with the cilia width b. Such a behaviour is also present in the case of ellipsoids (Happel & Brenner, 1986).

The flow as a function of the spacing p' for various widths for $n = 4$ is also shown in Fig. 9.5(b). The flow created by the cilia is larger when they are further apart. The beating of a cilium imparts velocity to a small fluid region around it (see Fig. 9.6(a)). When four cilia are used, the region influenced by the cilia strongly depends on the their spacing. When the spacing between them is small these regions overlap so that they collectively influence only a small region of the fluid, see Fig. 9.6(b). The total fluid region that can be influenced by the cilia increases as the spacing is increased (see Fig. 9.6(c)), reaching a maximum for spacings when the cilia do not hydrodynamically interact. In these cases, the flow converges to four times the flow caused by one cilium. This can also be rationalised from a force point-of-view. When the cilia are spaced closer, they can move the fluid with less effort; this reduces the forces acting on the fluid due to the cilia motion. Consequently, the flow generated is low. A similar behaviour can also be seen in the case of two spheres which are translating at a given velocity (Happel & Brenner, 1986). The force exerted by the spheres on the fluid is reduced when they are brought closer together.

A practically-relevant question is: How much flow can be generated by the cilia per unit width? This question can be answered by normalising the flow in Fig. 9.5(b) with the width of the cilia row (np). It can be seen that when the spacing p' is very low

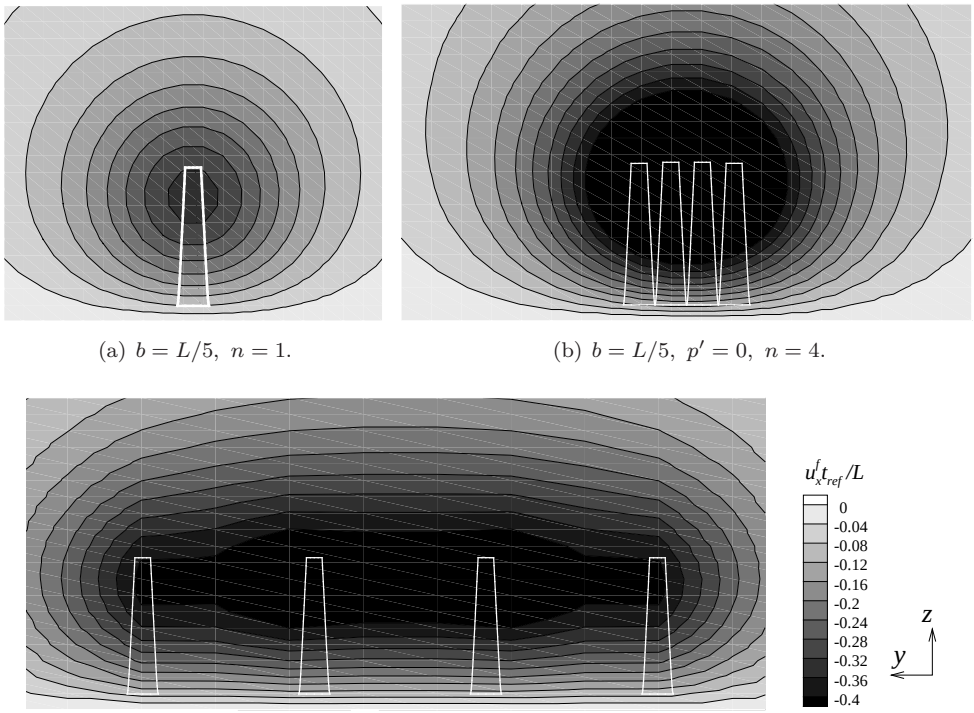

(a) $b = L/5,\ n = 1.$

(b) $b = L/5,\ p' = 0,\ n = 4.$

(c) $b = L/5,\ p' = 0.9L,\ n = 4.$

Figure 9.6: *Front view ($y - z$ plane) of the cilia at $t = t_{\text{ref}}/2$ (see Fig. 9.4(f)). The contours correspond to the fluid velocity in the x-direction on a plane parallel to $y - z$ plane at a distance of $1.1L$ from the cilia fixed edge. The cilia influence a larger region of the fluid when the spacing is large, thus creating a larger flow as the spacing is increased.*

compared to the length L, the narrow cilia produce more flow; when the spacing is comparable to the length, the broader cilia create a higher flow. Note that for a given width, many narrow cilia spaced close together create the largest flow. Interestingly, this is the option chosen by nature. The natural cilia are hair-like structures that are spaced very close together.

9.3.3 Effect of metachronal waves in the out-of-plane direction

We now analyse the flow when an array of cilia move out-of-phase in the direction of their beat motion (antiplectic and symplectic metachrony) and in the direction orthogonal to it (laeoplectic and diaplectic metachrony) (Childress, 1981). In laeoplectic and diaplectic metachrony, the effective stroke is to the left and right of the direction of propagation of the metachronal wave (see Fig. 9.7). To perform the simulations we choose 5 rows[3] of cilia, with each row containing 5 cilia (see Figs. 9.7 and 9.1(b)). The cilia have an uniform width $b = 0.1L$ and a tapering in the thickness, such that the thickness of the cilia at the fixed end is 2 microns, which decreases linearly along the length to a thickness of 1 micron at the free end. The cilia spacings are $a = 1.1L$ (along the length) and $p = 0.2L$

[3]A row refers to the arrangement of cilia in the y-direction.

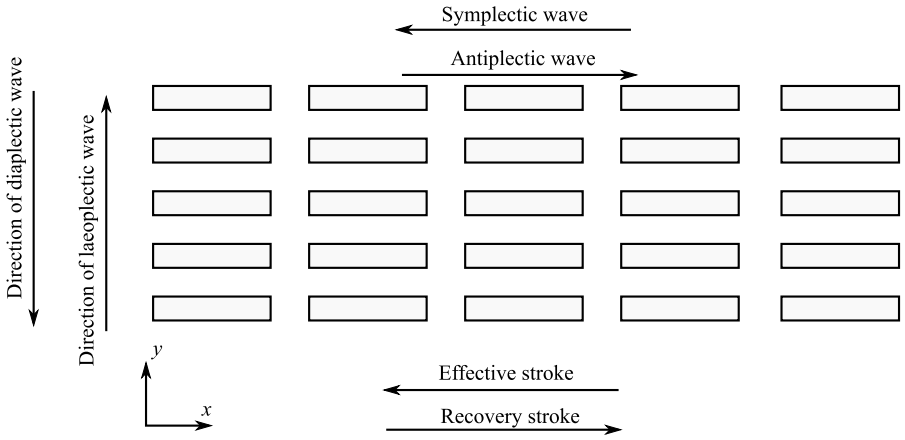

Figure 9.7: *Schematic diagram showing the arrangement of cilia, the direction of effective and recovery strokes along with different kinds of metachronal waves.*

(along the width). A rotating magnetic field with a magnitude of 20 mT is applied to every cilium at a frequency of 50 Hz. The phase difference in the magnetic field between adjacent cilia is varied from $\Delta\phi_x = -\pi/2$ to $\pi/2$ in the beat direction, and from 0 to $\Delta\phi_y = 2\pi/10$ in the direction normal to beat plane[4]. A zero phase difference in any direction represents uniformly beating cilia in that direction, and a phase difference of $\pi/2$ represents the situation when adjacent cilia are in anti-phase (standing wave). As the metachronal wave can also travel in a direction normal to the cilia beat, we also analyse the flow in this direction. In the following, the flow in the plane of the ciliary beat is referred to as primary flow and the flow normal to this plane is called secondary flow. The primary and secondary flow are plotted as a function of the phase differences $\Delta\phi_x$ and $\Delta\phi_y$ in Fig. 9.8.

The flow is always larger for the cilia beating with antiplectic metachrony compared to synchronously beating cilia (in accordance with chapter 7). In the case of symplectic metachrony, the cilia obstruct the flow caused by their neighbours during the effective stroke (as also seen in the two-dimensional case, see chapter 7). As a result, for antiplectic metachrony the flow is larger and for symplectic metachrony the flow is smaller than synchronously beating cilia, although the magnitude of increase is larger (for antiplectic metachrony) than the decrease (for symplectic metachrony). The flow obstruction is maximum for $-0.2\pi < \Delta\phi_x < 0$, in such cases the flow created is less than that created by synchronously beating cilia. In these cases, however, when $\Delta\phi_y > 0$ the decrease is lower because of the relaxation of the obstruction of positive flow. The flow exhibits a fluctuating behaviour only for the cases enclosed in the white curve, outside this region (in the direction of the arrow) the flow is unidirectional.

The laeoplectic metachrony (LM) creates a significant secondary flow (see Fig. 9.8(b)). To investigate the cause for the secondary flow, we look at the velocity created by two row of cilia in y-direction at the instance where the third cilium in each row of cilia is pointing towards the z axis, see Fig. 9.9. In the cases (a) and (b) of Fig. 9.9, the cilia are exhibiting the effective stroke and are moving to the left. For synchronously beating

[4]The metachrony normal to the beat plane will create symmetric waves about $\Delta\phi_y = 0$. Hence, simulations are performed only for $\Delta\phi_y > 0$.

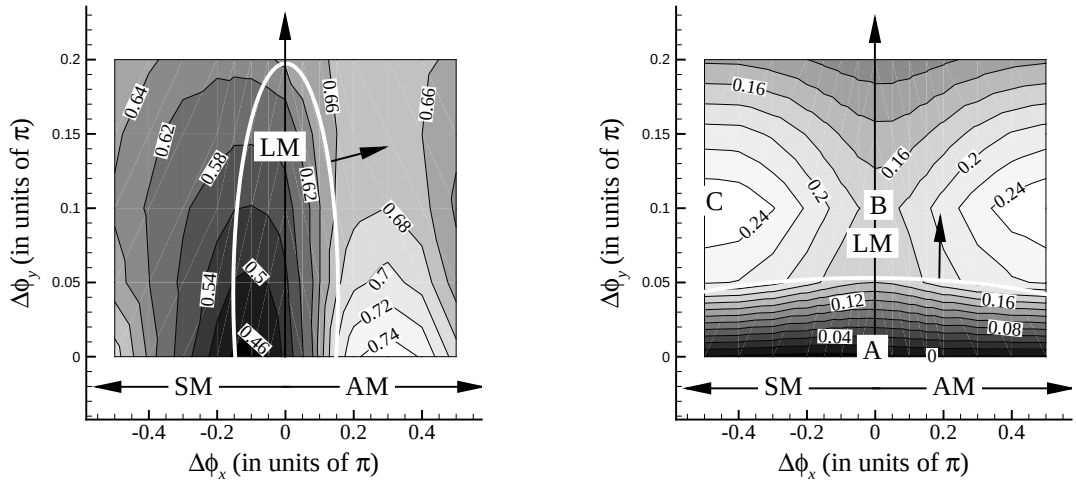

(a) Primary flow

(b) Secondary flow

Figure 9.8: *Primary and secondary flow created by cilia due to metachrony along and normal to the beat direction, respectively. The primary flow is larger when the cilia beat out-of-phase compared to synchronously beating cilia except for* $-2\pi/10 < \Delta\phi_x < 0$ *and* $0 < \Delta\phi_y < \pi/10$. *The secondary flow is created due to the plate-like motion of the rows of cilia, which reaches a maximum when the cilia motion between rows is anti-phase and* $\Delta\phi_y = \pi/10$. *AM, SM and LM represent antiplectic, symplectic and laeoplectic metachrony, respectively. The velocity profiles for the set of phase differences corresponding to A, B and C are shown in Fig. 9.9.*

cilia the velocity in the y-direction is symmetrically distributed (see Fig. 9.9(a)). Such a velocity distribution creates no net flux in the y-direction. However, when the cilia beat out-of-phase normal to the beat plane, the position of individual cilia leads to an asymmetric distribution of the y-velocity (see figure Fig. 9.9(b)). This asymmetry in the velocity profile is present at all y-positions and leads to a net flux in the y-direction.

The displacement of fluid particles initially near the right most row at different time instances is shown in Figs. 9.10 and 9.11 for cilia beating synchronously ($\Delta\phi_y = \Delta\phi_x = 0$) and out-of-phase ($\Delta\phi_y = \pi/10$ and $\Delta\phi_x = 0$), respectively. In the case of synchronously beating cilia, the symmetric velocity distribution about the $x - z$ plane leads to a symmetric displacement of the particles throughout the cycle and leads to a net displacement only in the plane of the beat (x-direction). However, the asymmetric velocity distribution in the case of laeoplectic metachrony leads to an effective displacement of particles in the beat-plane as well as in the y-direction, thereby creating the secondary flow.

When the cilia move in anti-phase in the beat plane ($\Delta\phi_x \pm \pi/2$), the cilia in the adjacent rows move opposite to each other leading to large secondary flows for $\Delta\phi_y = \pi/10$ (see Fig. 9.8(b)). The velocity field at a particular instance is shown in Fig. 9.9(c), where the left row of cilia are exhibiting the effective stroke and the right row the recovery stroke. Such a motion of cilia creates a negative pressure between them that sucks-in the fluid whose velocity has a prominent component in the y-direction (see Fig. 9.9(c)) and leads to a larger flux in the y-direction compared to cilia beating synchronously in the beat plane.

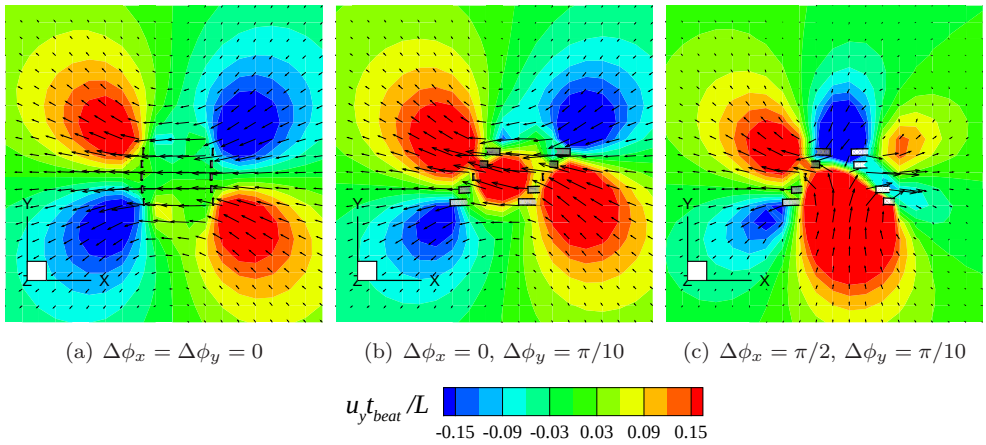

(a) $\Delta\phi_x = \Delta\phi_y = 0$ (b) $\Delta\phi_x = 0$, $\Delta\phi_y = \pi/10$ (c) $\Delta\phi_x = \pi/2$, $\Delta\phi_y = \pi/10$

Figure 9.9: *Velocity field for two rows of cilia beating (a) in-phase, (b) out-of-phase in the y-direction and (c) out-of-phase in both the x and y-directions. The contours represent the velocity in y-direction on a plane parallel to the $x - y$ plane at a distance of $0.5L$ from the substrate. The arrows represent the velocity in the $x - y$ plane. The velocity contours correspond to the set of phase differences marked by A, B and C in Fig. 9.8(b).*

9.3.4 Out-of-plane actuation of cilia

In nature, the cilia on a Paramecium beat in a plane normal to the surface during the effective stroke, and during the recovery stroke they beat in a plane parallel to the surface. To achieve such a motion, we apply a magnetic field so that the magnetic field vector can be oriented in three-dimensional space (see Fig. 9.12).

Figure 9.13 shows the motion of a SPM cilium in which the cilium performs the effective stroke in the $x - z$ plane and the recovery stroke in the $x - y$ plane near the no-slip boundary. This results in large flow during the effective stroke and a small flow during the recovery stroke. The effective stroke consists of a uniform bending of the cilium in the $x - z$ plane. During the recovery stroke, the cilium undergoes a significant amount of twisting, and comes back to the initial position (see Figs. 9.13(d) - (f)).

In Fig. 9.14(a), we show the flow as a function of the width of the cilium. It can be seen that flow drastically decreases as the width of the cilium is increased. This is because, the cilia can no longer twist and stay closer to the bottom boundary (see Fig. 9.14(b)). In such cases, we see a significant amount of flow during the recovery stroke, and this reduces the net amount of fluid propelled.

9.4 Summary

We have developed a fluid-structure interaction model to simulate the interaction of thin shells with the surrounding fluid. The shell structures are modelled using finite elements, while the fluid is modelled using boundary elements. The magnetic field is calculated from the magnetostatic boundary conditions. The developed model was used to simulate the flow due to magnetic artificial cilia, where it is shown that our model captures the essential physical phenomena governing the ciliary motion. Extensions of the present

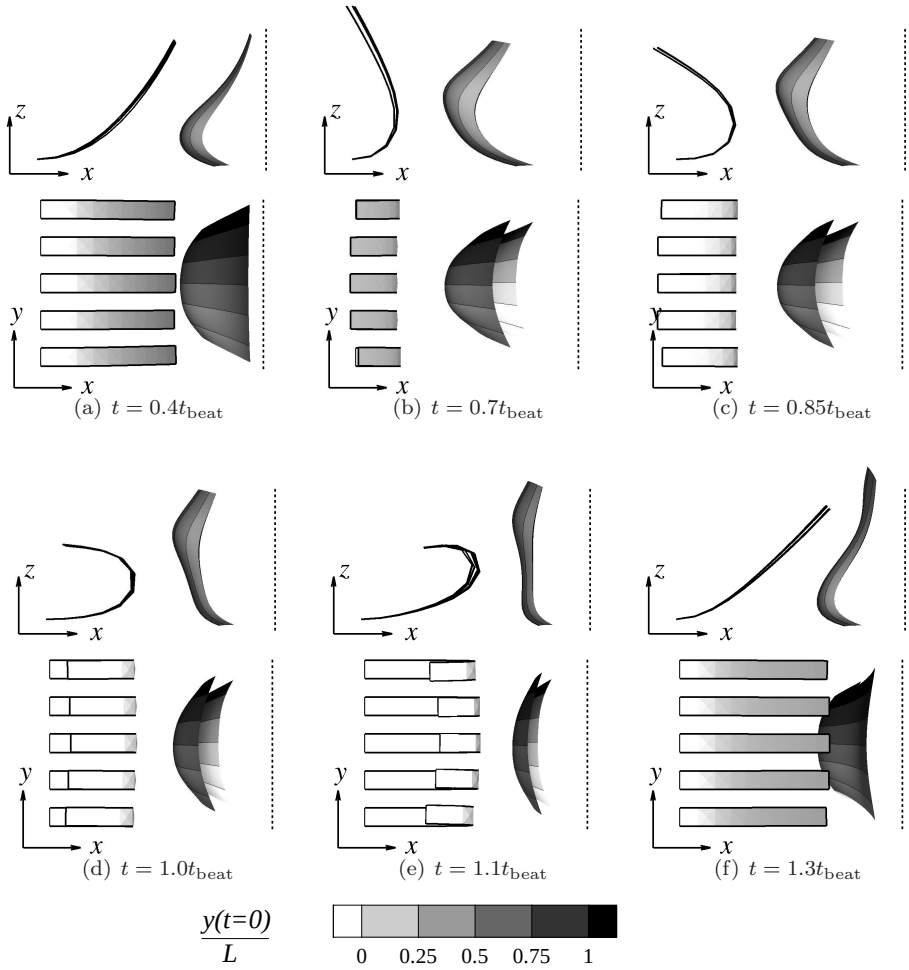

Figure 9.10: *Synchronous motion ($\Delta\phi_y = \Delta\phi_x = 0$) of one row of cilia and the resulting motion of a plane of particles at different time instances. The top figure represents the front view and the bottom represents the top view. The initial position of the particles plane in both the views is shown by the dashed lines. The particles move only in the plane of beat.*

model include the implementation of a fast multipole method for the fluid model and implementing a boundary element method to calculate the local magnetic field in and around the cilia (Khaderi *et al.*, 2009).

The three physical problems studied are the effect of (i) cilia width and spacing, (ii) metachronal wave formation along the width and (iii) three-dimensional cilia motion on the flow generated. The outcomes are that narrow and closely spaced cilia create the largest flow, the metachronal wave along the width of the cilia creates a significant flow in the direction of the cilia width and that the recovery stroke in the case of the three-dimensional motion of the cilia strongly depends on the cilia width. It is interesting to note that if we are able to create the laeoplectic metachrony of the cilia inside a microchannel, the primary flow will cause a net fluid transport, while the secondary flow

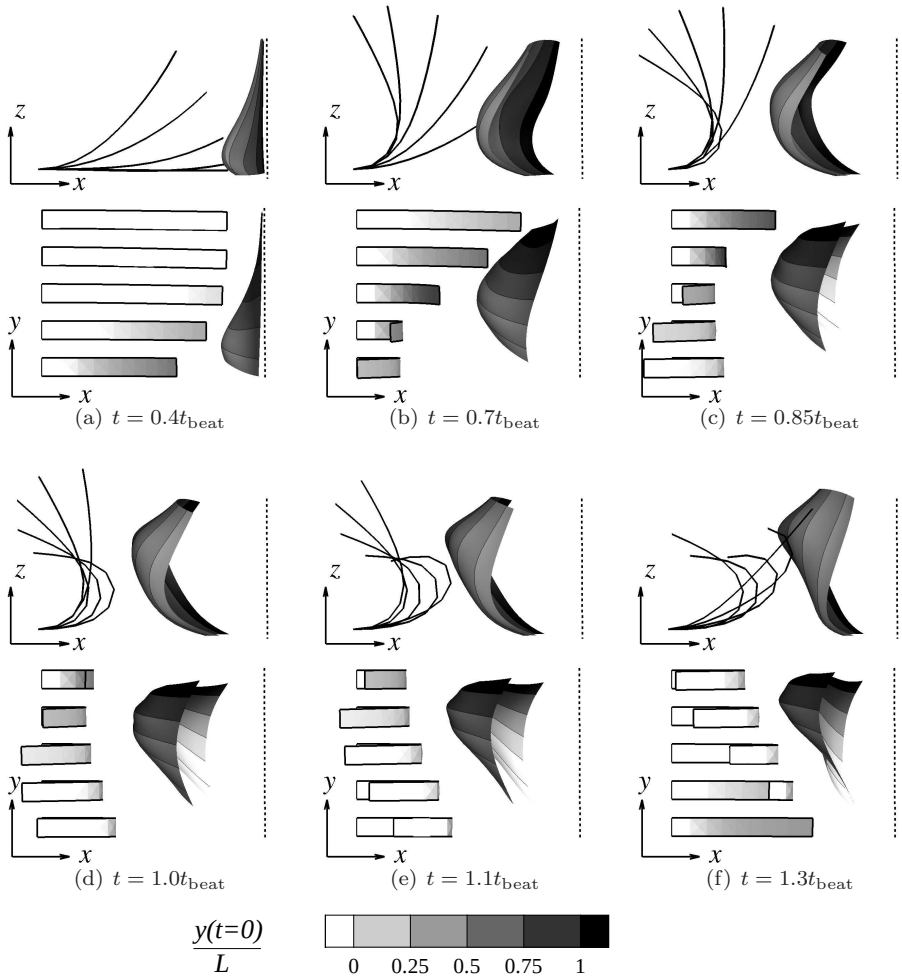

Figure 9.11: *Out-of-phase motion ($\Delta\phi_y = \pi/10$ and $\Delta\phi_x = 0$) of one row of cilia and the resulting motion of a plane of particles at different time instances. The top figure represents the front view and the bottom represents the top view. The initial position of the particle plane in both the views is shown by the dashed lines. The particles move in the plane of beat and also orthogonal to the beat plane (compare instant (f) with Fig. 9.10(f)).*

can be used for the mixing of fluids.

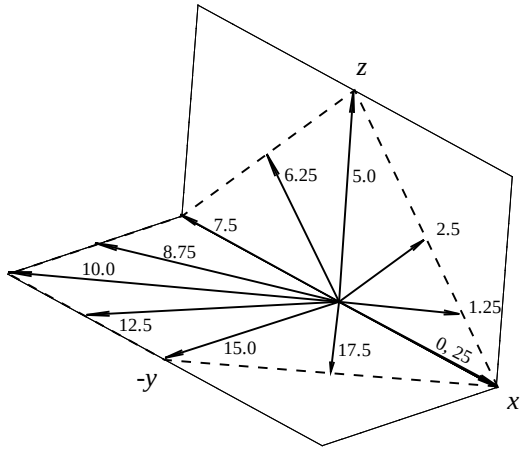

Figure 9.12: *The arrows represent the applied magnetic field vector at different instances in time for a cilium to exhibit the effective stroke in the $x-z$ plane and the recovery stroke in the $x-y$ plane. The numbers adjacent to the arrows show the time in milliseconds. The magnitude of the magnetic field at time instances 0, 5, 7.5 15 and 25 ms is 20 mT.*

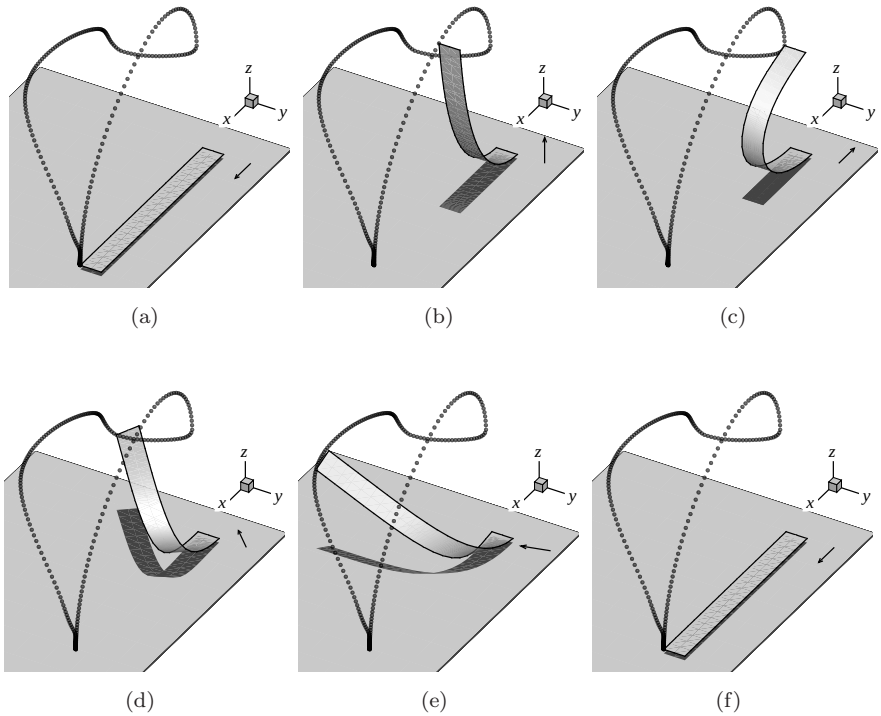

Figure 9.13: *Snap shots of the motion of a SPM cilium due to a 3D magnetic field. The arrow shows the applied magnetic field. The cilium performs the effective stroke in the $x-z$ plane (see (a)-(c)) and the recovery stroke in the $x-y$ plane (see (d)-(f)). Significant twisting of the cilium during the recovery stroke can be observed from the instances shown in (d) and (e).*

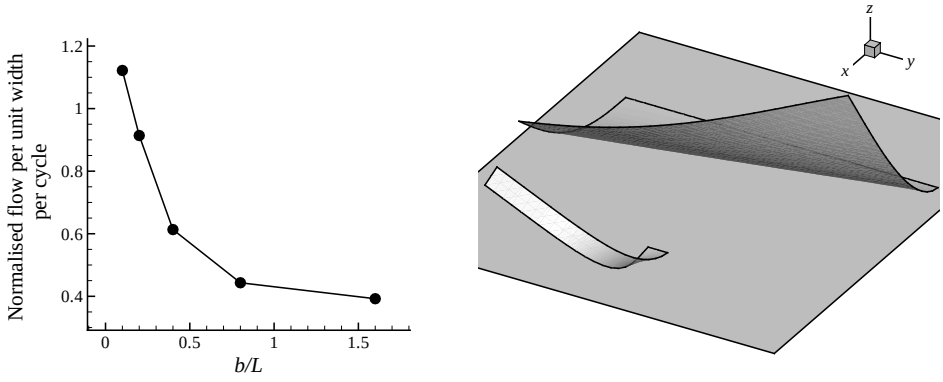

(a) (b)

Figure 9.14: *(a) Flow caused due to the 3D motion of a cilium (see Fig. 9.13) as a function of the width b/L (only one cilium is used in these simulations). The flow comes down drastically as the width b is increased. (b) Snapshots of two cilia of $b = L/10$ and $b = 1.6L$ when the cilia are half way through their recovery strokes (16 ms). The narrow cilium nicely twists, causing less flow during the recovery stroke.*

Chapter 10
Summary

This work has addressed the computational design of magnetically-driven artificial cilia for microfluidic propulsion. The objective of the thesis, as mentioned in section 1.5, was two-fold:

1. To identify under what conditions a magnetic film can mimic the asymmetric beat motion of natural cilia.

2. To explore how the flow created by the artificial cilia can be controlled and optimised.

The first question is answered in chapter 3 and the second in the subsequent chapters.

In this thesis a coupled solid-fluid magneto-mechanical model has been developed that captures the deformation of the cilia, the distribution of the magnetic field in and outside the cilia, and the resulting motion of the fluid (chapter 2). The results are shown as a function of the physical parameters that govern the flow created by the cilia in addition to geometric parameters such as the cilia spacing (a), channel height (H) and phase difference between the cilia ($\Delta\phi$). The four physical parameters involved are (i) the magnetic number M_n - the ratio of magnetic to elastic forces, (ii) the fluid number F_n - the ratio of fluid viscous forces to the elastic forces, (iii) the Reynolds number Re - the ratio of fluid inertia forces to the viscous forces and (iv) the inertia number I_n - the ratio of inertia forces of the cilia to their elastic forces.

In Chapter 3, we have shown several configurations that can mimic the motion of natural cilia with pronounced asymmetry. One configuration is based on a curled permanently magnetic cilium. When a magnetic field is applied that is opposite to the magnetization of the permanently magnetic cilium, it undergoes a buckling-kind of instability, mimicking a recovery stroke. When the magnetic field is switched off, the cilium performs the effective stroke and returns to its initial curled position because of elastic forces. Another configuration is based on super-paramagnetic cilia that have a tapered cross section. When these cilia are subjected to a rotating magnetic field, they follow the applied magnetic field and stay straight, performing an effective stroke. On further rotation of the magnetic field, the magnetic couple distribution near the fixed end forces the cilia to come back to the initial position, while the couple near the free end makes the cilia to stay closer to the channel wall. As the cross section is tapered, the magnitude of the couple near the fixed end is larger than at the free end. This causes the cilia to come back with a whip-like recovery stroke. In these configurations the recovery stroke takes place at much higher velocity than the effective stroke. The fluid flow created by the cilia was found to scale linearly with the area swept by the tip of the cilia. We subsequently studied the area swept by the cilia as a function of the dimensionless numbers in the limit of low Reynolds numbers. It was found that a larger magnetic number was needed to sweep a given swept area when the fluid number was increased, and that the

inertia number does not significantly influence the area swept by the cilia. Also, when the fluid number was increased, it took a long time for the cilia to come back to their initial position.

The pressure and flow generated by the cilia as a function of cilia spacing and channel height were studied in chapter 4. The analysis was performed using two channel configurations that are of practical importance - an open-loop channel and a closed-loop channel. When the cilia spacing decreases, the resistance offered by the fluid decreases and this causes the fluid flow to increase. When the channel height was increased, the cilia create a Couette flow in the channel that leads to a linear increase in the flow with the channel height. When the cilia spacing is decreased for a given channel length, many cilia are present per unit length of the channel. Consequently, the pressure generated by the cilia increases. On the other hand, when the channel height is increased, the pressure generated drastically decreases. This chapter provides guidelines for the cilia spacing, length and channel height for optimal performance.

The effect of fluid inertia on the flow generated was studied in chapter 5. The fluid inertia has two effects; firstly, the momentum diffusion from the cilia into the channel is delayed and secondly, a part of the energy input to the fluid during the effective stroke is retained after the effective stroke has completed. These effects enrich the fluid-structure interaction of the artificial cilia. The artificial cilia also possess a temporal asymmetry by performing a slow effective stroke and a quick recovery stroke. When the inertial forces are larger than the viscous forces, the flow created is unidirectional and larger than that of the Stokes regime. Interestingly, for certain sets of parameters, due to the temporal asymmetry and large inertia forces, the fluid transported can be in the direction of the recovery stroke. Moreover, we found that the direction of the fluid flow can be changed by simply changing the operation frequency of the cilia.

As the flow created by the artificial cilia depends on the fluid inertia, spatial, temporal and orientational asymmetry, we used a model problem to probe the effect of each of these parameters individually in chapter 6. It was found that, irrespective of the Reynolds number, the fluid flow scales linearly with the swept area. At high Reynolds numbers the fluid transported is unidirectional and larger than that of the Stokes limit, which can be further enhanced by a fast effective stroke. At high Reynolds numbers the orientational asymmetry is sufficient to cause a fluid transport. The effects of the three symmetries were generalised into a definition of configurational symmetry, whose absence might create a flow in microchannels.

In chapter 7, we investigated the effect of the out-of-phase motion of the cilia on the fluid flow using two approaches: by externally prescribing a phase difference between adjacent cilia and by applying a non-uniform magnetic field. In the former case the area swept by the cilia remains nearly the same for all phase differences. In the latter case the cilia sweep a larger area when the applied magnetic field travels in the direction opposite to the effective stroke (antiplectic metachrony) compared to the situation when the magnetic field and the effective stroke are in the same direction (symplectic metachrony). The out-of-phase motion of the cilia results in a pressure distribution in the channel that causes a local vortex formation during the recovery stroke, resulting in a zero negative flow. This leads to an unidirectional flow with a subsequent increase in the net fluid transported. When the area swept remains constant, the cilia create a larger flow which is unidirectional and independent of the phase difference for large cilia spacings. However, for small cilia spacings, they create a larger flow for antiplectic metachrony compared to symplectic metachrony.

The fluid transport due to the out-of-phase motion of symmetrically beating cilia was studied in chapter 8. The out-of-phase beating of cilia leads to a collective non-reciprocal motion, which leads to a net pressure gradient in the direction of the wave and a fluid flow in the opposite direction. The fluid flow is created mainly due to the unidirectional displacement of fluid particles near the cilia, leading to a net flow that is also unidirectional. The flow was found to be maximum when the wavelength of the applied magnetic field is four times the cilia length.

To analyse the effect of the cilia width and out-of-plane motion of the cilia, a three-dimensional numerical method was developed in chapter 9. The cilia are modelled using shell elements and the fluid using boundary elements, while the magnetic field was calculated using the magneto-static boundary conditions. Using this model we verified that an asymmetric motion of the cilia can also be generated using a tapering in the width. The width of the cilia and their spacing in the width direction were investigated for the maximum flow condition. We found that per unit width of the channel and for a given tapering, many narrow cilia spaced close together create a larger flow compared to a few broad cilia. In chapter 7, we analysed the flow caused by cilia that were beating out-of-phase in the beat plane. The three-dimensional model allowed us to study the out-of-phase beating perpendicular to the beat plane. We found that such a motion causes a flow normal to the beat plane which is of comparable magnitude as the flow in the plane of beat. This suggests a way to simultaneously mix and propel fluids in microchannels.

The cilia-based fluid manipulation systems in the recent past are summarised in table 10.1 with the aim of classifying the mechanisms that are responsible for the fluid transport. It can be seen that in the majority of the cases the actuation is performed through a magnetic field. The cilia that were able to successfully demonstrate a flow relied on (i) three-dimensional motion (items 2, 4, 5 and 10 in table 10.1) – mimicking the motion of nodal cilia – (ii) a combination of temporal and orientational asymmetry (item 1 in table 10.1), (iii) spatial asymmetry (items 7, 9 and 11 in table 10.1) and (iv) orientational asymmetry (items 5 and 12 in table 10.1). The orientational asymmetry was used in combination with inertial forces and non-reciprocal motion by Fahrni *et al.* (2009) and Alexeev *et al.* (2008*b*), respectively.

We would like to conclude by providing guidelines on the design of artificial ciliary systems based on the studies performed in this thesis. Let us start by assuming that the material properties of the cilia, the channel height and the fluid viscosity are known. The design parameters are assumed to be the geometry of the cilia (length, thickness and width), magnetic field, cilia spacing and frequency. As we want the cilia to operate under moderate pressure heads, we propose the length of the cilia to be half that of the channel height (chapter 4). From chapter 5, we find that for a given magnetic number, the cilia create large and unidirectional flows for $\mathrm{Re} > 1$ and $F_n < 1$. Using the first condition, we can find the frequency of operation. Using the second condition (on F_n), we can arrive at the ratio of the cilia length to thickness (the aspect ratio). Once we know the aspect ratio, we can find the magnetic field to be applied using the magnetic number.

Table 10.1: *Artificial cilia in microfluidics. E and T refer to experimental and theoretical work.*

No.	Reference	Force field	Length scale	Frequency	Asymmetry	E / T
1	den Toonder *et al.* (2008)	Electrostatic	100 μm	80 Hz	Temporal and orientational	E
2	Evans *et al.* (2007); Shields *et al.* (2010)	Magnetic	10 μm	35 Hz	3D motion	E
3	Oh *et al.* (2009)	Base excitation	400 μm	100 Hz	None	E
4	Vilfan *et al.* (2010)	Magnetic	30 μm	1 Hz	3D motion	E, T
5	Fahrni *et al.* (2009)	Magnetic	300 μm	50 Hz	Orientational and 3D motion	E
6	van Oosten *et al.* (2009)	Photo actuation	10 mm	0.04 Hz	Spatial	E
7	Belardi *et al.* (2011); Hussong *et al.* (2011*b*)	Magnetic	70 μm	20 Hz	Spatial	E
8	Timonen *et al.* (2010)	Magnetic	6 mm	Not reported	3D motion	E
9	Gauger *et al.* (2009)	Magnetic	-	-	Spatial	T
10	Downton & Stark (2009)	Magnetic	-	-	3D motion	T
11	Kim & Netz (2006)	External motors	-	-	Spatial	T
12	Alexeev *et al.* (2008*b*)	Point force	-	-	Orientational	T
13	Ghosh *et al.* (2010)	Point force	-	-	None	T

Appendices

A Solid dynamics model

The artificial cilia are modelled as a discrete assemblage of Euler-Bernoulli beam elements. The beam element has two nodes at the ends and has three degree of freedom (DOF) at each node: u the axial displacement, v the transverse displacement and $\phi = \partial v/\partial x$ the rotation, where x is the axial coordinate along the beam. The axial displacement along the beam (or film) is interpolated linearly and the transverse displacement is interpolated cubically,

$$u = \boldsymbol{N_u p}, \qquad v = \boldsymbol{N_v p},$$

where $\boldsymbol{N_u}$ and $\boldsymbol{N_v}$ being the standard interpolation matrices (Cook *et al.*, 2001) and $\boldsymbol{p} = \{u_1\ v_1\ \phi_1 l_0\ u_2\ v_2\ \phi_2 l_0\}^T$, where the subscripts 1 and 2 refer to the node numbers and l_0 is some reference length. The nonlinear axial strain ϵ in the beam is

$$\epsilon = \frac{\partial u}{\partial x} + \frac{1}{2}\left(\frac{\partial v}{\partial x}\right)^2 - y\frac{\partial^2 v}{\partial x^2} \equiv \bar{\epsilon} - y\chi.$$

The principle of virtual work is used as a condition to establish equilibrium (Malvern, 1977): When a consistent virtual displacement field is applied on a body, the body will be in equilibrium when the virtual work done by the internal forces equals the virtual work done by the external force,

$$\delta W_{\text{int}}^{t+\Delta t} = \delta W_{\text{ext}}^{t+\Delta t},$$

with

$$\delta W_{\text{int}}^{t+\Delta t} = \int_{V_0} \left(\sigma\delta\epsilon + \rho(\ddot{u}\delta u + \ddot{v}\delta v)\right) dV,$$

where $\delta(\cdot)$ represents the variation of a quantity, σ is the axial stress, ρ is the density of the film and a $\ddot{(\cdot)}$ implies a second derivative w.r.t. time. By substituting the strains and defining $\int \sigma dA = P$ and $-\int \sigma y dA = M$ ($A = bh$ is the area of the cross section, h is the thickness and b is the out-of-plane width of the film), the internal virtual work at time $t + \Delta t$ can be written as the sum of an elastic and an inertial part

$$\delta W_{\text{int}}^{t+\Delta t} = \int_{x_0} \left(P^{t+\Delta t}\delta\bar{\epsilon}^{t+\Delta t} + M^{t+\Delta t}\delta\chi + \rho A(\ddot{u}^{t+\Delta t}\delta u + \ddot{v}^{t+\Delta t}\delta v)\right) dx.$$

We now expand the elastic part of the internal work linearly in time by substituting ($Q^{t+\Delta t} = Q^t + \Delta Q$) for the field parameters in the above equation which gives

$$\begin{aligned}\delta W_{\text{int}}^{t+\Delta t} \quad = \quad & \int_{x_0} \left[\left(P^t\delta\bar{\epsilon}^t + M^t\delta\chi\right) + \left(\Delta P\delta\bar{\epsilon}^t + \Delta M\delta\chi\right)\right. \\ & \left. + P^t\Delta\delta\bar{\epsilon} + \rho A(\ddot{u}^{t+\Delta t}\delta u + \ddot{v}^{t+\Delta t}\delta v)\right] dx,\end{aligned}$$

in which terms of order higher than one are neglected. The following notations are introduced for convenience: $\partial u/\partial x = \boldsymbol{B_u p}$, $\partial v/\partial x = \boldsymbol{B_v p}$, $\partial^2 u/\partial x^2 = \boldsymbol{C_v p}$. The constitutive relations are $\Delta P = EA\Delta\bar{\epsilon}$, $\Delta M = EI\Delta\chi$, with $E = \bar{E}/(1-\nu^2)$ being the effective elastic modulus, ν being the Poisson's ratio and I being the second moment of area defined as $I = bh^3/12$. By choosing the domain of integration to be the current

configuration (i.e. using an updated Lagrangian framework), the total displacements are zero, $\boldsymbol{p} = 0$ and we get

$$\delta W_{\text{int}}^{t+\Delta t} = \delta \boldsymbol{p}^T \boldsymbol{f}_{\text{int}}^t + \delta \boldsymbol{p}^T \boldsymbol{K} \Delta \boldsymbol{p} + \delta \boldsymbol{p}^T \boldsymbol{M} \ddot{\boldsymbol{p}}^{t+\Delta t}, \tag{1}$$

where

$$\boldsymbol{f}_{\text{int}}^t = \int \left[P^t \boldsymbol{B_u}^T + M^t \boldsymbol{C_v}^T \right] dx$$

is the nodal internal force vector,

$$\boldsymbol{K} = \int EA \boldsymbol{B_u}^T \boldsymbol{B_u} dx + \int EI \boldsymbol{C_v}^T \boldsymbol{C_v} dx + \int P^t \boldsymbol{B_v}^T \boldsymbol{B_v} dx$$

is the stiffness matrix, the first two terms of which represent the material stiffness and the third term represents the geometric stiffness, and

$$\boldsymbol{M} = \int \rho A (\boldsymbol{N_u}^T \boldsymbol{N_u} + \boldsymbol{N_v}^T \boldsymbol{N_v}) dx$$

is the mass matrix. The corresponding external virtual work is

$$\begin{aligned}
\delta W_{\text{ext}}^{t+\Delta t} &= \int \left(f_x^{t+\Delta t} \delta u + f_y^{t+\Delta t} \delta v + N_z^{t+\Delta t} \frac{\partial \delta v}{\partial x} \right) A dx + \int \left(t_x^{t+\Delta t} \delta u + t_y^{t+\Delta t} \delta v \right) b dx \\
&= \delta \boldsymbol{p}^T \int \Big[(f_x^{t+\Delta t} \boldsymbol{N_u}^T + f_y^{t+\Delta t} \boldsymbol{N_v}^T + N_z^{t+\Delta t} \boldsymbol{B_v}^T) A \\
&\quad + b \left(t_x^{t+\Delta t} \boldsymbol{N_u}^T + t_y^{t+\Delta t} \boldsymbol{N_v}^T \right) \Big] dx \\
&= \delta \boldsymbol{p}^T \boldsymbol{f}_{\text{ext}}^{t+\Delta t},
\end{aligned} \tag{2}$$

where f_x and f_y are the body forces in axial and transverse directions (for example, magnetic body forces), N_z is the body couple in the out-of-plane direction (for example, magnetic body couple) and t_x and t_y are the surface tractions (for example, fluid drag). By equating the internal and external virtual work and noting that the resulting equation holds for arbitrary $\delta \boldsymbol{p}$ we get

$$\boldsymbol{K} \Delta \boldsymbol{p} + \boldsymbol{M} \ddot{\boldsymbol{p}}^{\text{t}+\Delta \text{t}} = \boldsymbol{f}_{\text{ext}}^{\text{t}+\Delta \text{t}} - \boldsymbol{f}_{\text{int}}^{\text{t}}. \tag{3}$$

The motion of the film with time is obtained by solving Eqn. 3 using Newmark's algorithm with appropriate initial and boundary conditions.

B Discretisation of various terms used in section 2.2

$$\begin{aligned}
\int_V \sigma_{ij} \delta D_{ij} dV &= \int_V \left(-p \delta_{ij} + 2\mu D_{ij} \right) \delta D_{ij} \\
&= \int_V \left(-p \delta_{ij} + \mu \left(\frac{\partial u_i}{\partial x_j} + \frac{\partial u_j}{\partial x_i} \right) \right) \frac{\partial \delta u_i}{\partial x_j} dV, \\
&= \mu \int_V \delta U_I \frac{\partial \phi_{Ii}}{\partial x_j} \left(\frac{\partial \phi_{Jj}}{\partial x_j} + \frac{\partial \phi_{Jj}}{\partial x_i} \right) U_J dV - \int_V \delta U_I \frac{\partial \phi_{Ii}}{\partial x_j} \psi_J P_J dV, \\
&= \mu \delta U_I \int_V \frac{\partial \phi_{Ii}}{\partial x_j} \left(\frac{\partial \phi_{Ji}}{\partial x_j} + \frac{\partial \phi_{Jj}}{\partial x_i} \right) dV U_J - \delta U_I \int_V \frac{\phi_{Ii}}{\partial x_j} \psi_J dV P_J, \\
&= \delta U_I^T \left(K_{IJ}^{UU} U_J + K_{IJ}^{UP} P_J \right) = \delta \boldsymbol{U}^T \left(\boldsymbol{K^{UU}} \boldsymbol{U} + \boldsymbol{K^{UP}} \boldsymbol{P} \right).
\end{aligned}$$

$$
\begin{aligned}
\int_V \frac{du_i^{t+\Delta t}}{dt}\delta u_i dV &= \rho\int_V \delta u_i\left(\frac{\partial u_i^{t+\Delta t}}{\partial t}+\frac{\partial u_i^{t+\Delta t}}{\partial x_j}u_j^{t+\Delta t}\right)dV\\
&= \rho\int_V \delta u_i\left(\frac{u_i^{t+\Delta t}-u_i^t}{\Delta t}+\frac{\partial(u_i^t+\Delta u_i)}{\partial x_j}(u_j^t+\Delta u_j)\right)dV\\
&= \rho\int_V \delta u_i\left(\frac{u_i^{t+\Delta t}-u_i^t}{\Delta t}+\frac{\partial u_i^t}{\partial x_j}\Delta u_j+\frac{\partial u_i^t}{\partial x_j}u_j^t+\frac{\partial \Delta u_i}{\partial x_j}u_j^t\right)dV\\
&= \rho\int_V \delta u_i\left(\frac{u_i^{t+\Delta t}-u_i^t}{\Delta t}-\frac{\partial u_i^t}{\partial x_j}u_j^t+\frac{\partial u_i^t}{\partial x_j}u_j^{t+\Delta t}+\frac{\partial u_i^{t+\Delta t}}{\partial x_j}u_j^t\right)dV\\
&= \rho\int_V \delta u_i\left(\frac{u_i^{t+\Delta t}}{\Delta t}-\frac{u_i^t}{\Delta t}-\frac{\partial u_i^t}{\partial x_j}u_j^t+\frac{\partial u_i^t}{\partial x_j}u_j^{t+\Delta t}+\frac{\partial u_i^{t+\Delta t}}{\partial x_j}u_j^t\right)dV\\
&= \rho\int_V \delta U_I\phi_{Ii}\left(U_J^{t+\Delta t}\frac{\phi_{Ji}}{\Delta t}-\left(\frac{u_i^t}{\Delta t}+\frac{\partial u_i^t}{\partial x_j}u_j^t\right)+\frac{\partial u_i^t}{\partial x_j}\phi_{Jj}U_J^{t+\Delta t}+\right.\\
&\quad \left.\frac{\partial \phi_{Ji}}{\partial x_j}U_J^{t+\Delta t}u_j^t\right)dV\\
&= \rho\delta U_I\int_V\frac{1}{\Delta t}\phi_{Ii}\phi_{Ji}dVU_J^{t+\Delta t}+\rho\delta U_I\int_V\frac{\partial u_i^t}{\partial x_j}\phi_{Ii}\phi_{Jj}dVU_J^{t+\Delta t}\\
&\quad +\rho\delta U_I\int_V u_j^t\phi_{Ii}\frac{\partial\phi_{Ji}}{\partial x_j}dVU_J^{t+\Delta t}-\rho\delta U_I\int_V\phi_{Ii}\left(\frac{u_i^t}{\Delta t}+\frac{\partial u_i^t}{\partial x_j}u_j^t\right)dV\\
&= \delta U_I\hat{M}_{IJ}U_J^{t+\Delta t}+\delta U_I K^1_{IJ}U_J^{t+\Delta t}+\delta U_I K^2_{IJ}U_J^{t+\Delta t}-\delta U_I F_I\\
&= \delta\boldsymbol{U}^T\hat{\boldsymbol{M}}\boldsymbol{U}^{t+\Delta t}+\delta\boldsymbol{U}^T\boldsymbol{K}^1\boldsymbol{U}^{t+\Delta t}+\delta\boldsymbol{U}^T\boldsymbol{K}^2\boldsymbol{U}^{t+\Delta t}-\delta\boldsymbol{U}^T\boldsymbol{F},\\
&= \delta\boldsymbol{U}^T\hat{\boldsymbol{M}}\boldsymbol{U}+\delta\boldsymbol{U}^T\boldsymbol{K}^1\boldsymbol{U}+\delta\boldsymbol{U}^T\boldsymbol{K}^2\boldsymbol{U}-\delta\boldsymbol{U}^T\boldsymbol{F}.
\end{aligned}
$$

$$
\begin{aligned}
\delta(\lambda_i^J(u_i^{Jf}-\dot{p}_i^J)) &= \lambda_i^J\delta u_i^J+\delta\lambda_i^J(u_i^J-\dot{p}_i^J)\\
&= \lambda_i^J\phi_{Ii}^J\delta U_I+\delta\lambda_i^J(\phi_{Ii}^JU_I-\dot{p}_i^J)\\
&= \delta\boldsymbol{U}^T\boldsymbol{\phi}^J\boldsymbol{\lambda}^J+\delta\boldsymbol{\lambda}^{JT}(\boldsymbol{\phi}^{\boldsymbol{JT}}\boldsymbol{U}-\boldsymbol{A}^J\dot{\boldsymbol{p}}^J).
\end{aligned}
$$

C Magnetic field caused by a magnetic segment

The magnetic field caused by a rectangular magnetic segment is,

$$
\begin{aligned}
\hat{H}_x = & \frac{\hat{M}_x}{2\pi}\left(-\tan^{-1}\left[\frac{-\frac{h}{2}-\hat{y}}{-\frac{l}{2}+\hat{x}}\right]+\tan^{-1}\left[\frac{\frac{h}{2}-\hat{y}}{-\frac{l}{2}+\hat{x}}\right]\right) \\
& -\frac{\hat{M}_x}{2\pi}\left(-\tan^{-1}\left[\frac{-\frac{h}{2}-\hat{y}}{\frac{l}{2}+\hat{x}}\right]+\tan^{-1}\left[\frac{\frac{h}{2}-\hat{y}}{\frac{l}{2}+\hat{x}}\right]\right) \\
& +\frac{\hat{M}_y}{2\pi}\left(\frac{1}{2}\ln\left[\left(-\frac{l}{2}-\hat{x}\right)^2+\left(-\frac{h}{2}+\hat{y}\right)^2\right]-\frac{1}{2}\ln\left[\left(\frac{l}{2}-\hat{x}\right)^2+\left(-\frac{h}{2}+\hat{y}\right)^2\right]\right) \\
& -\frac{\hat{M}_y}{2\pi}\left(\frac{1}{2}\ln\left[\left(-\frac{l}{2}-\hat{x}\right)^2+\left(\frac{h}{2}+\hat{y}\right)^2\right]-\frac{1}{2}\ln\left[\left(\frac{l}{2}-\hat{x}\right)^2+\left(\frac{h}{2}+\hat{y}\right)^2\right]\right), \\
\hat{H}_y = & \frac{\hat{M}_y}{2\pi}\left(-\tan^{-1}\left[\frac{-\frac{l}{2}-\hat{x}}{-\frac{h}{2}+\hat{y}}\right]+\tan^{-1}\left[\frac{\frac{l}{2}-\hat{x}}{-\frac{h}{2}+\hat{y}}\right]\right) \\
& -\frac{\hat{M}_y}{2\pi}\left(-\tan^{-1}\left[\frac{-\frac{l}{2}-\hat{x}}{\frac{h}{2}+\hat{y}}\right]+\tan^{-1}\left[\frac{\frac{l}{2}-\hat{x}}{\frac{h}{2}+y}\right]\right) \\
& +\frac{\hat{M}_x}{2\pi}\left(\frac{1}{2}\ln\left[\left(-\frac{l}{2}+\hat{x}\right)^2+\left(-\frac{h}{2}-\hat{y}\right)^2\right]-\frac{1}{2}\ln\left[\left(-\frac{l}{2}+\hat{x}\right)^2+\left(\frac{h}{2}-\hat{y}\right)^2\right]\right) \\
& +\frac{-\hat{M}_x}{2\pi}\left(\frac{1}{2}\ln\left[\left(\frac{l}{2}+\hat{x}\right)^2+\left(-\frac{h}{2}-\hat{y}\right)^2\right]-\frac{1}{2}\ln\left[\left(\frac{l}{2}+\hat{x}\right)^2+\left(\frac{h}{2}-\hat{y}\right)^2\right]\right),
\end{aligned}
$$

where $\hat{M}_x$, $\hat{M}_y$ are magnetizations in the tangential (or length) and normal (or thickness) directions, h is the thickness and l is the length of the segment. Here, $\hat{x}$ and $\hat{y}$ are the local coordinates having their origin in the centre of the segment.

D Validation of the magneto-static model

In this appendix we validate the magneto-static model used in section 2.2.4 based on a super-paramagnetic film whose magnetic properties are anisotropic. The length of the film is 100 μm and its thickness is 2 μm. The film has a susceptibility of 4.6 and 0.8 in the tangential and normal direction, respectively. Six configurations of the film are chosen to validate the magneto-static model, see Fig. 1. The configurations chosen reflect the deformed geometry of the film during one cycle of ciliary motion (Khaderi *et al.*, 2009). The solution for the magnetic flux density $\boldsymbol{B}$ is compared with the solution from a commercial multiphysics software program (COMSOL). The field values are normalised with the absolute value of the applied field. The comparison is shown only for positions 2, 4 and 6 in Figs. 2. The solid lines represent the solution from our magneto-static model and the '+' symbols represent the solution from COMSOL. The agreement is excellent.

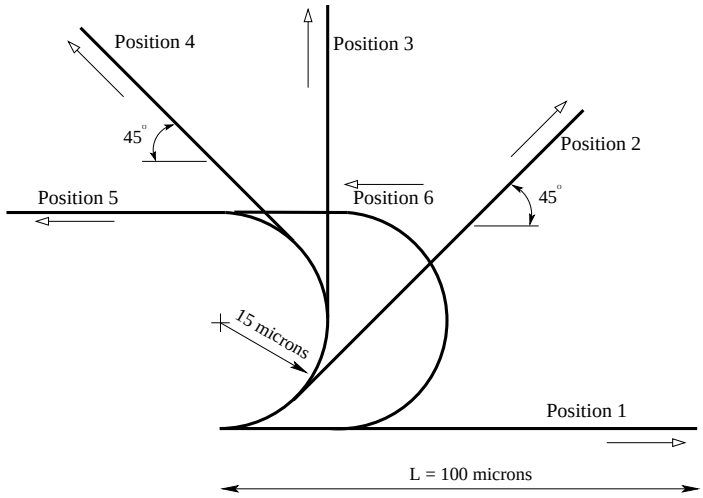

Figure 1: *Positions of film used to test the magneto-static model. The hollow arrows show the direction of applied field for the respective positions.*

E Validation of the fluid-structure interaction model

To compare the performance of the present approach with a solution available in the literature we choose to study the deformation behaviour of a cantilever beam under an imposed pulsating flow. This problem has been numerically solved by (Baaijens, 2001) using the fictitious domain method in which the solid was discretised using continuum finite elements. The width W is four times the height H of the fluid domain. H is taken to be unity. The length of the film is $0.8H$. The thickness of the film is $0.0212H$. The elastic modulus of the film and viscosity of the fluid were specified in dimensionless units to be $E = 10^7$ and $\mu = 10$, respectively. The mesh used for the computation is shown in Fig. 3. The dots represent the nodes of the Euler-Bernoulli beam element. The boundary conditions are as follows: the left and right boundaries are periodic. A pulsating flow of magnitude $10\sin(2\pi t/T)$ is prescribed on the left boundary, where T is the time period which is taken to be sufficiently large to avoid inertia effects in the film. The bottom boundary is a no slip boundary. On the top boundary, the normal flow is constrained. The solution from our formulation is plotted along with the solution from (Baaijens, 2001) in Fig. 4(a) in terms of the displacement of the free end of the cantilever. It can been seen that the two solutions are in good agreement. In Fig. 4(b), we plot the x displacement of the free end of the beam as a function of time for different discretisations of the solid beam (using 12, 24 and 48 beam elements). It can be seen that the displacements nicely converge as the mesh is refined.

F Convergence of the numerical model

We now report on the spatial and temporal convergence of the two-dimensional numerical method used in this thesis in the limit of low Reynolds numbers. We study the case of an array of straight, magnetically anisotropic super-paramagnetic cilia (having susceptibilities 4.6 and 0.8 in the tangential and normal directions, respectively (van

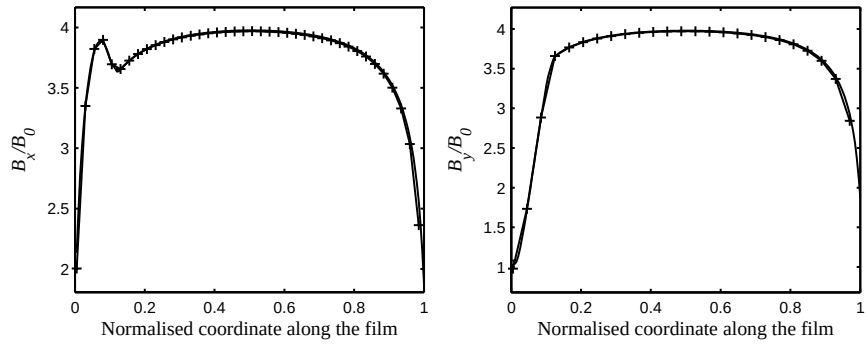

(a) Flux density comparison at position 2.

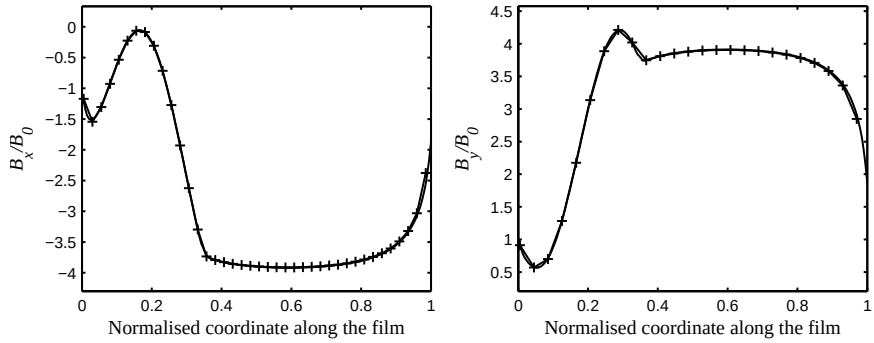

(b) Flux density comparison at position 4.

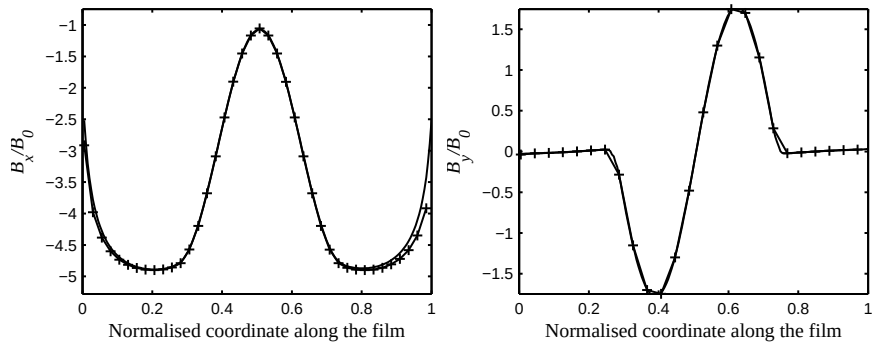

(c) Flux density comparison at position 6.

Figure 2: *Flux density comparison; the symbols represent the solution from COMSOL and lines represent the field calculated from the present model*

Rijsewijk, 2006)). A uniform rotating magnetic field with a frequency of 50 Hz and magnitude $B_0 = 31.5$ mT is applied. Each cilium has a length $L = 100$ μm, with the thickness varying linearly along its length, having $h = 2$ μm at the left (attached) end and $h = 1$ μm at the right end. The fluid has a viscosity $\mu = 1$ mPas. The elastic modulus is taken as 1 MPa and the density $\rho = 1600$ kg/m^3. The inter-cilia spacing is

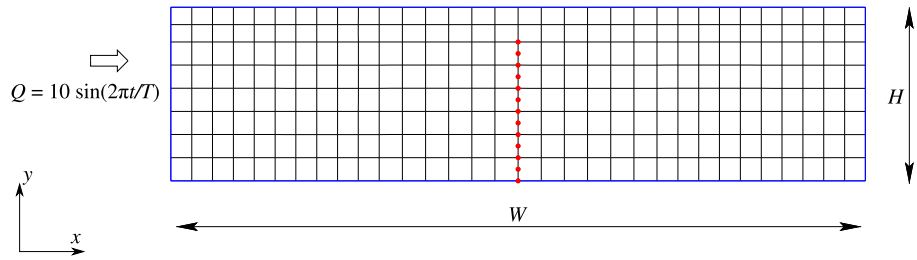

Figure 3: *Coarsest mesh used for benchmarking.*

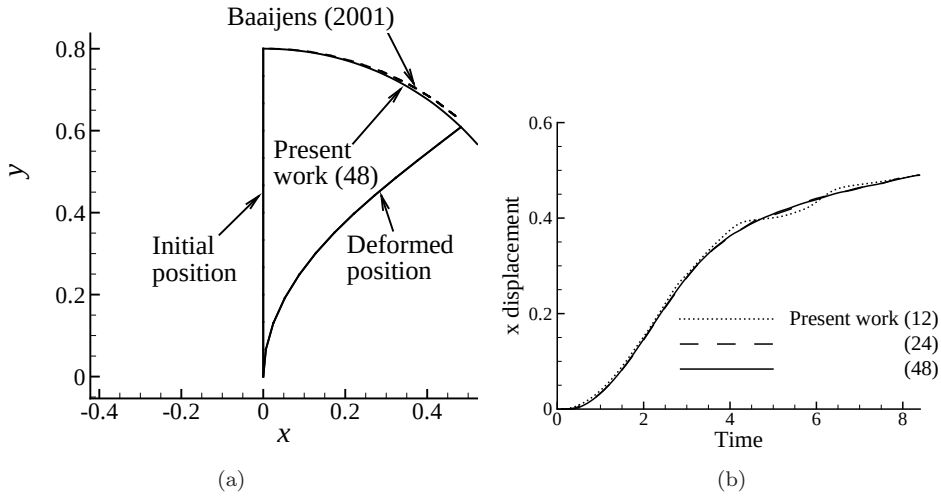

Figure 4: *A cantilever subjected to a pulsating flow: Comparison of solution obtained from the present work with (Baaijens, 2001). (a) Comparison of the displacement of the free end and (b) comparison of the displacement of the free end as a function of time for various mesh refinements. The number in parenthesis of the legend refer to the number of elements used to discretise the cantilever.*

$a = 1.67L$ and the channel height $H = 2L$. A unit-cell consisting of one cilium is chosen for the simulations. As the deformed shape of the cilium is an outcome of the model, we compare the position of the free end for different temporal discretisations. The mesh used to discretise the cilium and the fluid domain is shown in Fig. 7.3 for the case when the cilium is divided into 40 elements and the fluid is divided into 28×30 elements. The number of elements on the cilium as well as the fluid are changed proportionally when the mesh is changed. In the following the spatial discretisation is defined in terms of the number of elements used to discretise the cilium.

The position of the tip of the cilium as a function of time and its trajectory for different time increments is shown in Fig. 5 (a)-(c). The time increment has to be small enough to capture the fast whip-like recovery stroke. It can be seen that a time increment of 1 μs is sufficient for temporal convergence. This time step of 1 μs is used to study the spatial convergence and the results are shown in Fig. 6. It can be seen that the results for these discretisations have fully converged as shown for the position of the free end of

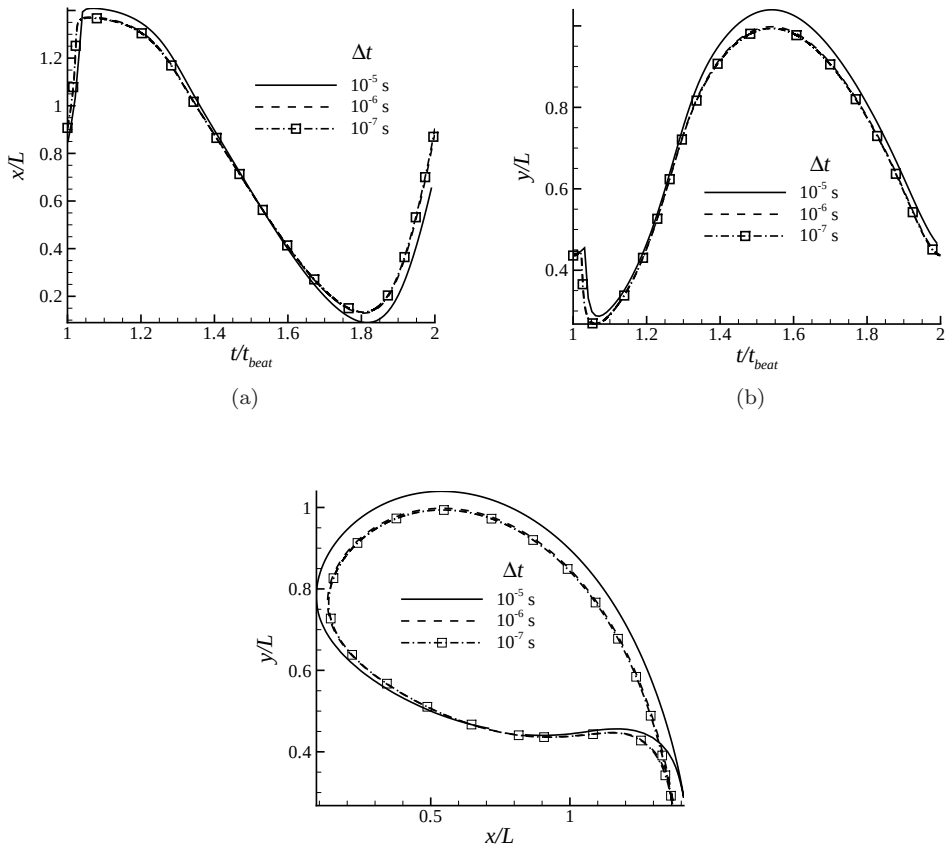

Figure 5: *(a)-(b) Temporal convergence: Position of the tip of the cilium as a function of time for different time increments Δt. (c) The trajectory of the free end of the cilium for different time increments. The cilium is divided into 40 elements.*

the cilium and the flux as a function of time.

G Effect of diffusion Reynolds number - analytical model

We now study the effect of the diffusion Reynolds number $\mathrm{Re_H}$ on the fluid propelled. To this end we analyse the case when the height of the channel is much larger than the cilia length. This allows us to assume that the cilia create an oscillating Couette flow (shear flow), such that the velocity at the bottom boundary of the channel ($f(t)$) has an oscillating component (u_0) and a steady component (u_{mean})

$$f(t) = u_0 \sin \omega t + u_{\mathrm{mean}}(1 - e^{-t/t_{\mathrm{ref}}}), \tag{4}$$

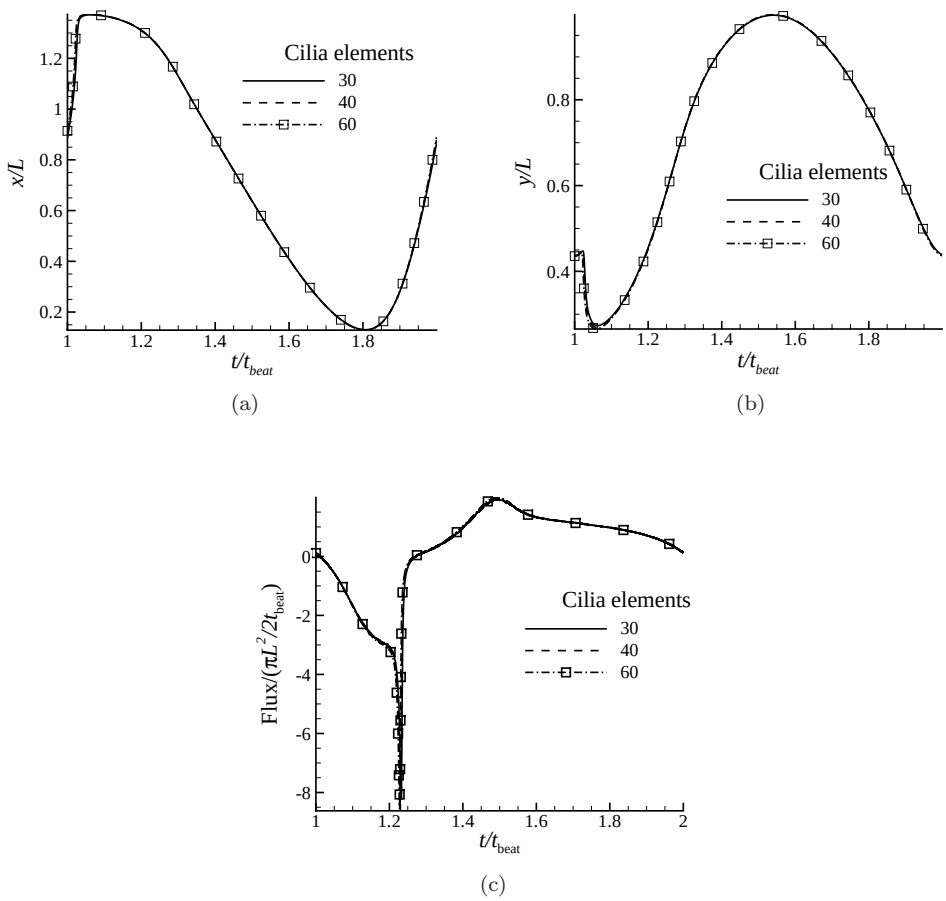

Figure 6: *(a)-(b) Position of the tip of the cilium as a function of the time for different spatial discretisations. (c) Flux as a function of time for different spatial discretisations.*

where $\omega = 2\pi/t_{\text{ref}}$ is the angular frequency. A similar approach was taken by Blake *et al.* (1982) to model the cilia induced flows in ducts in the limit of low Reynolds numbers. The solution to the problem of oscillating shear flow can be obtained by solving the one-dimensional Navier-Stokes equation. The one-dimensional Navier-Stokes equation is (in a shear flow the pressure is an arbitrary constant, hence vanishes):

$$\rho \frac{\partial u}{\partial t} = \mu \frac{\partial^2 u}{\partial y^2}, \tag{5}$$

where $u = u(y,t)$ is the fluid velocity. The initial and boundary conditions for the Couette flow are:

$$\begin{aligned} u(0,t) &= f(t), \\ u(H,t) &= 0, \\ u(y,0) &= 0. \end{aligned} \tag{6}$$

The solution to the one-dimensional Navier-Stokes equation is given by (Polyanin, 2001):

$$u(y,t) = \frac{\mu}{\rho}\int_0^t f(\tau)H(y,t-\tau)d\tau, \tag{7}$$

where,

$$H(y,t) = \left[\frac{\partial}{\partial\xi}G(y,\xi,t)\right]_{\xi=0}, \tag{8}$$

and

$$G(y,\xi,t) = \frac{2}{H}\sum_{n=1}^{\infty}\sin\left(\frac{n\pi y}{H}\right)\sin\left(\frac{n\pi\xi}{H}\right)\exp\left(-\frac{\mu n^2\pi^2 t}{\rho H^2}\right). \tag{9}$$

By using Eqns. 9 and 8, Eqn. 7 can be written as

$$u(y,t) = \sum_{n=1}^{\infty} 2n\pi\frac{\mu}{\rho H^2}\int_0^t f(\tau)\sin\left(\frac{n\pi y}{H}\right)\exp\left(-\frac{\mu}{\rho H^2}n^2\pi^2(t-\tau)\right)d\tau. \tag{10}$$

The ratio $\rho H^2/\mu$ is a characteristic timescale of the system. We now normalise the time in the above equation with t_{ref} to get:

$$u(y,t) = \sum_{n=1}^{\infty} 2n\pi\frac{\mu t_{\text{ref}}}{\rho H^2}\int_0^t f(\tau)\sin\left(\frac{n\pi y}{H}\right)\exp\left(-\frac{\mu t_{\text{ref}}}{\rho H^2}\frac{n^2\pi^2(t-\tau)}{t_{\text{ref}}}\right)\frac{d\tau}{t_{\text{ref}}}. \tag{11}$$

Equation 11 shows that the velocity of the fluid at any time and location depends on the dimensionless parameter $\text{Re}_{\text{H}} = \rho H^2/\mu t_{\text{ref}}$. The velocity $u(y,t)$ has transient behaviour due to two reasons: namely, the inertia of the fluid and the transient part of the boundary velocity associated with u_{mean}. The inertial transience is represented by the exponential term in Eqn. 11, whose duration scales with $\rho H^2/\mu$. The transient period due to the boundary condition is represented by the exponential term in Eqn. 4, and its duration is 10 t_{ref}. As the boundary velocity is oscillatory, the steady state will also be oscillatory in nature. The instantaneous flux $Q(t)$ at any time t is $Q(t) = \int_0^H u(y)dy$, and the fluid transported is $\bar{Q} = \int_{\text{cycle}} Q(t)dt/t_{\text{ref}}$.

The instantaneous flux (normalised with H) is plotted as a function of time (normalised with the characteristic timescale $\rho H^2/\mu$), for finite Re_{H} in Fig. 7(a). It can be seen that the instantaneous flux ($Q(t)$) reaches the steady state when $t = \rho H^2/\mu$. Similarly, the fluid transported (see the inset of Fig. 7(a)) reaches a saturation in Re_{H} cycles.[1] Interestingly, the flow transported is the same for systems with different Re_{H}. This is unexpected; intuitively one might presume that as Re_{H} is increased only the fluid around the bottom boundary will be displaced, while the rest of the fluid will remain undisturbed. However, this is the case only during the transient period. Figure 7(b) shows the velocity as a function of y/H at different time instances. Initially, fluid near the bottom boundary is moving, while the rest of the fluid is stationary, see the solid line in Fig. 7(b). As time progresses, the momentum is transferred to the rest of the fluid, and during the steady state, the fluid throughout the channel is in motion, see the dashed line in Fig. 7(b). While the fluid transported is independent of Re_{H}, the duration of the transient period scales with Re_{H}. The fluid transported averaged over a cycle,

[1] For small Re_{H}, the time taken to reach the steady state is $10t_{\text{ref}}$. This is the time taken for the exponential term in Eqn. 4 to vanish.

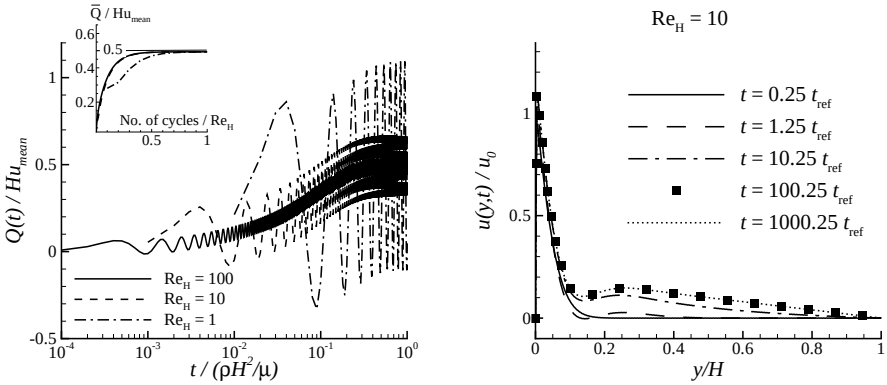

Figure 7: *(a) Instantaneous flux through the channel as a function of the time. The inset shows the flow rate averaged over each cycle as a function of the No. of cycles. (b) Instantaneous velocity as a function of y/H for different instances of time ($n = 420$ and $Re_H = 10$).*

after the system has reached a steady state, can be calculated analytically and is given by

$$2H\frac{u_{\text{mean}}}{\pi^2}\sum_{n=1}^{\infty}\frac{1}{n^2}-\frac{\cos n\pi}{n^2}=2H\frac{u_{\text{mean}}}{\pi^2}\left(\frac{\pi^2}{6}-\frac{-\pi^2}{12}\right)=\frac{Hu_{\text{mean}}}{2}.$$

The mean flow rate depends only on u_{mean} and scales linearly with the height of the channel, but is independent of Re_H.

H Resistive force theory

The drag forces of the fluid on the film can be accounted for in an uncoupled manner using drag forces. The tractions in section 3.2.6 are assumed to be proportional to the velocity in the low Reynolds number regime,

$$t_x = -C_x v_x, \quad t_y = -C_y v_y, \tag{12}$$

where t_x and t_y is the traction exerted by the fluid in the axial and transverse direction to the film, C_x and C_y are the axial and transverse drag coefficients and v_x and v_y are the respective axial and transverse velocities. This assumption is in the spirit of the resistive force theory (Johnson & Brokaw, 1979). For the finite element discretisation, the drag force is assumed to vary linearly along the film. Analytical expressions for the drag coefficients are available only for simple rigid geometries, but as the film is modelled as a deforming slender object such analytical expressions are not available. Hence, we calibrate these drag coefficients with reference to the coupled solid-fluid model.

The calibration is done as follows. First, a simulation using the coupled solid-fluid code is performed and the trajectory of the free end is recorded. Then, simulations are performed using the solid dynamic model with velocity-proportional drag forces using assumed drag coefficients. The trajectory thus obtained is matched with the trajectory obtained from the coupled solid-fluid code by varying the drag coefficients. The calibrated drag coefficients, when the fluid viscosity is 1 mPas, are $C_x = 8.75$ Ns/m^3 and

$C_y = 105$ Ns/m^3 for the PM film and $C_x = 80$ Ns/m^3 and $C_y = 160$ Ns/m^3 for the SPM film. A comparison between the coupled solid-fluid model and the uncoupled solid-drag model is shown in Figs. 8(a) and 8(b), showing good agreement, especially for the SPM configuration. The discrepency between the two trajectories comes from the fact that the resistive force theory does not account for the interaction of the film with the substrate and with itself.

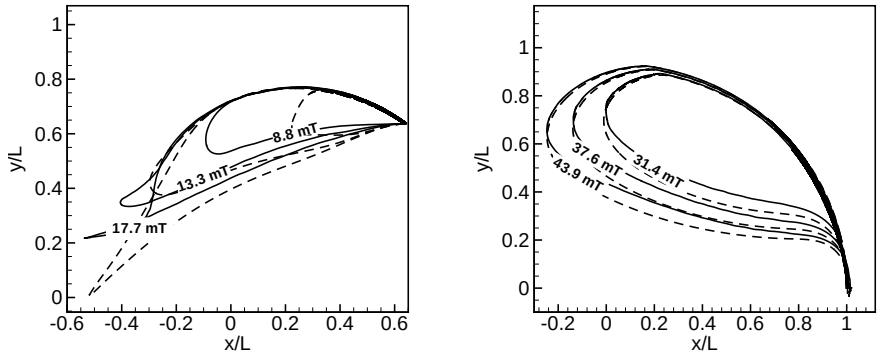

(a) (b)

Figure 8: *The trajectory of the free end for the PM configuration (a) and the SPM configuration (b) for three different values of the applied magnetic field. The solid lines are for the coupled solid-fluid simulations and the dashed lines for the uncoupled solid-drag calculations.*

I Magnetic buckling analysis

We now study the buckling behaviour of a straight permanently magnetic film. When the applied field B_0 is opposite to the magnetization M and the film is straight, no couple is induced for the motion of the film (see the inset of Fig. 9). However, if the film is slightly perturbed, a magnetic couple will act on the film, which will increase when the film is deflected further from the initial, straight configuration. Clearly, the straight configuration is an unstable equilibrium state, so that buckling will occur above a critical value of the magnetic field. This situation is similar to a cantilever with a compressive end load. The total moment of the body couple on an infinitesimal element of length dx at x (see the inset of Fig. 9) is

$$dN = MAB_0 \sin\theta dx, \tag{13}$$

where θ is the angle between the beam axis and the horizontal and A is the cross-sectional area of the film. The bending moment at x (assuming small deformations) is (Gere & Timoshenko, 1984)

$$\begin{aligned} M_B(x) &= -\int_x^L dN_x dx = -\int_x^L MAB_0 \sin\theta dx = -\int_x^L MAB_0 \frac{dv}{dx} dx \\ &= -MAB_0 \left(v(L) - v(x)\right). \end{aligned}$$

The equilibrium equation of the beam is

$$\begin{aligned} EI\frac{d^2v(x)}{dx^2} &= MAB_0(v(L)-v(x)) \\ \frac{d^2v(x)}{dx^2} &= k^2(v(L)-v(x)), \end{aligned} \tag{14}$$

where $k^2 = \frac{MAB_0}{EI}$ and EI is the bending stiffness of the beam. The non-trivial solution of the equilibrium equation gives the critical magnetic field:

$$B_{\text{critical}} = \frac{EIn^2\pi^2}{4AML^2}, \quad n = 1, 3, 5, \ldots. \tag{15}$$

By choosing $n = 1$ we get the lowest magnetic field needed to cause the buckling of the film. The tip displacement of the film with varying field is shown in Fig. 9. When the applied field is more than the critical field, the film undergoes enormous deformations due to magnetic buckling. Note that this kind of behaviour cannot be observed in a super-paramagnetic film.

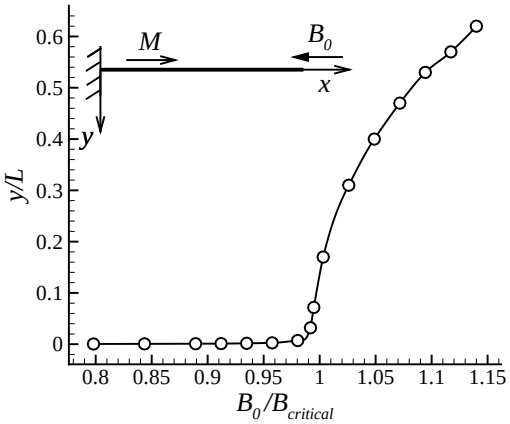

Figure 9: *Position of the free end as a function of the applied field.*

J Metachronal wave velocity

The metachronal wave velocity is obtained by dividing the distance between two cilia with the time it takes for the magnetic couple to travel from a cilium to its neighbour. If the neighbour is to the right, then the wave travels to the right, and when the neighbour is to the left, the wave travels to the left. The magnetic couple N_i at any cilium i is proportional to $\sin(2\omega t - 2\phi_i)$, and travels with a phase velocity of $\omega/\Delta\phi$ (in number of cilia per second) to the right.

In the schematic of Fig. 10, three cilia C_1, C_2 and C_3 are depicted. At any given instance of time, let the magnitude of the magnetic couple at C_1, C_2 and C_3 be N_1, N_2 and N_3, respectively. The magnitude of the magnetic couple at the 'periodic' cilium H,

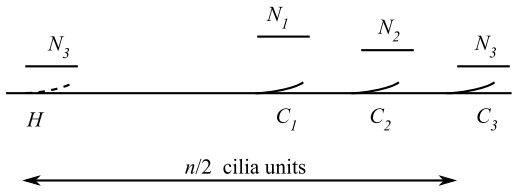

Figure 10: *Schematic diagram used to calculate the metachronal wave velocity.*

which is separated from C_3 by $n/2$ units, is also N_3. The metachronal wave is said to have traveled to the right when the magnetic field at C_2 is N_1 after a time interval. Now, the distance traveled by the magnetic couple is 1 cilia spacing, and the time taken to travel this distance is $1/(\omega/\Delta\phi)$. Therefore, the velocity of the magnetic couple is $\omega/\Delta\phi$, in cilia units per second. The metachronal wave is said to have traveled to the left when the magnetic field at C_2 is equal to N_3 after an interval of time. As the applied magnetic couple travels to the right, this situation is possible when the magnetic couple at the periodic cilium H travels to the cilium C_2. The time needed for the magnetic couple to travel from H to C_2 is equal to $(n/2-1)/(\omega/\Delta\phi)$. However, the apparent distance travelled is one cilium spacing to the left (i.e. from C_3 to C_2), so that the wave velocity is now $\omega/(\pi-\Delta\phi)$. The (apparent) metachronal wave velocity is now determined by the maximum of the two competing wave velocities: $\omega/\Delta\phi$ to the right and $\omega/(\pi-\Delta\phi)$ to the left. As a result, the metachronal wave velocity is equal to $\omega/\Delta\phi$ (i.e. to the right) when $\omega/\Delta\phi > \omega/(\pi-\Delta\phi)$ (i.e. $0<\Delta\phi<\pi/2$), and it is equal to $-\omega/(\pi-\Delta\phi)$ (i.e. to the left) when $\omega/\Delta\phi < \omega/(\pi-\Delta\phi)$ (i.e. $\pi/2<\Delta\phi<\pi$), see Fig. 7.2.

K Calculation of the net pressure gradient

In this appendix we derive an expression for the net pressure gradient in the channel due to the out-of-phase motion of cilia. For simplicity, we take the case where $0<a<\lambda$; i.e., the metachronal wave velocity and the applied wave velocity are the same (to the right). The position of the cilia is dictated by the magnetic field vector, while its velocity is dictated by the rate of change of the magnetic field vector. The current x position of the tip of a cilium is $x_0+\delta_0\sin(\omega t-2\pi x/\lambda)$ and its velocity is $\delta_0\omega\cos(\omega t-2\pi x/\lambda)$, where δ_0 is assumed to scale with the amplitude of the applied magnetic field in the x-direction B_{0x} and x_0 is the position of the cilia base. Figure 11 shows the current velocity (solid lines) and displacement (dashed lines) for $a/L=2/7$, with the wave travelling to the right. The pressure will be positive when two cilia come close and will be negative when they move apart, i.e., the positive and negative pressures will occur when the velocity gradient is negative and positive, respectively. At any time t, this happens at $t\lambda/T-\lambda/4$ (negative pressure), $t\lambda/T+\lambda/4$ (positive pressure) and $t\lambda/T+3\lambda/4$ (negative pressure). The position of cilia with its velocity at a particular time instance is shown in Fig. 11. It can be seen that two neighbouring cilia move apart in regions 1 and 3, thereby generating a negative pressure $-p$. In region 2, two neighbouring cilia come closer, this generates a positive pressure p. (we have assumed that the positive pressure is equal to the negative

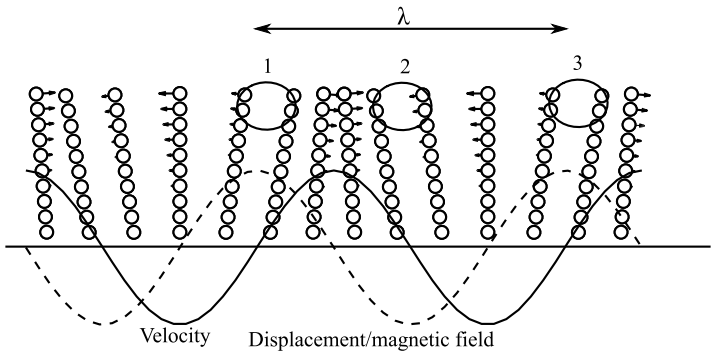

Figure 11: *Velocity (arrows and solid lines) and deformation (dashed line) of the cilia at any time instant, neglecting the inter-cilium interaction.*

pressure). At any time t, the position of region 1 is

$$x_1 = \frac{t}{T}\lambda - \frac{\lambda}{4} + \delta_0 \sin\left(\omega t - \frac{2\pi x}{\lambda}\left(\frac{t}{T}\lambda - \frac{\lambda}{4}\right)\right) = \frac{t}{T}\lambda - \frac{\lambda}{4} + \delta_0. \tag{16}$$

Similarly, the respective positions of the regions 2 and 3 are

$$x_2 = \frac{t}{T}\lambda + \frac{\lambda}{4} - \delta_0, \tag{17}$$

$$x_3 = \frac{t}{T}\lambda + 3\frac{\lambda}{4} + \delta_0. \tag{18}$$

The pressure gradient between regions 1 and 2 can be written to be proportional to

$$\frac{p - (-p)}{x_2 - x_1} = \frac{4p}{\lambda - 4\delta_0},$$

and the pressure gradient between the region 2 and 3 can be written to be proportional to

$$\frac{-p - (p)}{x_3 - x_2} = -\frac{4p}{\lambda + 4\delta_0}.$$

The average pressure gradient in the unit-cell is now given by,

$$16p\delta_0/(\lambda^2 - 16\delta_0^2).$$

By invoking that p scales with $\mu\delta_0\omega/\lambda$, it can be seen that the pressure gradient that drives the flow increases with an increase of the cilia deflection and with a decrease of the wavelength:

$$16\mu\delta_0^2\omega/\lambda(\lambda^2 - 16\delta_0^2).$$

Assuming small cilia deflection ($\lambda >> \delta_0$), we observe that the average pressure gradient scales with $(\mu\delta_0^2\omega/\lambda^3)$. Therefore, the pressure gradient is positive when the wave is moving in the positive x-direction; this creates a flow in the negative x-direction. Although the applicability of the expression for the pressure gradient is limited to large wavelengths and small cilia deflections, it explains all the trends observed in the simulations (the direction of flow, the increase in flow because of decreasing wavelength and increasing cilia deflection).

L Benchmark tests for the 3D model

Benchmark tests for the solid mechanics model

The three-dimensional numerical model is benchmarked using three reference problems: (1) Nonlinear deflection of a square clamped plate (Hughes & Liu, 1981), (2) deflection of a hinged cylindrical roof (Jog & Kelkar, 2006), and (3) pinching of an open-ended cylinder (Masud *et al.*, 2000). All the problems analysed possess a significant amount of non-linearity. The tests have been performed with a fixed load increment. Symmetries present in the problems have been used to reduce the time for computations. The results plotted in Fig. 12 show that the shell element formulation is in good agreement with the results available in the literature.

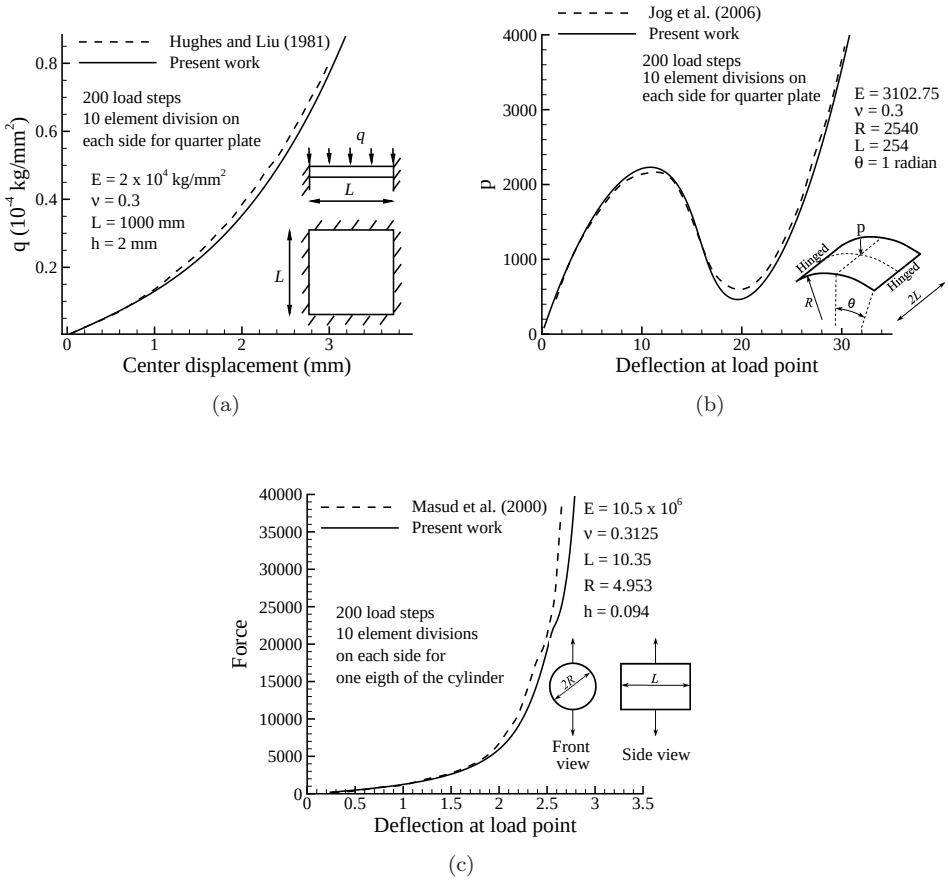

Figure 12: *Benchmark tests for the shell element. (a) Load-deflection curve for the clamped square plate subjected to a uniform pressure on its surface, compared against (Hughes & Liu, 1981). (b) Load-deflection curve for the hinged cylindrical roof subjected to a point load at the centre, compared with (Jog & Kelkar, 2006). (c) Load-deflection curve for the pinched cylinder problem, compared with (Masud* et al.*, 2000).*

Benchmark tests for the fluid dynamic model

To benchmark the fluid dynamic model we choose the problem of the translation of a sphere near a no-slip surface. This problem was also solved numerically using the method of regularised Stokeslets (Ainley *et al.*, 2008). The analytical values of the forces (per unit velocity) when the sphere translates parallel and perpendicular to the no-slip boundary are 2.6475 and 23.6605 (in units of $6\pi\mu rv$), respectively. The spacing between the sphere and the no-slip plane is very small compared to the radius of the sphere r ($0.0453r$). This results in a large velocity gradient between the sphere and the no-slip plane. The singular and non-singular integrals encountered during the integration of Eqn. 9.23 are integrated using 36 and 7 gauss points, respectively (Pozrikidis, 2002). For comparison we use the same discretisation as that of (Ainley *et al.*, 2008); the surface of the sphere is covered with equally spaced points using a spherical coordinate system and then triangulated.

The error in the forces are plotted as a function of the number of nodes used to discretise the sphere, see Fig. 13. The convergence is slow in the case when the sphere translates perpendicular to the wall. However, the convergence obtained from our method is much better than that obtained in (Ainley *et al.*, 2008). The sphere was discretised into 2718 points for an error of 11% in the perpendicular force compared to 370 points in our case.

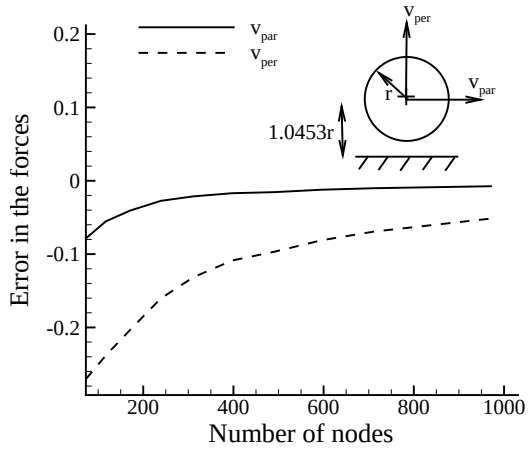

Figure 13: *A sphere translating parallel/perpendicular to the wall: Error in the forces as a function of the number of nodes used to discretise sphere.*

Benchmark test for the fluid-structure interaction model

As benchmark tests for the fluid-structure interaction (FSI) models are not available in the literature, we use a 2D FSI model (Khaderi *et al.*, 2009) to validate the present formulation. The problem chosen is the relaxation of a plate of length L, width b and thickness h subjected to an initial displacement. The plate is placed parallel to the no slip plane at a distance of $0.1L$, see Fig. 14(a). The elastic modulus of the plate is taken to be 1 MPa, and the viscosity of the fluid is taken to 1 mPas. The plate is clamped along its width, while the corresponding opposite edge of the plate is given an initial transverse

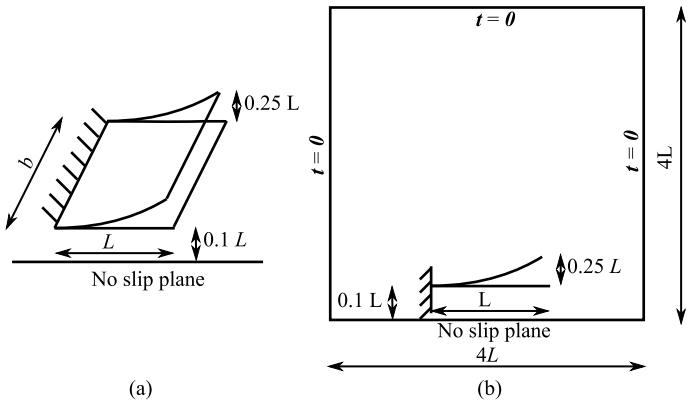

Figure 14: *Benchmark test for the fluid-structure interaction problem: (a) Schematic representation of the geometry used to benchmark the three-dimensional model. (b) The two-dimensional model.*

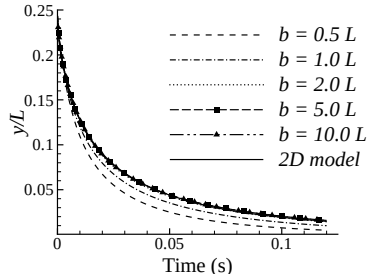

Figure 15: *Benchmark test for the fluid-structure interaction problem. Comparison of relaxation of a plate subjected to an initial displacement of the free end with the two-dimensional model.*

displacement of $0.25L$ in the direction opposite to the no-slip plane, and is released at time $t = 0$. The geometry and boundary conditions for the two-dimensional model are shown in Fig. 14(b). The response of the plate as a function of time, for different widths of the plate in the direction normal to the plane of its motion, is shown in Fig. 15. It can be seen that as the width of the plate increases the response of the three-dimensional model converges to the two-dimensional model. The beam in the two-dimensional model is discretised into 80 elements. The plate element is divided into 12 elements along L and into $12b/L$ elements along b. 36 and 7 gauss points were used to integrate the singular integral and non-singular integrals, respectively.

Benchmarking the magnetostatic model

We use the previously developed two-dimensional magneto-mechanical model (Khaderi *et al.*, 2009) to benchmark the magneto-mechanical model presented in section 9.2.4. To this end we subject a magnetic cilium to an external magnetic field, and compare the tip displacement resulting from the 2D model (Khaderi *et al.*, 2009) with the tip displacement obtained from the present model. We would like to remind that in the 2D case, the magnetic field is calculated by solving the Maxwell's equations. We take

the case of a super-paramagnetic cilium which is tapered in the thickness direction and subject it to a rotating magnetic field of $B_0 = 20$ mT with a time period of 20 ms. The length L of the film is 100 microns, the thickness h is 2 μm at the fixed end and decreases uniformly along the length, so that the thickness at the free end is 1 μm. The width of the cilium b is taken to be $2L$ (when $b > 2L$ the 3D model converges to the 2D model, see section L). The elastic modulus of the cilium is taken to be 1 MPa. The tip displacements are compared in Fig. 16. We see that the tip displacement resulting from the present model is in good agreement with the displacement computed by the 2D model in which the magnetic field is obtained from the solution of Maxwell's equations. The discrepancy between the approaches results from two sources: The fluid-solid coupling and the way the magnetic fields are calculated. To show that the error due to the fluid-solid coupling is low, we also plot the displacement of the tip of the cilium for the 2D case with the magnetic fields calculated from the magneto-static boundary conditions similar to the 3D model, see the dotted lines in Fig. 16. It can be seen that the error in the solid-fluid coupling is indeed small and the main difference comes from the way the magnetic fields are calculated.

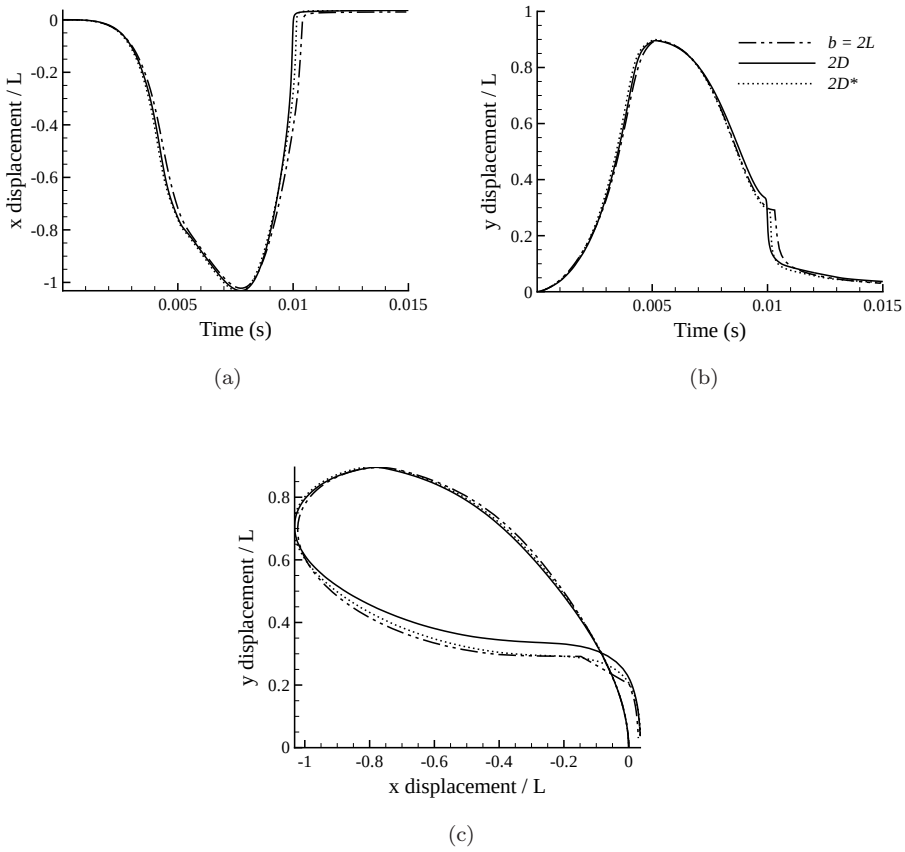

Figure 16: *Cilium tip displacement computed by solving the Maxwell's equations in a two-dimensional model (solid lines) and by using the magneto-static boundary conditions for the 3D model with $b = 2L$ (broken lines). Dotted lines represent the results from the two-dimensional model, with the magnetic field calculated using the magneto-static boundary conditions.*

Samenvatting

Lab-on-a-chip is een technologie die zich richt op het miniaturizeren van klinische tests op biologische vloeistofmonsters (zoals bloed en urine), die traditioneel worden uitgevoerd in klinische laboratoria. Een lab-on-a-chip bestaat uit een collectie 'micro-kamers' (waar de bio-analytische tests worden uitgevoerd), verbonden via micro-kanalen waar vloeistoftransport plaats vindt. In dit werk presenteren we een nieuwe manier om deze vloeistoffen voort te bewegen door transportmechanismen uit de natuur na te bootsen. Deze transportmechanismen werken in de natuur op de micrometer lengteschaal op basis van trilhaartjes (cilia genaamd) die uit-fase bewegen en hierdoor een collectieve golfbeweging vertonen (een metachronische golf). Daarnaast bewegen de individuele cilia in een asymmetrische manier met een aparte effectieve en herstelslag. Tijdens de effectieve slag zijn de cilia recht en duwen een grote hoeveelheid vloeistof, terwijl ze tijdens de herstelslag buigen, laag blijven en hierdoor slechts een kleine hoeveelheid vloestof terugduwen. De netto vloeistofvoortstuwing is hierdoor in de richting van de effectieve slag.

In dit werk hebben we kunstmatige trilhaartjes ontworpen die kunnen worden gerealiseerd met behulp van dunne polymeerlagen gevuld met magnetische nano-deeltjes. Hierdoor kunnen ze worden vervormd met behulp van een extern aangebracht magnetisch veld. Op basis van een gekoppeld magneto-mechanisch, 'solid-fluid', numeriek model hebben we uitgezocht hoe het magnetisch veld moet worden ontworpen om de asymmetrische beweging van natuurlijke cilia na te bootsen. Het fysische gedrag van de kunstmatige cilia hebben we verder bestudeerd in termen van dimensieloze parameters en de effectieve parameter-ruimte is bepaald waarin de trilharen een maximale vloeistofstroming genereren.

Het effect van verschillende factoren, zoals vloeistoftraagheid en metachronische golven, hebben we in detail in kaart gebracht. In het geval van metachronisch golven wordt de stroming tijdens de herstelslag van een cilium belemmerd door de effectieve slag van de rest van de trilharen. Dit leidt tot een drastische toename van de vloeistofstroming. De vloeistof stroomt dan continue in een richting, in tegenstelling tot de fluctuerende stroming in het geval van synchronisch bewegende trilharen. In aanwezigheid van vloeistoftraagheid zorgt de kinetische energie-input ervoor dat de stroming nog steeds in de richting van de effectieve slag plaatsvindt, ook al zijn de trilharen hun herstelslag begonnen. Ook hier leidt dit tot een aanzienlijke verhoging van de netto getransporteerde vloeistof. In aanwezigheid van vloeistoftraagheid speelt tijds-asymmetrie (verschil in snelheid van de trilharen gedurende de effectieve en herstelslag) ook een rol. Door het uitvoeren van

een parameterstudie hebben we geconstateerd dat de richting van de vloeistofstroming kan worden gecontroleerd door het afstemmen van de frequentie van het aangelegde magnetische veld.

Tot slot hebben we een numeriek model ontwikkeld om de driedimensionale 'solid-fluid' interactie van kunstmatige cilia te beschrijven. De nauwkeurigheid van het model hebben we aangetoond op basis van vele 'benchmark'-studies en we hebben de toepassingen van het model gellustreerd met behulp van een aantal fysisch-relevante voorbeelden.

Bibliography

Ainley, Josephine, Durkin, Sandra, Embid, Rafael, Boindala, Priya & Cortez, Ricardo 2008 The method of images for regularized stokeslets. *Journal of Computational Physics* **227** (9), 4600–4616.

Alexeev, Alexander, Yeomans, J. M. & Balazs, Anna C. 2008*a* Designing synthetic, pumping cilia that switch the flow direction in microchannels. *Langmuir* **24** (21), 12102–12106.

Alexeev, A., Yeomans, J. M. & Balazs, A. C. 2008*b* Designing synthetic, pumping cilia that switch the flow direction in microchannels. *Langmuir* **24**, 12102–12106.

Allman, D.J. 1984 A compatible triangular element including vertex rotations for plane elasticity analysis. *Computers and Structures* **19** (1-2), 1 – 8, special Memorial Issue.

Annabattula, R. K., Huck, W. T. S. & Onck, P.R. 2010 Micron-scale channel formation by the release and bond-back of pre-stressed thin films: A finite element analysis. *Journal of the Mechanics and Physics of Solids* **58**, 447–465.

Baaijens, Frank P. T. 2001 A fictitious domain/mortar element method for fluid-structure interaction. *International Journal for Numerical Methods in Fluids* **35** (7), 743–761.

Baltussen, M. G. H. M., Anderson, P. D., Bos, F. M. & den Toonder, J. M. J. 2009 Inertial flow effects in a micro-mixer based on artificial cilia. *Lab Chip* **9**, 2326 – 2331.

Bathe, Klaus-Jurgen 1996 *Finite Element Procedures*. Prentice-Hall, Inc.

Bathe, Klaus Jurgen & Ho, Lee Wing 1981 A simple and effective element for analysis of general shell structures. *Computers and Structures* **13** (5-6), 673 – 681.

Batoz, J. L., Bathe, K. J. & Ho, L. W. 1980 A study of three-node triangular plate bending elements. *International Journal for Numerical Methods in Engineering* **15**, 1771–1812.

Belardi, J., Schorr, N., Prucker, O. & Ruhe, J. 2011 Artificial cilia: Generation of magnetic actuators in microfluidic systems. *Advanced Functional Materials* Accepted.

Belardi, J., Schorr, N., Prucker, O., Wells, S., Patel, V. & Ruhe, J. 2010 Fabrication of articial rubber cilia by photolithography. In *Second European Conference on Microfluidics - paper no. 112*.

Blake, J. R. 1971*a* Infinite models for ciliary propulsion. *Journal of Fluid Mechanics* **49** (02), 209–222.

Blake, J. R. 1971*b* A note on the image system for a stokeslet in a no-slip boundary. *Mathematical Proceedings of the Cambridge Philosophical Society* **70** (02), 303–310.

Blake, J. R. 1971*c* A spherical envelope approach to ciliary propulsion. *Journal of Fluid Mechanics* **46** (01), 199–208.

Blake, J. R. 1972 A model for the micro-structure in ciliated organisms. *Journal of Fluid Mechanics* **55** (01), 1–23.

Blake, J. R., Liron, N. & Aldis, G. K. 1982 Flow patterns around ciliated microorganisms and in ciliated ducts. *Journal of Theoretical Biology* **98**, 127 – 141.

Blake, J. R. & Sleigh, M. A. 1974 Mechanics of ciliary locomotion. *Biological Reviews* **49**, 85–125.

Brennen, C. 1974 An oscillating-boundary-layer theory for ciliary propulsion. *Journal of Fluid Mechanics* **65** (04), 799–824.

Brennen, Christopher & Winet, Howard 1977 Fluid mechanics of propulsion by cilia and flagella. *Annual Review of Fluid Mechanics* **9**, 339–398.

Bruss, Henrik, Brask, Anders & Kutter, Jorg P. 2004 Nanofluidic components for electrokinetic micropumps. In *The Second International Workshop on Nanophysics and Nanotechnology*, pp. 149–156.

Chang, Suk Tai, Paunov, Vesselin N., Petsev, Dimiter N. & Velev, Orlin D. 2007 Remotely powered self-propelling particles and micropumps based on miniature diodes. *Nature Materials* **6**, 235–240.

Chen, Lingxin, Ma, Jiping, Tan, Feng & Guan, Yafeng 2003 Generating high-pressure sub-microliter flow rate in packed microchannel by electroosmotic force: potential application in microfluidic systems. *Sensors and Actuators B: Chemical* **88**, 260–265.

Chen, Z. S., Hofstetter, G. & Mang, H. A. 1998 A galerkin-type be-fe formulation for elasto-acoustic coupling. *Computer Methods in Applied Mechanics and Engineering* **152** (1-2), 147 – 155, containing papers presented at the Symposium on Advances in Computational Mechanics.

Childress, Stephen 1981 *Mechanics of swimming and flying*. Cambridge university press.

Cook, Robert D., Malkus, D.S., Plesha, M.E., Malkus, David S. & Plesha, Michael E. 2001 *Concepts and Applications of Finite Element Analysis*. John Wiley and Sons.

Cooper, G. M. & Hausman, R. E. 1992 *The Cell: A Molecular Approach*. John wiley and Sons.

Darnton, N., Turner, L., Breuer, K. & Berg, H. C. 2004 Moving fluid with bacterial carpets. *Biophysical Journal* **86**, 1863–1870.

Dauptain, A., Favier, J. & Bottaro, A. 2008 Hydrodynamics of ciliary propulsion. *Journal of Fluids and Structures* **24** (8), 1156 – 1165, unsteady Separated Flows and their Control.

Donea, J., Giuliani, S. & Halleux, J.P. 1982 An arbitrary lagrangian-eulerian finite element method for transient dynamic fluid-structure interactions. *Computer Methods in Applied Mechanics and Engineering* **33** (1-3), 689 – 723.

Downton, M. T. & Stark, H. 2009 Beating kinematics of magnetically actuated cilia. *EPL (Europhysics Letters)* **85** (4), 44002.

Dreyfus, R., Baudry, J., Roper, M. L., Fermigier, M., Stone, H. A. & Bibette, J. 2005 Microscopic artificial swimmers. *Nature* **437**, 862–865.

Ehlers, K M, Samuel, A D, Berg, H C & Montgomery, R 1996 Do cyanobacteria swim using traveling surface waves? *Proceedings of the National Academy of Sciences of the United States of America* **93** (16), 8340–8343.

Evans, B. A., Shields, A. R., Carroll, R. Lloyd, Washburn, S., Falvo, M. R. & Superfine, R. 2007 Magnetically actuated nanorod arrays as biomimetic cilia. *Nano Letters* **7** (5), 1428–1434.

Fahrni, Francis, Prins, Menno W. J. & van IJzendoorn, Leo J. 2009 Micro-fluidic actuation using magnetic artificial cilia. *Lab on a Chip* **9**, 3413 – 3421.

Fulford, G.R. & Blake, J.R 1986 Muco-ciliary transport in the lung. *Journal of Theoretical Biology* **121** (4), 381 – 402.

Gardiner, M. B. 2005 Importance of being cilia. *HHMI Bulletin* **18**, 32–37.

Gauger, E. M., Downton, M. T. & Stark, H. 2009 Fluid transport at low Reynolds number with magnetically actuated artificial cilia. *The European Physical Journal E* **28**, 231–242.

Gere, J. M. & Timoshenko, S. P. 1984 *Mechanics of materials*. Brooks/Cole Engineering Division.

Gerstenberger, Axel & Wall, Wolfgang A. 2008 An extended finite element method/lagrange multiplier based approach for fluid-structure interaction. *Computer Methods in Applied Mechanics and Engineering* **197** (19-20), 1699 – 1714, computational Methods in Fluid-Structure Interaction.

Gerstenberger, A & Wall, W A 2010 An embedded dirichlet formulation for 3d continua. *International Journal for Numerical Methods in Engineering* **82** (5), 537–563.

Ghosh, Rajat, Buxton, Gavin A., Usta, O. Berk, Balazs, Anna C. & Alexeev, Alexander 2010 Designing oscillating cilia that capture or release microscopic particles. *Langmuir* **26**, 2963–2968.

Golestanian, Ramin & Ajdari, Armand 2008 Analytic results for the three-sphere swimmer at low Reynolds number. *Physical Review E* **77** (3), 036308.

Gray, J. 1922 The mechanism of ciliary movement. *Proceedings of the Royal Society of London, B* **93** (650), 104–121.

Grover, William H., Skelley, Alison M., Liu, Chung N., Lagally, Eric T. & Mathies, Richard A. 2003 Monolithic membrane valves and diaphragm pumps for practical large-scale integration into glass microfluidic devices. *Sensors and Actuators B: Chemical* **89** (3), 315 – 323.

Gu, Wei, Zhu, Xiaoyue, Futai, Nobuyuki, Cho, Brenda S. & Takayama, Shuichi 2004 Computerized microfluidic cell culture using elastomeric channels and Braille displays. *Proceedings of the National Academy of Sciences of the United States of America* **101** (45), 15861–15866.

Gueron, S. & Levit-Gurevich, K. 1999 Energetic considerations of ciliary beating and the advantage of metachronal coordination. *Proceedings of the National Academy of Sciences of the United States of America* **96** (22), 12240–12245.

Gueron, S., Levit-Gurevich, K., Liron, N. & Blum, J. J. 1997 Cilia internal mechanism and metachronal coordination as the result ofhydrodynamicalcoupling. *Proceedings of the National Academy of Sciences of the United States of America* **94** (12), 6001–6006.

Halbert, SA, Tam, PY & Blandau, RJ 1976 Egg transport in the rabbit oviduct: the roles of cilia and muscle. *Science* **191** (4231), 1052–1053.

Happel, John & Brenner, Howard 1986 *Low Reynolds Number Hydrodynamics: with special applications to particulate media*. Martinus Nijhoff Publishers.

Harrison, D. J., Flury, K., Seiler, K., Fan, Z., Effenhauser, C. S. & Manz, A. 1993 Micromachining a miniaturized capillary electrophoresis-based chemical analysis system on a chip. *Science* **261**, 895–897.

Homsy, Alexandra, Koster, Sander, Eijkel, Jan C. T., van den Berg, Albert, Lucklum, F., Verpoorte, E. & de Rooij, Nico F. 2000 A high current density dc magnetohydrodynamic micropump. *Lab on a Chip* **5** (4), 466–471.

Hughes, Thomas J. R. & Liu, Wing Kam 1981 Nonlinear finite element analysis of shells: Part i. three-dimensional shells. *Computer Methods in Applied Mechanics and Engineering* **26** (3), 331 – 362.

Hussong, J., Breugem, W. P. & Westerweel, J. 2011*a* A continuum model for flow induced by metachronal coordination between beating cilia. *Journal of fluid mechanics* Under review.

Hussong, J., Schorr, N., Belardi, J., Prucker, O., Ruhe, J. & Westerweel, J. 2011*b* Experimental investigation of the flow induced by artifiial cilia. *Lab on a chip* **11**, 2017–2022.

Ibanez-Tallon, Ines, Heintz, Nathaniel & Omran, Heymut 2003 To beat or not to beat: roles of cilia in development and disease. *Hum. Mol. Genet.* **12**, R27–35.

Jackson, John David 1974 *Classical Electrodynamics*. John Wiley and Sons.

Jang, Jaesung & Lee, Seung S. 2000 Theoretical and experimental study of magnetohydrodynamic micropump. *Sensors and Actuators A: Physical* **80**, 84–89.

Jeon, N.L., Dertinger, S.K.W., Chiu, D.T., Choi, I.S., Stroock, A.D. & Whitesides, G.M. 2000 Generation of solution and surface gradients using microfluidic systems. *Langmuir* **16** (22), 8311–8316.

Jog, C. S. & Kelkar, P. P. 2006 Non-linear analysis of structures using high performance hybrid elements. *International Journal for Numerical Methods in Engineering* **68**, 473–501.

Johnson, R E & Brokaw, C J 1979 Flagellar hydrodynamics. A comparison between resistive-force theory and slender-body theory. *Biophys. J.* **25** (1), 113–127.

Khaderi, S. N., Baltussen, M. G. H. M., Anderson, P. D., Ioan, D., den Toonder, J. M. J. & Onck, P. R. 2009 Nature-inspired microfluidic propulsion using magnetic actuation. *Physical Review E* **79** (4), 046304.

Khaderi, S. N., Baltussen, M. G. H. M., Anderson, P. D., den Toonder, J. M. J. & Onck, P. R. 2010 The breaking of symmetry in microfluidic propulsion driven by artificial cilia. *Physical Review E* **82**, 027302.

Khaderi, S. N., Craus, C. B., Hussong, J., Schorr, N., Belardi, J., Westerweel, J., Prucker, O., Ruhe, J., den Toonder, J. M. J. & Onck, P. R. 2011*a* Magnetically-actuated artificial cilia for microfluidic propulsion. *Lab Chip* **11**, 2002–2010.

Khaderi, S. N., den Toonder, J. M. J. & Onck, P. R. 2011*b* Fluid flow in microchannels due to asymmetric and out-of-phase motion of magnetically-actuated artificial cilia, submitted .

Kim, Y. W. & Netz, R. R. 2006 Pumping fluids with periodically beating grafted elastic filaments. *Physical Review Letters* **96** (15), 158101.

Kinosita, H. & Murakami, A. 1967 Control of ciliary motion. *Physiological Reviews* **47**, 53–82.

Klonoff, David C. 2007 Benefits and limitations of self-monitoring of blood glucose. *Journal of Diabetes Science and Technology* **1**, 130–132.

Kopp, M. U., de Mello, A. J. & Manz, Andreas 1998 Chemical amplification: Continuous-flow pcr on a chip. *Science* **280**, 1046–1048.

Kost, G. J., Tran, N. K., Tuntideelert, M, Kulrattanamaneeporn, S. & Peungposop, N. 2006 Katrina, the tsunami, and point-of-care testing. *American Journal of Clinical Pathology* pp. 513–520.

Kundu, P. K. & Cohen, I. M. 2008 *Fluid mechanics*. Academic press.

Lai, H. & Folch, A. 2011 Design and dynamic characterization of single-stroke peristaltic pdms micropumps. *Lab Chip* **11**, 336 342.

Lanczos, C. 1952 *The variational principles of mechanics*. University of Totonro Press.

Langelier, Sean M., Chang, Dustin S., Zeitoun, Ramsey I. & Burns, Mark A. 2009 Acoustically driven programmable liquid motion using resonance cavities. *Proceedings of the National Academy of Sciences* **106** (31), 12617–12622.

Laser, D J & Santiago, J G 2004 A review of micropumps. *Journal of Micromechanics and Microengineering* **14** (6), R35–R64.

Lauga, E. & Powers, T. R. 2009 The hydrodynamics of swimming microorganisms. *Reports on Progress in Physics* **72**, 096601.

Lemoff, Asuncion V. & Lee, Abraham P. 2000 An ac magnetohydrodynamic micropump. *Sensors and Actuators B: Chemical* **63**, 178–185.

Liao, Chia-Sheng, Lee, Gwo-Bin, Liu, Hsiao-Sheng, Hsieh, Tsung-Min & Luo, Ching-Hsing 2005 Miniature RTPCR system for diagnosis of RNA-based viruses. *Nucleic Acids Research* **33** (18), e156.

Lighthill, James 1976 Flagellar hydrodynamics. *SIAM Review* **18** (2), 161–230.

Liron, N. 1978 Fluid transport by cilia between parallel plates. *Journal of Fluid Mechanics* **86** (04), 705–726.

Litster, Shawn, Suss, Matthew E. & Santiago, Juan G. 2010 A two-liquid electroosmotic pump using low applied voltage and power. *Sensors and Actuators A: Physical* **163** (1), 311 – 314.

van Loon, R., Anderson, P.D., van de Vosse, F.N. & Sherwin, S.J. 2007 Comparison of various fluid-structure interaction methods for deformable bodies. *Computers & Structures* **85** (11-14), 833 – 843.

van Loon, R., Anderson, P. D. & van de Vosse, F. N. 2006 A fluid-structure interaction method with solid-rigid contact for heart valve dynamics. *Journal of Computational Physics* **217**, 806–823.

Malone, Amanda M. D., Anderson, Charles T., Tummala, Padmaja, Kwon, Ronald Y., Johnston, Tyler R., Stearns, Tim & Jacobs, Christopher R. 2007 Primary cilia mediate mechanosensing in bone cells by a calcium-independent mechanism. *Proceedings of the National Academy of Sciences* **104** (33), 13325–13330.

Malvern, Lawrence E. 1977 *Introduction to the Mechanics of a Continuous Medium*. Prentice-Hall.

Manz, A., Effenhauser, C. S., Burggraf, N., Harrison, D. J., Seiler, K. & Flury, K. 1994 Electrosmotic pumping and electrophoretic separations for miniaturised chemical analysis systems. *Journal of micromechanics and microengineering* **4**, 257–265.

Manz, A., Graber, N. & Widmer, H. M. 1990 Miniaturized total chemical analysis systems-a novel concept for chemical sensing. *Sensors and Actuators B* **1**, 244–248.

Marmottant, P. & Hilgenfeldt, S. 2003 Controlled vesicle deformation and lysis by single oscillating bubbles. *Nature* **423**, 153–156.

Masud, A., Tham, C. L. & Liu, W. K. 2000 A stabilized 3-d co-rotational formulation for geometrically nonlinear analysis of multi-layered composite shells. *Computational Mechanics* **26**, 1– 12.

Mitran, S. M. 2007 Metachronal wave formation in a model of pulmonary cilia. *Computers and Structures* **85**, 763774.

Murase, M. 1992 *Dynamics of cellular motility*. John wiley and Sons.

Najafi, Ali & Golestanian, Ramin 2004 Simple swimmer at low Reynolds number: Three linked spheres. *Phys. Rev. E* **69** (6), 062901.

Nguyen, N. T. & White, R. M. 1999 Design and optimization of an ultrasonic flexural plate wave micropump using numerical simulation. *Sensors and Actuators A: Physical* **77** (3), 229 – 236.

Niedermayer, Thomas, Eckhardt, Bruno & Lenz, Peter 2008 Synchronization, phase locking, and metachronal wave formation in ciliary chains. *Chaos: An Interdisciplinary Journal of Nonlinear Science* **18** (3), 037128.

Oh, Kieseok, Chung, Jae-Hyun, Devasia, Santosh & Riley, James J. 2009 Bio-mimetic silicone cilia for microfluidic manipulation. *Lab on a Chip* **9** (11), 1561–1566.

van Oosten, Casper L., Bastiaansen, Cees W. M. & Broer, Dirk J. 2009 Printed artificial cilia from liquid-crystal network actuators modularly driven by light. *Nature Materials* **8**, 677 – 682.

Peskin, Charles S. 2002 The immersed boundary method. *Acta Numerica* **11** (-1), 479–517.

Pilarski, Patrick M., Adamia, Sophia & Backhouse, Christopher J. 2005 An adaptable microvalving system for on-chip polymerase chain reactions. *Journal of Immunological Methods* **305** (1), 48 – 58, the 8th International Workshop on Human Leucocyte Differentiation Antigens.

Polyanin, A. D. 2001 *Handbook of Linear Partial Differential Equation*. CRC, section 1.1.2-5.

Pozrikidis, C. 2002 *A practical guide to boundary element methods*. Chapman & Hall/CRC.

Purcell, E. M. 1977 Life at low Reynolds number. *American Journal of Physics* **45** (1), 3–11.

Qian, Bian, Jiang, Hongyuan, Gagnon, David A., Breuer, Kenneth S. & Powers, Thomas R. 2009 Minimal model for synchronization induced by hydrodynamic interactions. *Phys. Rev. E* **80** (6), 061919.

van Rijsewijk, L. 2006 Electrostatic and magnetic microactuation of polymer structures for fluid transport. Master's thesis, Eindhoven University of Technology.

Rossi, Anthony F. & Khan, Danyal 2004 Point of care testing: improving pediatric outcomes. *Clinical Biochemistry* **37** (6), 456 – 461, special Issue: Proceedings of the IX International Congress on Pediatric Laboratory Medicine.

Roth, Yehudah, Kimhi, Yosef, Edery, Habib, Aharonson, Ephram & Priel, Zvi 1985 Ciliary motility in brain ventricular system and trachea of hamster. *Brain Research* **330** (2), 291 – 297.

Sale, W S & Satir, P 1977 Direction of active sliding of microtubules in Tetrahymena cilia. *Proceedings of the National Academy of Sciences of the United States of America* **74** (5), 2045–2049.

Salsac, A. V., Biesel, D. Barthes & Tallec, P. Le 2010 Coupling of finite element and boundary integral methods for a capsule in a stokes flow. *International Journal for Numerical Methods in Engineering* pp. 829 – 850.

Satir, P & Sleigh, M A 1990 The physiology of cilia and mucociliary interactions. *Annual Review of Physiology* **52** (1), 137–155, pMID: 2184754.

Schilling, E.A., Kamholz, A.E. & Yager, P. 2002 Cell lysis and protein extraction in a microfluidic device with detection by a fluorogenic enzyme assay. *Analytical Chemistry* **74** (8), 1798–1804.

Schneider, S. 2008 Fe/fmbe coupling to model fluidstructure interaction. *International Journal for Numerical Methods in Engineering* pp. 2137 – 2156.

Schorr, N., Belardi, J., Prucker, O., Wells, S., Patel, V. & Ruhe, J. 2010 Magnetically actuated polymer flap arrays mimicking artificial cilia. In *Second European Conference on Microfluidics - paper no. 105*.

Shields, A. R., Fiser, B. L., Evans, B. A., Falvo, M. R., Washburn, S. & Superfine, R. 2010 Biomimetic cilia arrays generate simultaneous pumping and mixing regimes. *Proceedings of the National Academy of Sciences* .

Sing, Charles E., Schmid, Lothar, Schneider, Matthias F., Franke, Thomas & Alexander-Katz, Alfredo 2010 Controlled surface-induced flows from the motion of self-assembled colloidal walkers. *Proceedings of the National Academy of Sciences* **107** (2), 535–540.

Smith, D.J., Gaffney, E.A. & Blake, J.R. 2008 Modelling mucociliary clearance. *Respiratory Physiology and Neurobiology* **163**, 178188.

Smith, D. J., Gaffney, E. A. & Blake, J. R. 2007 Discrete cilia modelling with singularity distributions: Application to the embryonic node and the airway surface liquid. *Bulletin of Mathematical Biology* **69**, 1477–1510.

Squires, T. M. & Quake, S. R. 2005 Microuidics: uid physics on the nanoliter scale. *Reviews of Modern Physics* **77**, 977 – 1026.

Stone, Howard A. & Samuel, Aravinthan D. T. 1996 Propulsion of microorganisms by surface distortions. *Phys. Rev. Lett.* **77** (19), 4102–4104.

Strathmann, R. 1973 Function of lateral cilia in suspension feeding of lophophorates (brachiopoda, phoronida, ectoprocta). *Marine Biology* **23**, 129 – 136.

Studer, Vincent, Pepin, Anne, Chen, Yong & Ajdari, Armand 2004 An integrated ac electrokinetic pump in a microfluidic loop for fast and tunable flow control. *The Analyst* **129** (10), 944–949.

Svensson, S., Sharma, G., Ogden, S., Hjort, K. & Klintberg, L. 2010 High-pressure peristaltic membrane micropump with temperature control. *Microelectromechanical Systems, Journal of* **19** (6), 1462 –1469.

Tamm, S. L. & Horridge, G. A. 1970 The relation between the orientation of the central fibrils and the direction of beat in cilia of opalina. *Proceedings of the Royal Society of London. Series B, Biological Sciences* **175**, 219 – 233.

Tecplot 2008 Tec360 user manual.

Timonen, J. V. I., Johans, C., Kontturi, K., Walther, A., Ikkala, O. & Ras, R. H. A. 2010 A facile template-free approach to magnetodriven, multifunctional artificial cilia. *ACS Applied Materials and Interfaces* **2**, 22262230.

den Toonder, Jaap, Bos, Femke, Broer, Dick, Filippini, Laura, Gillies, Murray, de Goede, Judith, Mol, Titie, Reijme, Mireille, Talen, Wim, Wilderbeek, Hans, Khatavkar, Vinayak & Anderson, Patrick 2008 Artificial cilia for active micro-fluidic mixing. *Lab on a Chip* **8** (4), 533–541.

Vilfan, Andrej & Jülicher, Frank 2006 Hydrodynamic flow patterns and synchronization of beating cilia. *Phys. Rev. Lett.* **96** (5), 058102.

Vilfan, Mojca, Potocnik, Anton, Kavcic, Blaz, Osterman, Natan, Poberaj, Igor, Vilfan, Andrej & Babic, Dusan 2010 Self-assembled artificial cilia. *Proceedings of the National Academy of Sciences* **107**, 1844–1847.

West, Jonathan, Karamata, Boris, Lillis, Brian, Gleeson, James P., Alderman, John, Collins, John K., Lane, William, Mathewson, Alan & Berney, Helen 2002 Application of magnetohydrodynamic actuation to continuous flow chemistry. *Lab Chip* **2**, 224–230.

Whitesides, George M. 2006 The origins and the future of microfluidics. *Nature* **442**, 368–373.

Woolley, David M. 2010 Flagellar oscillation: a commentary on proposed mechanisms. *Biological Reviews* **85** (3), 453–470.

Wu, Jie, Lian, Meng & Yang, Kai 2007 Micropumping of biofluids by alternating current electrothermal effects. *Applied Physics Letters* **90** (23), 234103.

Y. Bourquin, J. Reboud, R. Wilson & Cooper, J. M. 2010 Tuneable surface acoustic waves for fluid and particle manipulations on disposable chips. *Lab Chip* **10**, 1898 – 1901.

Yeo, L. Y. & Friend, J. R. 2009 Ultrafast microfluidics using surface acoustic waves. *Biomicrofluidics* **3**, 012002.

Zeng, S., Chen, C., Santiago, J. G., Chen, J., Zare, R. N., Tripp, J. A., S., F. & Frechet, J. M. J. 2002 Electroosmotic flow pumps with polymer frits. *Sensors and Actuators B: Chemical* **82** (2-3), 209 – 212.

Zienkiewicz, O. C. & Taylor, R. L. 2002 *The finite element method*. Butterworth-Heinemann.

List of publications

Journal publications

- S. N. Khaderi, M. G. H. M. Baltussen, P. D. Anderson, D. Ioan, J. M. J. den Toonder and P. R. Onck, Nature-inspired microfluidic propulsion using magnetic actuation. *Physical Review E*, 2009, **79**, 046304.
- S. N. Khaderi, M. G. H. M. Baltussen, P. D. Anderson, J. M. J. den Toonder and P. R. Onck, The breaking of symmetry in microfluidic propulsion driven by artificial cilia. *Physical Review E*, 2010, **82**, 027302; selected for the September 1, 2010 issue of the Virtual Journal of Biological Physics Research.
- S. N. Khaderi, C. B. Craus, J. Hussong, N. Schorr, J. Belardi, J. Westerweel, O. Prucker, J. Rühe, J. M. J. den Toonder and P. R. Onck, Magnetically-actuated artificial cilia for microfluidic propulsion. *Lab Chip*, 2011, **11**, 2002–2010.
- S. N. Khaderi, J. M. J. den Toonder and P. R. Onck, Fluid flow in microchannels due to asymmetric and out-of-phase motion of magnetically-actuated artificial cilia. *Journal of Fluid Mechanics*, 2011, accepted.
- S. K. Namdeo, S. N. Khaderi, J. M. J. den Toonder and P. R. Onck, Swimming direction reversal of flagella through ciliary motion of mastigonemes. *Biomicrofluidics*, 2011, accepted.
- S. N. Khaderi, J. M. J. den Toonder and P. R. Onck, Fluid flow due to collective non-reciprocal motion of symmetrically-beating artificial cilia, submitted.
- S. N. Khaderi and P. R. Onck, Implicitly-coupled finite element/boundary element method for the three-dimensional fluid-structure interaction of magnetic artificial cilia, submitted.
- S. N. Khaderi, J. M. J. den Toonder and P. R. Onck, Magnetically-actuated artificial cilia: the effect of fluid inertia and metachrony, submitted.
- S. K. Namdeo, S. N. Khaderi and P. R. Onck, Chirailty-induced bi-directional swimming of artificial flagella, submitted.

Conference proceedings

- S. N. Khaderi, M. G. H. M. Baltussen, P. D. Anderson, D. Ioan, J. M. J. den Toonder and P. R. Onck, Nature-inspired microfluidic manipulation using magnetic actuators. Materials Research Society Symposium Proceedings, 2007, **1052**, 1052-DD08-06.

- S. N. Khaderi, M. G. H. M. Baltussen, P. D. Anderson, D. Ioan, J. M. J. den Toonder and P. R. Onck, Fluid propulsion in microchannels using magnetically actuated artificial, paper No. FLU08-162, 1^{st} European Conference on Microfluidics - Microfluidics 2008.

- S. N. Khaderi, M. G. H. M. Baltussen, P. D. Anderson, D. Ioan, J. M. J. den Toonder and P. R. Onck, Bio-inspired microfluidic propulsion through magnetically-actuated cilia. Materials Research Society Symposium Proceedings, 2009, **1191**, 1191-OO05-12.

- S. K. Namdeo, S. N. Khaderi, J. M. J. den Toonder and P. R. Onck, Swimming direction reversal of flagella through ciliary motion of mastigonemes, paper No. FLU2010-54, 2^{nd} European Conference on Microfluidics - Microfluidics 2010.

- S. N. Khaderi, M. G. H. M. Baltussen, P. D. Anderson, D. Ioan, J. M. J. den Toonder and P. R. Onck, Fluid propulsion in microchannels using magnetically-actuated artificial cilia: a bio-mimetic approach, paper No. FLU2010-38, 2^{nd} European Conference on Microfluidics - Microfluidics 2010.

Acknowledgements

The most important thing that I learnt during the course of my PhD is how to conduct research; and the credit goes to Patrick. Patrick, the enthusiasm you showed in every part of the work was the driving force for progress. The patience with which you tolerated all my mistakes, no matter how silly, was exceptional. Your attitude of 'tell me the physics' enabled me to see beyond the chores of computations. I consider myself to be fortunate to have you as my guide.

My sincere thanks goes to Jaap den Toonder, Erik van der Giessen and Patrick Anderson for encouraging my work by providing critical comments during every meeting we had. I also would like to thank Michiel Baltussen for the extensive discussions we had and for the enormous help provided in programming during the initial part of the project.

I would also like to acknowledge the consortium members of the European artificial cilia project for their comments and feedback on my work during the course of the project. My thanks goes to Oswald Prucker, Jerry Westerweel, Vijay Patel, Jurgen Rühe, Julian Vincent, Craus Bogdan, Daniel Ioan, Jeanette Hussong, Nicolas Schorr and Jacob Belardi.

A big thanks goes to all the members of the micromechanics department Ria, Ratna, Can, Goran, Kodanda, Ranjeet, Kapil, Ali, Siva, Sandeep, Liu, Dogan, Radu, Mathieu and Siamak for the technical and non-technical discussions we had. Outside work my interactions were mainly with Martin and Sriram. Thanks to you guys for giving me the social touch.

I would also like to thank Kapil, Siva, Sandeep, Liu, Michiel and Naveen for proof-reading the first version of the thesis and giving valuable comments.

I would like to thank the support of my parents, without which I would not have pursued a PhD degree. Finally, I would like to acknowledge the support of my wife, Mohsina, who makes sure that I realise that work is not the only thing in the world.